DOCTOR OF PHILOSOPHY

The Design and Development of a High Precision Resonator Based Tactile Sensitive Probe

Cole, Marina

Award date:
1998

Awarding institution:
Coventry University

The Design and Development of a High Precision Resonator Based Tactile Sensitive Probe

Marina Cole

A thesis submitted in partial fulfilment
of the University's requirements
for the Degree of Doctor of Philosophy

JUNE 1998

Coventry University

Declaration

This thesis is presented in accordance with the regulations for the degree of doctor of philosophy. All work reported has been carried out by the author unless otherwise stated, including the production of this document.

Acknowledgements

I would like to thank the following:

Dr. Salam M. Harb, School of Engineering, Coventry University, for his help, guidance, advice and encouragement throughout this PhD.

Mr. Peter Brennan, School of Engineering, Coventry University, for his assistance in the construction of instrumentation.

Mr. Bernard Pittaway, School of Engineering, Coventry University, for help and technical assistance.

Dr. Stuart. T. Smith, Precision Engineering Laboratory, University of North Carolina at Charlotte, USA, for invaluable help and advice in developing the mathematical model.

All the members of the Sensors Research Laboratory, Department of Engineering, University of Warwick, for encouragement during my writing up.

My husband Oliver Cole for all his patience and support.

Publications from this thesis

Journal papers:

1. Harb, S. M. and Vidic, M. *Resonator-based Touch-sensitive Probe*, Sensors and Actuators A 50 (1995) 23-29, (under maiden name Vidic).
2. Vidic, M. and Harb, S. M. and Smith, S. T. *Observations of contact measurements using a resonance based touch sensor,* Precision Engineering, Vol. 22, January/February 1998, pp. 19-36.

Conference papers:

1. Harb, S. M., Vidic, M. *Characterisation of resonator-based touch-sensitive probe,* Proc of 1st World Congress on Intelligent Manufact. Proc. & Sys., San Juan, Puerto Rico, USA, Feb. 1995.
2. Vidic, M., Harb, S. M. *Verification of high precision touch sensitive probe,* Proc. of 8th Internat. Conf. Precision Engineering, Compiegne, France, May 1995.
3. Vidic, M., Harb, S. M. and Smith, S. T. *Observations of contact measurements using a resonance based touch sensor,* Proceedings of 1996 ASPE (American Society for Precision Engineering) Annual meeting, Monterey, California, USA, Vol. 14, Nov. 1996, pp. 41-46
4. Harb, S.M., Vidic, M. and Smith, S.T. *Resonator based Profilometer Instrument,* Proceedings of Laser Metrology and Machine Performance Conference, 1997, Huddersfield, UK.

Abstract

This PhD thesis describes the design and development of a new resonator based tactile sensitive probe. This new sensor was proposed because of the increasing need for high-sensitivity, high-speed touch-sensitive probes in coordinate metrology due to the ever-growing demand for precision and reliability at sub-micron level accuracy. Extensive background research on the current development of touch trigger probes has shown that designs based on the resonator principle have potential for minimising lobing effects and the false triggering associated with most commercially available probes. Resonant based sensors have been investigated over many decades and used very successfully in a wide range of applications. However their commercial exploitation in the field of precision engineering has not been particularly successful. One reason for such slow progress is the complexity of the interaction between oscillatory probes and typical engineering surfaces in less than ideal environments. The main aim of this research was to design a high precision resonator based tactile sensitive probe and to investigate the causes of parametric changes on resonant touch sensors both before and during contact with a variety of engineering surfaces in order to achieve a better understanding of contact mechanisms. The four main objectives were: preliminary design and characterisation of a resonator based touch sensor; development of the mathematical model which predicts parametric changes on a resonant probe considering both near surface effects and mechanical contact; experimental verification of mathematical predictions; and an investigation into possible commercial exploitation of the new probe in precision applications.

A novel resonator based tactile sensor that utilises the piezoelectric effect was designed and characterised. The design exploits the fact that when a stiff element (probe) oscillating near or at its resonance frequency comes into contact with the surface of another body (workpiece), the frequency of vibrational resonance of the probe changes depending on the properties of the workpiece. The phase-locked loop frequency detection technique was employed to track changes in frequency as well as

in the phase of the resonant system. The initial characterisation of the touch sensor has shown a sensitivity to contact of less then 4 mN, a high triggering rate and good repeatability. The potential for application in measuring material properties was also demonstrated. As a result of the characterisation a comprehensive mathematical model was developed. This novel model was based on Hertzian contact mechanics, Rayleigh's approximate energy method and work carried out by Smith and Chetwynd on the analysis of elastic contact of a sphere on a flat. The model predicts that phase and frequency shift of a resonator based sensor can either increase or decrease depending on the dominant phenomena (added mass, stiffness and damping) in the contact region. Observation of dynamic characteristics at either side of the resonant frequency can be used to identify the predominant effect. In order to confirm the model experimentally, another prototype probe was developed. The new sensor was engaged in observations of contact mechanisms with engineering surfaces. The experimental results have showed favourable agreement with the developed mathematical model. This enabled a better understanding of contact phenomena uncovering possibilities for the application of resonant sensors in many other areas. The research has shown that the new probe has potential in contact measurements where it can be used for the quantitative assessment of the physical properties of different materials (modulus of elasticity, density and energy dissipation) and also in non-destructive hardness testing. It was shown that the device can be successfully used in coordinate metrology as a touch trigger probe and as a 3D vector probe. Finally, applications can also be found in surface topography as a surface characterisation instrument.

It is intended that the research described in this thesis will make an important contribution in the area of resonator based probes, providing a better understanding of the causes of parametric changes on the oscillatory sensor during contact with the object being measured. Consequently, this will enable a more effective exploitation of resonant probes for a broad range of precision applications.

Contents

Chapter 1

Introduction

1.1. Aims and objectives

A touch-trigger probe, as defined by Butler [1], is a probe that delivers a signal to indicate contact with a component. This signal could be a short pulse or a step change in voltage used to detect the coordinates at or shortly after contact. The signal could also be of continuously changing form, which is subsequently processed to produce the same effect. The last decade has seen an increasing need, both scientific and industrial, for high-sensitivity, high speed touch sensitive probes. The requirement for measurement precision, reliability at sub-micron level accuracy and the necessity to meet the ever-growing demand for high precision coordinate measuring machines (CMM) due to the expansion of coordinate metrology into many fields of industrial quality assurance as well as research and science, has already led many researchers [2-5] to investigate alternatives to the existing designs of touch sensitive probes [6,7]. The capability of measuring machines depends largely on the performance of the

probe used, therefore there is a necessity to constantly improve their performance. One of the main aims of the research described in this thesis was the design of the new resonator based tactile sensitive probe in order to overcome measurement errors associated with lobing characteristics and false triggering of traditional kinematic/resistive designs. The lobing effect is the effect of variations in the direction of approach to a surface referred to the probe itself, and eliminating it or even minimising it would be a significant contribution to measurement technology. One reason for utilising the resonator principle was that the designs based on this technology, developed in late 1980s, have been proven to meet the measurement accuracy, operational reliability, and operational life demands of modern manufacturing.

Resonator based sensors have been proposed and used successfully in wide range of applications, such as in measuring liquid or gas density and viscosity, liquid level [8], for sensing stress, pressure and mechanical forces [9,10]. Resonator sensors have also been very popular in the design of scanning probe microscopy (SPM) used for high (nm range) resolution imaging of surface structures and surface electron spectroscopy [11-14]. Other applications include coordinate measuring machine probes, stylus transducers, friction measurement, surface mechanical probes (i.e. elastic modulus, density and energy dissipation). The design of the new tactile probe exploits the fact that when a stiff element -probe oscillating near or at its resonance frequency, comes into contact with the surface of another body (workpiece), the frequency of vibrational resonance of the probe changes depending on the latter's properties. The initial design of the resonator sensor consisted of a simple tip holder attached to the end of an aluminium rod that was rigidly mounted to the probe base using piezoelectric ceramics as actuators and sensors. Drive and response signals were readily monitored in terms of frequency and phase shift of the resonant system using standard phase locking circuits.

The initial characterisation of the new touch sensor has shown a good sensitivity to contact, high triggering rate and good repeatability. A potential for application in measuring material properties was also demonstrated. As a result of the characterisation a comprehensive mathematical model was developed. The model deals with the complexity of the interaction between the resonator probe and measured specimen. Although a considerable amount of work has been carried out by many researchers on the development of resonant touch sensors, commercial exploitation for precision applications have not been particularly successful. One of the reasons for this is the complex interaction between a resonant sensor and typical surfaces in less than ideal environments. Implementation of oscillatory systems requires an understanding of the nature of the interaction between the resonating sensor and a broad variety of surfaces. Analysing the simplest type of contact, that is a contact between a smooth, frictionless sphere on a flat horizontal surface, an approximate mathematical model has been developed in this thesis in order to gain better understanding of contact mechanisms and to predict the effects characteristic of added mass, stiffness and damping. The model also considers near surface contact phenomena and the squeeze films and surface films effects. The Hertzian contact mechanics, Rayleigh's approximate energy method and work carried out by Smith and Chetwynd on the analysis of elastic contact of a sphere on a flat were used as a basis for this novel method. In general, any changes in force at the end of the probe affects the dynamics of the system causing parametric changes on the resonant sensor. The mathematical model predicts that phase and frequency shifts of the oscillator, which behaves like a second order system, can either increase or decrease depending on the dominant phenomena in the contact region. Observation of dynamic characteristics at either side of the resonant frequency can be used to identify the predominant effect.

In order to confirm the model experimentally, another prototype sensor was developed based on the same principle as the initial probe. The new design was adopted in order to achieve miniaturisation in design and versatility in applications. A practical assessment of the interaction between a resonant sensor and typical engineering

surfaces ranging from rough rubber to polished, hardened steel, and surfaces covered by liquid films having different viscosities was conducted. The interactions between the probe-tip and specimen were detected by monitoring phase or frequency shift using phase locking techniques. The experimental results have showed favourable agreement with the developed mathematical model. This part of the research has enabled a better understanding of contact phenomena revealing possibilities for the application of resonant sensors in many other areas. The new probe could have potential application in contact measurements where it can be used for quantitative assessment of physical properties of materials in contact (modulus of elasticity, density and energy dissipation) and also in non-destructive hardness testing.

The new resonant sensor was also characterised for coordinate metrology applications including a precision touch trigger probe and touch sensitive 3D vector probe. As a touch trigger probe, the new sensor has shown high accuracy, especially in the z direction (4μm) and good repeatability. However, two small areas of increasing triggering force were revealed and further refinement of the current design will be necessary in order to eliminate them. The preliminary experiments in investigating the application as a 3D vector probe to detect position and direction of approach have also been very promising, although only one contact plane was considered in this first instance of research. The angular sensitivity of the new sensor was estimated to be around 0.5 degrees in the area of higher sensitivity.

Finally, the utilisation of the probe as a profilometer instrument is also proposed in this thesis. In this application, the probe could simply be used as a nulling device in a closed loop system to profile a range of different substrates with different properties. Thus, this instrument provides useful information about engineering surfaces such as height variations, edge point detection and some surface property variations, mainly elastic modulus and density. The principle behind this application is that the resonator probe monitors the interfacial forces between the stylus and a surface specimen along z-axis by providing a feedback error signal into a digital piezoelectric

translator (DPT) which will move the probe along the vertical axis, in this way maintaining constant contact force.

To summarise, *the aims* of this thesis can be identified as the design of a high precision resonator based tactile sensitive sensor utilising the piezoelectric effect and also as a research in the causes of parametric changes on resonant tactile sensors both before and at contact with a variety of engineering surfaces in order to achieve a better understanding of contact mechanisms.

During the work on this thesis several *objectives* were achieved:

1. Design and construction of the prototype resonator probe and the associated electronic circuitry.
2. Characterisation of the new probe for applications in coordinate metrology as a touch-trigger probe
3. Developing of the mathematical model which predicts parametric changes on resonant probes due to effects of added mass, stiffness and damping for contacts with both clean solids and solids coated with contaminant films. Mechanical contact and near surface effects were considered.
4. Experimental verification of the mathematical model conducted on engineering surfaces ranging from rough rubber to polished, hardened steel, and surfaces covered by liquid films of different viscosity's.
5. Investigation into possible applications of the probe as a high precision touch-trigger probe and touch sensitive vector probe for detecting position and direction of approach.
6. Proposal that the new sensor could be used in surface topography applications for extracting parameters from the scanned specimen such as height variations, edge point detection and some surface property variations, mainly elastic modulus and density

1.2. Contents of the thesis

The way the above aims and objectives were achieved is described in seven chapters of the thesis including this introductory chapter.

Chapter 2, a literature survey set in three sections, gives an overview of the current state-of-the-art in high precision touch sensors, an overview of piezoelectric effects and resonator based sensors utilising this effect, and also gives an introduction into extracting control parameters from tactile data.

Chapter 3 deals with the problems of resonance detection and phase locked loop (PLL) technique as an important tool in determining phase or frequency shift. The characteristics of the NE 565 PLL chip (introduced by Signetics) used in this project, obtained theoretically and via the simulation program are also presented.

Chapter 4 outlines an initial design of a tactile sensitive sensor and its characterisation as a touch trigger probe. Chapter 4 also demonstrates the implementation of the touch trigger probe in monitoring the curing process of Glass Reinforced Polyester (GRP) laminate.

Chapter 5 introduces a mathematical model developed to predict effects of added mass, stiffness and damping on the resonant sensor when near or in contact with clean solids. The model also considers near surface contact phenomena and the squeeze film and surface film effects.

Chapter 6 in its main part describes experimental verification of the mathematical model presented in Chapter 4. It outlines characterisation of the new sensor as a touch trigger probe and also its possible application as a high precision touch sensitive vector probe for detecting position and direction of approach. A proposal for the application of the new design in surface topography is presented in this chapter.

Chapter 7 discusses the work carried out during this project outlining the advantages of the new tactile sensitive sensor, main contributions to the knowledge and also possibilities for improvement. It gives some ideas and guidance how this work could be carried and developed further.

Chapter 2

Literature survey

2.1. Introduction

In the introduction to this thesis the main objective has been set up as the design and development of a high precision resonator based tactile sensitive probe. The possible applications of the probe in coordinate metrology, contact measurements and in scanning applications were the main areas of research interest. Therefore it was necessary to have a view on the current state-of-the-art in high precision touch sensors and to carry out a literature review in the areas of interest for this project.

The literature survey is set out in three sections. The first section gives an overview of the design and applications of the probes in current use and reasons and motivation for designing a new touch-sensitive resonator -based probe.

The second section is a detailed review of the key papers in the field of resonator based probing systems, highlighting those which utilise piezoelectric properties and their applications in scanning probe microscopy. The introduction to this section explains the piezoelectric effect itself giving support for the discussion on performance of systems with piezoelectric actuators. Vibrations of piezoelectric bars and plates are also reviewed to a certain extent to give an overall understanding of the dynamic applications of piezoelectric crystals.

Finally, the third section deals with tactile sensors giving an introduction to the terminology with a focus on piezoelectric based sensors. Extracting control parameters from tactile data is an important part of this section, which gives an insight on the different applications of tactile sensors.

2.2 Design principles of currently used touch trigger probes

This section examines a number of touch trigger probe designs which have motivated the study in this thesis. It includes examples of the most commonly used probes such as touch trigger probes based on a electro-kinematic design, an optoelectronic probe, a fibre optic touch probe, and a touch trigger probe with a polyvinilidene film (PVDF) sensor.

Coordinate metrology and the performance of measuring machines is highly dependent on the accuracy of the probes used. Some coordinate measuring machines (CMM), in current use, employ touch-trigger probes which rely on the breaking of electrical continuity when the probe makes contact with a surface. These are mainly Renishaw-type probes with small ruby beads (down to 0.3 mm in diameter) used as a probe heads. Others CMMs use the Carl Zeiss'* dynamic probe head with a piezoelectric sensor, Heidenhain† optoelectronic probe etc.

* Carl Zeiss, D-7082 Oberkochen, Germany
† Dr. Johannes Heidenhain GmbH, Dr.-Johannes-Heidenhain-Strase 5, D-83301 Traunreut, Germany

2.2.1. Electro-kinematic probe

The electro-kinematic probe has been designed by McMurtry [15] and has currently been mainly produced by Renishaw. The distinguishing feature of most Renishaw-type probes (TP1 (S), TP2, TP6) [7] is the kinematic mount to which the probe base is fixed. A typical design is shown in Figure 2.1. It consists of three rollers located on three pairs of ball bearings, or alternatively, three balls located on three pairs of rollers. The contact between the rollers and the balls form a part of an electrical circuit. When the probe tip contacts the surface being measured the probe stylus is deflected from its normal resting position. This contact causes at least one of the three circuits to open, providing a signal to the controlling circuits to register the point of contact. The probe is designed to provide a trigger signal as soon as possible after mechanical contact with the surface occurs The kinematic mount, with its three point contact, leads to variation in the measurement force and in the displacement of the measuring tip from the initial position before the trigger signal is generated. This variation depends on the speed of approach, angle of contact and the length of the probe stylus.

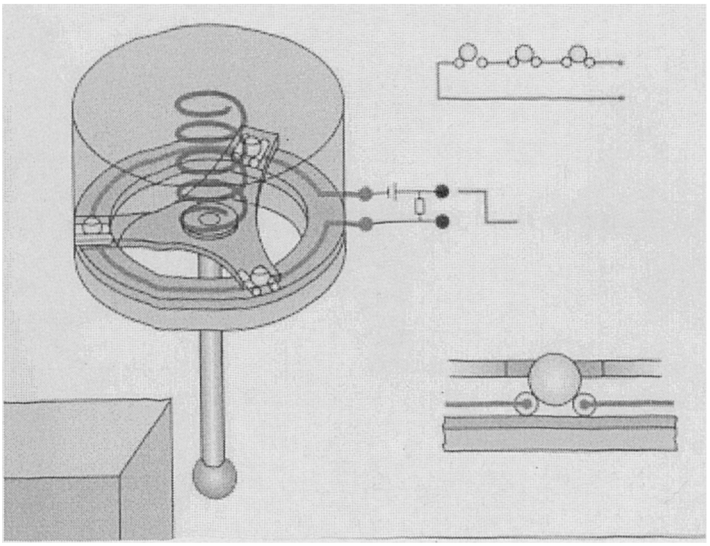

Figure 2.1. Switching probe head: an electro-mechanical principle [6]

The probe error sources which affect Renishaw touch trigger probes [7] are probe repeatability, pre-travel variation (lobing) and probe hysteresis.

2.2.2. Piezo sensor probe

Probes incorporating piezo-based sensors were developed to overcome measurement errors associated with lobing characteristics of electro-kinematic design. The designers of Carl Zeiss [6] find that the electromechanical principle [15] is subject to a certain loss in accuracy, this being a function of the prestressing and the probing direction. The difficulties could be eliminated by using a piezoelectric sensor which displays identical sensitivity from all probing directions and always generates the trigger pulse before the mechanical contact opens. Dynamic probe heads of this design are a good choice in cases where individual points must be measured at high speed. For automatic operation, it is possible to probe up to 60 points per minute [6]. In 1994 Carl Zeiss introduced a probe element for coordinate measuring systems [16] comprising a set of piezo-resonators configured in a polygonal pattern on which a set of micro-probes was mounted, also in polygonal pattern. It has been designed to trace inner and outer surface contours at various coordinates. Contact between the micro probes and the surface of the sample is detected by measuring the changes in the resonance characteristics of the piezo-resonators. Since the triggering point in piezo-based sensors is dependent on the stress generated at the moment of contact, care must be taken when selecting component material, stylus tip mass and touch speeds.

A contact sensing head introduced by Sigg *et al.* [17] should also be mentioned because of its ability to use a piezoelectric mechanism. It was designed for a measuring device able to detect the position of contact points between a sensor and an object to be measured. It comprises a sensor having a free end vibrated with low amplitude (order of ± 0.1 μm) at the resonant frequency. A transducer detects the vibrations and feeds a signal to an electronic system. When a sensor contacts an object, the frequency and amplitude of its oscillation change. This is picked up by the

detection system, and the coordinates of the contact point are recorded. According to the inventors, the measurement precision supplied by the sensing head was only to a slight extent dependent on the length of the sensor.

2.2.3. The touch trigger probe with PVDF sensor

A touch trigger probe with polyvinilidene film (PVDF) sensors for use in a 3D coordinate measuring machine (CMM) is described in [3] by Haeusler and Rech. The sensor consists of a circular PVDF film sheet (diameter 2 cm, thickness 20 μm) divided into three electrically insulated segments (Figure 2.3.).

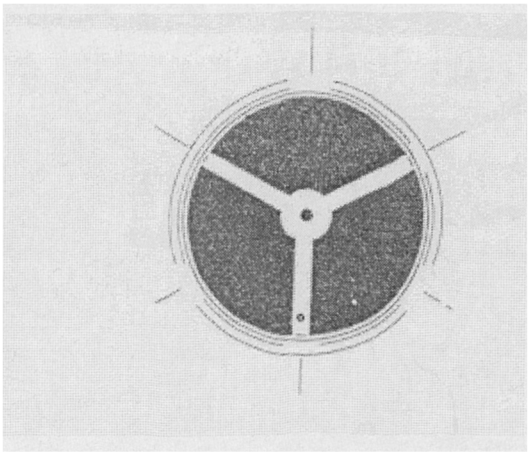

Figure 2.2. A circular PVDF film sheet divided into three insulated segments [3]

The mechanically prestressed PVDF film sensor generates an electric signal if the probe touches an obstacle, which is independent of the direction of contact (axial or transverse). A purpose of this design is to overcome problems with high contact force associated with commercially available touch trigger probes. In this case Haeusler and Rech aimed at reducing the required contact force using very sensitive piezoelectric sensors. The touching stylus is fixed at the force initiation plate. Tangential force at the stylus produces bending stresses of the piezoelement. By dividing the piezoelement into three segments, three separate trigger signals will be

generated by bending forces. In this case the contact force is, depending on the stylus length, in the order of 10 mN. One of the disadvantages associated with this probe is false triggering. To overcome this Haeusler and Rech suggest another mechanical switch to be included in circuitry which would be activated after the electric trigger signal. The coordinate values of the trigger point will be valid only after the mechanical switch is activated. This affects the speed of the probe, increases cost and makes the design more complicated. Another problem associated with this probe is lower sensitivity in the z-direction. The authors suggested that axial sensitivity can be obtained with changes in electrical signal processing which would affect the design of the electronic circuitry.

2.2.4. Spherical potentiometer touch probe

A touch probe based on a spherical potentiometer [4] is able to directly detect the contact point between the surface of the measuring object and itself. The proposed probe is made of an insulating ceramic ball covered with a thin resistant film and four electrodes which are symmetrically allocated on the upper part of the probe ball (Figure 2.4.). The probe is of a simple construction and does not have any complex sliding, moving and positioning mechanisms. The four electrodes located on the probe ball are connected to a positive electrode of a constant current source, while the object being measured is connected to a negative electrode of the source.

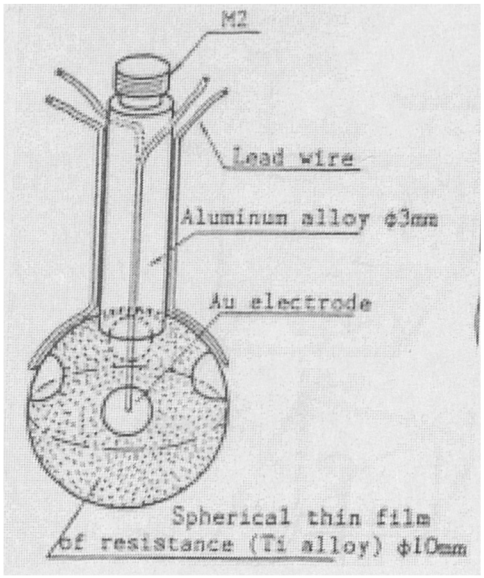

Figure 2.3. The spherical potentiometer touch probe [4]

If the probe ball is in contact with the object to be measured, a constant current flows from the contact point to each electrode. The developed probe did not have any functions to prevent collision with the measuring object. Therefore, the Renishaw TP2 probe head and the Renishaw PH9 motorised probe head were used when developing the probe for practical measurement. The TP2 probe head had the ability to release the developed probe on collision with the object being measured. The PH9 motorised probe head had a function to control the measuring attitude of the developed probe. The main disadvantage associated with this probe is that it can only be used on object made out of conducting materials. Application of the spherical potentiometer touch probe in circumstances where high flexibility is required is limited because detection of contact point requires a constant current circuit.

Development of the above probe has been carried further towards its application for detecting position vectors and unit normal vectors [18]. Since the centre of the sensor can be detected by a CMM and the sensor is a sphere, the direction from a contact point to the centre of the sensor becomes equivalent to the normal direction of a measured point, that is, the unit normal vector of it. The position vector is derived

from the radius of the sensor, the unit normal vector of a measured point, and the position vector of the centre of the sensor. The measurement accuracy of the developed contact sensor is 10 μm on detecting a position vector and 0.1 degrees on detecting a normal direction.

Another spherical tactile sensing probe for coordinate measuring machines was developed by Shinoda et al. [5] utilising piezoelectric material, very similar in design to one of Aoyama et al. [4]. The proposed sensor is composed of piezoelectric polymer film, resistance layer and electrodes, and is able to detect the contact point from an electric charge on the electrodes, which is generated at the contact point. The thickness of the sensor (100 - 150 μm) and its softness allow its application to a curved surface. A column-shaped probe utilising the above sensor was also developed for the detection of the θ-coordinate. Results of θ-coordinate detection obtained by experiment were not accurate enough to contribute to the improvement of measuring accuracy, but authors claim that they could be improved by using electric signal with better signal to noise (S/N) ratio. The main advantage of Shinoda's design over Aoyama's is that detection of contact point does not require a constant current circuit.

2.2.5 Optoelectronic probe

Butler and his co-authors [2,19,20] proposed a probe which employs optical switching rather than mechanical switching for triggering (Figure 2.2.). An optoelectronic system (OS), working on polar coordinates, has been developed for this probe. The light is conveyed from an infra-red source through an optical fibre on to a concave mirror. The radius of curvature of the mirror is such that all of the light is reflected back into the fibre when the probe is in its undisturbed position. T his probe system was used to record the coordinates of a point repeatedly fifty times and the designers claim that an error in measurement was within one micron. It requires relatively low contact force of about 5 mN which is an improvement in comparison with

commercially available probes. The main disadvantage of the system is the asymmetry of the spring assembly.

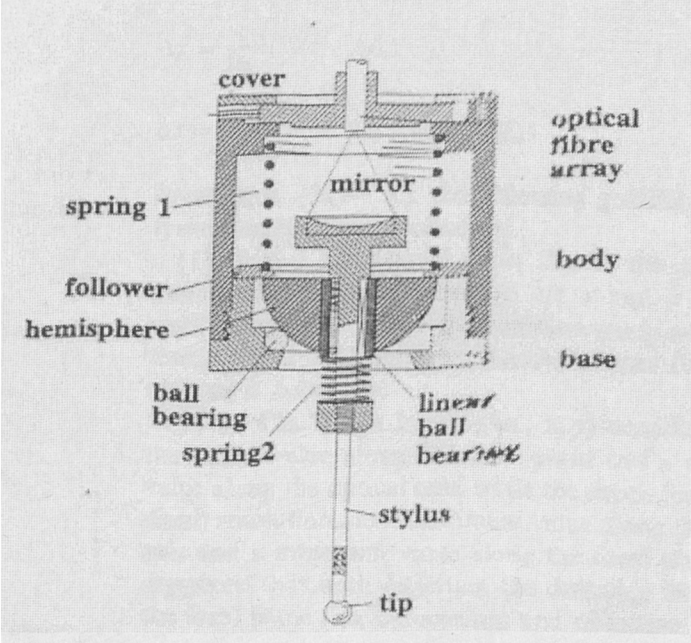

Figure 2.4. An optoelectronic probe [20]

The triggering signal level and sensor sensitivity depend on several factors, including the light-source intensity, the fibre parameters (e.g. diameter), and the position of the fibre. According to ring gauge results for the optoelectronic (OE) probe [20] the overall error of the OE probe is slightly less than the touch trigger probe, namely 6 microns compared to more than 7 microns for a 40mm long stylus which suggests that the OE probe is still suffering from 'lobing effects'.

The German company Heidenhain[‡] manufactures another type of optoelectronic touch trigger probe.

[‡] DR. JOHANNES HEIDENHAIN GmbH, Dr.-Johannes-Heidenhain-Strase 5, D-83301 Traunreut, Deutschland

2.2.6. Micro-strain gauge probe

Probes based on strain gauge technology were developed in the late 1980s and have been proven to meet the measurement accuracy, operational reliability, and operational life demands of modern manufacturing [21]. To measure the three coordonates a minimum of three silicon strain transducers are arranged on a stiff structure, electrically forming half-bridges, such that as the stylus is displaced, the resulting strains are measured. Semiconductor strain gauges are grown from mono-crystaline silicon with a controlled electrical impurity, so when the gauge is strained by movement, a change in resistance occurs. The example for such probes is the Renishaw TP200 [22].

Probe error in terms of pre-travel variation is minimised since the stiff probe structure can be made sensitive to micro-strains. Probe repeatability is in order of 0.25 μm (2 sigma). One characteristic of strain gauges is that temperature gradients cause changes in gauge resistance and the gauge factor, together with apparent strains due to the differential expansion of the gauge and the substrate. Therefore, a reference device for comparison, which remains unaffected by such changes, is essential for the operation of this type of sensor.

2.2.8. Quartz micro probe

The Quartz Micro Probe (QMP) has advantages in measuring very small components and miniature features. It has originated from the quartz clock technology. A quartz tuning fork is activated by an oscillator and the vibrations are transferred to a glass fibre [21]. A miniature probing sphere is located at the end of the glass fibre. Contact with the workpiece is recognised via the resonance frequency and registered as a probing impulse. This system operates as a touch trigger probing system. The

probing uncertainty of 2.5 μm in the direction of glass fibre and less than 5 μm with lateral probing enables the measurements of precision parts made of plastic or metal.

2.2.9. Probes on coordinate measuring machines

All probes used on coordinate measuring machines contribute to the uncertainty of measurement of the machine [7]. The magnitude of error depends on the probe type and the way in which it is used. Currently there is no standard (Butler [19]) or other generally agreed method of describing the performance of probes, except those advocated by manufacturers. Probe errors are typically small when compared to overall system accuracy. However under certain circumstances, such as when using long styli, the probe can contribute significantly to the uncertainty of measurement.

Most touch trigger probes show a variation in pre-travel which is dependent on the direction of probing [23]. This is due to difference in stylus bending prior to trigger caused by variations in trigger force. These points of increasing trigger force often reach maximum at three points roughly 120° apart in a 360° probing plane. This is often known as a probe 'lobing'. The presence of probe lobing can be a dominant source of error in highly repeatable machines and my cause significant errors in many CMM measurements. Calculating a model for error compensation for CMM touch trigger probes Estler *et.al.* [23] found that for most probe trigger events, displacement of the probe tip is also accompanied by sliding on the part surface, a motion that is resisted by the frictional force between the stylus tip and the surface.

Renishaw's latest TP200 probe [24] reduces errors associated with pre-travel variation, by isolating measuring sensor from the re-seating mechanism, reduces measurement uncertainty from the probe by as much as factor of ten as Renishaw claims, even with stylus lengths of 70 mm. The TP200 uses solid state sensors and ASIC (Application Specific Integrated Circuitry) micro electronics, creating a fundamental change in the basic technology used in touch-trigger probes.

Probe hysteresis is an, often overlooked, systematic error which is present in virtually all types of probe design. It occurs as a direct consequence of the direction of the previous trigger and reset. It is claimed that in kinematic/resistive touch trigger probes, hysteresis error is of the same order of magnitude as probe repeatability, but is more sensitive to increased stylus length and trigger force. In the field of precision engineering there can be problems using forces greater then 0.1 N which could result in the distortion of thin samples.

The probe stylus is tipped by a spherical head (usually ruby) and compensation for the stylus tip diameter, by computation, is always required since the initial coordinates recorded are not the true coordinates of the contact point. Thus, the diameter of the spherical head can not be ignored and could be another error source [21].

False triggering is another source of error which can occur in probes. One of the latest Renishaw probes, TP12, had good accuracy (0.25 μm) when tested on Renishaw test rigs and it did not suffer from lobing error, but when mounted on a CMM the motion of the machine caused false triggering to such degree that the probe was unusable. Another disadvantage associated with this probe was that to ensure high accuracy readings and trouble free operations, all components measured with a TP12 had to be thoroughly cleaned, which is unlikely in engineering environment.

2.3. Resonator sensors based on piezoelectric properties

Resonator based sensors have been proposed and used successfully in a wide range of applications, including sensors for liquid or gas density and viscosity [8,25], liquid level, mass, microbalance [26], and also for sensing stresses, pressure and mechanical forces[9.10]. Many variants on the basic resonator principle can be devised for different sensor requirements, while the measurement of electric field through the piezoelectric effect opens the door to the use of resonator devices in a wide range of

measurements. Resonator sensors have also been very popular in the design of scanning probe microscopy (SPM), which is used for high resolution imaging of surface structures and surface electron spectroscopy [27-30].

2.3.1. Introduction to resonator-based sensors

Describing principles of resonant sensing Beeby [31] defines that *at the heart of the sensor is the resonator, an oscillating structure vibrating at its resonant frequency. The sensor is designed such that the resonator's natural frequency is a function of the measurand. The measurand typically alters the stiffness, mass or shape of the resonator hence causing a change in resonant frequency.* Important components of a resonant sensor are the excitation and detection mechanisms. The drive or excitation mechanisms can be thermal, using either implanted resistors or pulsed laser light, piezoelectric, electrostatic or magnetic. Detection mechanisms can use change in resistance of an implanted resistor (piezoresistance), change in capacitance between electrodes or optical techniques to detect vibrations. The output of the sensor is the frequency of detected vibration and this signal is at the same time feed back to the drive mechanism. This way the structure is maintained at resonance over the entire mesurand range. A block diagram of a resonant sensor is shown in Fig. 2.5 [31].

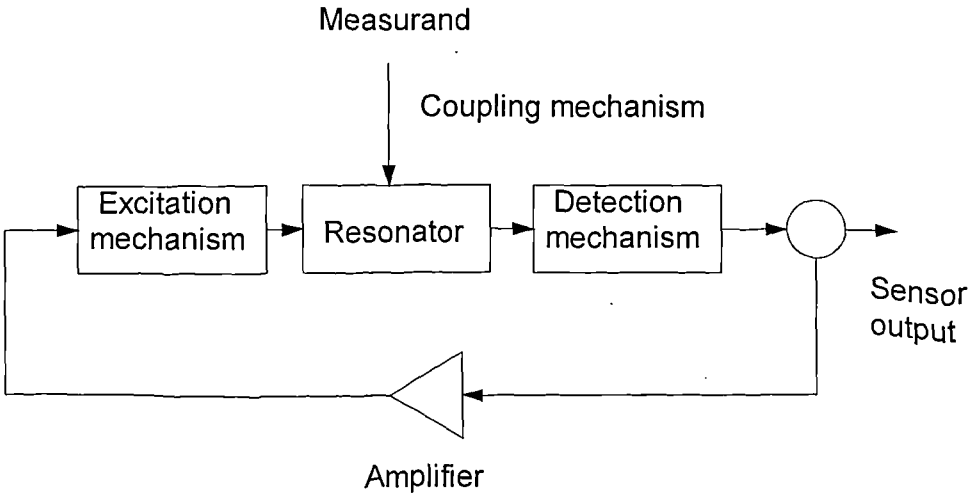

Figure 2.5. Block diagram of resonant sensor layout

The most common sensing mechanism uses frequency of vibration which is affected by applying a stress through the contact with the resonator, increasing its stiffness, which results in an increase in its resonant frequency. This principle is commonly applied to force sensors, micromachined pressure transducers and accelerometers.

As well as by varying the tension in a resonator, its frequency of vibration can also be affected by changing its mass, for example by surrounding it by liquid or gas, or by depositing solid material on its surface. The vibrations of the resonator cause some movement in the surrounding material which effectively increases its inertia, therefore decreasing its resonant frequency. If this technique is used for measuring solids, it is generally restricted to applications where the applied mass is small such as film thickness gauges and microbalances. A good example of a mass coupled resonant device for solid material applications is the quartz crystal sensor, used to detect the thickness of thin film deposited on a substrate in a vacuum chamber [31].

2.3.2. Piezoelectric effect and linear piezoelectric model

Piezoelectric excitation and detection mechanisms were employed in the design of a new resonator sensor which will be described in this thesis, so this section will give an introduction into piezoelectricity.

Piezoelectricity is one of the basic properties of, ceramics, polymers and liquid crystals. There are several ways to describe the piezoelectric effect. Perhaps the most common definition is that *a material is piezoelectric if the application of an external mechanical stress causes the development of an internal dielectric displacement* [32]. This displacement is manifested as an internal electric polarization or a surface electric charge.

The piezoelectric effect itself was discovered in 1880, by Jacques and Pierre Curie[§]. They demonstrated that when a stress in the form of a weight was applied to a crystal of quartz a proportional electrostatic polarization was generated along an axis at an angle to the direction of the stress to a sufficient magnitude that the charge on the surface could be detected by an electrometer. By the end of 1881, the Curie brothers had also demonstrated the existence of the inverse piezoelectric effect.

A very simple mathematical definition of piezoelectric effect could be based on the fact that if any crystal is exposed to a force, its atoms would be displaced slightly from their normal positions in the lattice. This displacement x is proportional to the applied force F:

$$x = \frac{1}{k} F \tag{2.1}$$

where the stiffness k of the crystal is large, typically $2 \times 10^9 \mathrm{Nm}^{-1}$ [34].

The dynamic relation between x and F can be represented by the second order transfer function [34]:

$$\frac{\Delta \bar{x}}{\Delta \bar{F}}(s) = \frac{1/k}{\frac{1}{\omega_n^2} s^2 + \frac{2\xi}{\omega_n} s + 1} \tag{2.2}$$

where $\omega_n = 2\pi f_n$ is large, typically $f_n = 10$ *to* $100 kHz$, and ξ is small, typically $\xi \approx 0.01$.

When force is applied to a piezoelectric crystal, the deformation of the crystal lattice results in the crystal acquiring a net charge q, proportional to x,:

$$q = Kx \tag{2.3}$$

where K is constant of proportionality.

[§]The detailed history of the discovery of piezoelectricity and its application in practical devices had been reviewed by Pointon [33].

Thus from the Equations (2.1) and (2.3) it could be derived a simple definition of the direct piezoelectric effect:

$$q = \frac{K}{k}F = dF \tag{2.4}$$

where $d=K/k$ in coulombs newton^{-1} is the charge sensitivity to force. This way a piezoelectric crystal gives a direct electrical output, proportional to applied force, so that a secondary displacement sensor is not required.

Similarly, an inverse effect could be defined as : $x=dV$, where a voltage V applied to the crystal causes a mechanical displacement x.

The applications of piezoelectricity arise from [33]

(i) the conversion of a mechanical stress into an electrical signal,

(ii) the generation of a controlled strain by an electric field,

(iii) the generation, detection and amplification of elastic waves,

(iv) the processing and storage of electrical signals by elastic waves or through electro-optic effects,

(v) the existence of electromechanical resonance.

The piezoelectric devices could be divided into three main categories:

(1) Low frequency devices: force sensors and transducers, accelerometers, position transducers, spark generators, fine displacement actuators.

(2) Audio devices: microphone heads, stereophonic pick-ups, stable oscillators, loudspeakers, audio tone generators, high voltage (HV) transformers.

(3) RF (bulk wave or surface wave)devices: high-power ultrasonic generators, high frequency ultrasonic generators/detectors, miniaturisation of guided-wave systems, delay lines, signal processors, resonators and filters, electroacustic devices, signal storage.

In crystals which show piezoelectric properties, mechanical quantities such as stress (T) or strain (S), and electrical quantities such as electric field (E), electric displacement (flux density (∅)) or polarisation (P), and a displacement D are interrelated. This phenomenon is called electromechanical coupling [35]. In the notation of IEEE Standard 176-1978 [36], the linear coupled electromechanical constitutive relations are:

$$D = dT + \varepsilon^{T} E \tag{2.5}$$

$$S = s^{E} T + d_t E \tag{2.6}$$

where ε^T, s^E, and d are permittivity, compliance and piezoelectric coefficient matrices. The superscripts T and E signify that these are quantities taken at constant (or zero) stress (called -"free"), and constant (or zero) field (called - "short circuit"). If the surface area is not changed by the stress (a condition not satisfied for polymer films) $d=d_t$.

Alternative equations can be written such as:

$$E = -gT + D\left(\varepsilon^{T}\right)^{-1} \quad \text{or} \quad E = -hs + D\left(\varepsilon^{S}\right)^{-1} \quad \text{or} \quad T = c^{E} S - eE \tag{2.7}$$

where $g=d/\varepsilon^T$ is called the piezoelectric voltage constant, $e=d/s^E$ is called the piezoelectric stress constant and $h=g/s^D$ is simply called the 'h constant'.

Some parameters that characterise a piezoelectric crystal also have following definitions:

1. *Piezoelectric strain constant.* The strain and applied voltage are proportional in a polarized crystal. The relationship can be expressed as

$$\frac{\Delta l}{l} = Ed, \tag{2.8}$$

where l is original length of the crystal, Δl is change in length and E is applied voltage. The proportionality constant d is called the piezoelectric strain constant.

2. *Poisson's ratio.* Poisson's ratio is a parameter which indicates relative deformations in the longitudinal and transverse directions. Specifically, it is the ratio of transverse elongation to longitudinal contraction when a pressure is applied to a solid at a constant voltage, or

$$\sigma^E = \frac{S_{31}}{S_{33}} \tag{2.9}$$

where a superscript denotes a non-varying parameter during state changes; thus σ^E is Poisson's ratio when the applied voltage is kept constant. Subscripts indicate axis directions for cause and effect, thus S_{31} is the strain in the x-direction caused by a pressure in z-direction; similarly a pressure in z-direction creates a strain in the z direction represented by S_{33}.

3. *Directionality of the piezoelectric strain constant.* If deformations are caused by an electric field,. Poisson's ratio cannot be used for determining the relative deformations. In this case, the piezoelectric strain constants, which possess directional qualities as well, are used. The strain constant in the z-direction (for the longitudinal effect) is usually represented by d_{33}. That is,

$$\Delta z/z_0 = d_{33}E_z \tag{2.10}$$

The values of all parameters are temperature sensitive, and there is an upper temperature at which the material will lose its piezoelectric characteristics; this upper temperature is known as the Curie temperature and it has different values for different piezoelectrics.

The electromechanical coupling has also a form of[**]:

[**] A complete treatment has been given by Huston and White [37]

$$\rho\frac{\partial^2 u}{\partial t^2} = c\left(\frac{\partial^2 u}{\partial x^2} - \frac{\partial E}{\partial x}\right) \tag{2.11}$$

where u is the material displacement at position x and time t, ρ is the density and c Young's modulus of the material.

Thus an alternating field will generate an elastic wave of the same frequency and the elastic wave will give rise to a varying polarisation. If the electrical energy stored in the material is W_e, and the corresponding mechanical energy to which it may be converted is W_m, then the coupling between them is defined as:

$$k^2 = \frac{W_m}{W_e} = \frac{d^2}{\varepsilon^T s^E} \tag{2.12}$$

where k is called coefficient of electromechanical coupling.

In the analysis of piezoelectric structures by a finite element method [38, 39] the constitute piezoelectric model was described. The model was derived having a basis in the equations of piezoelectricity (2.7) and equations corresponding to both mechanical and electrical balances and decupling (2.11). The piezoelectric model has been derived using tensorial equations and it has a form:

$$\begin{aligned} &T = C^E S - e^t E \\ &D = eS + \varepsilon^S E \\ &\rho\frac{\partial^2 U}{\partial t^2} = \nabla T \\ &\nabla D = 0 \\ &\textit{with} \quad S = \hat{\nabla} U, \quad E = -\nabla e \end{aligned} \tag{2.13}$$

where C^E is the elasticity tensor, ∇ is divergence operator, $\hat{\nabla}$ is the symmetric gradient operator and e is electric potential.

In a restricted environment the above model must be completed by boundary conditions. The boundary and initial conditions, as well as the governing equations were, also, described by Tanaka *et. al.* [40] applying a boundary element method to linear piezoelectric problems.

Among various piezoelectric phenomena, the longitudinal and transverse effects (Figure 2.6) are particularly important. In the longitudinal effect, deformations take place parallel to the electric axis; in the transverse effect, deformations occur at right angles to the electric axis. In practice these two types of effect take place at the same time. Moreover, a third torsional effect is also known.

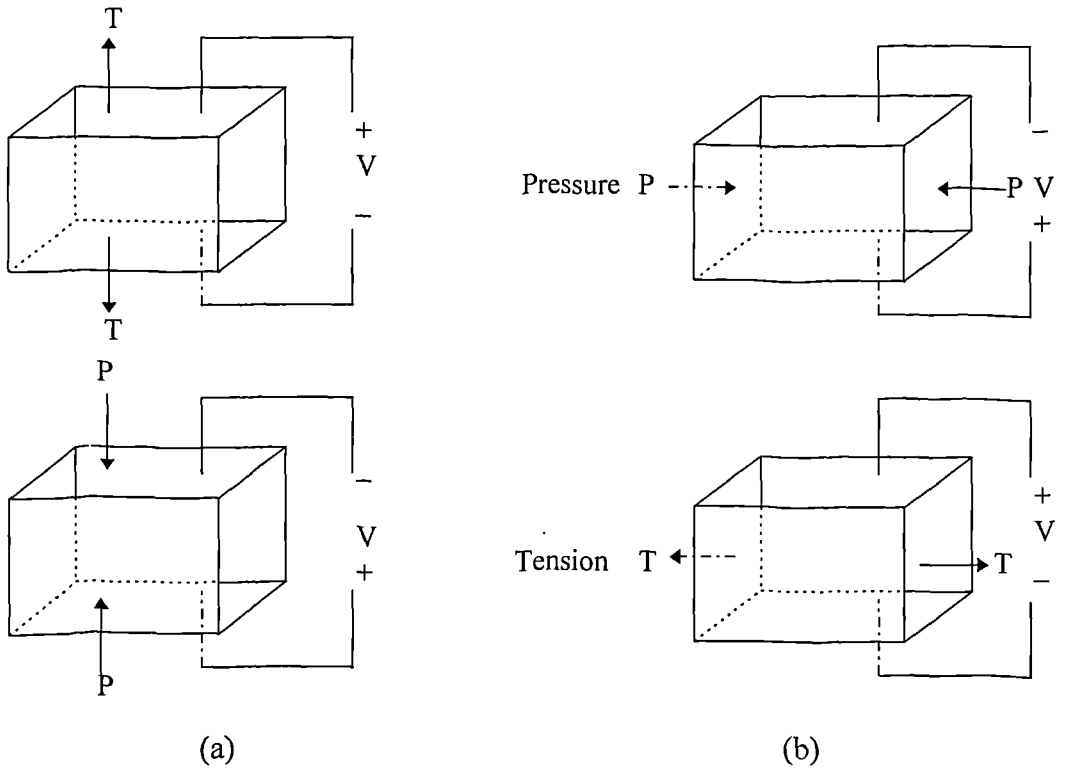

Figure 2.6. The piezoelectric effect: **(a)** longitudinal effect; **(b)** transverse effect

Piezoelectric materials in current use include poly-vinylidene fluoride (PVDF) [3], a semicrystalline polymer film, and lead zirconate titanate (PZT), a piezoelectric ceramic material. As well as the other piezoelectrics, these materials strain when exposed to a voltage and produce voltage when strained. This property exists because

of the permanent dipole nature of the materials; during the manufacture of piezoceramics, a large (> 1 kV/mm) electric field is applied across the ceramic to orient the crystallites into an initial polarization. The properties of ideal piezoelectric material would include:

1) chemical and physical stability;
2) cheapness and reproducibility;
3) easily manufactured to a desired configuration;
4) insensitive to temperature and ageing;
5) appropriate elastoelectric coefficients;
6) linear to high amplitude oscillations.

There is no material which would satisfy all these requirements simultaneously, but there are some of trade-offs which could be made between the single crystals, quartz and lithium niobate in particular, and as it has been stated, the lead-zirconate-titanate ceramics and, now, the PVF_2 (or PVDF) polymers.

In [33] Pointon has presented review of piezoelectric devices including their application as low-frequency devices such as: force transducers, accelerometers, spark generators, pressure transducers, bimorph systems and strain gauges. He had also reviewed 'acoustic' devices, bulk oscillators, piezoelectric bulk filters, surface-acoustic-wave devices and very-high-frequency transducers. Application of piezoelectrics as strain gauges has been exploited in this project and will be detailed in due course.

2.3.3. Vibrations of piezoelectric bars and plates

From the preceding text it could be concluded that in piezoeletricity the quasistatic electric field is coupled to the dynamic mechanical motion, and that the equations of linear elasticity are coupled to the charge equations of electrostatics by means of piezoelectric constants. Tiersten [41] gives a systematic derivation of the equations

and relevant boundary conditions of the linear piezoelectric plate vibrations. All calculations were based on the linear theory of piezoelectricity foundations of which were also given in the preceding text. Hence only the basic elements of piezoelectric vibrations will be given in this section.

A piezoelectric parallelepiped, as a physical body with a higher degree of freedom, can vibrate in several different modes [35, 42-44] but the vibration of a very thin and narrow bar can be taken as a one-dimensional problem, as the dominant deformations appear only along the longitudinal axis of the bar. In the first approach, the piezoelectric properties of the bar could be taken to be negligible.

The differential equation describing the free vibration of a one dimensional system is given by the well known equation:

$$\frac{\partial^2 U}{\partial t^2} = c^2 \frac{\partial^2 U}{\partial x^2} \tag{2.14}$$

where:

U = displacement of a point in the vibrating body relative to its equilibrium position;

c = velocity with which a disturbance corresponding to the displacement U is propagated in the body;

x and t = space and time coordinates, respectively.

The solution of Equation. 2.14 can be found having the form:

$$U(x,t) = [T(x)][X(x)] \tag{2.15}$$

where T is function only of time and X is function of the space coordinate x. Taking partial derivatives of $U(x,t)$ with respect to t and x, and substituting these into Equation 2.14 gives:

$$\frac{1}{T}\frac{d^2 T}{dt^2} = \frac{c^2}{X}\frac{d^2 X}{dx^2} \tag{2.16}$$

$$\frac{1}{T}\frac{d^2T}{dt^2} = -\omega^2 \qquad \text{and} \qquad \frac{c^2}{X}\frac{d^2X}{dx^2} = -\omega^2 \tag{2.17}$$

The solution of the equation in t is:

$$T = A\sin(\omega t) + B\cos(\omega t) \tag{2.18}$$

and that of the equation in x is

$$X = D\sin\left(\frac{\omega x}{c}\right) + E\cos\left(\frac{\omega x}{c}\right) \tag{2.19}$$

where ω is the angular frequency, A,B,D and E are constants and can be determined from boundary conditions. For a fixed-free bar (Figure 2.7.), the boundary conditions are [44]:

$x=0$	displacement	$U(0)=0$
$x=l$	strain	$(dU(l)/dx)=0$
$t=0$	displacement	$U(0)=0$

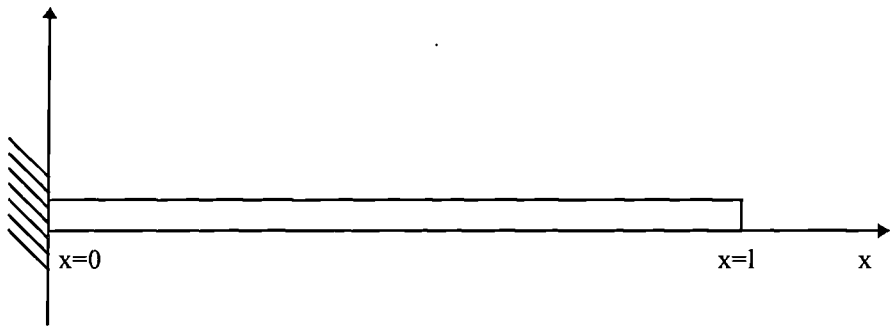

Figure 2.7. Fixed-free bar terminated rigidly at one side

The first condition requires that E=0. Condition 2 requires that

$$\frac{\omega l}{c} = n\pi \qquad \text{n=1,2,3,...} \qquad (2.20)$$

The solution of Equation 2.14 after considering boundary conditions is:

$$_n = A_n \sin\left(\frac{n\pi c}{l}t\right)\sin\left(\frac{n\pi}{l}x\right) \qquad (2.21)$$

It is important to notice that a one-dimensional system may vibrate in many different modes depending on the value of n which must be an integer (Figure 2.8.).

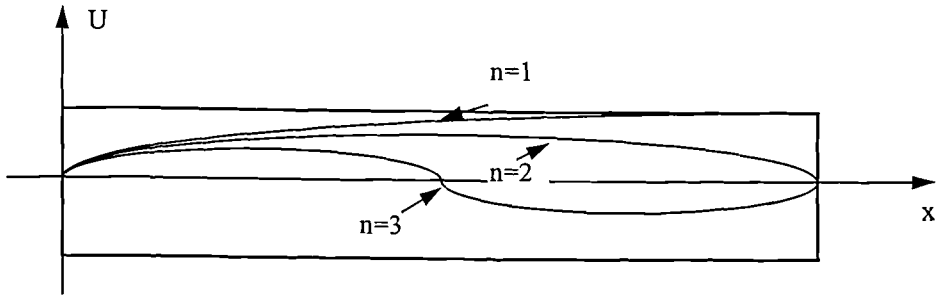

Figure 2.8. Modes of vibrations of a one dimensional system

The frequency of the vibration in each of these modes is found by setting

$$\omega_n = \frac{n\pi c}{l} = 2\pi f_n \qquad \text{or} \qquad f_n = n\frac{c}{2l} \qquad (2.22)$$

The excitation of vibrations can be accomplished by applying an electric field to electrodes placed on suitable planes of piezoelectric parallelepiped. The amplitude of the vibration depends on the frequency of the exciting harmonic waveform. If the ceramic element is bonded to the metal, then obviously the metal will also vibrate. The vibrational magnitude and phase will be affected by the spring constant K, and also by the mass m of the ceramic / metal combined and also by the damping factor of

the materials. The equation representing the forced vibration of the mass-spring system under a force F, generated by the a.c. voltage V is given by

$$m\frac{d^2x}{dt^2} + Kx = F(x) \tag{2.23}$$

Substituting $q=Ax$, where A is the force factor, into Equation 2.23 and then dividing both sides by A the equation of motion is given by

$$\frac{m}{A^2}\frac{d^2q}{dt^2} + \frac{K}{A^2}q = \frac{F(x)}{A} \tag{2.24}$$

The deformations created when a piezoelectric ceramic element is subjected to an applied voltage are small. An effective method of creating relatively large deformations with low voltages is to take advantage of the resonance phenomena. If a device which includes a piezoelectric ceramic element is excited at a frequency sufficiently close to its characteristic frequency, the vibrations are likely to reinforce each other and increase the amplitude. This implies great use of piezoelectricity in detecting small movements, in high precision applications and resonating sensors.

It is convenient to use an equivalent circuit approach for the analysis of vibrators in the case where the boundary conditions are compatible with those in the derivation of the equivalent circuit. Therefore, many works for the equivalent circuit analysis of various piezoelectric systems have been reported [45-47] all having in common that the piezoelectric body vibrating near fundamental resonance could be represented by an equivalent CL series circuit (Figure 2.9) [45-47]. The characteristic angular frequency is then given by

$$\omega_0 = 1/\sqrt{CL} = \sqrt{K/m} \tag{2.25}$$

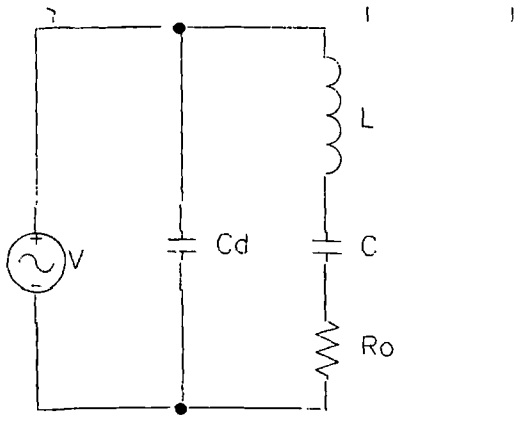

Figure 2.9. Equivalent CL series circuit.

R_o - internal resistance;

C_d - capacitance due to the element's dielectric properties. C_d is the capacitance measured when the ceramic element is fixed (or 'blocked') so that no vibrations can occur (no motions in the system).

The equivalent circuit approach is, also, very convenient in the calculation of the transient response of piezoelectric elements in order to test a transducer device or to measure some physical properties of piezoelectric materials. Challis and Harrison [48], in their analysis of a transient response of a piezoelectric element, have defined that the equivalent circuits are normally Fourier transform representations of the piezoelectric element and therefore yield solutions in terms of angular frequency ω. The equivalent circuit presented is a very interesting model which describes the relationship between the electrical variables (voltage V and current I) at the device terminals and the force F and velocity U of motion at the mechanical faces of the device (Figure 2.10). The ideal transformer represents the electromechanical conversion.

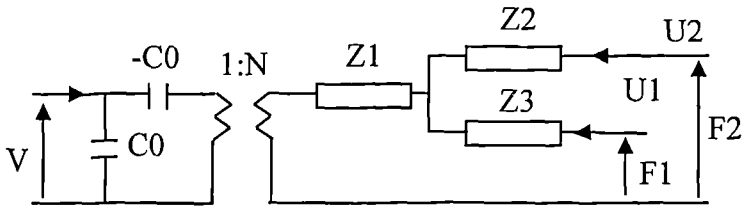

Figure 2.10. Equivalent circuit of thickness expander plate [48] with electric field parallel to the direction of wave propagation.

In the equivalent circuit analysis of piezoelectric bending vibrators by Aoyagi and Tanaka [49] the equivalent circuit has one pair of electrical terminals and four pairs of mechanical terminals. The applied force and bending moment at the mechanical terminals were treated as equivalent voltages while the velocity of displacement and the velocity of angular displacement at the mechanical terminals were treated as currents. The equivalent CL parallel and series resonance circuit representation could be also used for measuring mechanical vibration loss and dielectric loss of piezoelectric transducers under high-power excitation [50].

2.3.4. Modeling of an active control system with piezoelectric actuators

The wide usage of piezoelectricity in detecting small movements, in high precision applications and resonating sensors led researchers to the conclusion that it was necessary to establish a complete analysing method for piezoelectric elements. According to Yang and Huang [51], the system driven by a piezoelectric element can be simplified as the general dynamic model shown in Figure 2.11.

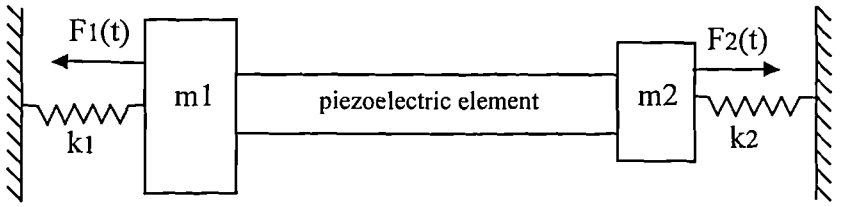

Figure 2.11. The general piezoelectric model for analysing piezoelectric elements[51]

In the above model m1 and m2 are masses clamped at the ends of piezoelectric element and k1 and k2 are elastic elements linking the masses and the base. The idea presented is that when a piezoelectric actuator is activated by a voltage on a certain pole plane its response in one direction is the same as the response of a piezoelectric actuator activated by two equal and opposite forces acting on two certain places and in certain directions. According to the authors, this idea could be especially applicable to analyse the dynamic response of a scanning probe microscope where the use of a piezoelectric element is almost necessary at the present time. The model neglects the dielectric loss of the piezoelectric ceramic [50] and all damping apart from the structure damping. In obtaining the solution for this dynamic model, the authors made use of the extended Equation 2.14:

$$\frac{\partial^2 u}{\partial t^2} = c^2 \frac{\partial^2 u}{\partial x^2} + \frac{1}{\rho A}[-F_1(t)\delta(x) + F_2(t)\delta(x-l)] \qquad (2.26.)$$

where ρ is the density of the piezoelectric material and A is the area of the cross section of the piezoelectric element.

The above equation is an ideal case where structure damping is not taken into account. In reality, structure damping exists and assuming the linear damping coefficient is H per unit length the equation (2.26) could be changed to :

$$\frac{\partial^2 u}{\partial t^2} = c^2 \frac{\partial^2 u}{\partial x^2} - \frac{H}{\rho A}\frac{\partial u}{\partial t} + \frac{1}{\rho A}[-F_1(t)\delta(x) + F_2(t)\delta(x-l)] \qquad (2.27.)$$

Solving the above equations a form of dynamic model for the piezoelectric element can be derived. In due course this theses will discuss in great detail and go into the development of a model of the system as a whole utilising a piezoelectric element. The model will combine the dynamic model and active vibration of a piezoelectricly activated system and it will also consider some additional damping mechanisms. Therefore, after referring to the dynamic model for piezoelectric element it is necessary to observe performance of an active control system with piezoelectric actuators.

In this project a piezoelectric plate bonded onto the aluminium surface was used as an excitation mechanism. To date a considerable amount of work [52-56] has been done to analyse the surface-bonded piezoelectric actuators exciting bending and extension in an elastic substructure. Crawley and de Luis [52] derived static and dynamic analytic models for segmented piezoelectric actuators that are either bonded to an elastic substructure or embedded in a laminated composite. When induced strain actuators are coupled to a structure, the actuators and structure may extend, bend, and shear. The relative importance of these three modes of deformation depends on the geometry and the relative stiffness of the actuators, structure, and bonding layers. It was shown that the strain in the piezoelectric, strain in the substructure and applied force or moment depend on two parameters - one primarily influenced by the stiffness and thickness of the bonding layer and the other which sets the maximum fraction of piezoelectric strain that can be influenced in the substructure. For the case of extension, the strain induced by a pair of actuators symmetrically located about the neutral axis (Figure 2.12a) is :

$$\varepsilon_a = \varepsilon_s = \frac{2\Lambda}{2+\Psi_e} \tag{2.28}$$

where ε_a is the strain in the actuators, ε_s the strain in the beam substructure, Λ the actuation strain, and Ψ the relative stiffness parameter is:

$$\Psi_e = \frac{(EA)_s}{(EA)_a} \tag{2.29}$$

For the case of induced bending (Figure 2.12b), the strain in the upper actuator and at the upper surface of the beam is:

$$\varepsilon_a = \varepsilon_s^{surf} = \frac{6\Lambda}{6+\Psi_b} \tag{2.30}$$

where the stiffness parameter in bending for a general cross-section is:

$$\Psi_b = \frac{12(EI)_s}{t_s^2(EA)_a} \tag{2.31}$$

where t_S is the thickness of the bonding layer.

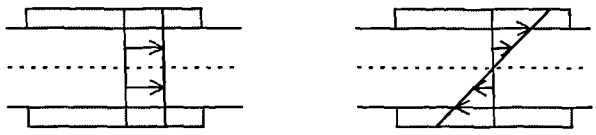

Figure 2.12. Piezoelectric -substructure strain distribution a) uniform strain extension, b) uniform strain bending.

The detailed model of the piezoelectric element coupled to a substructure was also integrated into a larger dynamic model of the system. Crawley and de Luis derived sets of equations where the influence of the actuators is incorporated into the model by calculating either the applied strain or generalised applied force on substructure[††]. These models can be used to estimate the effects of the piezoelectric on the structural modes and could be used to examine scaling, actuator choice and its placement.

Based on the uniform strain model [52], Crawley and Anderson published the study [53] with developed detailed models of the interaction between induced strain actuators and one-dimensional structures to which they are bonded or in which they are embedded. All these models where derived in terms of the generalised actuation strain, and then specific characterisation of piezoceramic actuation strain was implemented. For piezoceramic materials, the relation between actuation strain and applied field is:

$$\Lambda = \begin{bmatrix} 0 & 0 & d_{31} \\ 0 & 0 & d_{31} \\ 0 & 0 & d_{33} \\ 0 & d_{15} & 0 \\ d_{15} & 0 & 0 \\ 0 & 0 & 0 \end{bmatrix} \begin{bmatrix} E_1 \\ E_2 \\ E_3 \end{bmatrix} \qquad (2.32)$$

If the $x3$ axis is assigned to the direction of the initial polarization of the piezoceramic and the $x1$ and $x2$ axes lie in the perpendicular plane the piezoelectric strain coefficient, d_{31} characterises strain in the $x1$ and $x2$ directions due to an electric field (E_3) in the poling (x_3) direction. The d_{33} coefficient relates field and strain in the x_3 direction and the d_{15} coefficient characterises x_2-x_3 or x_3-x_1 shear strain due to field E_2 or E_1, respectively.

In practice, the relationship between actuation strain and applied field in piezoceramic materials departs from the ideal linear relationship shown by the above Equation 2.32. According to Crawley and Anderson, four characteristic behaviours - depoling of ceramic, the dependence of $d31$ on strain, field - strain hysteresis, and frequency dependence and creep - could affect linearity between actuation strain and applied field. Figure 2.13 shows a typical hysteresys loop and associated strain. Depoling will occur if, during the use of piezoceramic, a steady field larger than the coercive field is applied opposite to the polarisation direction. Within the depoling limits, the

[††]Complete derivation can be found in reference [52]

most evident nonlinearity in piezoceramic actuation is in the relation between applied electric field and resulting actuation strain which means that there is the divergence between the ideal linear model ($\Lambda_1=d_{31}E_3$) and the actual behaviour of ceramic. A single constant, d_{31}, cannot adequately relate strain to field except in the case of small signals where linearity could be preserved. Another non-ideality is the increased d_{31} at low frequencies (100 Hz or less) which could be related to the tendency for piezoceramic materials to creep under prolonged application of electric fields. For high frequency applications, creep can be ignored, but for low frequency or static applications, creep must be accounted for. An important conclusion could be drawn from Crawley and Anderson's study: in the case of a small electric field applied to the piezoceramic and for frequency applications of about 100Hz and grater it could be said that linear model keeps its validation. As will be seen in due course, application of piezoceramic in this project will be kept well within the above limitations.

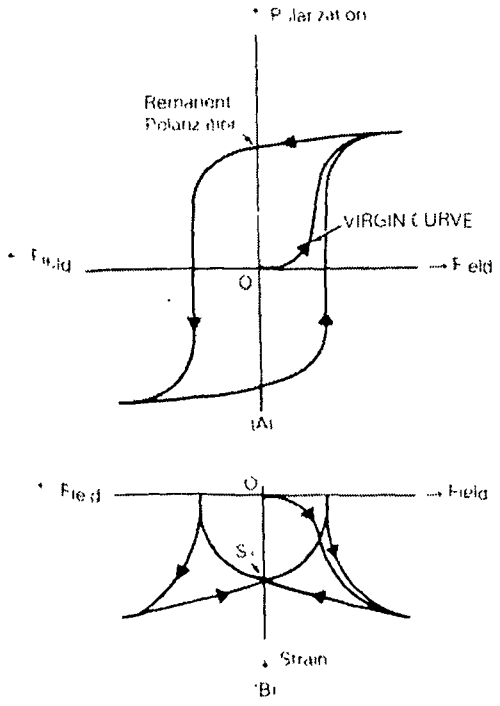

Figure 2.13. Typical hysteresis loop (A) and associated lateral strain or contraction [75 a]

2.3.5. Sensors based on piezoelectric resonators

Piezoelectric resonators are commonly known especially because of their wide use for frequency control in watches, TV apparatus, video recorders, computers, etc. The main reasons for their use are high thermal stability due to the use of quartz and high resonator quality factor (Q-value of 100 or greater). This stable resonators can also be used for different sensors with high sensitivity to various measurand quantities such as for a temperature or pressure sensors. In the frequency control case the resonator is usually vacuum encapsulated and decoupled from mechanical stress caused by environment, while in the sensor application the resonator is kept in contact with the medium that carries the information about the quantity of interest. Also, the anisotropy of piezoelectric single crystals allows different angles of cuts (different orientations of the resonator shape with the respect to the crystallographic axis), with very different properties allowing different applications of piezoelectric resonators [57].

For sensor applications, a clean resonance spectrum is necessary because the resonance selected for the particular sensor shifts within a certain frequency range depends on the measurand. If there are any spurious modes with different dependencies upon the measurand, resonance-frequency crossings and mode coupling may occur within the measurement frequency range. This can produce significant deviations from linearity and also frequency jumps and activity dips in the frequency versus measurand curve. According to Benes [57] there are two possibilities to avoid this. The first is to utilise the lowest mechanical resonance frequency of all, and second - to keep the resonator geometry as close to the one-dimensional theoretical description as possible. In the second case, resonators exhibit a simple resonance spectrum described by Equation 2.22: $f_n = nc/2l$; where $c=(E/\rho)^{1/2}$ with E being the Young's modulus of elasticity and ρ the density of the crystal material. The equation shows that a change of resonance frequency can take place only if the measurand

changes the effective elastic stiffness constant, the resonance-determining dimension and/or the density of the crystal.

An extensive use of piezoelectric resonators led to an extensive further research and therefore literature covering wide applications of piezoelectric sensors. Dokmeci, in his four papers [58 - 61] gives an extensive review of the open literature concerned with the dynamic applications of piezoelectric crystals covering the period up to 1989. This review also covers representative theoretical and experimental papers on waves and vibrations in piezoelectric one-dimensional and two-dimensional structural elements.

Describing applications of piezoelectric beams in sensors and actuators, Soderkvist [62] shows that the piezoelectric effect is superior to electrostatic activation and capacitive detection in many applications. Analysing an electric equivalent circuit of a vibrating piezoelectric beam and the vibrations at the phase close to resonance it has been shown an easy piezoelectric activation of the resonance frequency. Langdon [8] emphasises that the electrical power needed to drive high-Q resonator sensors is extremely low. In small quartz devices with piezoelectric drive, the power dissipated in the resonator itself is usually insignificant in comparison with that dissipated in the oscillator and output circuits. Mecea [63] presents results obtained in the development of the vibrating piezoelectric sensors loaded with any medium, either solid, liquid or gas. The common feature of such a loading is its ability to vibrate synchronously with the piezoelectric resonator as a compound resonator. In the same paper Mecea introduces a new concept in vibrating sensors, where the vibrational characteristics of a piezoelectric resonator, namely, the nominal frequency and vibrational amplitude, are correlated with the physical characteristics of a medium vibrating synchronously with a piezoelectric resonator.

Among the other applications, piezoelectric resonators have been exploited as temperature, force, stress and pressure sensors. A first systematic approach towards a

development of an attractive temperature sensor was published in 1962 by Wade and Slutsky [64] and further improved by Smith and Spencer [65]. Tuning-fork resonator based temperature sensors have been developed by Ueda et al. [66] and EerNisse and Wiggins [67]. A highly sensitive temperature sensor using a SAW (surface acoustic wave) resonator oscillator was developed by Viens and Cheeke [68].

The first investigations in using quartz resonator disks as a stress sensors were reported by Ballato and Bechmann [69], Ratajski [70] and Dauwalter [71]. A high performance pressure transducer was reported by Karrer and Ward [72]. The double-ended pressure transducer was an inportant contribution by EerNisse and Paros [73] in pressure sensing, while a single-ended tuning-fork resonators which could be successfully used for monitoring vacuum pressure were reported by Ono et al. [74]. Morten *et al.* [9] describe the design, implementation and performance of a resonant sensor for gas-pressure measurement based on screen-printed and fired PZT-based layers [75] on an alumina diaphragm. They introduced a new application areas for PZT-based pastes and thick-film sensors. Both direct and inverse piezoelectric effects have been exploited in a sensor/actuator system used in the development of a simple gas-pressure resonant sensor whose output can be directly measured in digital systems. The gas-pressure sensor prototypes working principle is based on the frequency modulation of an oscillating diaphragm induced by a differential pressure.

The frequency-force effect in piezoelectric sensors was thoroughly characterised by several researchers [76,77]. The simplest kind of force sensor consists of a flexurally vibrating quartz beam with stress applied through the mountings at the end. A number of different designs of quartz force sensing element have been proposed based on this principle [78-80]. These designs were followed by quartz resonator force sensors produced by photofabrication [81,82]. The accuracy and repeatability of the force-frequency relationship for such devices is very high, but the accuracy of sensors which incorporates them is largely affected by the mechanical stability of the associated sensor structure. The use of piezoelectric sensors in force detection is of particular importance because of their simplicity, ability to provide good sensitivity to force and possibility to be batch fabricated [10-12,14,30,83].

Force measurement has found wide and important application in atomic force (AFM) and scanning force microscopes (SFM). The first atomic force microscope (AFM) using a scanning tunneling microscope (STM) tip [13] was introduced by Binnig *et. al.* in 1986 [28]. Since then several inventors have reported atomic force microscopes of various sorts. The AFM and other scanning probe microscopes (SPM), measure topography (potentially of atomic resolution) by scanning a small tip, attached to a cantilever spring, over a sample. The AFMs are divided into two categories: contact [28] and non-contact [29] AFMs. The contact operates in the repulsive force region. In this AFM, a cantilever beam is brought into contact with a sample and the deflection of the cantilever is measured by a sensor. On the contrary, the non-contact AFM, which is operated in the attractive force region, has the advantage of allowing non-destructive measurement of surface topography. In 1987 Martin *et al.* [29] introduced a modified version of AFM [28] which enables measurement of the force between a tip and a material surface. They proposed a system where the lever deflectiion is optically detected, making it more reliable and easier to implement. The cantilever, which is vibrated at or near its resonant frequency, responds to changing force gradients by shifts in resonant frequency. To measure changes in the resonant frequency Martin *et al.* [29] introduced *the slope method* in which the oscillation amplitude is measured when the cantilever is driven at a frequency slightly off resonance. The force signal is used to maintain the tip/sample spacing constant and the simultaneous measurement of force and surface profile is allowed. Takata, introduced the force measurement by detecting an electric property of piezoelectric material incorporated into the cantilever [84]. When a force acts on the spacing between the tip and the sample, the force gradient shifts the resonant frequency at the same time causing a shift in the impedance curve of the piezoelectric material. Sensing the impedance of the piezoelectric cantilever reveals the force interaction. The tip-to-sample spacing is maintained by keeping changes in impedance constant.

Detection of surface forces between the tip and a sample has been demonstrated with a piezoelectric cantilever in a scanning force microscope (SFM) [11]. The use of

piezoelectric force scanning is particularly advantageous in semiconductor applications where stray light from conventional optical force-sensing methods can significantly modify the local carrier density. Tansock and Williams [11] have demonstrated the use of piezoelectric bimorphs as force sensors with a sensitivity of 105pN/Hz.

Itoh and Suga [30] constructed a dynamic scanning force microscope using a piezoelectric force sensor which enables direct detection of signals related to the deflection amplitude, by a piezoelectric layer formed on the probe. The sensor consists of a cantilever with a piezoelectric thin film deposited on one side. The cantilever is excited near its first natural resonance by an external piezoelectric oscillator. The force is maintained by detecting the charge from the piezoelectric layer induced by the piezoelectric effect.

Piezoelectric resonators have also been widely used in precision applications having advantages, such as high frequency response, relatively long motion range and low heat generation, over the other types of high precision actuators. The scanning probe microscope (SPM) is one of many piezoelectric applications, which requires atomic level precision control at high speed. The piezotube actuator [85] is widely used for the SPM design due to three axes control capability , a thermally symmetric structure, and a relatively high natural frequency. Ohara and Youcef-Toumi [86] derived a dynamic model of the piezotube actuator approximating a piezotube as a forced bar/beam with a mass attached at the end. Based on this model, a high speed and high precision displacement piezoelectric sensor was proposed. Also, based on piezoelectric tube actuators Hara et al. [87] developed a micro-step XYθ stage mechanism. This stage consists of three piezoelectric tube actuators and facilitates the positioning of the point to be measured in SPM and it can also be used as a precision XYZ positioning stage. Olin [12] describes the design of a compact, cylindrically symmetric, resonating scanning probe microscope (SPM), for operation in air and liquid. The mechanical part of SPM has a typical scanning range of a few micrometers

and it consists of a piezoelectric scanner and a coarse positioning device. The scanner described by Olin is a standard single piezoelectric tube (PZT-5H) (PZT-5H is a modified lead-zirconate-titanate ceramic, which has an exceptionally high dielectric constant, electromechanical coupling coefficient and charge sensitivity [75]) while the compact and concentric microscope head is built around a commercial piezoelectric inchworm motor [88]. The other researchers, [89,90] also focused their research on finding an appropriate method for driving piezoelectric actuators for ultraprecision position and motion control and. Main et al. [89] developed a new control relationship based on the piezoelectric material constitutive relationships that relates actuator displacement to an amount of applied charge showing that charge control is significantly more linear and less hysteretic than voltage control over the same actuator displacement range.

A simple piezoelectric microbalance based on resonator principle, using a vibrating quartz wire, was introduced by Mulder [26]. This is another example in long list of possible usage of piezoelectric resonators. The microbalance is based on the mass dependence of the resonance frequency of a vibrating quartz wire, from which loads are suspended, and whose two ends are connected to two piezoelectric flexure elements. One of the elements functions as a driver, thus setting the quartz wire vibration. The vibration of the wire is sensed by the second element. The AC voltage produced in the latter is measured at a number of frequencies centred around the resonance frequency of the loaded quartz wire, for a constant driving voltage. The set-up can be used in various ambient conditions (temperature, pressure, humidity and gas composition), it is essentially drift free and extremely simple in design.

Contact location, force and pressure sensing discussed above are among most useful parameters in tactile sensing and many researchers dedicated their studies to the subjects concerning this technology. One of the main objectives of the research which will be discussed in this thesis was to design a high precision resonator-based tactile-sensitive probe, therefore a need for an introduction into this area.

2.4. Tactile sensing with a focus on piezoelectric based sensors

2.4.1. Introduction to tactile sensors

There are many kinds of tactile sensors, among which tactile array sensor sensing distributed contact stress or strain is one of most commonly used types for robotics applications [91-93]. Apart from these sensors which typically consist of two-dimensional arrays of sensing sites mounted on the hard backing there are some other type of devices that utilise thin plate [94], TiN film [18] technologies or piezoelectric effect in the form of tensor cell [95], piezoelectric ceramic [27,96,97] or piezoelectric polymer film [5].

2.4.2. Vibrating quartz resonators used as tactile and nontactile sensors

Vibrating quartz resonators used as tactile and nontactile sensors were introduced by Weinmann *et al.* [27] as a scheme developed for the measurement of both profile and position. Measuring of profile and position on the nanometer size level is necessary in the field of precision engineering, thin films, micromachining, etc. Mechanical coordinate measuring units and profilometers are used effectively, but there is great disadvantage with respect to sensitive samples made out of delicate materials. The principle of measurement relies on a loaded contact tip switch, which may result in the distortion of the surface being measured. Also, the optical processes are only suitable for samples which reflects the light, hence they cannot be used with tarnished or highly scattering surfaces. In an attempt to overcome these problems associated with currently used measuring devices the principle developed by Weinmann [27] is based on vibrating quartz resonators used as tactile and nontactile sensors. If a vibrating quartz resonator gets close to a surface, its Q factor decreases. The closer the resonator is to the surface the more it is damped due to the viscosity between the probe tip and the measurement tip. If the new quartz resonator touches the surface, the

vibration is stopped. For non contacting acoustic surface scanning, two different types of miniaturised quartz resonators are used. These are extensional vibration mode resonators for general electronic applications such as those used in wrist watches. Piezoelectric actuators with feedback control are used to enable the sensor to be scanned across the sample. Using a slightly different detection scheme, the vibrating quartz can be used as a tactile position sensor. If tuning forks are used as tactile probe heads, only the electrical amplitude of the vibration is needed as a trigger signal. Small glass fibres with diameters between 30 and 70 μm are used as probe heads. The force between sample and vibrating probe tip at trigger level is less than 1mN.

2.4.3. Extracting control parameters from tactile data

Extracting control parameters from tactile data is a very important task. In the case of tactile array sensor sensing, distributed contact stress or strain, making use of the sensor's output requires two distinct steps [91,93]. Firstly, a forward model must be established to relate subsurface stress/strain from the surface stress and the material properties of the covering layer. Secondly, an inverse model must be constructed in order to calculate contact parameters such as contact force and location from the subsurface strain measured by the tactile transducers. In the case of discrete tactile sensors [5,18,27,94-97] extracting control parameters from tactile data is much simplified.

An application of piezoelectric properties and piezoelectric actuation in resonator based tactile systems was exploited by Omata and Teruama in a design of a tactile sensor for detecting the hardness and/or softness of an object [96]. This type of sensor operates with a piezoelectric element and it is constructed as a probe type. The rectangular transducer is designed to operate with piezoelectric plate made of PZT ceramics and a vibration pickup made out of PZT or polyvinilidene film. The PZT element is able to vibrate freely in a direction of its length. The wave equation, in terms of displacement, may be written in the familiar form (Equation 2.14)

$$\frac{\partial^2 u}{\partial x^2} = \frac{1}{v_r^2} \cdot \frac{\partial^2 u}{\partial t^2}, \qquad v_r = \sqrt{E/\rho}, \tag{2.33}$$

where v_r is the velocity of propagation of longitudinal waves in a rod, E is the Young's modules, ρ is the density of the rod. After considering the boundary conditions, the change in resonance frequency (Δf) for the first mode can be written:

$$\Delta f = -\frac{v_r}{2\pi l} \cdot \frac{\beta}{z_\varphi} \tag{2.34}$$

for the loaded and unloaded conditions where the impedance of unknown object, z_φ, may be expressed in the form

$$z_\varphi = \alpha + j\beta, \tag{2.35}$$

where α is the resistance and β is the reactance.

The changes in values of the resonant frequency provide information about the physical properties related to Equation 2.35 which in turn can be related to hardness and/or softness of an object.

Using a piezoceramic AE (acoustic emission) sensor, Chonan et al. [97] developed a tactile sensor that, as the authors claim, has the sensitivity of human skin. The device is placed and moved over the material to be identified. The voltage signal from the sensor is first stored in the digital memory, analysed and then compared with the training set of data in neural networks. The authors claim that the sensor system identifies the material 85% correctly for 120 samples of 6 different materials. Shida and Li [94] developed another type of tactile sensor for discrimination of material properties. The plane surface of a mono-structural thin plate touch sensor, consisting of a pair of thin spiral wires on a thin insulating substrate, is placed on the surface of

the test material to detect its physical properties. Depending on the electrical connection of the sensor terminals, this device exhibits four sensing functions: thermal sensing, capacitive sensing, inductive sensing and hardness sensing functions. The technique of pattern recognition by the multi-dimensional indication of data was adopted to discriminate material properties but materials could only be roughly separated into different groups.

The above sensors, designed for material identification and discrimination of material properties, together with some spherical tactile sensing probes (Section 2.2.4., [e.g. 6,18]) for detection of contact location have shown the high potential of such devices in tactile sensing technology. Their distinctness, possible versatility and simplicity in extracting control parameters from tactile data could justify further research and development interests in this area.

2.5. Conclusion

An overview of several disciplines important for achieving the aims and objectives during the work on the thesis is given in this chapter. The survey was organised in three parts not because topics covered could be treated completely separately, but as an attempt to give a clear view on the background material that supported this project. The subjects covered are touch-probing systems, resonator based sensors with the emphasis on the piezoelectric effect, and finally, tactile sensors and the mechanisms of extracting control parameters from tactile data.

Several touch-trigger probe designs are covered starting from the traditional electro-kinematic design and including piezo-sensor probes, touch trigger probes with PVDF sensors, spherical potentiometer, optoelectronic, micro-strain gauge touch-trigger probes and quartz micro-probes. From such a large number of different designs, most of them recent or in the process of development, it is apparent that there is still a need

for further research and expansion in this area. Currently there is no standard (Butler [19]) or other generally agreed method of describing the performance of probes, except those given by manufacturers. Probe errors are typically small when compared to overall system accuracy but in certain circumstances, such as when using long styli, they can contribute to the measurement error as a whole. The errors associated with traditional electro-kinematic 3D designs are mainly caused by variations in stylus bending prior to the point of trigger. These points of increasing trigger force often reach a maximum at three points roughly 120° apart in a 360° probing plane, and the error also becomes magnified when using a long stylus configuration. In industry requirements, the importance of continuous, error-free operation of probes is essential for flexible inspection systems Therefore all different probe designs promoted in recent years were developed, with more or less success, in order to overcome errors connected with the electo-kinematic design. Renishaw's TP12 probe has overcome the lobing effect, it has excellent accuracy but suffers from severe false triggering problems. Another probe from the Renishaw, TP200 micro-strain gauge probe, has impressive accuracy, repeatability and has pre-travel variation minimised, as claimed by manufacturer. A downside characteristic of strain gauges is that temperature gradients cause changes in gauge resistance and gauge factor, therefore a reference device is essential for the operation of this type of the sensor. The optoelectronic probe [2,19,20] requires a relatively low contact force of about 5 mN but the lobing effect still influences its performance. Touch trigger probes using a PVDF sensor [3] have reduced contact force but still suffer from false triggering. In the case of the touch probe based on a spherical potentiometer [4] computation is not required because the initial coordinates recorded are the coordinates of the contact point; accuracy has been improved but application of this probe is limited due to a constant current circuit required for the detection of the contact point. Finally, piezo-sensor probes, have overcome measurement errors associated with lobing characteristics, but have a triggering point dependent on the stress generated at the moment of contact. Therefore care must be taken when selecting component material, stylus tip mass and touch speeds. It is also essential that the component under inspection is clean of any

film on the surface, because this could reduce the probe's sensitivity and may cause it not to record the touch. These disadvantages of piezo-sensor probes in touch-trigger applications were considered advantageous for exploitation in this project. Namely the idea occurred that the device based on the principle of touch-trigger probes utilising piezoelectric effect could also be employed to study complex contact mechanisms between a resonator probe sensor and a range of engineering surfaces.

Exploitation of piezoelectric principles in this project required a closer analysis of the effect itself and also of linear piezoelectric models. This was elaborated in the second part of the literature survey. The mathematical definition of the piezoelectric effect was given and linear coupled electromechanical constitutive relations, standardised by IEEE Standard 167-1978, were also analysed concluding that in piezoelectricity the quasistatic electric field is coupled to the dynamic mechanical motion, and that the equations of linear elasticity are coupled to the charge equations of electrostatics by means of piezoelectric constants. Vibrations of piezoelectric bars and plates were also reviewed and frequencies of vibration in different modes derived. Use of an equivalent circuit approach for the analysis of vibrations was also considered, as well as the modelling of an active control system with piezoelectric actuators. Specific emphasis was given to the analysis of surface-bonded piezoelectric actuators exciting bending and extension in an elastic substructure. An important conclusion drawn from these studies was that, in the case of a small electric field applied to the piezoceramic and for a frequency application of about 100 Hz and greater, it could be said that the linear piezoelectric model keeps its validation. This conclusion was used as a guidance in application of piezoceramics in this project.

An extensive survey of sensors based on piezoelectric resonators was also conducted. Piezoelectric ceramics used in these systems have shown good application in terms of activation of a resonator system, simplicity and power dissipation [62,63]. Also, they have the ability to provide good sensitivity to force and the possibility to be batch fabricated [11,12]. In precision applications piezoelectric resonators have shown

advantages such as a high frequency response, relatively long motion range and low heat generation, over the other types of high precision actuators.. Moreover, the nominal frequency and vibrational amplitude of a piezoelectric resonator is correlated with the physical characteristics of a medium vibrating synchronously or medium that is in contact with it [63,96].

Finally, the last part of the literature survey concerning tactile sensing, had an emphasis on some different types of sensors. Namely, tactile sensors, in a strict sense, typically consist of two-dimensional arrays of sensing sites mounted on the hard backing for sensing distributed contact stress or strain. More interesting for this project were discrete devices that utilise thin plate, TiN film technologies or piezoelectric effect in the form of tensor cell, piezoelectric ceramics or piezoelectric polymer films. It could be concluded that, in the case of discrete tactile sensors, extracting control parameters from tactile data is much simplified in comparison to the tactile array sensors. Different techniques could be employed to discriminate material properties such as pattern recognition, neural networks or simple monitoring of resonant frequency. It has to be revealed that so far, using these techniques, materials could only be roughly separated into different groups, but distinctness, possible versatility and simplicity of these devices in extracting control parameters from tactile data could justify further research and development interests in this area.

To summarise: extensive background research has realised a strong belief that it is possible to design and develop a high precision, high sensitive, resonator based tactile sensitive device, which would have the simplicity of touch trigger probes, the advantages of utilising the piezoelectric resonator principle and the capability of tactile sensors to discriminate material properties. From the design principle versatility and possible applications of a such device can be predicted: investigation of contact mechanisms, coordinate metrology applications, non-destructive material testing, surface topography applications, and possibly many others.

Chapter 3

Resonance detection - Phase Lock Loop (PLL)

3.1. Introduction to frequency shift detection techniques

Various frequency shift detection techniques have been proposed and used. *The slope method* in which the oscillation amplitude is measured when the probe is driven at a frequency slightly of resonance was introduced by Martin *et al.* [29]. To measure changes in the resonant frequency a *frequency modulation (FM) technique* has been demonstrated by Albrecht *et al.* [98]. Proksch and Dahlberg [99] described an alternative method of measuring resonant frequency through the use of precision gated frequency counter in place of the analog FM demodulator. An *impedance sensing method* has also been reported as a means of detecting the change in load conditions [84]. Rodhal *et al.* [100] have designed quartz crystal microbalance set-up for frequency, Q-factor and the amplitude of oscillations measurements in gaseous and liquid environments. This approach is based on the *decay method* introduced by

Spencer and Smith [101] in 1966 study of defect concentration in natural quartz. Rodhal *et al.* [100] measures the free decay of oscillation of a quartz crystal to determine the Q-factor which is very attractive for high Q systems. Disadvantage of this method is that requires relativelly expensive apparatus to record the decay profile. Wajid [102] offers an alternative method to one of Rodhal et al's. A new approach relies on the passive measurement of the activity [103] or the relative amplitude of vibration of the quartz crystal at resonance and slightly off-resonance frequencies. The measurement system consists of a frequency measurement card based on a direct digital synthesiser and a phase sensitive detector. This system can measure the resonance frequency, and at same time the amplitude of vibration of the quartz crystal at any drive frequency. Using this information the absolute Q factor of the crystal resonator could be estimated. The advantage of this passive measurement technique is that the resonance can be detected even when the crystal is highly damped.

Among the most efficient and most common methods of detecting frequency shift, amplitude or phase of oscillations are methods based on lock-in amplifiers, the phase locked loop (PLL) technique or combination thereof.

3.1.1. Lock-in amplifiers

Lock-in amplifiers are characterised by a wide dynamic range which gives the ability to measure signals accompanied by relatively high levels of noise and interference. Both analogue and digital lock-in amplifiers are existent in modern instrumentation. Although digital lock-in amplifier techniques have been around for about 15 years [104-106], they are still not widely used between researches. In a digital lock-in amplifier, both the signal of interest and reference signal are digitised at a rate much greater than the reference frequency and then fed into the computer which performs the Fourier analysis to measure the amplitude of both signals and the relative phase

between them. In a conventional and widely used analog lock-in amplifier [14, 107-109], the signal of interest is mixed both in- and out-of-phase with a reference at the same frequency and then the outputs of the multipliers are fed through low-pass filters. This way, an analogue lock-in amplifier can measure both the amplitude and phase of the signal effectively filtering out broadband noise.

Mead [107] has given detailed principles of conventional lock-in amplifiers together with their specifications and limitations. They are all based on essentially the same principle. Briefly, if it is assumed that the signal of the form [$\alpha \cos(\Omega t)$] is been fed into the signal input of the lock-in amplifier and the reference wave form [$\beta \cos(\Omega t + \phi)$] is fed into the reference input the output of the lock-in is then dc voltage proportional to the ac voltage of the input signal. Internally, the lock-in performs a phase sensitive multiplication of a reference input wave form and input signal wave form giving:

$$[\alpha\cos(\Omega t)][\beta\cos(\Omega t+\Phi)]=\frac{\alpha\beta}{2}\{\cos[(\Omega-\Omega)t+\Phi]+\cos(2\Omega t+\Phi)\}. \qquad (3.1)$$

where α and β are amplitudes of the signals, while Ω and ϕ are the frequency and phase, respectively.

This process generates signals at the sum and difference frequencies of the initial sine waves, which means it generates a dc signal at zero frequency and ac signal at 2Ω. This product is passed through a low pass filter, completely attenuating the component at 2Ω and the only remaining signal is then a dc voltage corresponding to the ac amplitude of the input sine wave.

Actual lock-in amplifiers use a variety of schemes much more advanced than the simple procedure outlined above. For instance phase-locked loops form an important component in the reference channels of some conventional lock-in amplifiers [110,111], especially when a reference triggering input signal is required, or in phase-

tracking lock-in amplifiers [112]. The Phase-Locked Loop (PLL) technique itself is very efficient method of detecting frequency shift [9,113,114] and as such it was applied in this project.

3.2. Introduction to Phase Locked Loops (PLLs)

In general a phase-locked loop circuit is a circuit which causes a particular system to track with another one. Best [115] defines a PLL as a circuit synchronising an output signal (generated by an oscillator) with a reference or input signal in frequency as well as in phase.

As Best showed [115] the very first PLLs were introduced in 1932 by the French engineer de Bellesize but they did not have broad applications until they became available as an integrated circuit (IC). The first PLL IC was designed in 1965 and it was purely analogue device. This type of PLL is referred to as the "linear PLL" (LPLL) today. The digital PLL (DPLL) appeared around 1970 and it was combination of digital and analogue blocks. A few years later, the "all-digital" PLL (ADPLL) was invented. This type is exclusively built from digital function blocks, hence does not contain any passive components like resistors and capacitors. The PLL can also be implemented by software in which case, the function of the PLL is no longer performed by a piece of specialised hardware, but rather by a computer program. This last type of PLL is referred to as SPLL (Software Phase-Locked Loop).

The linear PLL (LPLL) will be used as an example to explain the operating principle of PLL. It consists of three basic functional blocks (Figure 3.1):

1. A phase detector (PD);
2. A loop filter (LF);
3. A voltage-controlled oscillator (VCO).

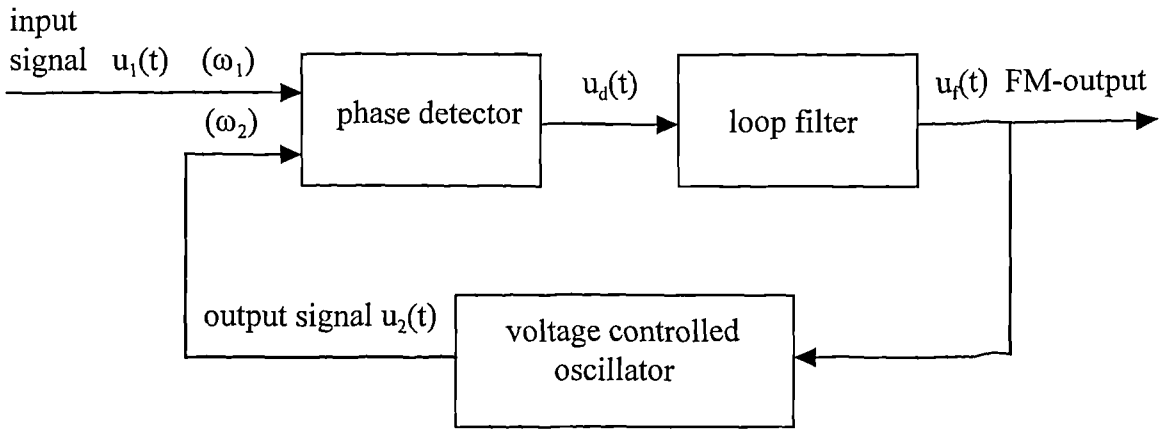

Figure 3.1. Block diagram of the PLL.

The following signals are signals of interest within the PLL circuit:

- The reference (or input signal) $u_1(t)$
- The angular frequency ω_1 of the reference signal
- The output signal $u_2(t)$ of the VCO
- The angular frequency ω_2 of the output signal
- The output signal $u_d(t)$ of the phase detector
- The output signal $u_f(t)$ of the loop filter
- The phase error θ_e, defined as the phase difference between signals $u_1(t)$ and $u_2(t)$

1. *The phase detector (PD).* The PD - also referred to as a *phase comparator* - compares the phase of the output signal from the VCO with the phase of the reference signal and develops an output signal $u_d(t)$ which is approximately proportional to the phase error θ_e :

$$u_d(t) = K_d \theta_e \tag{3.2}$$

where K_d represents the gain of the PD and its physical unit is volts. The output signal $u_d(t)$ of the PD consists of a dc component and a superimposed ac component.

2. *The loop filter (LF).* The dc component of the output signal $u_d(t)$ is roughly proportional to the phase error θ_e, and the ac components have frequencies of $2\omega_1$,

$4\omega_1$... The ac components are undesired and they are cancelled by the loop filter. In practical applications the usage of a first-order low-pass filters is common practice because all higher frequencies have to be filtered out. There are three most commonly used types of loop filters in linear PLLs: passive lag filter, active lag filter and active PI (proportional - integral) filter. Figure 3.2 shows schematic diagrams of these filters [115].

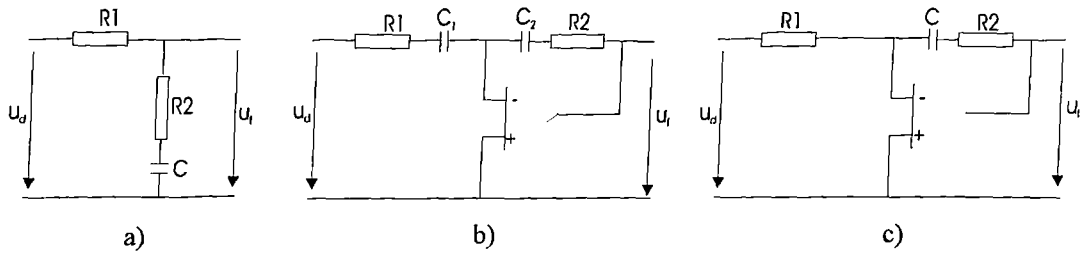

Figure 3.2. Schematic diagram of loop filters used in linear PLLs: **a)** Passive lag filter; **b)** Active lag filter; **c)** Active PI filter

3. *The voltage-controlled oscillator (VCO).* The VCO oscillates at an angular frequency ω_2, which is determined by the output signal u_f of the filter. The angular frequency ω_2 is given by [113]:

$$\omega_2(t) = \omega_0 + K_0 u_f(t) \tag{3.3}$$

where ω_0 is the center (angular) frequency of the VCO and K_0 is the VCO gain in $s^{-1}V^{-1}$.

If the angular frequency of the input signal $u_1(t)$ is equal to the centre frequency ω_0, the VCO then operates at its centre frequency ω_0 and the phase error θ_e is zero. The output signal u_d of the PD must also be zero. Consequently, the output signal of the loop filter u_f will also be zero. This is the condition that permits the VCO to operate at its centre frequency. If the phase error θ_e was not zero initially, the PD would develop a nonzero output signal u_d. After some delay the loop filter would also

produce a finite signal u_f. This would cause the VCO to change its operating frequency in such a way that the phase error finally vanishes. If the frequency of the input signal is changed suddenly at the time t_0 by the amount $\Delta\omega$, the phase of the input signal starts leading the phase of the output signal. A phase error increases with time and the output signal $u_d(t)$ of the PD also increases with time. The output signal $u_f(t)$ of the loop filter will also rise with a delay given by the filter. The VCO increases its frequency, the phase error becomes smaller and after some time the VCO will oscillate at the frequency that is exactly the frequency of the input signal. depending on the type of the loop filter used the final phase error is reduced to zero or to a finite value. The VCO operates at a frequency which is greater than its centre frequency ω_0 by an amount $\Delta\omega$ forcing the signal $u_f(t)$ to settle at a final value of $u_f = \Delta\omega/K_0$. As Best [115] showed, the PLL was always able to track the phase of the output signal to the phase of the reference signal and the system was *locked* at all times. However, if a larger frequency step is applied to the input signal it could cause system to "unlock" which will be explained later.

3.3. The linear mathematical model for the LPLL systems

As it could be seen from introduction to PLLs a phase-locked loop is essentially a frequency or phase control system. An important first step in the analysis and design of the PLL is the mathematical modelling of the control system. The linear mathematical method for the LPLL developed by Best [115] has been adopted in this project assuming at the beginning that the LPLL *has locked and stays locked.* This assumption was made for practical reasons in order that this system could be studied using linear system theory. Dynamic analysis of control systems is normally performed by means of its transfer function $H(s)$. Defined by Kuo [116] *the transfer function between a pair of input and output variables is the ratio of the Laplace transform of the output to the Laplace transform of the input.* In conventional

electrical networks, the input and the output are represented by voltage signals $u_1(t)$ and $u_2(t)$ respectively, so $H(s)$ is given by:

$$H(s) = \frac{U_2(s)}{U_1(s)} \tag{3.4}$$

where $U_1(s)$ and $U_2(s)$ are Laplace transforms of signals $u_1(t)$ and $u_2(t)$ respectively, and the s is the Laplace operator. In the case of the PLL, the input and output signals are *phases* therefore a phase-transfer function $H(s)$ relates the phase θ_1 of the input signal to the phase θ_2 of the output signal:

$$H(s) = \frac{\Theta_2(s)}{\Theta_1(s)} \tag{3.5}$$

where $\Theta_1(s)$ and $\Theta_2(s)$ are the Laplace transforms of the phase signals $\theta_1(t)$ and $\theta_2(t)$ respectively.

3.3.1. Phase transfer function of the LPLL in the locked state

As it could be seen from Figure 3.1, the LPLL consists of three different building blocks. In order to derive an expression for phase transfer function $H(s)$ transfer functions of the individual building blocks have to be defined.

The input signal of an LPLL is usually a sine wave:

$$u_1(t) = U_{10} \sin(\omega_1 t + \theta_1) \tag{3.6}$$

whereas the output signal is usually a square wave with an amplitude U_{20}, frequency ω_2 and the phase θ_2. The output signal of the phase detector is given by Equation 3.2: $u_d(t) = K_d \theta_e$, where $\theta_e = \theta_1 - \theta_2$ is the phase error and K_d is detector gain. Therefore the transfer function of phase detector is given by:

$$U_d(s) = K_d\,\Theta_e(s) \tag{3.7}$$

where K_d is proportional to both amplitudes U_{10} and U_{20}.

The transfer function of a passive lag filter having one pole and one zero is given by:

$$F(s) = \frac{1 + s\tau_2}{1 + s(\tau_1 + \tau_2)} \tag{3.8}$$

where $\tau_1 = R_1C$ and $\tau_2 = R_2C$. The other two types of filters were not taken into account while deriving the LPLL model because only a passive lag filter was used in this project.

For the third building block of a PLL system, the VCO, the angular frequency is given by Equation 3.3 as:

$\omega_2(t) = \omega_0 + \Delta\omega_2(t) = \omega_0 + K_0 u_f(t)$

where K_0 is called VCO gain. By definition, the phase θ_2 is given by the integral over the frequency variation $\Delta\omega_2$:

$$\theta_2(t) = \int \Delta\omega_2 dt = K_0 \int u_f dt \tag{3.9}$$

In the Laplace transform, integration over time corresponds to division by s, so the Laplace transform of the output phase θ_2 is given by:

$$\Theta_2(s) = \frac{K_0}{s} U_f(s) \tag{3.10}$$

Therefore the transfer function of the VCO is given by:

$$\frac{\Theta_2(s)}{U_f(s)} = \frac{K_0}{s} \tag{3.11}$$

Having the transfer functions for all three building locks defined, it is possible to derive a simplified linear mathematical model of the LPLL. Graphical presentation of this model is shown on Figure 3.3.

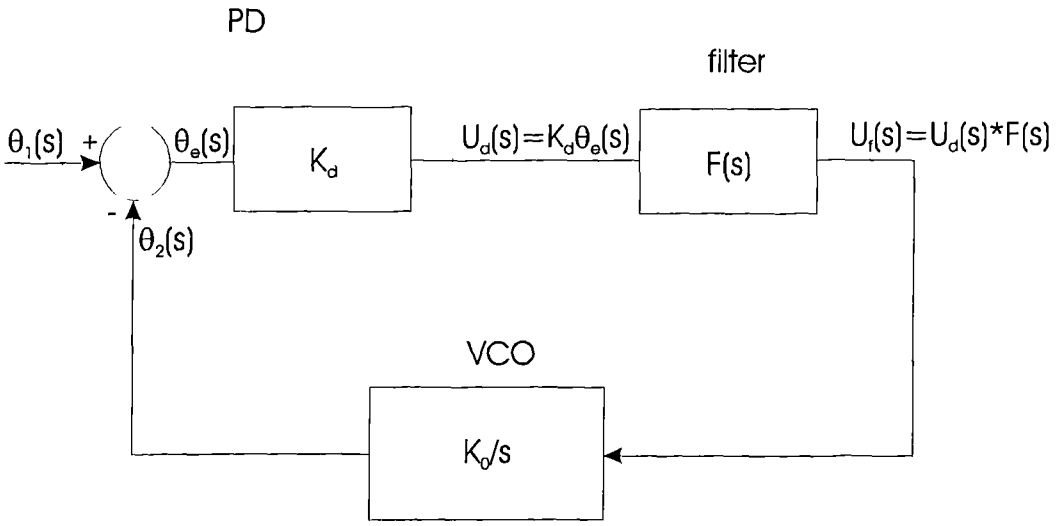

Figure 3.3. Block diagram of the linear model of the PLL [115].

From the Figure 3.3 phase transfer function could be calculated as:

$$H(s) = \frac{\Theta_2(s)}{\Theta_1(s)} = \frac{\Theta_e(s)}{\Theta_1(s)} \frac{U_d(s)}{\Theta_e(s)} \frac{U_f(s)}{U_d(s)} \frac{\Theta_2(s)}{U_f(s)} \tag{3.12}$$

where: $\Theta_1(s) = \Theta_e(s) + \Theta_2(s)$;

$U_d(s) = K_d\Theta_e(s)$;

$U_f(s) = U_d(s)*F(s)$; (3.13)

$\Theta_2(s) = U_f(s)K_0/s$.

Substituting Equation 3.13 into 3.12 phase transfer function for the passive lag filter becomes:

$$H(s) = \frac{K_0 K_d \dfrac{1+s\tau_2}{\tau_1+\tau_2}}{s^2 + s\dfrac{1+K_0 K_d \tau_2}{\tau_1+\tau_2} + \dfrac{K_0 K_d}{\tau_1+\tau_2}} \tag{3.14}$$

The characteristic equation of the closed-loop second order system could be obtained by expressing the denominator of the Equation 3.13 in the normalised form [116]:

$$\Delta(s) = s^2 + 2\zeta\omega_n s + \omega_n^2 \tag{3.15}$$

where ω_n is the natural frequency and ζ is the damping factor [116] and these two parameters basically determine PLL loop characteristics.

The natural frequency may be considered as the bandwidth of the loop. The damping constant determines the transient response characteristics. The natural frequency, ω_n and the damping constant, ζ for a second order LPLL loop using a passive lag filter could be defined as [113]:

$$\begin{aligned} \omega_n &= \sqrt{\frac{K_0 K_d}{\tau_1+\tau_2}} \\ \zeta &= \frac{\omega_n}{2}\left(\tau_2 + \frac{1}{K_0 K_d}\right). \end{aligned} \tag{3.16}$$

It has to be emphasised that the natural frequency ω_n is not the centre frequency ω_0 of the PLL. Inserting (3.16) into (3.14) and assuming that $K_d K_0 >> \omega_n$ which is true for most practical LPLLs Equation 3.14 becomes:

$$H(s) \approx \frac{2\zeta\omega_n s + \omega_n^2}{s^2 + 2\zeta\omega_n s + \omega_n^2} \tag{3.17}$$

A simple program has been written using a Matlab software to implement above function and to plot the Bode diagram [115] of the phase transfer function in order to explain transient response of the LPLL control system.

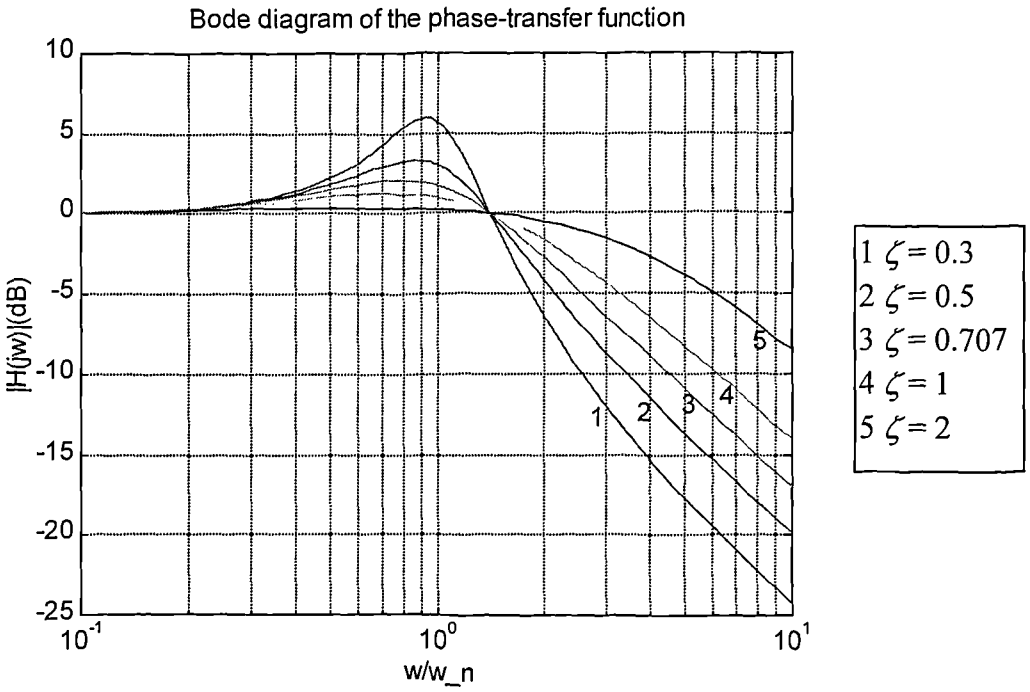

Figure 3.4. Bode diagram of the phase-transfer function $H(j\omega)$ [113,115].

From the Figure 3.4 it could be seen that the second order PLL acts as a low-pass filter for input phase signals $\theta_1(t)$ whose frequency spectrum is between zero and approximately the natural frequency ω_n. This means that the second-order PLL is able to track phase and frequency modulations of the reference signal as long as modulation frequencies remain roughly between zero and ω_n.

The dynamic performance of the LPLL depends on the value of the damping factor ζ. For ζ=1 the system is said to be critically damped. For ζ smaller than unity, the transient response becomes oscillatory which means that there is a relatively large overshoot and the settling time is long for a step phase change in $\theta_1(s)$. If, on the other hand, the damping constant is larger than unity, the overshoot is small and the

settling time is short but the response time for a ramp frequency change in $\theta_1(s)$ is longer [113]. Regarding dynamic performance of the LPLL, care should be taken when frequency ramp is applied to the reference input. Namely, if the reference frequency is swept at a rate larger than ω_n^2, the system will unlock. Also, if the system is initially unlocked, it cannot become locked if the reference frequency is simultaneously swept at a rate larger than ω_n^2. ω_n^2 is a theoretical limit, but a more practical design limit for $\Delta\omega_{max}$ is considered to be:

$$\Delta\dot{\omega} = \frac{\omega_n^2}{2} \tag{3.18}$$

As it could be seen from the above mathematical model, the LPLL considered was second-order system. The loop filter had one pole and generally the order of a PLL is always higher by one than the order of the loop filter. In LPLL applications, first-order systems are rarely used because they do not offer noise suppression [113,115], but higher order systems are used more frequently, especially in some critical applications [115]. The LPLL used in this project is one of second order and mathematical model derived above could be successfully applied in this particular implementation.

3.4. Mathematical model of the NE/SE 565 PLL

In this project *an analogue phase lock loop circuit* was used to drive and monitor the shift in resonance frequency. Appendix A. shows the schematic diagram of an electronic circuit which implements a feedback control technique to detect frequency shift. A LM565 [117] single chip PLL device was used in this particular circuit implementation and its block diagram is shown on Figure 3.5.

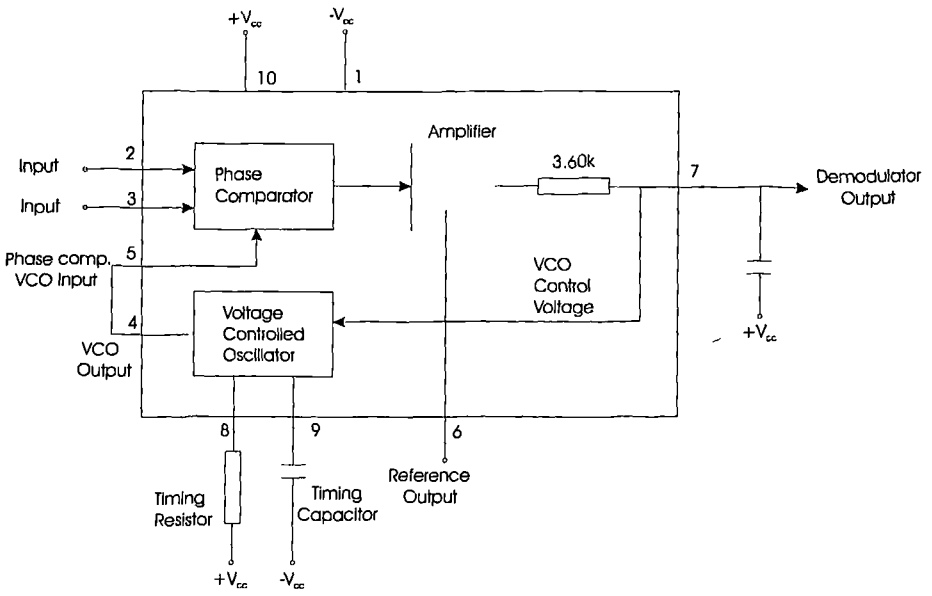

Figure 3.5. NE 565 Phase Locked Loop functional block diagram

The NE 565 is capable of operating over a wide frequency range (0.001Hz to 500 kHz)with the use of the internal highly linear voltage-controlled oscillator (VCO). The main application area for the 565 is in FM demodulation. When locked, the average dc level of the phase comparator output is directly proportional to the frequency of the input signal. As the input frequency shifts, it is this output signal which causes the VCO to shift its frequency to match that of the input. Consequently, the linearity of the phase comparator output with frequency is determined by the voltage-to-frequency transfer function of the VCO. Because of the linearity of the VCO (typically, within 0.5%), the NE 565 PLL can lock to and track an input signal over a very wide bandwidth (typically ±60%).

In order to derive a mathematical model and phase transfer function of NE 565 PLL, it is necessary to define circuit constants such as the phase conversion gain of the phase detector, K_d, the VCO conversion factor K_0 and low-pass filter factors τ_1 and τ_2.

Referring to the circuit diagram of the NE 565 [118] it could be seen that the output voltage of the phase detector is limited to a maximum of ± 0.7 V. When the incoming signal frequency is above the VCO centre frequency, the phase detector output ranges from 0 to -0.7 V, and when the incoming signal frequency is below, it ranges from 0 to +0.7 V [119]. This minimises the effect of high amplitude noise pulses and other transient effects on the operation of PLL. Therefore the phase conversion gain K_d of the phase detector is:

$$K_d = \frac{0.7-(-0.7)}{\pi} = \frac{1.4}{\pi} \tag{3.19}$$

The amplifier following the phase detector has a gain of $A_V = 1.4$, so the output voltage from the amplifier is (0.7 V×1.4), or ±0.98 V.

A low-pass filter chosen for application in this project was a passive lag filter (Figure 3.2 a)) with the components R_1=3.60 kΩ, R_2=0 and C=0.1 μF. The characteristic constant of this filter, therefore are:

$\tau_1 = 0.00036\ s$;

$\tau_2 = 0\ s$.

Based on the Equation 3.3 and parameters of NE 565, the VCO conversion factor K_0 of this particular PLL is given as [118, 119]:

$$K_0 = \frac{50 f_0}{V_{CC}} \frac{rad}{V/s} \tag{3.20}$$

where V_{CC} is the total supply voltage (supply voltage for the circuitry shown in Appendix 1 was ± 9 V) and f_0 is the free-running (idle) frequency of the VCO. The free-running frequency of the VCO is adjusted by means of timing resistor R_1 and timing capacitor C_1 and is determined by:

$$f_0 = \frac{1.2}{4R_1C_1} \tag{3.21}$$

where R_1 should be within the range of 2 to 20 kΩ for the best operation.

For the application exploited in this project the free-running frequency of the VCO was determined to be around 38 kHz (this will be explained in details in Chapter 6), therefore setting the value of the K_0 at:

$K_0 = 105555.55$ *rad/Vs.*

Knowing the parameters K_d, A_v, K_0 and low-pass filter factors τ_1 and τ_2 of the NE 565 PLL it is possible to calculate natural frequency ω_n and the damping factor ζ of the system in order to investigate its transient response and therefore plot the Bode diagram of NE 565 phase transfer function.

Substituting the values of K_d, A_v, K_0, τ_1 and τ_2 into the Equation 3.16, the value for the natural frequency ω_n could be determined as:

$$\omega_n = \sqrt{\frac{K_0 K_d A_v}{\tau_1 + \tau_2}} = \sqrt{\frac{105555.55*0.4456*1.4}{0.00036 + 0}} = 13524.65 \text{ rad/s} \tag{3.22}$$

and the damping factor ζ as:

$$\zeta = \frac{\omega_n}{2}\left(\tau_2 + \frac{1}{K_0 K_d A_v}\right) = \frac{\omega_n}{2K_0 A_v K_d} = \frac{13524.65}{2*105555.55*0.4456*1.4} = 0.103. \tag{3.23}$$

Moreover, substituting above values for ω_n and ζ into Equation 3.17, the phase transform function of NE 565 PLL becomes:

$$H(s) \approx \frac{2\zeta\omega_n s + \omega_n^2}{s^2 + 2\zeta\omega_n s + \omega_n^2} = \frac{2786.0779s + 13524.65^2}{s^2 + 2786.0779s + 13524.65^2} \tag{3.24}$$

The Bode diagram of the phase transfer function can be obtained by replacing $s = j\omega$ into Equation 3.24 and plotting the magnitude $|H(j\omega)|$ as a function of angular frequency ω. A simple Matlab program was written to implement this procedure and Figure 3.6 shows a Bode plot of the phase-transfer function $H(j\omega)$ for the NE 565 PLL.

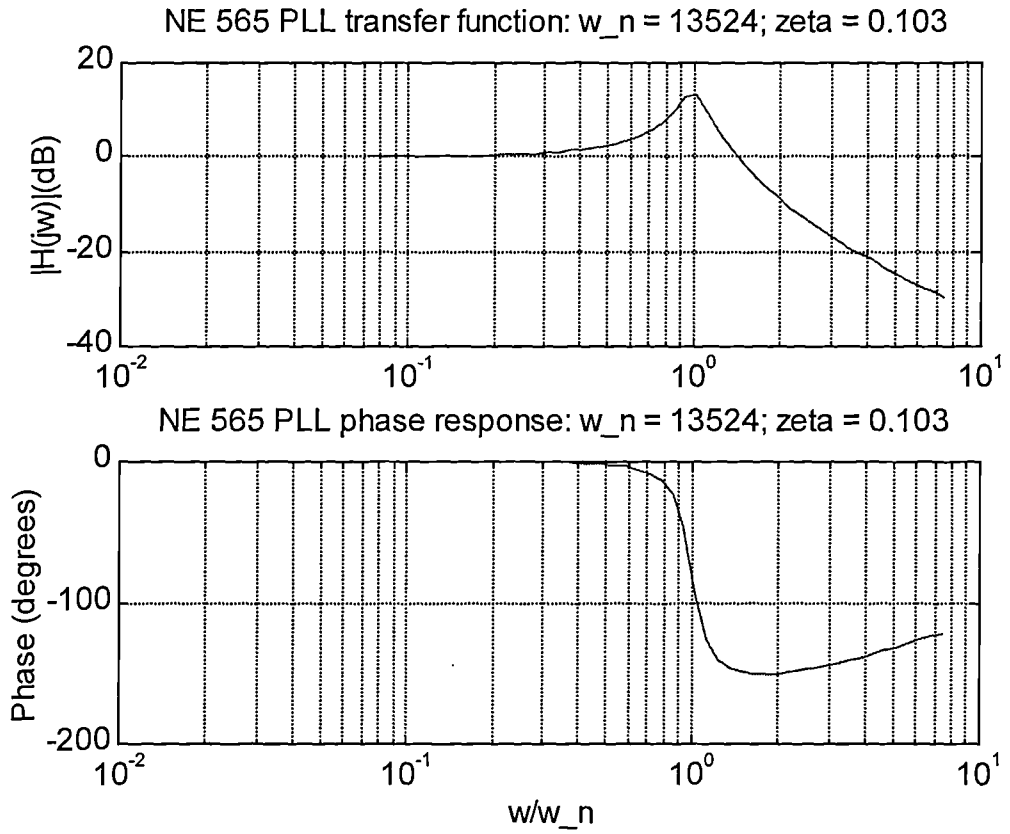

Figure 3.6. Frequency response of a second order NE565 phase locked loop ($w\_n=\omega_n$)

From the Figure 3.6 and the Equation 3.24 it is apparent that the design of PLL implemented in this project is a compromise between the range within which the NE 565 PLL is able to track for phase and frequency modulations and its dynamic response. As it was seen in Section 3.3.1, the second order PLL is able to track phase

and frequency modulations of the reference signal as long as they remain whitin the range of zero to ω_n therefore larger value for ω_n is highly desirable. On the other hand for ζ smaller than unity the transient response becomes oscillatory meaning that there is relatively large overshooting and the settling time is relatively long for a step phase changes in input signal. This will become evident in the proceeding section where the results of NE 565 PLL simulation using a specificly designed software [115] will be presented.

3.5. Simulation of the NE 565 PLL on the PC

A software designed by Best [115], dedicated for the simulation of PLLs to help their design and implementation, was used in order to simulate behavior of the NE 565 PLL. The output signal of the PLL (the output of the loop filter $u_f(t)$) and the output signal of the phase detector $u_d(t)$ were monitored while either a phase step or a frequency step were applied at the reference input of the PLL.

The first simulation of NE 565 PLL was conducted by applying a frequency step of 2 kHz at the reference input. Prior to the simulation parameters for all building blocks were entered (Section 3.4) and simulation parameters specified as follows:

Positive supply voltage	9 V
Negative supply voltage	-9 V
Phase detector:	
Positive saturation level	8.5 V
Negative saturation level	-8.5 V
Phase detector gain K_d	0.4456 V/rad
Loop filter (passive lag):	
τ_1	360 μs
τ_2	0 μs

Voltage controlled oscillator:

Centre frequency $f0$	38 kHz
VCO gain K_0	105555.55 rad s^{-1} V^{-1}
Positive saturation level	8.5 V
Negative saturation level	-8.5 V

Simulation parameters:

Sampling frequency/centre frequency	4
Ecitation	Frequency step
Frequency step size	2000 Hz
Duration	8 ms

Figure 3.7 shows result of NE 565 LPL simulation when a frequency step of 2000 Hz was applied to the reference input.

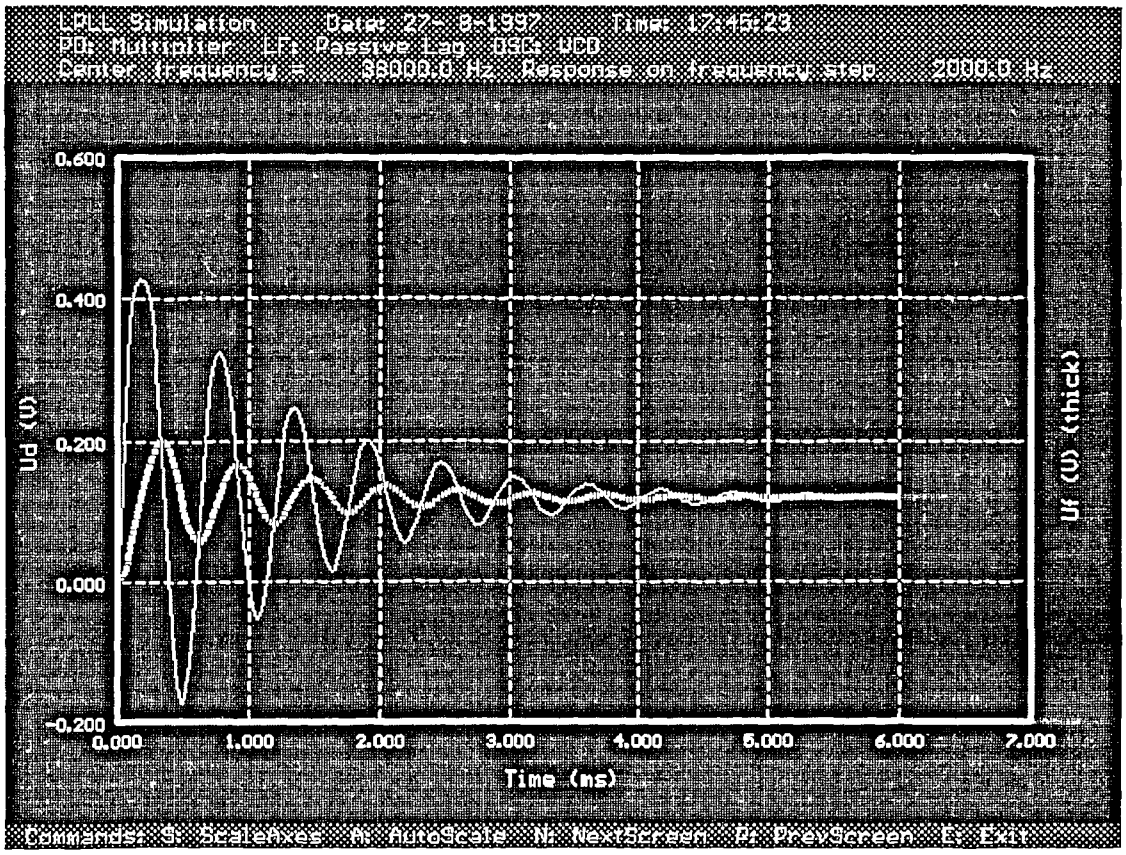

Figure 3.7. Result of NE 565 LPL simulation when frequency step of 2 kHz was applied to the reference input.

From the Figure 3.7 it could be seen that the response to the frequency step becomes oscillatory before it settles to a particular value after approximately 4ms. In some applications this could be a relatively long time but for implementation in this project time was not considered as critical.

The simulation program calculated the values for the natural frequency ω_n and damping factor ζ as 11430.4 s^{-1} and 0.12, respectively which is very close to the values calculated theoretically in Section 3.4. Based on these values some key parameters which govern the dynamic performance of the NE 565 PLL could be estimated. The governing parameters are defined as [115]:

1. *The hold range* $\Delta\omega_H$ which is the frequency range in which LPLL can statically maintain phase tracking. For the passive lag filter used in the design of NE 565 it could be calculated as:

$$\Delta\omega_H = K_0 K_d. \tag{3.25}$$

2. *The pull-out range* $\Delta\omega_{PO}$ which is the dynamic limit for stable operation of a PLL can be approximated as:

$$\Delta\omega_{PO} = 1.8\omega_n(\zeta + 1) \tag{3.26}$$

3. *The pull-in range* $\Delta\omega p$ is the range within which LPLL will always become locked, but at the expense of process speed. For the passive lag filter this is given as:

$$\Delta\omega_p \approx \frac{4\sqrt{2}}{\pi}\sqrt{\zeta\omega_n K_0 K_d} \tag{3.27}$$

4. *The lock range* $\Delta\omega_L$ which is the frequency range within which a PLL locks within on single-beat note between reference frequency and output frequency. For all type of filters it is given as:

$$\Delta\omega_L \approx 2\zeta\omega_n \tag{3.28}$$

For all above key parameters a simple identity is valid:

$$\Delta\omega_L < \Delta\omega_{PO} < \Delta\omega_P < \Delta\omega_H \tag{3.29}$$

Substituting values for ζ and ω_n into the equations 3.25 - 3.28 values for the key parameters of the NE 565 PLL can be derived as:

Lock range:

$\Delta\omega_L = 2786.08\ s^{-1}$

$\Delta f_L = 443.418\ Hz$

Pull-out range:

$\Delta\omega_{PO} = 26851.84\ s^{-1}$

$\Delta f_{PO} = 4273.603\ Hz$

Pull-in range:

$\Delta\omega_P = 14575.38\ s^{-1}$

$\Delta f_P = 2319.74\ Hz$

Hold range:

$\Delta\omega_H = 47035.55\ s^{-1}$

$\Delta f_H = 7485.94\ Hz$

Some text books [108, 109] and the data sheet for NE 565 PLL [34] define Lock-in Range as: $\Delta f_L = \pm 7.8 f_0/V$, which for the centre frequency of 38 kHz is given as:

$$\Delta f_L = \pm 16466.66\ Hz.$$

Also, a term Capture Range could be found defined as:

$$\Delta f_c \approx \pm\left[\frac{\Delta f_L}{2\pi(3.6\times 10^3)C}\right]^{\frac{1}{2}}$$

and for C=0.1μF (Appendix 1) yields:

$$\Delta f_C = \pm 853.22\ Hz$$

A second simulation of the NE 565 PLL was performed applying a frequency step of 4 kHz to the reference input, and result is shown on Figure 3.8.

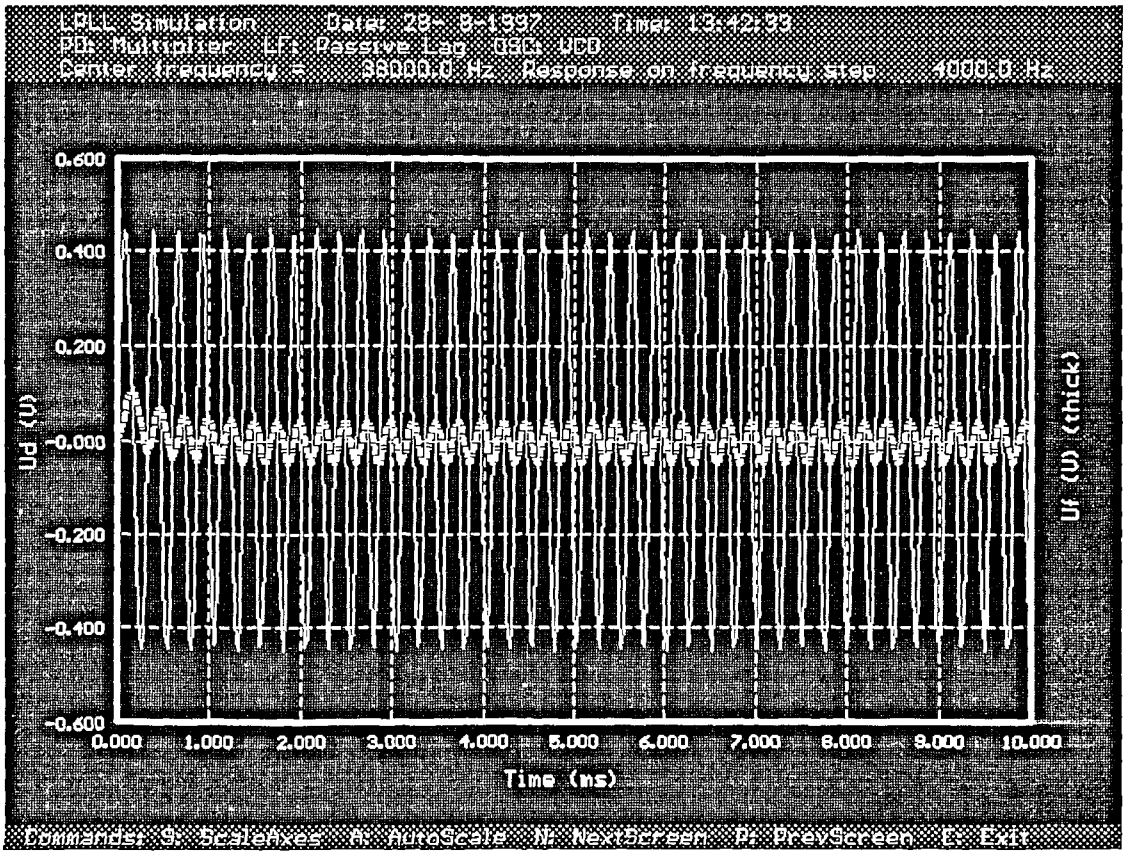

Figure 3.8. Result of NE 565 LPL simulation when frequency step of 2 kHz was applied to the reference input.

Figure 3.8 shows that the simulation result agrees with the calculated values of the key parameters of the NE 565 PLL. It is evident that the circuit fails to lock when the

frequency step of 4 kHz is applied to its input. This also agrees with the calculated value for the pull-out range of $\Delta f_{PO} = 4273.603$ *Hz.*

Finally, a simulation was performed with a phase step of 50 degrees applied to the reference input. Figure 3.9 shows result of the simulation.

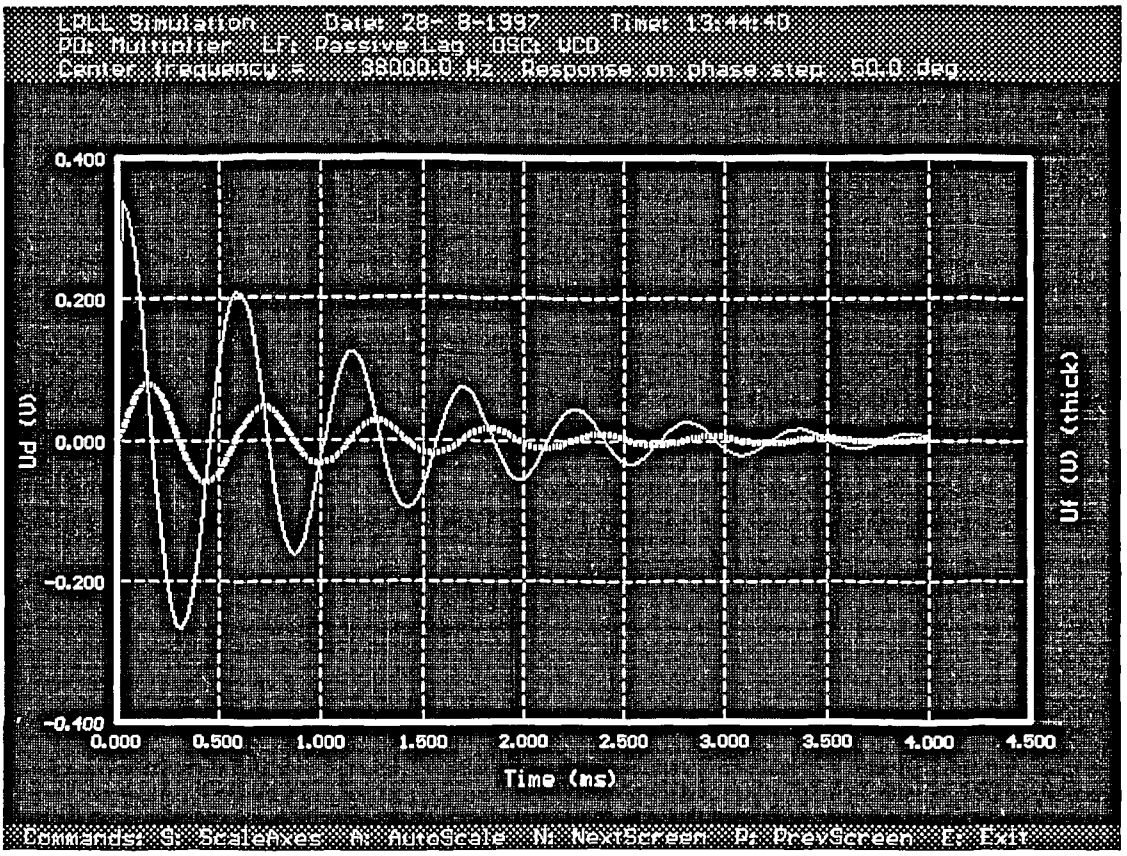

Figure 3.9. Result of NE 565 LPL simulation when phase step of 50 degrees was applied to the reference input.

Figure 3.9 shows that, immediately after applying a large 50 degrees phase step to its reference input, the NE 565 PLL exhibits oscillatory behaviour but succeeds in settling and locking after 3 ms. The simulation program had shown very similar behaviour of the PLL when phase steps of 90 and -90 degrees were applied to the

reference input. This is a very encouraging result having in mind that the NE 565 PLL will be used in this project to track both frequency and phase shift.

3.6. Conclusion

A linear mathematical model of the analog phase-locked loop proposed to be used in this project to track changes in frequency as well as in phase has been developed in this Chapter. Static and dynamic behaviour of the linear phase-locked loop (LPLL) was elaborated through an evaluation of the phase transfer function and through the influence of the natural frequency ω_n and damping factor ζ on its performance. The general mathematical model was applied to the second order NE 565 PLL to derive its phase transfer function and to plot the Bode diagram in order to investigate the transient response. Prior to this, values of the natural frequency ω_n and damping factor ζ of the NE 565 were calculated as13524.65 s^{-1} and 0.103, respectively for the given idle frequency of the VCO: f_O = 38 000 Hz. From the plot of the Bode diagram it was evident that the proposed design of the NE 565 is a compromise between the range within which the NE 565 PLL is able to track the phase and frequency modulations and its dynamic response. The relatively small value of ζ meant initial oscillation of the transient response and relatively long settling time. Performing a simulation technique on the NE 565 PLL, it was found that its settling (locking) time was 4ms and 3ms when subjected to the frequency and phase step respectively. This delay was not considered to be critical for the particular application of the the NE 565 in this project. The main consideration was the range within which the PLL was able to respond to frequency and phase changes. The simulation program has shown that NE 565 was able to lock when phase step ranges between -90 and +90 degrees are applied at the reference input, whilst its pull-out range was $\Delta fpO = 4273.603$ *Hz.* The characteristics of the NE 565 PLL obtained theoretically and via the simulation program have been found to be satisfactory for implementation in this project.

Chapter 4

Initial design of a tactile sensitive probe

4.1. Introduction

The proposal for a new resonator tactile sensor was based on the design of a touch sensitive probe which exploits the piezoelectric effect, oscillates at certain frequency (Chapter 2) and uses a phase locked loop (PLL) frequency detection technique (Chapter 3). Development of a touch sensitive probe was a good choice for the preliminary design because it allowed the testing of the probe on the Coordinate Measuring Machine (CMM) and it also allowed a comparison of the probe's characteristics (such as sensitivity, repeatability, lobing, false triggering etc.) with commercially available probes.

The basic design of the probe consists of a stiff cantilever beam vibrated longitudinally by a PZT layer cemented onto one side and of another PZT layer which

acts as a pick-up element cemented on the other side of the beam. Figure 4.1 shows the body structure of the touch sensitive probe. The probe consists of an aluminium bar (4×8×30 mm) with both ends threaded. One end was fixed to a platform which can in turn be mounted kinematically onto a probe head, rigidly attached to the machine quill, whilst on the other end of the probe an M2 threaded stylus, with a 4mm diameter ruby ball, was mounted. In Figure 4.2 a 3D representation of the probe together with the stylus is shown.

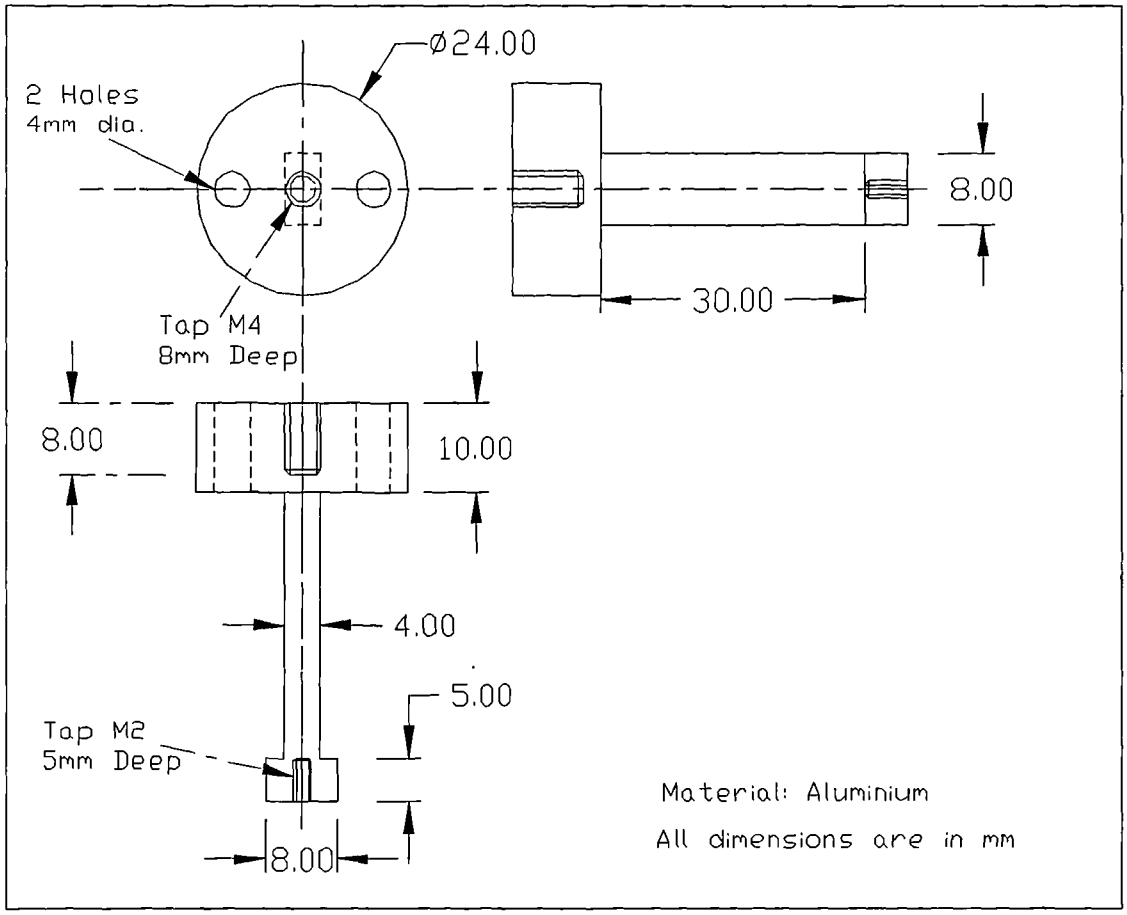

Figure 4.1. The initial design of the resonator based tactile sensitive probe

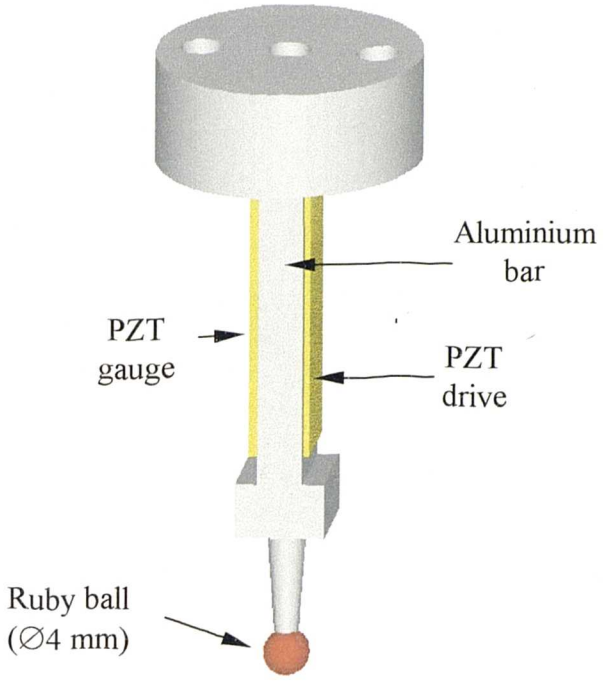

Figure 4.2. 3D Representation of the new probe design with 4mm probe tip

The design principle exploits the fact that when a rigid element (probe) is oscillated at near its resonance frequency and comes into contact with the surface of another body (workpiece), regardless of the latter's rigidity there is a change in the force gradient acting on the probe tip. This change results in a shift in the frequency of vibrational resonance, Δf, of the probe. By detecting this frequency shift , a threshold circuit can be used to provide a *trigger signal* for the controller to record the current position of the probe in space with respect to the machine's coordinate system.

4.1.1. Characteristics of PZT-5H ceramics

For this initial design two rectangular plates of piezoelectric PZT-5H [75] materials were used. PZT-5H is a modified lead-zirconate-titanate ceramic, which has an exceptionally high dielectric constant, electromechanical coupling coefficient and charge sensitivity, compared with some other piezoelectric ceramic materials. It is the

good ceramic material for mechanical to electrical energy conversion. This material is used in sensitive receivers and applications requiring fine movement control. It has been used in a wide range of applications from hydrophones to ink jet printers [75]. Table 4.1. [120] summarises the relevant properties of piezoelectric materials in common use.

	Material	Charge sensitivity d pCN^{-1}	Dielectric constant ε	Young's modulus E $\times 10^9 Nm^{-2}$
Natural	Quartz	2.3	4.5	80
	Tourmaline	1.9,2.4	6.6	160
Piezoelectric ceramics	Lead zirconate -titanate	265	1500	79
	Lead metaniobate	80	250	47

Table 4.1. Properties of piezoelectric materials

The standard gauge, BEG/1-6, was used as an excitation gauge whilst BSG/1-6 was employed as a pick-up strain gauge. PZT gauges are polarised through the thickness with fired silver electrodes. The electrodes are arranged so that both electrical connections may be made onto their back faces. Both gauges were manufactured by Morgan Matroc Limited, Southampton. Dimensions (in mm) and characteristics of these two elements are:

BSG/1-6: Length = 25.4; Width = 6.35; Thickness = 1.016;
Capacitance = 2,100 pF; Sensitivity(volts/unit strain) = 7.4×10^5.

BEG/1-6: Length = 25.4; Width = 6.35; Thickness = 0.508;
Capacitance = 3,200 pF.

Working temperature range: -270°C to +250°C;

Maximum permissible dynamic strain 2.5×10^{-4} for linear operation.

The gauges were attached to the probe as per standard practice (ie. to cement them securely to the structure with a superglue, using M-BOND 200 ADHESIVE (M-LINE ACCESSORIES - Welwyn which contains methil-2-cyanoacrylate)[†] .

4.1.2. Determination of resonance frequency

In order to calculate the resonant frequency of the probe system the dimensions of the aluminium bar and properties of the PZT-5H plates were taken into account. Using the formula for the displacement of piezoelectric plates

$$\Delta L = \frac{d_{31} V L}{thk}, \tag{4.1}$$

where d_{31} is the piezoelectric charge constant which for PZT-5H is -274×10^{-12}m/V, L and *thk* are the length and the thickness of PZT plate, respectively, while the V is the applied voltage. Assuming that the required displacement of the PZT plate (i.e. the amplitude of excitation) is no more than 0.05μm, then the applied voltage can be calculated from the Equation 4.1 to be:

$$V = \frac{\Delta L \times thk}{d_{31} L} = 3.65V \tag{4.2}$$

Also V can be also expressed in terms of force (F) [75]:

$$V = \frac{g_{31} F}{L} \tag{4.3}$$

[†] M-BOND 200 adhesive, Measurement Group, Basingstoke, Hants, UK

where g_{31}=-9.1×10^{-3}Vm/N is piezoelectric voltage constant. Therefore, the estimated force on the probe is given by:

$$F = \frac{VL}{g_{31}} = 10.18N \tag{4.4}$$

For the aluminium structure, the longitudinal displacement can be estimated from

$$x = \frac{FL}{AE} = 113\,nm, \tag{4.5}$$

where A is the cross-sectional area of the probe, 3.2×10^{-5} m^2 and E is Young's modulus for aluminium with a value of 71×10^{9}N/m^2.

Using a simplified model of a longitudinal bar with negligible damping, the natural frequency can be estimated as a function of the mass and stiffness of the system. That is

$$\omega_r = \sqrt{K/m}, \tag{4.6}$$

where stiffness of the longitudinal bar is given by

$$K = \frac{AE}{L} = 7.57 \times 10^7 \text{ N/m} \tag{4.7}$$

and mass $m=\rho V$ is 4.34×10^{-3} kg. The density ρ for aluminium is 2710kg/m^3.

Therefore the natural frequency of the probe can be estimated as:

$$f_r = 20.994 \text{ kHz}. \tag{4.8}$$

In the above model, however, the M2 thread stylus which was mounted on one side of the probe was not taken into account, so the theoretically obtained natural frequency

was higher than the one expected in an experimental test set-up. This compares favourably with the experimental attempts to evaluate the resonance frequencies.

Figure 4.3 shows a typical frequency spectrum of the system measured by high precision AND 3525 Dual Channel Fast Fourier Signal Analyser. The sweep sine wave signal was used to drive the excitation gauge in order to obtain the frequency response of the whole system. The frequency was swept from 0 to 100 kHz with an amplitude of $3V_{0\text{-}p}$.

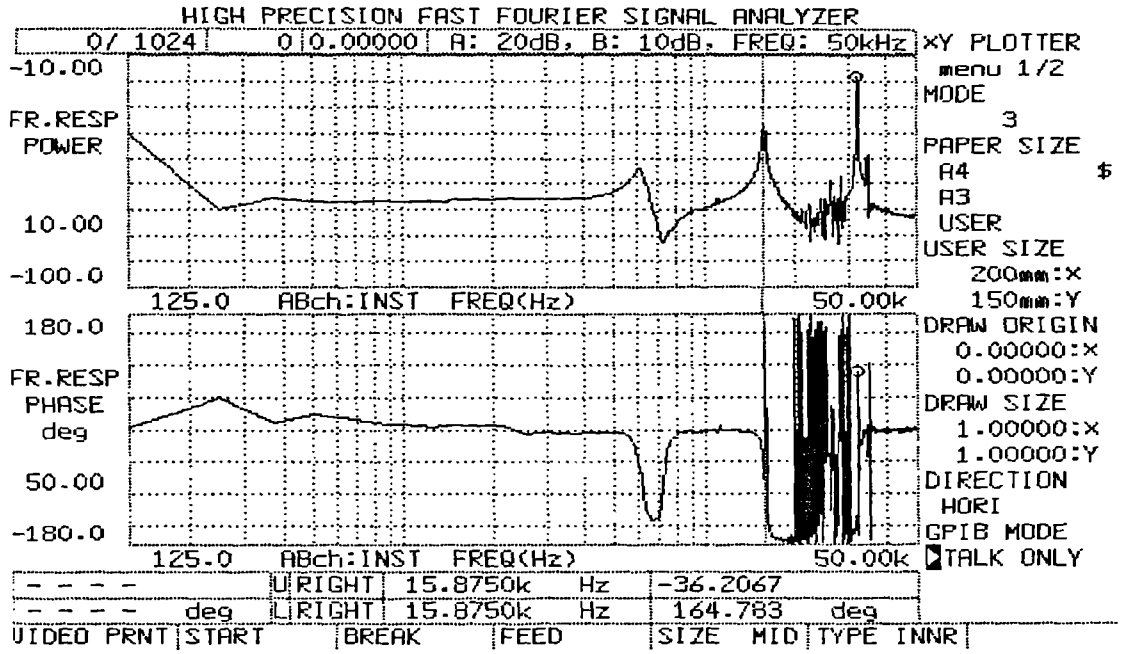

Figure 4.3. Frequency spectrum of the system

The voltage applied to the PZT layer induces axial stresses along the length of the probe, with some bending moment proportional to the lateral offset between the centre line of the probe and PZT plane. An experimental test was performed to establish the vibrational modes of the tactile probe. This was achieved by sweeping the frequency of sine wave, with constant amplitude, through the excitation gauge of the PZT and measuring the r.m.s. piezoelectric voltage of the strain gauge (Figure 4.4). Although

the fundamental resonance frequency occurs at 14.3kHz (±5Hz), the second mode at 25.179kHz was selected during further experiments simply to eliminate the audible noises. This was an adequate choice because it provided good static and dynamic performance.

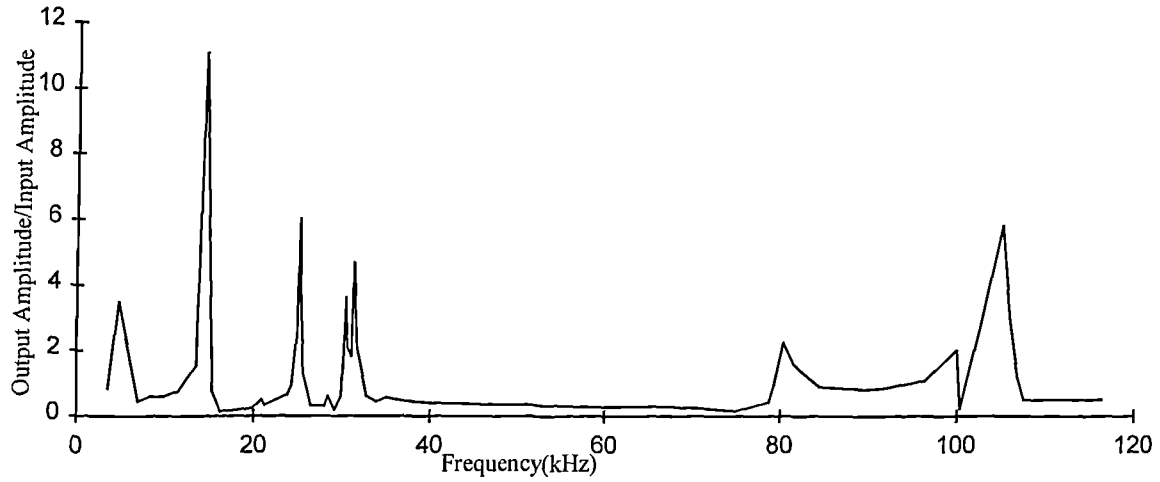

Figure 4.5. AC voltage generated in strain gauge element at various frequencies

4.2. Characterisation of the probe

4.2.1. Instrumentation and experimental method

To fully evaluate the performance of the probe, a dedicated test rig was constructed. Figure 4.5. shows the set-up used. The trigger force of the probe was generated by a simple linear flexure translation stage machined from an aluminium monolith and driven by a solenoid. A SmCo (Samarium Cobalt) permanent magnet is rigidly cemented to the moving platform of the stage and surrounded by, but not touching, a uniformly-wound cylindrical solenoid coil. Current through the coil produces a magnetic field inducing a force on the magnet which bends the flexure springs. The

coil was controlled by a Darlington pair current driver whose input was taken from a function generator. The flexure has a spring constant of 59N/mm and the actuator has an overall gain of 8.2μm/V. Displacement of the flexure was continuously monitored by an LVDT which was periodically calibrated against a Hewlett Packard laser interferometer system (HP 5528A). The type of LVDT used was a D5/00G8, with linear range of ±0.2 mm and with 0.15% of linearity. The conversion rate of the LVDT output was 20μm/V. To provide coarse adjustment of the actuator position with respect to the probe, the flexure was mounted onto a 3 degree of freedom (X,Y,θ) manually operated micro positioning table. The probe is attached onto a steel bracket which in turn can be rotated about the longitudinal axis of the probe to give a fourth degree of freedom. Both, the flexure and the probe were aligned horizontally in the same plane and placed at very close proximity.

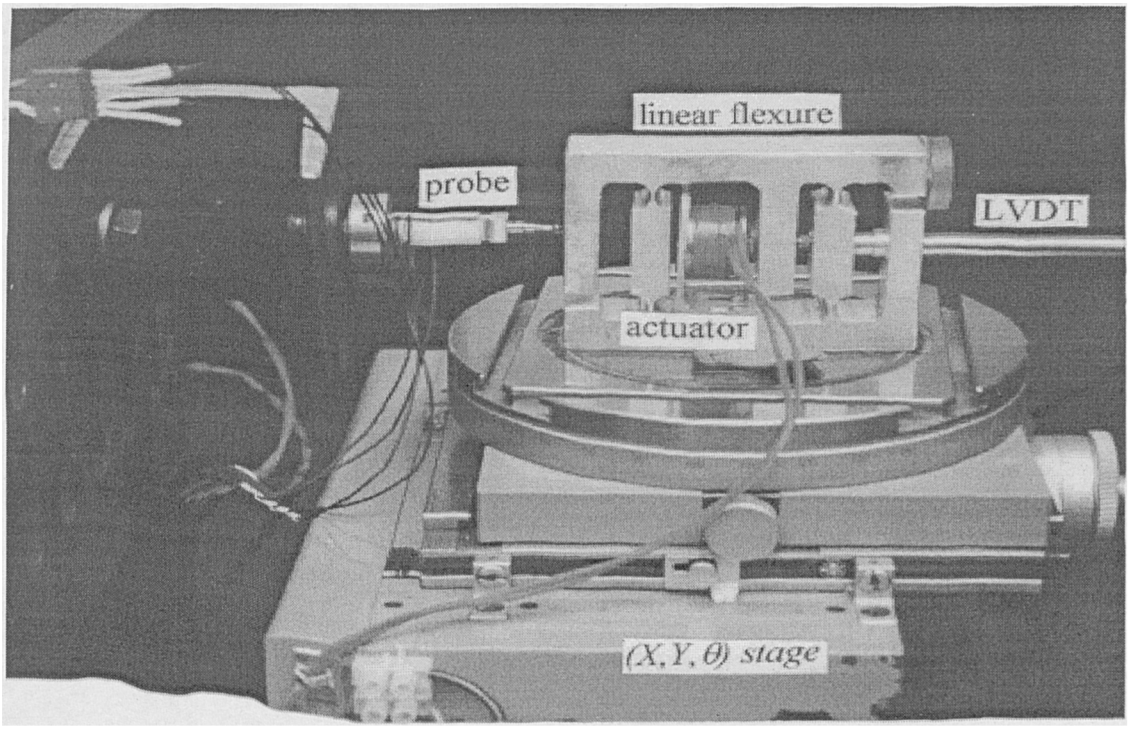

Figure 4.5. Photograph of the set-up used

Prior to each test, a separation gap of 0.1 mm was set between the probe's tip and the moving platform. The contact force vector was always aligned along the coil's centre line, while the contact arrangement was in the form of a sphere on a flat surface.

Appendix A shows a schematic diagram of an electronic circuit (using NE 565 PLL chip) which implements a feedback control technique to detect frequency shift. The block diagram of the control system is shown in Figure 4.6.

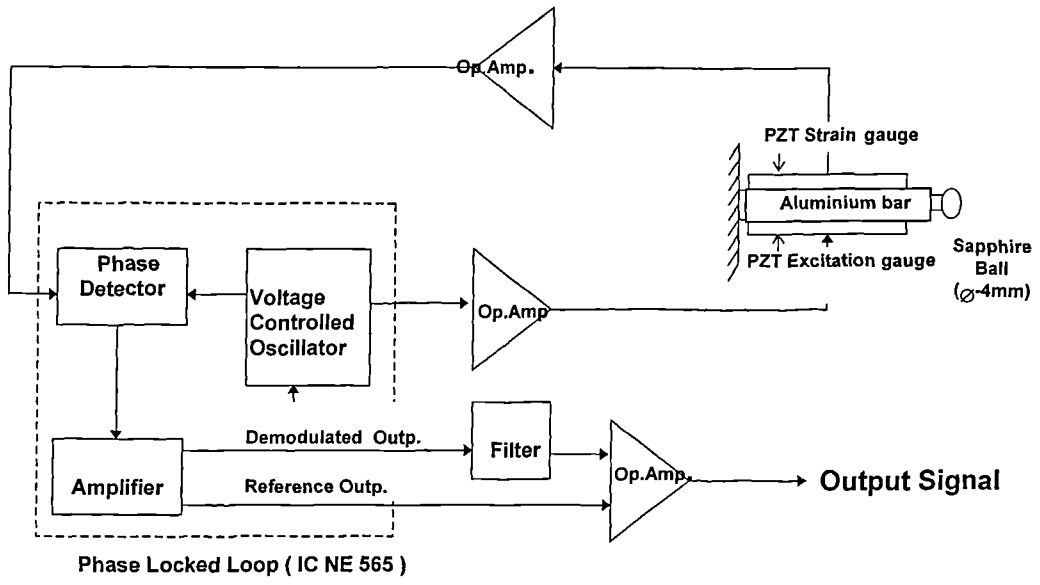

Figure 4.6. The body structure of the touch sensitive probe and its control system

The voltage-controlled oscillator of the NE 565 phase-locked loop (Chapter 3, Figure 4.2 and Appendix A) provides the driving signal (a highly stable triangular wave), feeding the drive plate after amplification by operational amplifier OPA121 to 10V peak-to-peak. The longitudinal strain generated in the probe is detected by the PZT strain gauge plate and converted into an appropriate voltage signal via a charge amplifier comprising of operational amplifier OPA121, 10pF capacitor and 1.5MΩ resistor. After being amplified 1.1 times through an inverting operational amplifier (OPA121) this signal is fed into the reference input of the NE 565 PLL. The phase

shift between the drive and the strain signal at the near resonance frequency was set at 180°. As contact takes place, the changes in the resonance frequency shifts the phase angle from its pre-set value. The PLL adjusts the driving signal frequency to null the change in the phase angle. The comparator provides an analog signal proportional to the phase difference between the VCO signal and the strain signal which feeds the VCO to adjust the input frequency so that the pre-set phase relationship can be restored (Chapter 3), hence maintaining the vibration of the mechanical system at the new resonance frequency. The output of the PLL (dc level) is proportional to the change in the resonance frequency, with a conversion sensitivityof 0.73mV/Hz and it was set just below 0V via a biasing 10 kΩ trimmer in order to give triggering signal when contact takes place. This output is then filtered by an RC filter and fed into an operational amplifier (OPA121) to generate the stable signal which can be used in scanning probing systems. With further filtering and passing through an open gain operational amplifier a clean on/off trigger signal can be generated. This signal is then fed into a small switching transistor circuit which was designed as an interface between the probe's driving system and CMM machines in order to provide suitable 12V triggering signal. Transistors used were NPN BC 337. Figure 4.7 shows a photograph of the printed circuit board whose schematic diagram is shown in Appendix A.

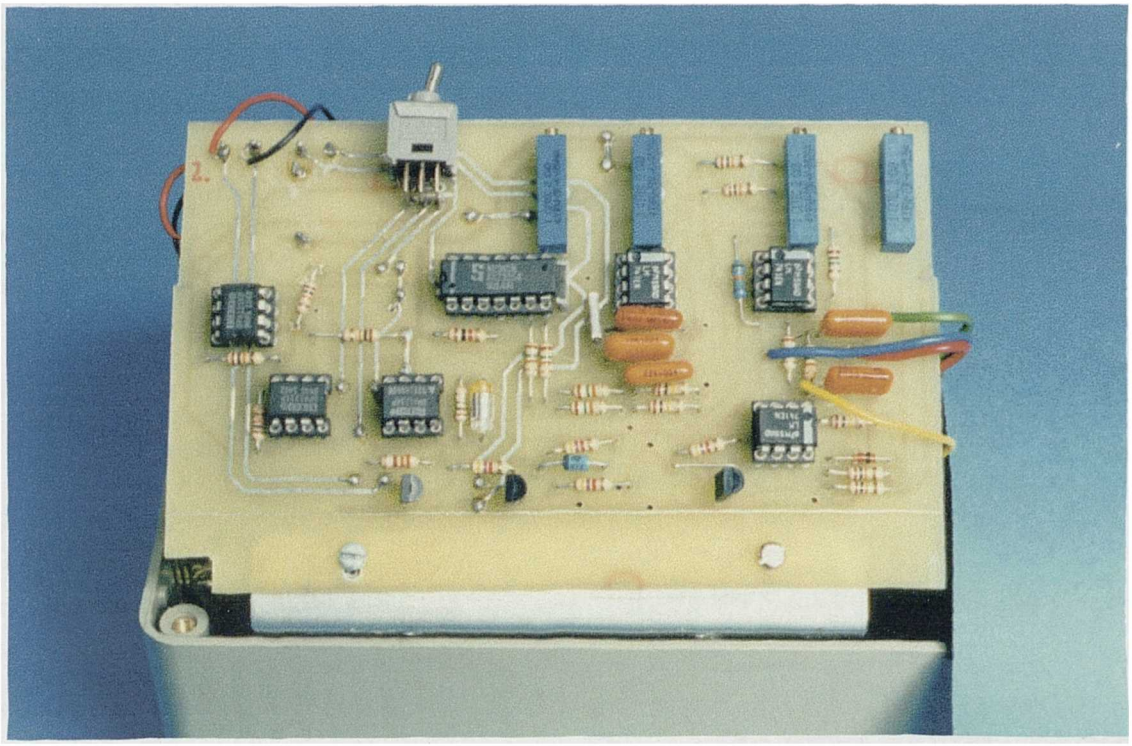

Figure 4.7. Photograph of the PCB designed to implement phase-locked loop technique

The PLL output voltage (V_{OPLL}), LVDT output voltage (V_{OLVDT}), solenoid input voltage (V_{INSOL}) and the resultant trigger signal were recorded and analysed. Data collection was done by a IBM compatible PC using a ADC data acquisition board (Amplicon Liveline Instruments PC74 16 I/O board with 12 bit resolution). Laser interferometer readings were recorded via a standard GPIB interface. A program written in Turbo Pascal 7.0 controlled data acquisition into the computer (Appendix B); while the Microsoft Excel spreadsheet was used for the data analysis.

The room in which these experiments were conducted was housed within a humidity and temperature controlled laboratory (a diurnal variation of approximately ±2°C was maintained).

4.2.2. Experimental results

Calibration of the probe was performed by driving the coil, using the triangular and sine wave output from a function generator, to bring the flexure into contact with the probe's tip. Various driving signal amplitudes (0.1-1.2V) and frequencies (0.1-700Hz) were tried. The input signal to the coil, output from the PLL, triggering signal and flexure displacement in the form of output voltage from an LVDT were recorded simultaneously. Several experiments were conducted and it was found that the moving platform could be best controlled if the coil was driven using a sine wave signal with an amplitude of 1.2 V p-p and frequency at 0.5Hz. Figure 4.8. shows a typical plot of the recorded signals [121,122].

The maximum amplitude of the input signal corresponds to the maximum flexure deflection of 10 μm for a free run (without making surface contact). This was calibrated using the laser interferometer system. The displacement of the LVDT was used both to detect the point at which the contact takes place and to measure the amount of indentation into the surface from which the contact force exerted at the probe can be evaluated. A typical value of indentation is shown in Figure 4.8.(e). It was derived by subtracting the trace of the LVDT when the probe is in contact (Figure 4.8 b) from contact-free trace of an LVDT. The actual contact point was deduced from the LVDT signal as the point where the output starts to slow down compared to that of a free run. The force F was estimated as the multiplication of the indentation δ by the spring constant of the flexure k ($F = \delta \times k$). When contact takes place the probe triggers; the PLL output increases by approximately 10 mV (corresponding to a shift of 14.5 Hz) from its pre-set value (-25 mV).

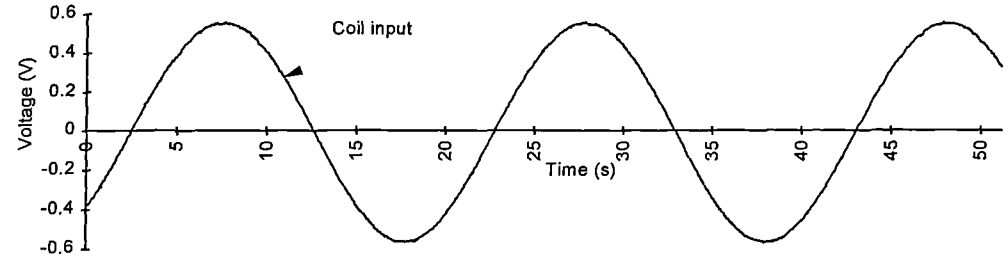

(a)

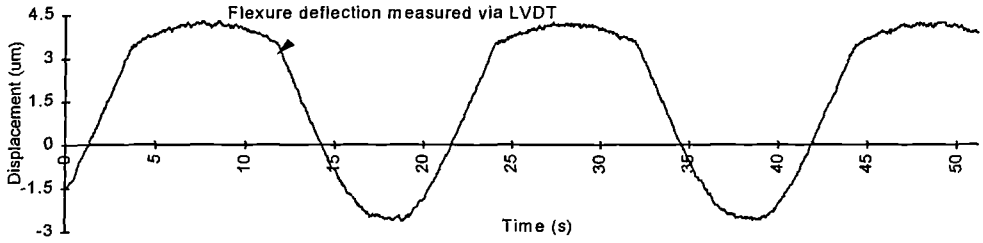

(b)

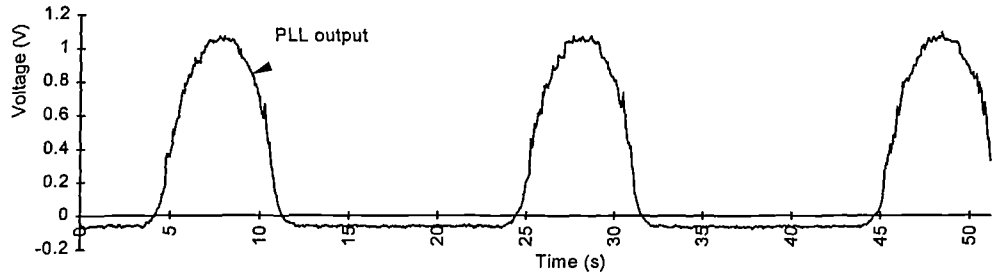

(c)

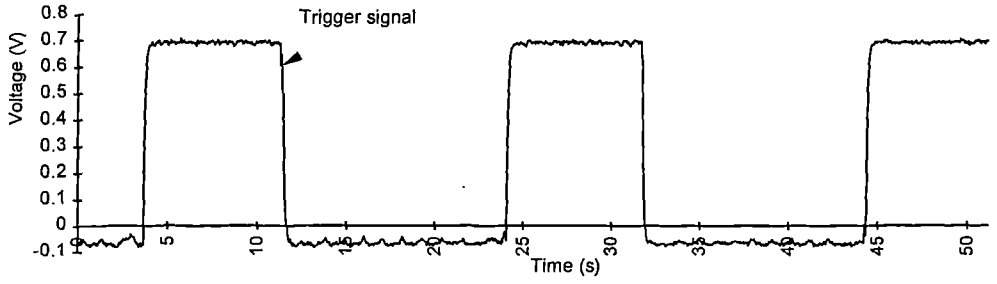

(d)

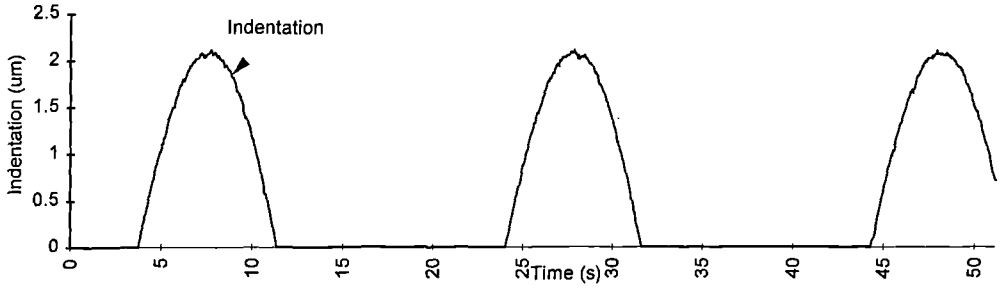

(e)

Figure 4.8. Typical plot showing Input sine wave (a), Flexure deflection (b), PLL output (c),Trigger signal (d) and amount of indentation (e)

Figure 4.9. represents the relationship between the PLL output (Hz) and the interaction force of the probe/sample. From the graph it can be seen that two linear regions can be assumed. The first one is up to 50 mN contact force with a gradient of 7.3 Hz mN^{-1} followed by a small jump and another linear trend up to 140 mN with a gradient of 12.8 Hz mN^{-1}. The maximum frequency shift measured was about 2 kHz which corresponds to 140 mN contact force in axial direction, whilst the minimum detectable trigger force was 3.8 mN.

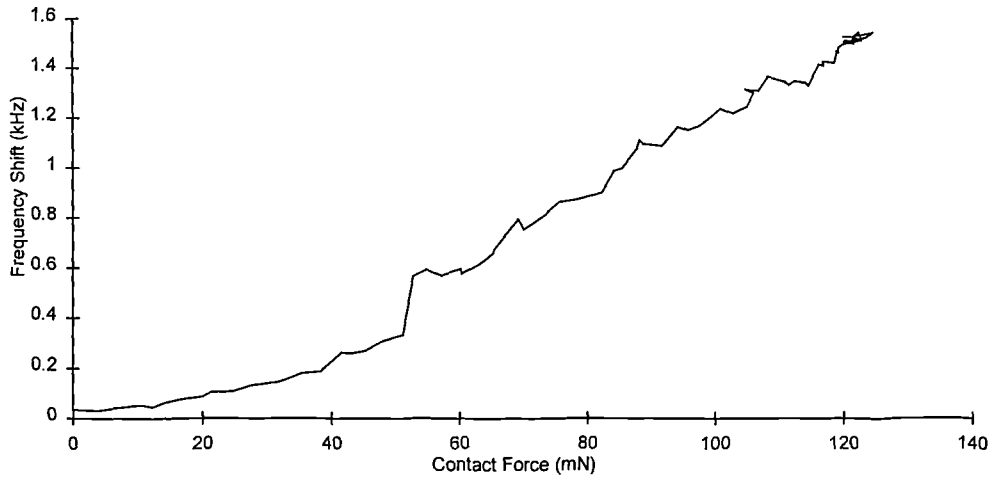

Figure 4.9. Frequency shift (kHz) versus applied contact force (mN)

The graph shown in Figure 4.9 is very similar to ones measured by a conventional nano-indentation hardness probe. Micro Materials Measuring Nanotechnology, UK, has reported results of hardness measurements obtained using NanoTest 550 [123]. The measurement results have shown that it was possible to clearly perceive two phases using relatively shallow indentations on a polished specimen. These were presented as 'soft phase' and 'hard phase' on hardness graphs. It could be assumed that the graph in Figure 4.9 also represents two hardness phases. The first one shows the interaction of the probe with the surface film of aluminium, but as the indentation increases it turns into the second phase which is the actual interaction of the probe with the subsurface. This assumption was of significant importance and the starting

point in understanding the complexity of contact mechanisms between the probe and the specimen.

A repeatability test was conducted by driving the coil in steps of 0.4μm over a 3μm ramp. At each position the average of 5 readings of the PLL output were recorded. This was repeated over 5 cycles. The repeatability of a probe is the ability of that probe to initiate a measurement at the same point each time. The measure of unidirectional repeatability of many probes is quoted as a maximum 2σ (2×standard deviation) value at the stylus tip. This gives a 95% confidence level that all readings taken in this mode will repeat within 2σ from a mean value. Figure 4.10. presents the mean value of the 5 cycles together with the ±2σ from the mean. At the trigger point, repeatability of 40Hz was estimated but deviated around ±200Hz as the indentation progressed. The minimum force required to trigger the probe was set at about 4mN. This compares favourably with most of the commercially available touch sensitive probes (e.g. Renishaw's TP12 touch trigger probe has trigger force of about 1 mN, while for TP7M the value was about 20mN)

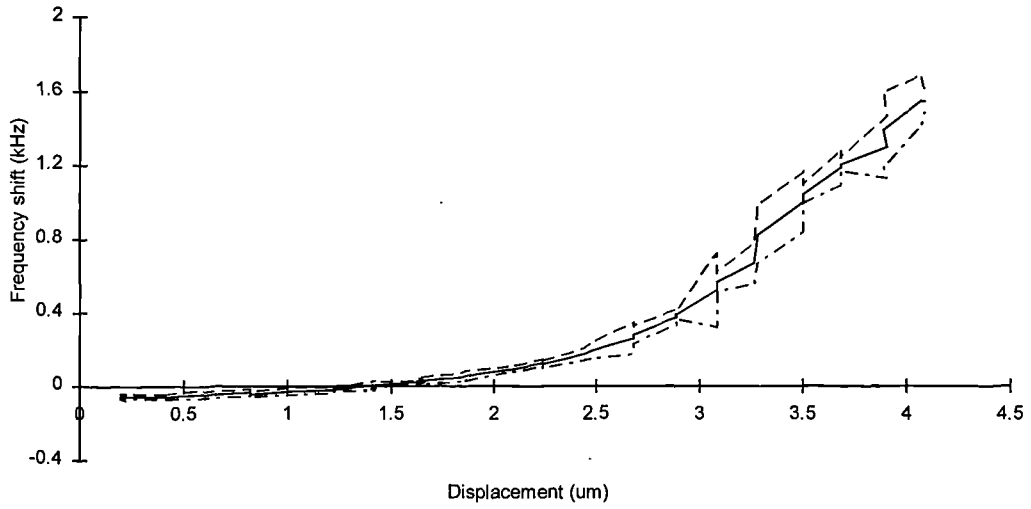

Figure 4.10. The mean value of five cycles together with the ±2σ from the mean value

Figure 4.11. shows the drift test of the PLL plotted together with the LVDT over a period of 1 hour. It demonstrates the stability and fidelity of the probe to slight variation in contact pressure compared with the LVDT reading. The slight drift was introduced because output was taken directly from the output pin of the IC 565. This was improved by processing the signal through a filter thereby stabilising it (see Appendix A.).

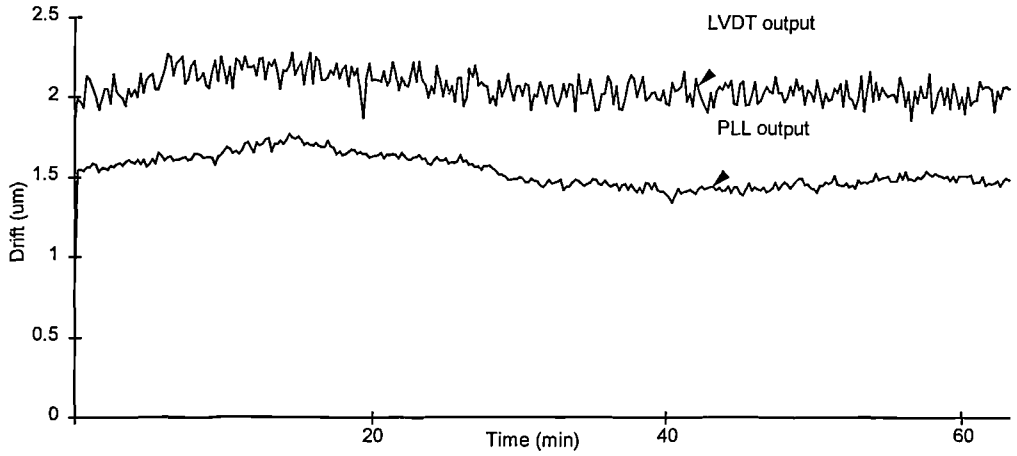

Figure 4.11. Drift test of the PLL and LVDT over a period of 1 hour.

Dynamic performance was defined as the maximum possible triggering rate. This however, was limited by the bandwidth of the flexure mechanism, (700 Hz) at which the probe was still able to provide a clean triggering signal.

Another set of experiments was conducted to test the sensitivity of the probe by setting the oscillated frequency at 16.350 kHz, just 2 kHz above probe's natural frequency [124]. The conversion factor of the PLL in this case was 1.04 mV/Hz. They are presented in the same form as the experiments conducted at 25.179 kHz. For a clearer view Figure 4.12 shows PLL output, contact force and a frequency shift versus applied contact force. The setup in this case was slightly altered. The probe was mounted onto a flexure mechanism stage driven by an electromagnetic solenoid actuator. The flexure was driven in small increments of 0.2 mV until contact between

the probe and the stationary high precision load cell occurred. The load cell was used to control the contact force. The sensitivity of the load cell was 0.036 mV/g. From the Figure 4 12 c) it could be seen that only 44.5 mN of contact force was required to cause a frequency shift of about 3 kHz. This indicates that the performance of the probe at its resonant (slightly off) frequency was better compared to sensitivity at 25.179 kHz but audible noises were not fully eliminated.

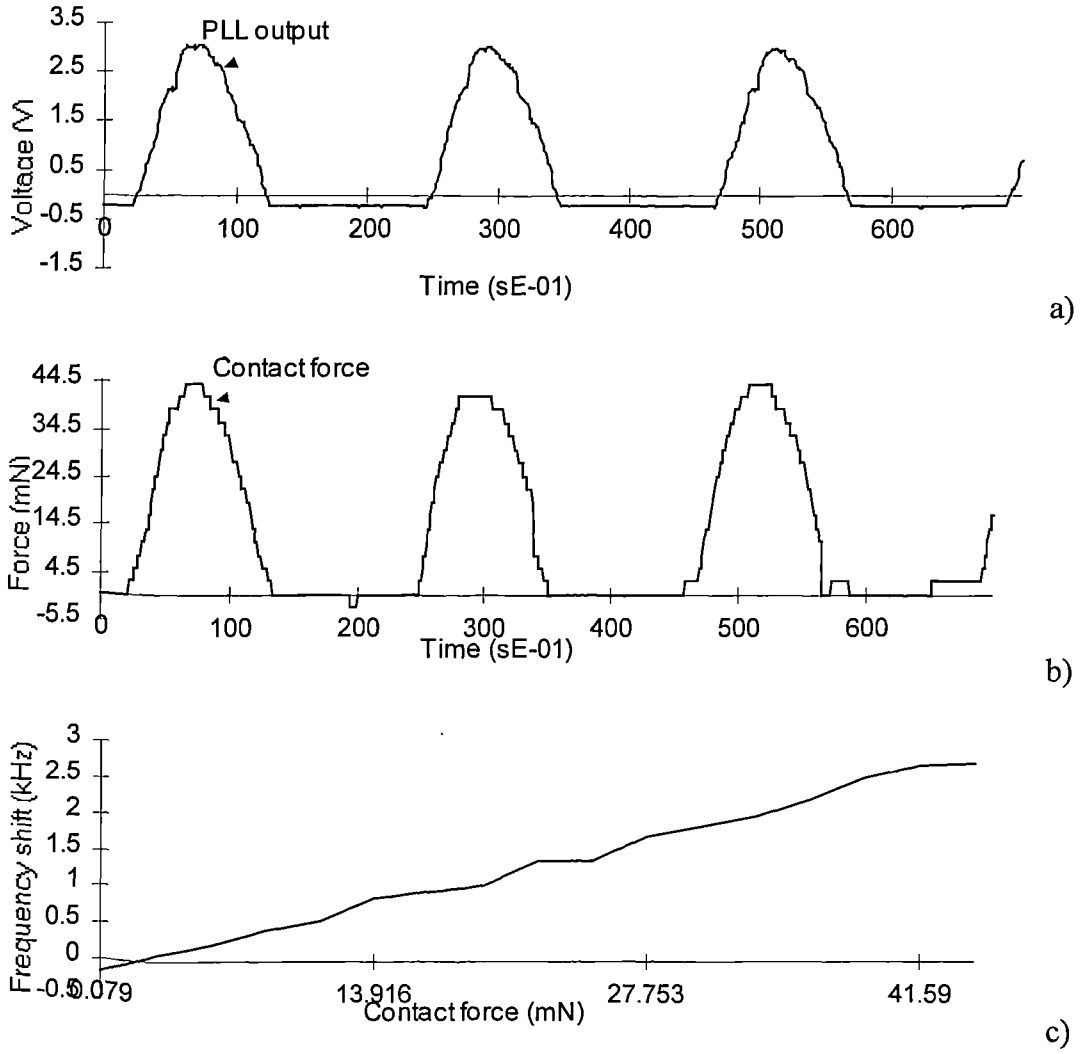

Figure 4.12. Plot showing PLL output voltage **a)**; Contact force **b)** and Frequency shift versus applied force **c)**, when operating frequency of the probe was set at 16.350 kHz

Further tests were conducted on the KEMCO E600 CNC CMM (600×500×500 mm). The probe was used to record the coordinates of the inside diameter of a master ring gauge (Figure 5.13). These tests were repeated over fifty times and the error in measurement was within the resolution limit of the CMM (±5μm). During these tests, the approach speeds were restricted to 20mm/s because the current probe has not yet been provided with a flexible kinematic mount to allow travel at high speeds.

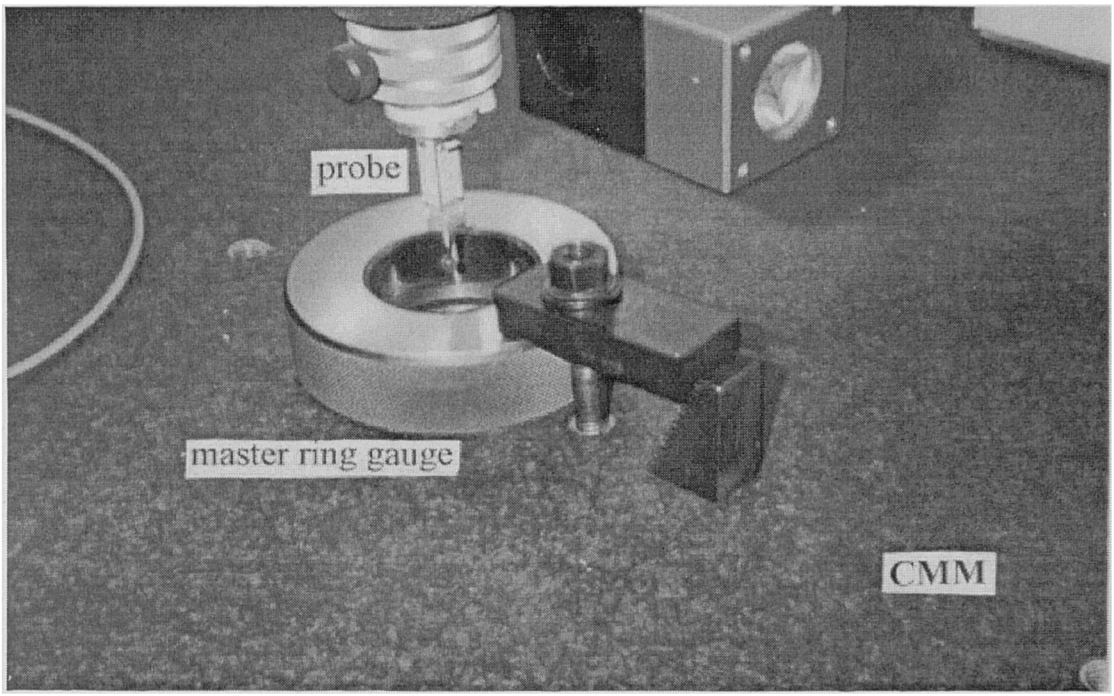

Figure 5.13. Photograph of the test rig on KEMCO E600 CNC CMM (600×500×500).

During the experiments it was noticeable that the sensitivity of the tactile sensor depends largely on the type of workpiece and its physical properties (i.e. modulus of elasticity, density, hardness). Namely, it was observed that the output signal of the PLL was directly dependent on the material of the specimen. For the same contact force between the probe and the workpiece frequency shift was different for different materials. This led to the conclusion that monitoring the shift in resonant frequency could provide information about physical properties of an object. The results could be related to hardness and/or softness of the material. The next section will demonstrate

possible applications of the tactile sensitive probe in the hardness testing of glass-fibre reinforced polyester laminate during the curing process.

4.3. Implementation of new tactile sensitive probe on hardness testing

Hartington Conway Ltd. Coventry is a manufacturer and distributor of Glass Reinforced Polyester (GRP) translucent sheeting and roofing accessories. A problem present on their production line is to accurately determine when the gel point of GRP laminates occurs. This is necessary due to the need to pass the GRP sheets through different formers in order to change their shape. Prior to entering the formers the laminate has to be viscous enough to take up the new shape and at the end of the process it should be rigid enough to maintain it. The shaping process should take place when the gel point occurs. So far, it was not possible to pick up this point accurately enough. A device which would provide such information would solve one of the difficult problems along the production line.

4.3.1. Cure monitoring and hardness detecting

Cure monitoring is of practical importance for the processing of a thermoset polymer material and a considerable amount of work has been done in this area. Among the frequently used monitoring techniques is dynamic dielectric analysis [125] which offers the advantages of non-destructive inspection and high sensitivity. One of the properties that may be evaluated using this technique is the dipole relaxation time which may be quantitatively utilised as a measure of degree of conversion, the glass transition temperature, the viscosity and the diffusion coefficient. Deng and Martin [125] found, using this method, *a phenomenological* similarity between the dielectric features of the resin during cure and those of stable materials.

Rapra, UK, has introduced a Scanning Vibrating Needle Curemeter (SVNC) for monitoring cures in liquid formulations as in cast elastomers, sealants, polyurethanes foams and thermoseting resins [126]. The standard instrument provides a continuous record of cure progression - even through gel point - giving a profile of both -pre-gelation and post-gelation stages. The SVNC provides two simultaneous recordings of the cure profiles: resonance frequency and amplitude. These two complementary cure profiles are related to changes in the in-phase stiffness and to the changes in damping.

It has been stated that the design of the new resonator based tactile probe, described in this Chapter, exploits the fact that when a probe is oscillated at or near resonance frequency and comes into contact with the surface of another body, it exhibits a change in resonance frequency depending on the nature of the load on the probe tip. The frequency shift depends also on the properties of the material in contact, particularly density and Young's modulus of elasticity which in turn can be related to the hardness of the material. One similar design was proposed by Omata and Terunama [96] and used with some success in hardness measurements. The sensor was also operated with piezoelectric elements and it was constructed as a probe type. Conducting experiments on different materials it was shown that changed values in resonant frequency provide information on the physical properties related to the hardness and/or softness of an object.

Tests were conducted on the GRP laminate using the new tactile probe to investigate the possibility of detecting the gel point during the curing process. Experiments were based on the idea that monitoring the hardening of the laminate and recording the change in resonant frequency of the probe would give enough information to determine the gel point.

4.3.2. Experimental set-up and methodology

The basic body structure and block diagram of the applied sensor system is shown in Figure 4.14. It consists of a resonator based tactile probe, phase circuit, filter and amplifiers as shown in previous section and Appendix A. A stylus with a 4mm ruby ball was attached to the end of the probe. For these experiments the probe was oscillated at near its natural resonance frequency of 16.831 kHz. This frequency was chosen as it gave the best touch sensitivity and the best conversion rate frequency/voltage. The output from the PLL circuitry, proportional to the changes in resonance frequency, in this case had a conversion factor of 1.04 mV/Hz [124]. The audible noise emitted at this frequency was not considered important, as it would be negligible compare to the noise produced from the actual process itself.

A number of GRP laminate samples (> 60) were prepared in the metrology laboratory following instructions given by Hartington Conway's technologists in order to simulate the curing process (Appendix C). Specimens were approximately 225cm^2 in size. Glass of a density of approximately 450g/m^2 was cut in a square, weighed and placed on nylon sheet. The weight of the resin, in ratio to glass of 2.3 to 1, was mixed with 2% of catalyst which was enabling gel point to occur approximately 5-6 minutes from the beginning of the curing process. One third of the mixture was evenly spread underneath the glass mat. The remaining resin was poured on the top of the mat trying to produce an equal distribution. Another nylon sheet was placed on the top and smoothed over in order to remove any trapped air bubbles.

All experiments were conducted under the controlled conditions of the metrology laboratory with an ambient temperature of 20°±2°C. Prior to each test, samples were prepared, as explained above, and while in a very viscous state were placed on a cast iron surface plate. The probe was than brought into contact with the specimen shifting the frequency from 16.350 kHz contact free to the 17.541 kHz when contact took place. During the curing process, solidification occurs and the specimens

structure changes from liquid to solid state. According to information supplied by Hartington Conway's technologists, the curing reaction takes place in several stages. Firstly, there is an induction period when nothing happens. Then gelation occurs, as the cross-linked network structure in the material begins to form. When solidification takes place, pressure on the probe tip should increase due to the changes in the specimen's Young modulus of elasticity and damping, causing a change in resonant frequency. This process should increase rapidly after the gel point occurs.

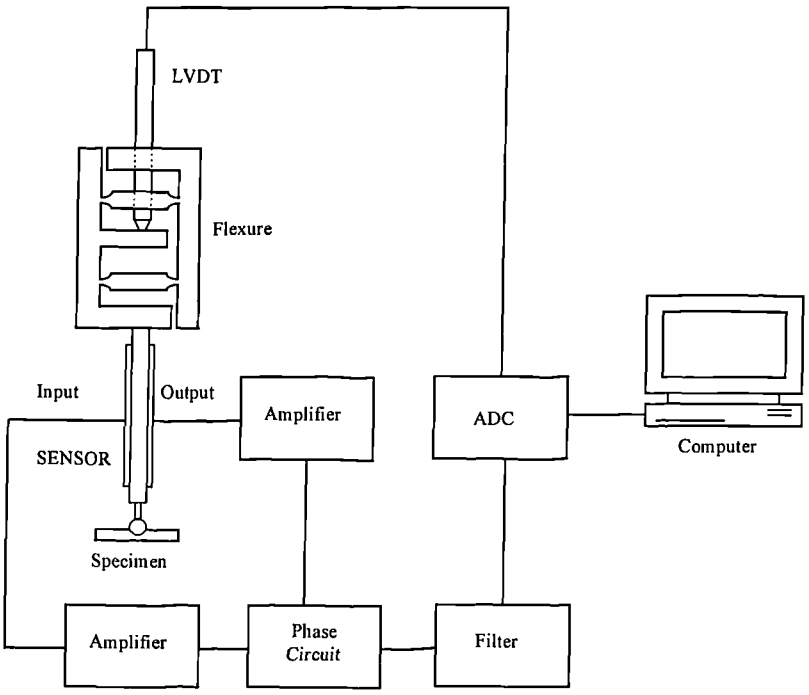

Figure 4.14. Block diagram of the applied probe system

The PLL output voltage was monitored during the curing process as a direct measure of the frequency shift. The PC74 data acquisition card was used for data collection; while data analysis was performed using Microsoft Excel software.

4.3.3. Results of the experiments

Figure 4.15 shows typical experimental result of measured change in hardness of laminate during the curing process. Vertical axis shows output voltage from the PLL circuitry which, being a direct measure of frequency shift, can be related to the hardness of the specimen.

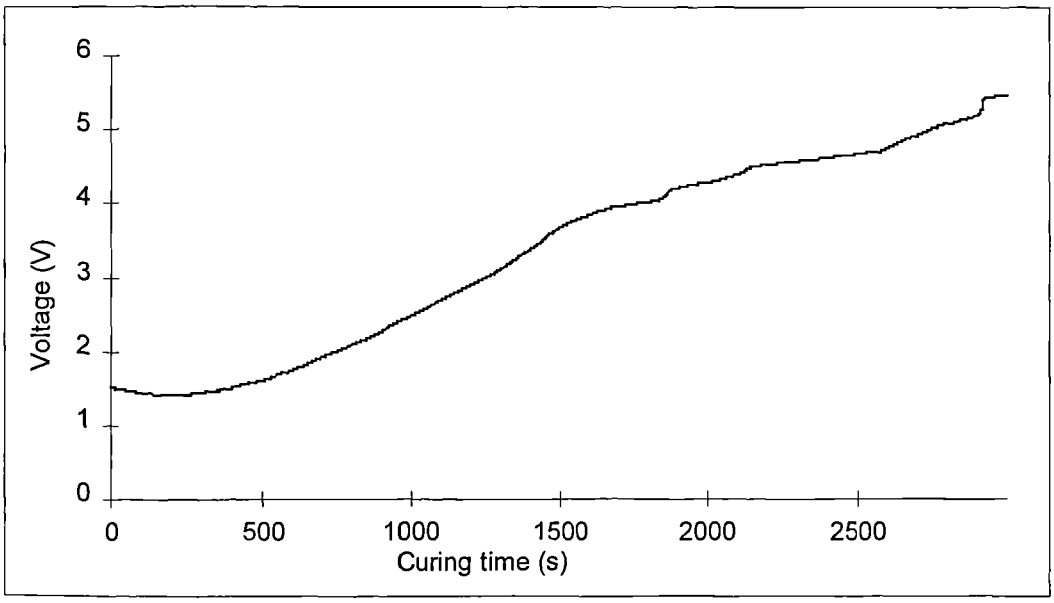

Figure 4.15. Hardening of laminate during the curing process.

It can be seen that the output voltage trend follows the predicted behaviour of the GRP laminate during the curing process. At the beginning of the process when the specimen is in a liquid state, the output voltage follows an almost constant trend for approximately 300-400 seconds. After this period, solidification starts to take place indicated by an increase in output voltage of the PLL due to increased pressure on the probe tip. The initial shift in the output voltage, and therefore in the resonance frequency, indicates the point where gel-point occurs. This increase in the resonance frequency could be explained as a result of the decrease of the damping in the curing material as the linked polymer network structure in the specimen begins to form. The

continuous increase in the resonant frequency indicates the increase in the added stiffens as the cure progresses beyond the gel point. This favourably compares with Rapra's SVNC traces of resonance frequency obtained during the cure of polyurethane elastomer [126]. The process was monitored for 3000 s. After this time the rise in the output signal was still noticeable showing that the solidification process of the laminate had not yet finished. As experiments were conducted in the metrology laboratory the curing process took longer that it would have done on the production line where temperature is normally around 60°C.

A number of experiments were conducted under the same conditions and typical results can be seen in Figure 4.16. All graphs show the same trend and change in output voltage is between 2.5V and 4 V depending on the specimen.

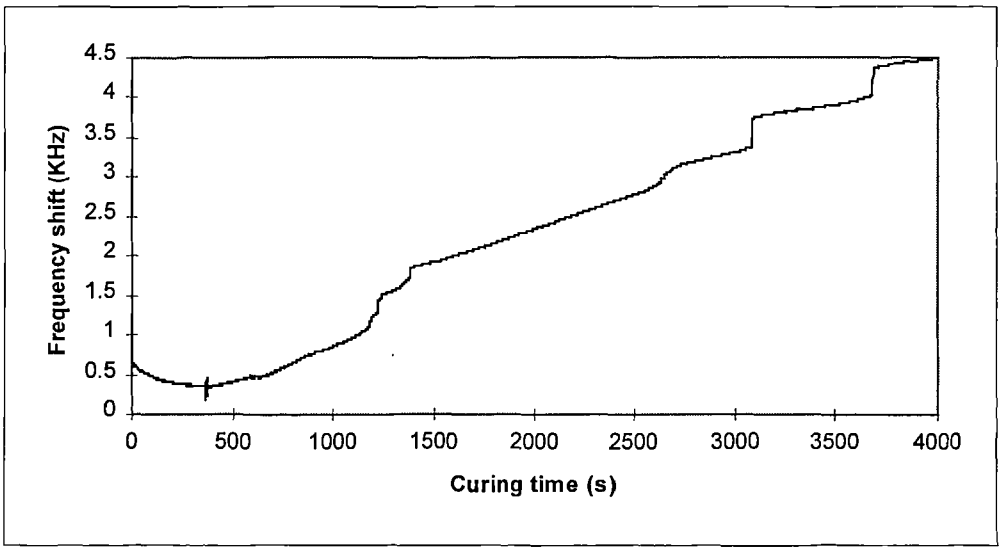

Figure 4.16. Typical results obtained during the cure of the GRP laminate.

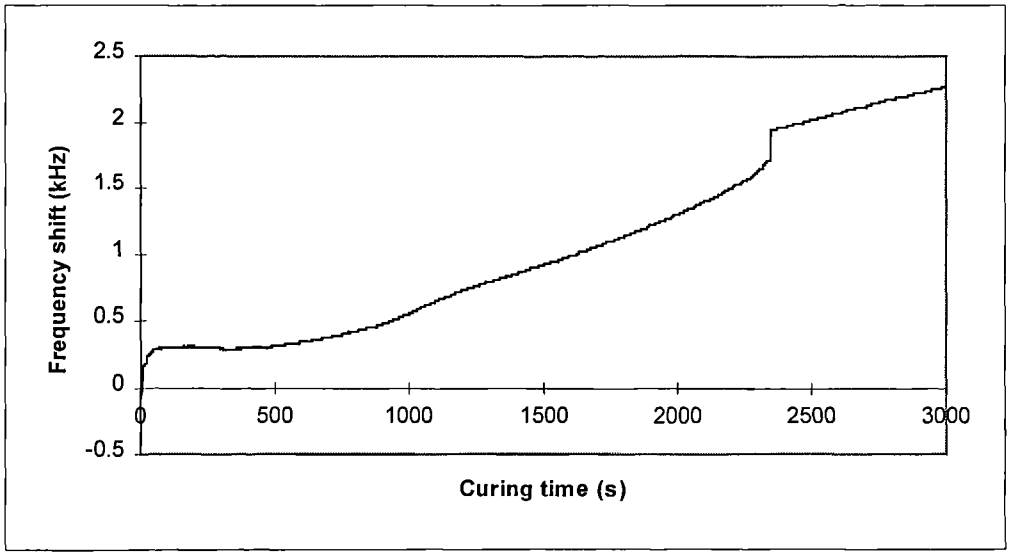

Figure 4.16. (Continued)

The results were very promising, showing capability of the new resonator based tactile probe to monitor the hardening process of a laminate and the possibility to determine the gel point during the curing process. Variations in change of output signal could be explained by random distribution of fibreglass filaments in the specimen; variations in the tension of the film covering the sample; variations in thickness of a specimen. These effects, except the random distribution of fibreglass filaments, were due to human factor because all samples were made individually in the metrology laboratory. Although there are variations in output readings, the trend of the output signal remains the same in all experiments following the theoretically predicted behaviour of polyesters during their curing which could be of great importance in GRP cure process monitoring.

4.4. Conclusions

A design and characterisation of a first prototype resonator probe using piezoelectric actuator/pick-up arrangement and utilising the phase locked loop technique has been described in this Chapter. The preliminary results gave great encouragement to the

further development of the probe. It has been shown that probe had a high sensitivity at both resonance frequency (1.04 mV/Hz) and when a second mode was selected (0.73 mV/Hz). The maximum frequency shift from the working frequency, as contact force progresses was 2 kHz for 25.179 kHz, and about 3 kHz for 16.350 kHz working frequency. Also, the characterisation showed a sensitivity to touch of less than 4 mN along three orthogonal axses, and triggering rate of more than 700 Hz. Higher sensitivity of the probe and better performance when the selected frequency was actually its natural frequency offered an idea that a slight alteration in mechanical design could be done in order to increase the natural frequency of the probe so it could be used at the first mode frequency without any audible noises.

Tests were conducted on the coordinate measuring machine to record the coordinates of the inside diameter of a master ring gauge but it has to be mentioned that coordinate metrology was just one initial application of the new tactile sensor. A possible application of the tactile sensitive probe in measuring the properties of different materials was demonstrated monitoring the hardening process of glass-fibre reinforced polyester laminate. Also, a typical relationship between the PLL output voltage and interaction force of the probe/sample (Figures 4.9 and 4.12) have indicated the possible application of the probe in scanning systems by maintaining constant contact force.

Preliminary results shown in this Chapter led to the development of a mathematical model to enable better understanding of contact mechanisms between the probe and the workpiece. This led to the further development of the probe and to the exploration of the possible versatile applications in contact measurements; in coordinate metrology; as a vector probe and in scanning applications.

Chapter 5

Mathematical modeling of the new resonator probe

5.1. Introduction

Although a considerable amount of work has been devoted towards the development of resonant touch sensors [4,5,8,27,31,96], especially in the area of scanned probe microscopy [11,12,13,99], commercial exploitation has not been particularly successful. One of the reasons for this is due to the complexity of the interaction between a resonant sensor and typical surfaces in less than ideal environments. Having in mind that the tactile probe proposed in this thesis will have main application on typical engineering surfaces, shifts in resonant frequency at constant phase (or shift in phase with a constant frequency) as a probe approaches a surface exhibit complex behavior. Therefore it is important to understand the mechanics of contact phenomena between two objects and it is necessary to examine the dominance of effects such as stiffness, mass, and damping when a probe is in contact with

different materials. It is also important to consider near surface contact phenomena and the squeeze film and surface films effects. In this section, a systematic study of the contact mechanisms between a resonator sensor, and broad range of engineering surfaces will be described. The initial design of a resonator sensor described in Chapter 4 will be used to present the mathematical model. The device consists of a simple tip holder attached to the end of aluminium rod that is rigidly mounted to the probe base using PZT piezoelectric materials as actuators and sensors. Contact is detected by oscillating the sensor, which behaves like a second order system, near to its resonance frequency and monitoring the rapid phase shift using phase locking techniques. To simplify this discussion, only relatively large radius probes attached to a relatively stiff oscillator mount will be considered. Also, only the simplest type of contact, that is a contact between a smooth, frictionless sphere on a flat horizontal surface, will be considered.

5.2. Elementary mechanics of contact

Based on simple models, this section investigates stationary contacts of a sphere on a flat surface. It is clear that the point contact of infinitely rigid spheres, cylinders or flats does not exist in practice as materials have a finite stiffness and will deform upon a real contact. The first analysis of the stresses between two contacting elastic solids was mathematically expressed by Heinrich Hertz and published in 1882. His theory showed that a distribution of contact pressure would produce elastic displacements in the two bodies which were compatible with the area of contact. The Hertz theory is restricted to frictionless surfaces and perfectly elastic solids. Latest progress in contact mechanics has been based on the removal of these restrictions. A considerable amount of work by many researchers has been collated by Johnson in 1985 [127].

5.2.1. Pressure applied to a circular region

Figure 5.1. shows circular region of a radius a over which a pressure p is distributed. Johnson shows that it is possible to find the displacement at a surface point B and the stresses at an internal point A due to applied pressure.

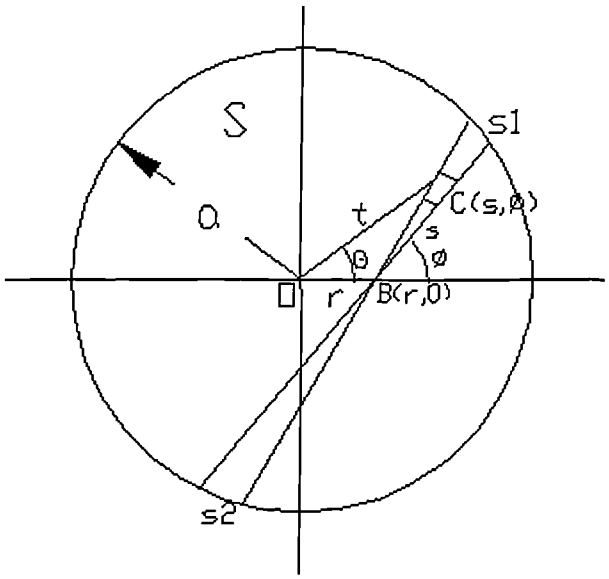

Figure 5.1. Pressure applied over the circular region [127]

Pressure distribution is given by:

$$p = p_0(1-r^2/a^2)^n \tag{5.1}$$

where p_0 is the maximum value in pressure distribution.

Factor n has different values for different pressure distributions. In case of the pressure given by Hertz theory (Hertz Pressure), which is exerted between two elastic solids in contact, n has the value of 0.5 which gives:

$$p(r) = p_0(a^2 - r^2)^{1/2}/a \tag{5.2}$$

from which the total load pressure is:

$$P = 2\pi\ p_0 a^2/3 \tag{5.3}$$

The deflections u_Z at a general point $B(x,y)$ produced by a normal distributed pressure p over an surface area S could now be calculated. Using polar coordinates (s,ϕ) with origin at B, such that the pressure $p(s,\phi)$ acting on a surface element at C is equivalent to a concentrated normal force, the displacement u_Z at B due to the pressure distributed over the area S is thus:

$$u_z = \frac{1-\nu^2}{\pi E}\iint_S p(s,\phi)\, ds\, d\phi \tag{5.4}$$

where ν and E are the Poisson's ratio and elastic modulus of the material, respectively.

Consequently, the normal displacement within the loaded circle is given by[†] :

$$\begin{aligned} u_z(r) &= \frac{1-\nu^2}{\pi E}\frac{p_0}{a}\int_0^{2\pi}\frac{\pi}{4}(a^2 - r^2 + r^2\cos^2\phi)\, d\phi \\ &= \frac{1-\nu^2}{E}\frac{\pi p_0}{4a}(2a^2 - r^2), \qquad r \le a \end{aligned} \tag{5.5}$$

From the Hertzian theory it can be seen that the contact area, stress and deformation might be expected to enlarge with increasing load, and also, the influence of curvature and elastic modulus could be found by simple dimensional comparison. In order to obtain absolute values for some of these quantities, the Hertz theory of elasticity should be considered.

[†] Complete derivation can be found in reference [127].

5.2.2. Hertz theory of elastic contact of a sphere on a flat

When two elastic solids are brought into contact, they will deform under the load, so that they touch over an area which is finite but small compared with the dimensions of the two bodies. Due to the contact pressure, the surface of each body will be displaced by an amount u_{z1} and u_{z2} measured positive into each body. Hertz formulated conditions expressed by an equation for the elastic displacements:

$$u_{z1} + u_{z2} = \delta - Ax^2 - By^2 \tag{5.6}$$

where δ is the mutual approach of distant points in two solids, x and y are the common coordinates of contact point projected onto the x-y plane and A and B are positive constants dependent on the contours of the contact area.

In formulating equation (5.6), few assumptions were made. Hertz assumed that the contact area is, in general, elliptical and that each body can be regarded as an elastic half-space loaded over a small elliptical region. For simplification Hertz introduced two conditions: the significant dimensions of the contact area must be small compared (1) with the dimensions of each body and (2) with the relative radii of curvature of the surfaces. Finally, the surfaces are assumed to be frictionless so that only a normal pressure (Johnson [127]) could be transmitted between them.

For the simplest case of contact between a smooth, frictionless sphere on a flat horizontal surface (Figure 5.2) Hertz equation (5.6) defining the boundary condition for displacements within the contact could be written in form of:

$$u_{z1} + u_{z2} = \delta - (1/2R)r^2 \tag{5.7}$$

where R is radius of the sphere.

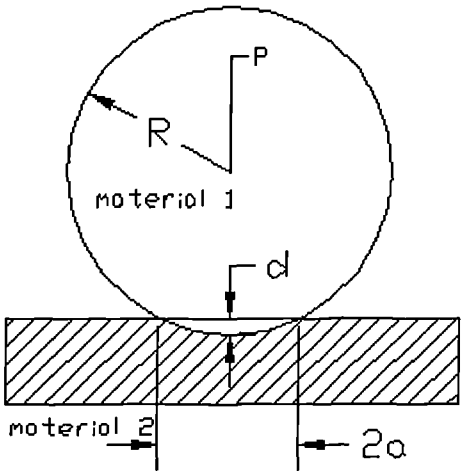

Figure 5.2. Stationary contact of a sphere and a flat surface

A pressure distribution over the circular area of contact which will enforce normal displacement (5.5) is given by equation (5.2). The pressure acting on the second surface is equal to pressure acting on the first, so it could be written that

$$\frac{1}{E^*} = \frac{1-\nu_1^2}{E_1} + \frac{1-\nu_2^2}{E_2} \tag{5.8}$$

where E represents elastic modulus of the two contacting materials. Taking above equation in consideration and substituting the expressions for u_{z1} and u_{z2} into equation (5.7) gives:

$$\frac{\pi p_0}{4aE^*}(2a^2 - r^2) = \delta - (1/2R)r^2 \tag{5.9}$$

from which reveals that the contact radius, a, and the mutual approach of distant points in the two materials, δ, are given by the equations:

$$a = \pi p_0 R/2E^* \tag{5.10}$$

$$\delta = \pi a p_0/2E^* \tag{5.11}$$

The total load applied to the solids is related to the pressure by

$$P = \int_0^a p(r) 2\pi r \, dr = 2\pi \, p_0 a^2 / 3 \tag{5.12}$$

In practice, the total load is usually specified, rather than pressure distribution, so using (5.12) in combination with (5.10) and (5.11) gives:

$$a = \left(\frac{3PR}{4E^*} \right)^{1/3} \tag{5.13}$$

$$\delta = \frac{a^2}{R} = \left(\frac{9P^2}{16RE^{*2}} \right)^{1/3} \tag{5.14}$$

$$p_0 = \frac{3P}{2\pi a^2} = \left(\frac{6PE^{*2}}{\pi^3 R^2} \right)^{1/3} \tag{5.15}$$

It can be concluded that the above model, derived for a contact of a sphere with a flat surface, is also valid in the case of resonator sensor with spherical probe. Therefore, it is valid for the new sensor design, proposed in this thesis, which, simplified for the purpose of theoretical modeling, consists of a simple tip holder attached to the end of aluminium rod that is rigidly mounted to the probe base with piezoelectric activation and detection mechanisms. Combining contact mechanics and Rayleigh's approximate energy method of sensor's vibrations it is possible to examine the causes of parametric changes on a resonant sensor at contact and near contact conditions.

5.3. Second order vibration model of an oscillatory system

5.3.1. Second order equation of motion

A well known fact [128] is that the basic vibration model of a simple oscillatory system consists of a mass, spring and damper. The mass is measured in kilograms. The stiffness k is measured in Newton/meter, following Hooke's law, $F = kx$, with its linear force-deflection relationship. The damping could be described by a force proportional to the velocity, or $F = c\dot{x}$. The damping coefficient c is measured in Newton/meter/second.

For a simple undamped spring-mass system, using Newton's second law of motion ($\sum F = m\ddot{x}$), the equation of motion can be written as a linear second order differential equation for any displacement x:

$$m\ddot{x} + kx = 0 \tag{5.16}$$

The quantity $\sqrt{k/m}$ is the frequency of the harmonic motion, in radians per second, and is generally called the natural circular frequency, ω_n. Equation (5.16) could be written in form of:

$$\ddot{x} + \omega_n^2 x = 0 \tag{5.17}$$

Equation (5.17), as a homogeneous second-order linear differential equation, has the following solution:

$$x = A\sin\omega_n t + B\cos\omega_n t \tag{5.18}$$

where A and B are arbitrary constants that depend on the initial conditions of motion.

The linear second order differential equation with constant coefficients which models damped free vibrations for a single degree of freedom with mass, spring and damper is:

$$m\ddot{x} + c\dot{x} + kx = 0 \tag{5.19}$$

Assuming a solution in a form of $x = e^{rt}$, where r is a constant, a characteristic equation could be obtained in form of:

$$r^2 + \frac{c}{m}r + \frac{k}{m} = 0 \tag{5.20}$$

Equation (5.20) has two roots:

$$r_{1,2} = -\frac{c}{2m} \pm \sqrt{\frac{c^2}{4m^2} - \frac{k}{m}} \tag{5.21}$$

From equation (5.21) the general solution for the displacement is then:

$$x = e^{-(c/2m)t}\left(Ae^{\sqrt{(c/2m)^2 - k/mt}} + Be^{-\sqrt{(c/2m)^2 - k/mt}}\right) \tag{5.22}$$

where A and B are again arbitrary constants that depend on the initial conditions of motion.

From the above mathematical exponential equation can be described a physical displacement time curve having three distinct forms, depending on whether the numerical value within the radical is real, zero or imaginary. In the case where the damping term $(c/2m)^2$ is larger than k/m, the radical is real and the motion of the system is dominated by damping. When the damping term $(c/2m)^2$ is less than k/m, oscillation about an equilibrium position occurs, with each successive amplitude diminished from the preceding amplitude. In the case where $(c/2m)^2 = k/m$, the

system is said to be critically damped. The value of damping constant in this case is called *critical damping constant* c_C:

$$c_c = 2m\sqrt{\frac{k}{m}} = 2m\omega_n = 2\sqrt{km} \tag{5.23}$$

The ratio of the actual damping constant to the critical damping constant is *the damping ratio,* ξ, and any damping can be expressed in terms of this nondimensional number ξ:

$$\xi = c/c_c \tag{5.24}$$

It can be said that the three cases of damping discussed above depend on whether ξ is greater than, less than, or equal to unity. Furthermore, the homogeneous differential equation of motion can be expressed in terms of ξ and ω_n as

$$\ddot{x} + 2\xi\omega_n\dot{x} + \omega_n^2 x = 0 \tag{5.25}$$

The above second-order equation (5.25) is very importan in identifying the natural frequency and the damping of the system.

5.3.2. Approximate Rayleigh's energy method

Solving vibration problems quite often is very simple and direct using energy methods. Energy methods involve an energy balance using scalars rather than a force balance with vectors. For the free vibration of an undamped system, the energy is partly kinetic and partly potential. Following the law for the Conservation of energy for the total energy, E,

$$E=T+U \tag{5.26}$$

where T is kinetic energy due to the velocity of the mass of the system, and U is potential energy due to the strain energy in elastic deformation or due to the work done in a force field such as gravity.

The total energy is always constant, so its rate of change is zero:

$$\frac{d}{dt}(T+U)=0 \tag{5.27}$$

Lord Rayleigh introduced the calculation of the fundamental frequency of vibrating system, which does not derive and solve the differential equations of motion. For this calculation motion was assumed to be in a form of simple harmonic:

$$x = X\sin\omega_n t \tag{5.28}$$

Differentiating with respect to time, the velocity is:

$$\dot{x} = X\omega_n \cos\omega_n t \tag{5.29}$$

The average kinetic and potential energy over one full cycle, $\tau=2\pi/\omega_n$, is given by

$$T_{av} = \frac{1}{\tau}\int_0^{\tau}\frac{1}{2}m\dot{x}^2 dt = \frac{1}{2}m\frac{X^2\omega_n^2}{\tau}\int_0^{\tau}\cos^2\omega_n t dt = \frac{1}{4}mX^2\omega_n^2 \tag{5.30}$$

$$_{av} = \frac{1}{\tau}\int_0^{\tau}\frac{1}{2}kx^2 dt = \frac{1}{2}\frac{kX^2}{\tau}\int_0^{\tau}\sin^2\omega_n dt = \frac{1}{4}kX^2 \tag{5.31}$$

Assuming

$T_{av}=U_{av}$

then

$$\frac{1}{4}mX^2\omega_n^2 = \frac{1}{4}kX^2 \tag{5.32}$$

and

$$\omega_n^2 = \frac{k}{m}$$

The vibration amplitude is eliminated from the expression for ω_n^2 and this independence of natural frequency from amplitude of motion is the basis of Rayleigh's Principle. The energy method is very powerful giving good approximation of the natural frequencies, and it is particularly useful for a system which has a single degree of freedom but geometric or kinematic complexity.

5.4. Vibration model of the proposed resonant sensor

Using elementary mechanics of contact and a second order vibration model of an oscillatory system, it is possible now to discuss the vibrations of the proposed resonant sensor. In general, any changes in force at the end of the probe will affect the dynamics of the system. One particularly problematic aspect of theoretical modeling is due to the changes in boundary conditions. For example, if the probe is undergoing lateral vibration, a 'rigid' contact would change the end condition from 'free' to either 'sprung' or 'hinged' or combinations thereof which are extremely difficult to predict. Adopting a system undergoing longitudinal vibrations could simplify modeling of the interaction between oscillating probe and contacting surfaces. The essential feature of this assumption is that the resonance can be considered to be a consequence of reflections of elastic waves from either end of the probe. Upon contact, it might be assumed that a physical barrier in the form of a change in velocity of elastic waves will still exist. Such process can be modeled as a simple longitudinal oscillator of length, L, with the boundary conditions of added mass, stiffness and damping at the free end. Applying Rayleigh's approximate method to this system, it is possible to derive a simple second order model with a natural frequency given by

$$\omega_n = \sqrt{\frac{k_c + k_e}{M + m_e / 3}} \tag{5.33}$$

where k_C, M, k_e, and m_e are the equivalent stiffness and mass of the probe and the effective added stiffness and mass during contact, respectively.

Under these conditions it is possible to investigate the effects of contact on a simple second order model. There are two modes of contact detection commonly used for resonant sensors:

1. Monitoring frequency at constant phase, hereafter called mode I
2. Monitoring phase at constant frequency, mode II

In both of these modes, modeling is considerably simplified if small variations about a 90 degree phase shift are considered. However, in reality this is not easy to achieve, and there is almost always a shift away from this ideal condition. Therefore it is necessary to consider the general effects of variations of the end condition on a second order system over a band of frequencies around the undamped resonance (not the same as the damped resonance).

In this discussion, the effects of added mass, stiffness and damping will be separately considered and assumption that superposition applies will also be made. If any one of these effects dominates, it will also be shown that the effect can be systematically extracted from a series of three contact measurements.

For example, consider the simple case of added stiffness which will result in an increase of the resonant frequency. Clearly, in mode I, an increase in frequency would result irrespective of the locking phase while in mode II there will always be a reduction in phase for a given frequency. Adding damping is not so straightforward. For a system originally (i.e. away from the specimen surface) at the resonant frequency, there will be no phase or frequency shifts in either mode reflecting the immunity of this sensor to changes in amplitude. If, however, the probe is originally offset to a frequency slightly below that for undamped resonance, additional damping

will result in an increase in phase in mode II and a reduction in frequency in mode I. With the sensor originally oscillating above the frequency for undamped resonance the effects will be the opposite. Finally, it can be readily verified that the effect of added mass is opposite to that of added stiffness.

To visualize this, Table 5.1 and Figure 5.3. show the direction of the output from a phase locking amplifier for different types of loading (inertial, compliant or dissipative) on the sensor. In a number of cases, it is possible that two of the three influences will be insignificant. Under such conditions, it is desirable to identify the dominant effect. This can be systematically measured by monitoring changes in output with the probe set either side of, and at, the resonant frequency. To see how this can be achieved, consider the generalized relationship between the output from the sensor and the end conditions

$$\begin{aligned} \phi &= f(k_e, m_e, \xi_e) \\ \omega &= g(k_e, m_e, \xi_e) \end{aligned} \tag{5.34}$$

For small changes, the above can be differentiated to give the equation, for mode I

$$d\omega = \frac{\partial \omega}{\partial k_e} dk_e + \frac{\partial \omega}{\partial m_e} dm_e + \frac{\partial \omega}{\partial \xi_e} d\xi_e \tag{5.35}$$

or for mode II

$$d\phi = \frac{\partial \phi}{\partial k_e} dk_e + \frac{\partial \phi}{\partial m_e} dm_e + \frac{\partial \phi}{\partial \xi_e} d\xi_e \tag{5.36}$$

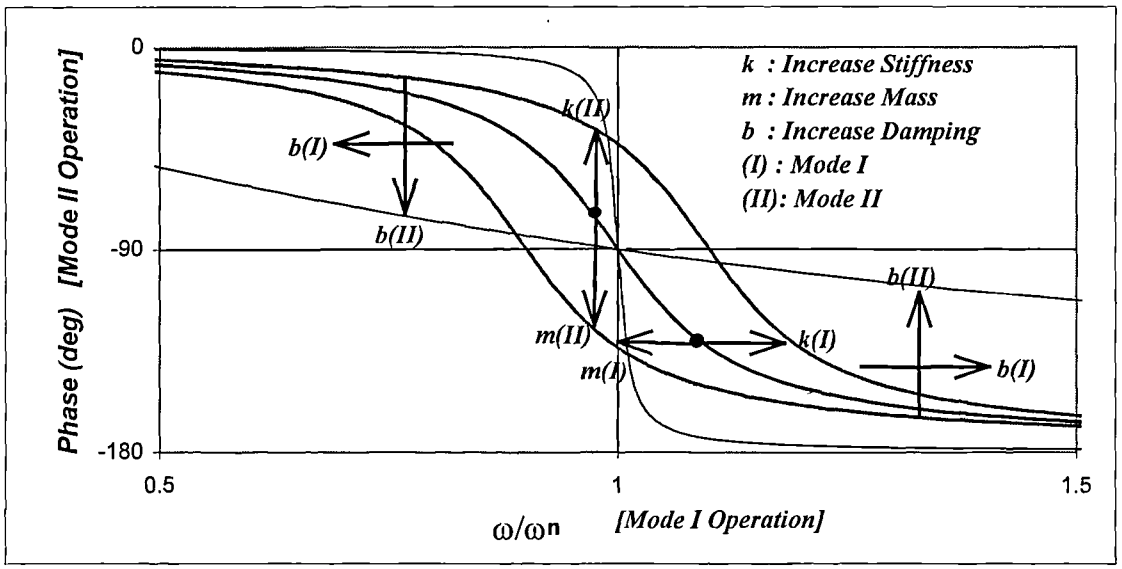

Figure 5.3. Direction of frequency shift for mode I and phase shift for mode II operation of resonant frequency

Table 5.1: Direction of frequency shift for mode I operation of resonant sensor

Dominant factor	Phase angle		
	$\|\phi\| < \|90\|$	$\|\phi\| = \|90\|$	$\|\phi\| > \|90\|$
Mass	Increase	Increase	Increase
Stiffness	Decrease	Decrease	Decrease
Damping	Increase	0	Decrease

Table 5.2: Direction of phase shift for mode II operation of resonant sensor

Dominant factor	Phase angle		
	$\|\phi\| < \|90\|$	$\|\phi\| = \|90\|$	$\|\phi\| > \|90\|$
Mass	Decrease	Decrease	Decrease
Stiffness	Increase	Increase	Increase
Damping	Decrease	0	Increase

Assuming that the simple second order model is valid, the partial derivatives in the above equations are fixed functions of the probe system and, for small perturbations, can be considered constants (ψ) representing the sensitivity of the system to changes in these parameters. Consequently, the above equations can be rewritten

$$d\omega = \Psi_{\omega k} dk_e + \Psi_{\omega m} dm_e + \Psi_{\omega \xi} d\xi_e \tag{5.37}$$

$$d\phi = \Psi_{\phi k} dk_e + \Psi_{\phi m} dm_e + \Psi_{\phi \xi} d\xi_e \tag{5.38}$$

The above constants will be a strong function of the original excitation frequency relative to the undamped resonance. The constant for the damped coefficient will reverse sign passing through zero at the resonant frequency while the sign of the other two coefficients will remain unaltered. To determine a single dominant factor, changes in ϕ or ω can be monitored as a function of the change in contact. The only restriction on the change is that it be small and repeatable for different settings of frequency and phase. For example, in the subsequent experiments it was possible to either measure the displacement, x, of the probe into the specimen or the force, F, on the end of the probe. For small changes in these parameters, equations (5.37) and (5.38) can be expressed in the forms

$$\begin{aligned} \frac{d\omega}{dF} &= \Psi_{\omega k} \frac{dk_e}{dF} + \Psi_{\omega m} \frac{dm_e}{dF} + \Psi_{\omega \xi} \frac{d\xi_e}{dF} \\ \frac{d\omega}{dx} &= \Psi_{\omega k} \frac{dk_e}{dx} + \Psi_{\omega m} \frac{dm_e}{dx} + \Psi_{\omega \xi} \frac{d\xi_e}{dx} \end{aligned} \tag{5.39}$$

$$\begin{aligned} \frac{d\phi}{dF} &= \Psi_{\phi k} \frac{dk_e}{dF} + \Psi_{\phi m} \frac{dm_e}{dF} + \Psi_{\phi \xi} \frac{d\xi_e}{dF} \\ \frac{d\phi}{dx} &= \Psi_{\phi k} \frac{dk_e}{dx} + \Psi_{\phi m} \frac{dm_e}{dx} + \Psi_{\phi \xi} \frac{d\xi_e}{dx} \end{aligned} \tag{5.40}$$

To unravel the complexity of these equations, it is important to realize that the constants represent values whose magnitude and sign depend upon the nominal values of phase and frequency. Each derivative on the right side of the equations represents the change in the system due to effects of the probe to specimen interaction. Considering the above discussion, three important points have to be emphasized:

1. The constants ψ remain so only for small perturbations about a given frequency or shift. As a result of this, a change in reference phase or frequency will result in a change in the values of these constants.
2. The change in the constants will be nearly symmetric about the resonant frequency.
3. The derivatives on the right-hand side of Equations (5.39) and (5.40) are function of the contact and are, therefore, independent of changes in the initial phase or frequency of the sensor.

As a consequence of these important points, it is possible to set up a test to determine which of the contact phenomena dominate as will be described in Chapter 6. However, before outlining how such a test might progress, it will be informative to examine some of the reasons for the dominance of different effects with different materials.

5.5. Causes of parametric changes on resonant sensors

To simplify this discussion, only relatively large radius probes attached to a relatively stiff oscillator mount will be considered for two touch regimes, these being:

1. Near surface phenomena
2. Mechanical contact.

Intermediate contact conditions characteristic of 'tapping' [129,130] or 'bouncing' types of sensor are outside the scope of this research.

5.5.1. Near surface phenomena

As a resonating touch sensor approaches a surface, a number of effects will be present which introduce a mechanical force. Such forces and their gradients will affect the frequency response characteristics of the probe. For non magnetic, clean materials in vacuum the only interactive forces will be those due to retarded and non retarded Van der Waals forces and electrostatic forces from surface charge. As evidenced by the rapid growth of the AFM (atomic force microscopy) industry, such effects can be significant for extremely compliant and sensitive probes. In investigation carried out in this project such effects are considered ignorable in relation to the effects that are likely to be present during measurement of engineering surfaces in air. Under these conditions, it is likely that the dominant near surface forces will be those due to squeeze film damping and contaminant films on either the probe and/or the surface.

5.5.1.1. Squeeze film damping between a sphere and a flat

In modeling the squeeze film damping effect on the sphere it has to be considered that for nanometer size oscillations, the velocity of the film between probe and specimen is extremely small. Consequently, the Reynold's number (ratio of inertial to viscous force) is low and its is possible to model this process as an incompressible fluid undergoing laminar flow. A solution for the normal force, F, between a sphere and a flat surface separated at distance x can be obtained by integrating the familiar Reynold's equation, which is a single differential equation relating pressure, viscosity, surface velocities, and film thickness [131]. Neglecting wedge effects and compressibility terms, Reynold's equation is:

$$\Delta^2 p = \frac{12\mu}{h^3}\frac{dh}{dt} \tag{5.41}$$

where $dh/dt=V$ is the squeeze velocity.

When axial symmetry exists and the pressure is only a function of the radius, cylindrical polar coordinates can be considered, under conditions of constant density and viscosity. Assuming the gravitational and inertial forces (i.e. Reynold's number) are low and the thickness of film is small compared to other dimension (i.e. the minimum film thickness $h_0 << R$) the appropriate Reynold's equation can be expressed as

$$\frac{d}{dr}\left(rh^3\frac{dp}{dr}\right) = -12\mu r\frac{dh}{dt} \tag{5.42}$$

where h, is the film thickness.

For a spherical surface and a plane where $h << R$, h can be approximated as:

$$h = h_0 + r^2/2R \tag{5.43}$$

Integrating Equation 5.42 once gives:

$$\frac{dp}{dr} = \frac{-6\mu rV}{h^3} + \frac{A}{rh^3} \tag{5.44}$$

Making use of the boundary condition that $dp/dr=0$ when $r=0$ results in $A=0$. Integrating again gives:

$$p = -6\mu V\int\frac{rdr}{h_0\left(1+r^2/2h_0R\right)^3} \tag{5.45}$$

or

$$p = -\frac{6\mu VR}{h_0^2}\int\frac{du}{u^3} = \frac{-6\mu VR}{h_0^2}\left[\frac{-1}{2\left(1+\frac{r^2}{2h_0R}\right)^2} + C\right] \tag{5.46}$$

The boundary condition is that $p=0$ when $r=R$, therefore

$$p = \frac{3\mu VR}{h_0^2}\left[\frac{1}{\left(1+\frac{r^2}{2h_0R}\right)^2} - \frac{1}{\left(1+\frac{R^2}{2h_0R}\right)^2}\right] \tag{5.47}$$

The normal load (squeeze film load) component can be written as:

$$F = \int_0^R 2\pi rp dr \tag{5.48}$$

$$F = \frac{3\mu VR}{h_0^2}\int_0^R \left(\frac{rdr}{\left(1+r^2/2h_0R\right)^2} - \frac{rdr}{\left(1+R^2/2h_0R\right)^2}\right) \tag{5.49}$$

Letting $R_1 = \frac{R^2}{2h_0R}$ and integrating Equation (5.49) above produces

$$F = -\frac{3\pi\mu VR}{h_0^2 R_1^4\left(1+R_1^2\right)^2} \tag{5.50}$$

where μ is the viscosity of the medium between sphere and flat surface.

It should be noted that the force is both proportional to the velocity and inversely as the square of the separation between two surfaces. For oscillation amplitudes much smaller than the probe to specimen separation, there will be a rapid increase in velocity dependent force as the probe approaches the surface. However, most surfaces will have surface roughness and this is likely to have a significant effect on the characteristic variation of squeeze film forces with separation.

Consequently this effect will add damping in the interfacial zone without adding significant mass (i.e. low density of air) or stiffness (high velocity of sound). However, as the squeeze film forces increase, these must be resisted by the surfaces of probe and specimen. Subsequent distortions would add an effective stiffness to the system.

5.5.1.2. Surface films

The surfaces considered above are assumed to be perfectly clean and contaminant free. This is far from the case for many engineering surfaces and their typical environments. Commonly surfaces will become covered by a condensed moisture film. As a consequence, there will be a surface tension force resulting in capillary action. It is speculated by Grigg *et al.*, [132], that this leads to long range attractive forces of the order of tens of nanoNewtons and, once contacted, will result in a force that can be calculated from the equation:

$$F = \frac{4AR\gamma\cos(\theta)}{(1+x/d)} \tag{5.51}$$

where θ is the contact angle, d is the film thickness on both probe and specimen (assumed equal) and γ is the free surface energy (72 mJ m^{-2} for water).

Being proportional to the probe radius, for a separation distance of 15 nm with a 7.5 nm water film on both probe and surface will result, as Grigg *et al.* show [132], in an attractive force of approximately 9R/30 which for a 10 mm radius probe gives a force in the region of 3 mN upon initial contact and a residual attractive force of 1 mN after the probe has physically contacted the surface. Once contact has been made, there is likely to be a large hysteresis due to the necking of the meniscus layer. A potential method for discrimination of this mechanism from true van der Waals forces is to

retract the probe prior to contact monitoring for any hysteresis. This should not be observed for true van der Waals attraction. Simple calculations based on Hertzian contact indicates that for thin films of thickness less than the radius of the contact there will be relatively low induced stress due to capillary action between two typical solids.

The effect of surface films on the adhesion between a sphere and flat was studied by McFarlane and Tabor, 1950 [133]. In this, a sphere was suspended from a thin wire to form a simple pendulum and contacted with a flat plate. The adhesion force was then determined by moving the flat away from the sphere and measuring the maximum deflection from the vertical position before separation occurred. For very small separations, the denominator of equation (5.51) becomes unity and a linear relationship between the adhesion and radius is predicted and confirmed by experiment. Using this modified equation, a force of 9 mN is predicted for a 10 μm radius probe irrespective of material. It was also found in these studies that glass was particularly susceptible to the formation of water layers with effects becoming visible at relative humidities of the order 50 % or more. These adhesion effects could be reduced by abrading the surface suggesting that asperities would be capable of protruding from the layer and would not accumulate any films. However, this roughness will also increase the net separation between solids and thus increase the denominator in equation (5.51). Viscous effects were also observed and these were predominant with castor oil. For metallic materials, adhesion was reduced by both exposure to the atmosphere and hardness (which for metals is a measure of the elastic recovery after indentation) with aluminum showing no measurable effect and indium having high adhesion. The coefficient of adhesion was found to reduce after time with that for lead becoming too low to measure after about 8 hours while indium reduced its adhesion strength by approximately half. The softness and adhesive properties of indium are what make it a well known cold solder material. Application of a fatty acid monolayer again reduced adhesion to below instrument resolution and this could only be observed after a load sufficient to rupture the film and enable

metal-metal contact which again accurately reflects the molecular dynamics models on a macroscopic scale. The effects of the adhesion as an energy dissipation mechanism are discussed in more detail in Chapter 6.

5.5.2. Mechanical contact

5.5.2.1. Effective stiffness (k_e)

Following the familiar Hooke's law, $F = kx$, and its linear force-deflection relationship, the stiffness k is measured in Newton/meter. From the Hertzian analysis can be calculated the local stiffness for an elastic contact of a sphere on a flat. Smith and Chetwynd [134] defined that the vertical stiffness, k_e, of this interface is the inverse of the compliance defined as a derivative of deflection (Equation 5.14) with respect to the applied load, that is

$$k_e = \frac{dP}{d\delta} = \left(6E^{*2} PR\right)^{1/3} \tag{5.52}$$

where, E, P and R are Young's modulus, contact force and probe radius, respectively.

5.5.2.2. Effective mass (m_e)

Upon physical contact with a material, the region of the interface must be moving at the same frequency as the motion of the probe tip and will thus add an inertial load. Clearly, this will extend into the specimen with diminishing amplitude. To assess the effective added mass, it will be assumed that the specimen is smooth and flat and the probe is also smooth, has an effective radius, R and the oscillation amplitude is sufficiently small that 'bouncing' does not occur. For velocities of the probe much less than those of stress waves in the contact materials, it is reasonable to assume that the strain field is the same as that derived from Hertz analysis. For a harmonic motion

of the probe at an amplitude X and frequency ω, the vertical component of inertial force on an element in a hemispherical contact zone beneath the probe is

$$dF = \rho dV\ddot{u}_z(r) \tag{5.53}$$

where ρ is the density of the specimen, dV is the volume element and $u_Z(r)$ in the z-axis component of strain in the hemispherical region under the probe.

It is considered that displacements outside this zone will not contribute significantly to the inertial forces. Assuming that the radial distribution at the contact extends in a like manner radially into the surface it is possible to determine u in terms of the mutual approach of distant points, δ, between the probe and surface as a function of applied, or 'nominal', force P_O. Although not precise, this assumption will attribute excessive mass within this region but it is expected that this error will be compensated, at least in part, by the ignored components of strain outside of the contact zone and those in the other two axes. Based on these assumptions it is possible to use the equations [127]:

$$u_z(r) = \frac{1-\upsilon^2}{E}\frac{\pi p_o}{4a}(2a^2 - r^2)$$

and

$$p_o = \frac{3P}{2\pi a^2} \tag{5.54}$$

$$a = \left(\frac{3PR}{4E^*}\right)^{1/3}$$

$$\delta = \frac{a^2}{R}$$

To visualize the origin of the inertial force, consider the elemental volume of Figure 5.4 undergoing a small displacement du due to a fluctuating force of magnitude F_o. The conditions of load and displacement can then be expressed by the equations

$$P = P_o + F_o \cos(\omega t)$$
$$u = u_o + du \tag{5.55}$$

Consequently the inertial reaction, ΔF_i of an elemental volume to the applied load is given by the equation

$$\Delta F_i = \rho dV \frac{d^2 u}{dt^2} \tag{5.56}$$

where

$$\begin{aligned} \frac{d^2 u}{dt^2} &= \frac{1-\nu^2}{E} \frac{3(2a^2 - r^2)}{8a^3} \frac{d^2 P}{dt^2} \\ &= \frac{1-\nu^2}{E} \frac{3(2a^2 - r^2)}{8a^3} F_0 \omega^2 \cos(\omega t) \end{aligned} \tag{5.57}$$

Combining (5.54) with (5.55) through (5.56) and integrating throughout the three dimensional region gives the total inertial force

$$\begin{aligned} F &= \rho F_o \omega^2 \iiint_V u_r(z) r^2 dr d\phi d\theta \cos(\omega t) \\ &= \frac{21 F_o \pi^2 \omega^2 F_o a^2 (1-\upsilon^2)\rho}{60E} \cos(\omega t) \\ &= m_e \omega^2 du(0) \cos(\omega t) \end{aligned} \tag{5.58}$$

For a probe having an elastic modulus of considerably higher value than that of the specimen we can reasonably replaced the elastic modulus used in all of (5.53) to (5.58) by the value for the specimen. Additionally, the ratio of the fluctuating force to change in deflection at the surface $du(0)$ is the probe-specimen interactive stiffness given in equation (5.52). Substituting these into (5.58) gives the effective mass

$$m_e = \frac{21\pi^2 a^2 (1-\upsilon^2)\rho (6E^2 PR)^{1/3}}{60E} \tag{5.59}$$

or

$$m_e \approx \frac{\pi^2 PR}{2E}(1-\upsilon^2)\rho \tag{5.60}$$

This equation indicates that the added mass becomes significant for materials with high density and low modulus of elasticity e.g. natural rubber and possibly some biological matter.

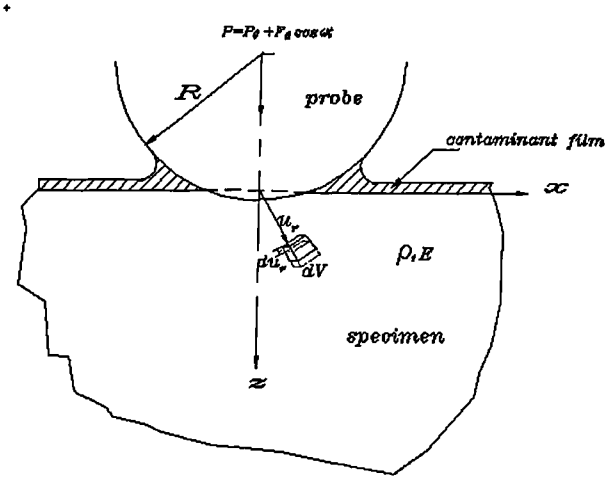

Figure 5.4. A simple model of spherical probe in contact with half space contaminated surface

5.5.2.3. Effective damping (h_e)

Upon repulsive contact, the squeeze film effect will be confined to the region within the meniscus and the circle of contact. The author is not aware of any studies in this field and it is therefore difficult to even comment on the magnitude of such an effect. However, there will also be the effects of cyclic stresses in the contact zone and this has been subject to considerably more analysis over the last 60 or so years. Unfortunately, this has not resulted in any simple conceptual models and it is recognized that there are a large number of physical mechanisms that will result in

energy dissipation under the action of a cyclic stress (Wert [135]). It is beyond the scope of this text to discuss these in any detail. Most prominent among these for metals and ceramics are

1. Thermal currents and atomic diffusion (internal friction in vibrating solids caused by diffusion of atoms [135]).
2. The Snoek effect ("changes of position of the peak in temperature with changes in frequency allow determination of the activation energy for diffusion in interstitial alloys" [135]).
3. Zener relaxation (determination of a pronounced internal friction peak in substitional alloys [135]).
4. Dislocation damping (manifestations of damping associated with discrete relaxation processes [135])
5. Dielectric relaxation ("relaxation peaks in polymers result from reorientation in the presence of an alternating electric field of molecular units possessing permanent electric dipoles" [135])

For most metals and ceramics this results in losses corresponding to **Q** values measured in thousands and are unlikely to be significant in measurements conducted during this project.

More compliant materials such as rubbers and plastics can be characterized as hysteretic. Mathematically, for steady state frequency response, this can be modelled as either a frequency independent factor $h\dot{x}/\omega$ or, equivalently as a complex stiffness (often referred to as structural damping). Choosing the latter approach, a second order system with hysteresis damping subject to a sinusoidal input can be characterized by the equation [128]:

$$m\ddot{x} + k(1 + ih/k)x = F_0 e^{i\omega t} \tag{5.61}$$

Assuming a solution of the form $Xe^{i\omega t}$, h can be solved to give the frequency response function

$$\frac{X}{F_o / k} = \frac{1}{\left(\left(1-\frac{\omega^2}{\omega_n^2}\right)+i\frac{h}{k}\right)} \tag{5.62}$$

Clearly, the gain and phase of such a system can be obtained from

$$\frac{X}{F_o / k} = \frac{1}{\left(\left(1-\frac{\omega^2}{\omega_n^2}\right)^2+\left(\frac{h}{k}\right)^2\right)^{1/2}} \tag{5.63}$$

$$\phi = -\tan^{-1}\left(\frac{h/k}{1-\frac{\omega^2}{\omega_n^2}}\right) \tag{5.64}$$

The frequency independence of the dissipation term leads to an increase in energy dissipation with frequency and a phase offset at low frequency. However, the general characteristics of hysteretic damping follow similar trends to viscosity damped systems. Consequently, identification of the dominant frequency response influences in contact using table 1 is valid for both types of mechanism.

Another potential dissipation mechanism is that due to the surface energy variation upon contact. Consider two surfaces in Hertzian contact. Before contact, each solid surface will have an associated surface energy. Upon contact, the interface can be considered a solid region with a different interfacial energy. If the two surfaces undergo no bonding or modification then the total energy is simply that of the two separate surfaces. On the other hand, if the surfaces were to form a perfect bond, then

there will be no interface energy. This energy change can be represented by the Dupre equation

$$\gamma_{12} = \gamma_1 + \gamma_2 - \gamma_{int} \tag{5.65}$$

The value of this equation represents the work required to separate the two surfaces. For simple oscillating contact there will not be complete separation but there will be a change in the area. Therefore the fractional amount of this work per cycle is given by

$$\begin{aligned} \gamma_{12} A \frac{\Delta A}{A} &= \gamma_{12}\pi(a_1^2 - a_2^2) = \gamma_{12}\pi\left(\frac{3P_2R}{4E}\right)^{2/3}\left(\left(\frac{P_1}{P_2}\right)^{2/3} - 1\right) \\ &= \gamma_{12}\pi\left(\frac{3R}{4E}\right)^{2/3}(\Delta P)^{2/3} = \gamma_{12}\pi\left(\frac{3R}{4E}\right)^{2/3}(k_e\Delta x)^{2/3} \end{aligned} \tag{5.66}$$

Therefore the power dissipated, W, is the product of work done per cycle and frequency (Hz) of excitation

$$W = \frac{\omega\gamma_{12}}{2}\left(\frac{3R}{4E}\right)^{2/3}(k_e\Delta x)^{2/3} \tag{5.67}$$

To equate this energy dissipation to an equivalent damping ratio for a viscosity damped system, the ratio of energies can be used [136]:

$$\frac{\Delta U}{U} = 4\pi\xi x^{m-2} \tag{5.68}$$

Consequently, substituting (5.66) into the left hand side of (5.68) and dividing through by $k_e(\Delta x)^2 / 2$ yields

$$4\pi\xi x^{m-2} = \gamma_{12}\pi\left(\frac{3R}{4E}\right)^{2/3}(k_e\Delta x)^{2/3}\frac{1}{k_e(\Delta x)^2/2} = \gamma_{12}\pi\left(\frac{3R}{4E}\right)^{2/3}\frac{2}{(\Delta x)^{4/3}k_e^{1/3}} \tag{5.69}$$

from which it can be seen that

$$m = 2/3$$
$$\xi = \gamma_{12}\left(\frac{3R}{4E}\right)^{2/3}\frac{1}{2(\Delta x)^{4/3}k_e^{1/3}} \tag{5.70}$$

also

$$\xi = \frac{h}{2k_e} \tag{5.71}$$

where ξ is ratio of the actual hysteretic damping to the amount neccesary to provide critical damping.

Substituting (5.52) and (5.71) into (5.70) and solving for *h,* yields:

$$h = 1.23\gamma_{12}\left[\frac{R^4P}{E\Delta x^6}\right]^{2/9} \tag{5.72}$$

where h is hysteretic damping.

Figure 5.5 a) the shows shift in the resonant frequency and Figure 5.5 b) and c) theorethical phase shift in the resonant probe for a selection of different materials under various loads, which was calculated using equations (5.33), (5.52) and (5.60) and estimated values for damping and coupling loss factor (ξ) [137,138]. Matlab programs shown in Appendix D were used to produce these figures.

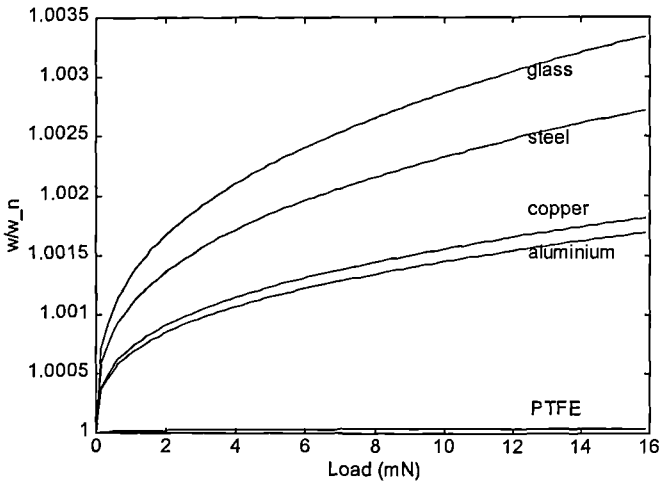

a)

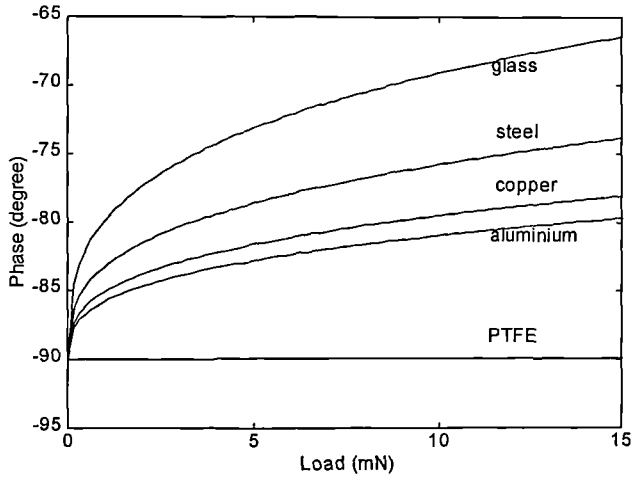

b)

Estimated values for Damping and Coupling loss factor (ζ):	
Aluminium :	0.0098
Copper:	0.0126
Steel:	0.0117
Glass:	0.0038
PTFE:	0.03
Rubber:	0.07

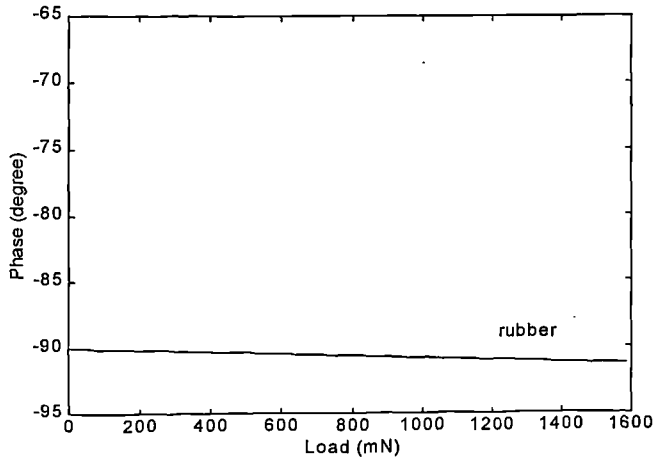

c)

Figure 5.5. Mathematical results representing the shift in the resonant frequency **a)** and the phase shift **b)** and **c)** for a selection of different materials.

5.6. Conclusion

The dynamics of a resonant probe sensor, as it approaches typical engineering surfaces, are subjected to a complex variety of forces. In order for the sensor to be successfully used in precision engineering applications, it is necessary to understand the complexity of this interaction. In this chapter an approximate mathematical theory has been developed in order to model contact mechanisms between a resonator based sensor and engineering surfaces and to predict the effects characteristic of added mass, stiffness and damping. The theory also considers near surface contact phenomena and the squeeze and surface films effects.

Combining Hertzian contact mechanics and Rayleigh's approximate energy method of sensor's vibrations it was possible to derive a simple second order vibration model of the proposed resonant sensor and to examine the causes of parametric changes at contact and near contact conditions (Section 5.4). In order to simplify modeling, the assumption of a system undergoing longitudinal vibrations was made. Two modes of contact detection commonly used for resonant sensors were considered: monitoring frequency at constant phase and monitoring phase at constant frequency. The model predicts that phase and frequency shifts can either increase or decrease depending on the dominant phenomena (added mass, stiffness and damping) in the contact region. It has been shown that observation of dynamic characteristics either side of the resonant frequency can be used to identify the predominant effect.

Analyzing the causes of parametric changes at near-contact conditions (Section 5.5.1), it was mathematically determined that the squeeze film effect will add damping in the interfacial zone without adding significant mass or stiffness. However, as the squeeze film forces increase, these must be restricted by the surfaces of probe and specimen. Subsequent distortions would add an effective stiffness to the system. For surface films, simple calculation (Section 5.5.1.2), based on Hertzian contact theory, indicates that for thin films of thickness less than the radius of the contact probe, there will be

relatively low induced stress due to capillary action between two typical solids. Mechanical contact conditions were also studied Section (5.5.2). The model for effective stiffness was based on the Hertzian theory and Smith and Chetwynd analysis [134], and it could be calculated as the local stiffness for an elastic contact of a sphere on a flat surface. The equation derived for the added mass indicates that the added mass becomes significant for materials with high density and low modulus of elasticity e.g. natural rubber. Effective damping was considered as hysteretic and it was calculated using energy dissipation for a viscosity damped system. In most materials, specific damping capacity will increase with amplitude of motion.

As a consequence of the developed mathematical model, it was possible to set up an experimental investigation using the proposed resonator based sensor in order to determine the predominant contact phenomenon and therefore verify its prediction and validity of the model itself. This will be described in Chapter 6.

Chapter 6

Resonant sensor characterisation and some engineering applications

6.1. Introduction

The initial design of the touch sensitive probe described in Chapter 4 was further improved and modified in order to achieve miniaturisation and greater versatility. The new multipurpose sensor consists of a beryllium copper (BeCu) rod of hexagonal cross section (6×3.64mm; length = 0.02m) with three pairs of piezoelectric drive and pick up sensor mechanisms bonded to its surface using M-BOND 200 adhesive. The new design is shown in Figure 6.1.

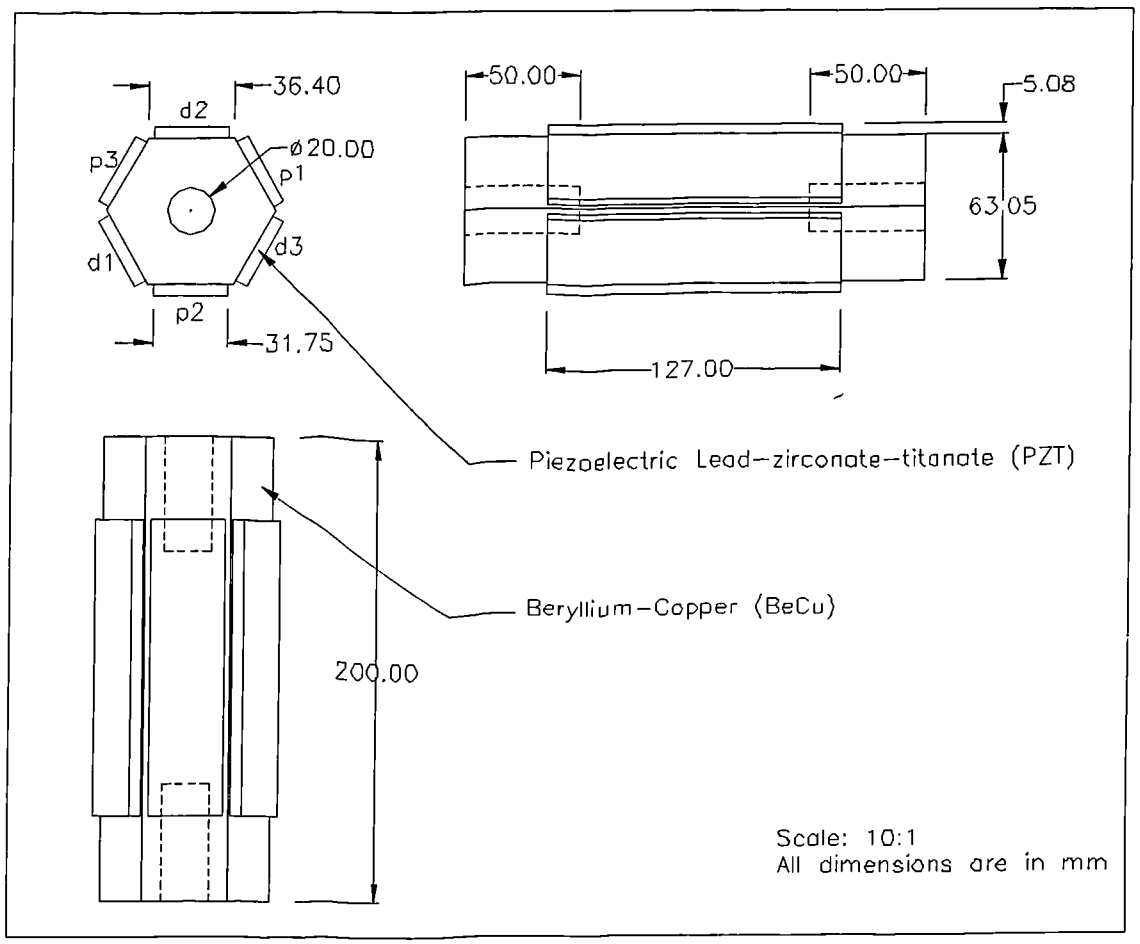

Figure 6.1. The design of the new resonant sensor

The rectangular piezoelectric lead-zirconate-titanate (PZT) plates used for the modified sensor were similar to those used for the initial probe. The standard gauges, BEG/1-3, were employed as excitation drives and BSG/1-3 as pick-up sensors. Dimensions (in mm) and characteristics of these elements are [75]:

BSG/1-3: Length = 12.7; Width = 3.175; Thickness = 0.508;
Capacitance = 900 pF; Sensitivity(volts/unit strain) = 3.7×10^{5}.

BEG/1-6: Length = 12.7; Width = 3.175; Thickness = 0.508;
Capacitance = 690 pF.

Working temperature range: -270°C to +250°C;

Maximum dynamic strain 2.5×10^{-4} for linear operation.

The probe itself consists of a standard coordinate measuring machine tip holder screwed into the free end of the hexagonal rod. Care was taken to keep the resonator geometry as close to the one-dimensional theoretical description as possible, to secure a clean resonance spectrum free of spurious modes. The resonance utilised for the sensor function shifts within a certain frequency range depends on the measurand. Figure 6.2 shows a photograph of the new resonant probe.

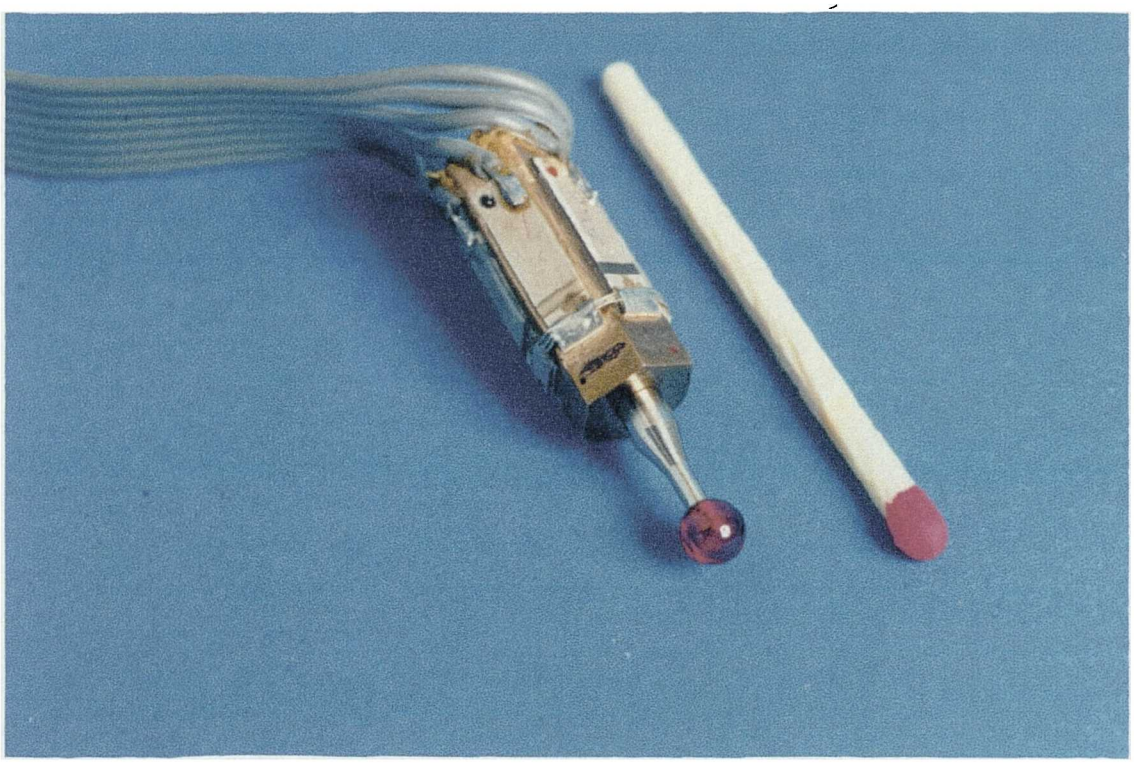

Figure 6.2. Photograph of the new resonant probe with Renishaw's 5 mm stylus tip.

To analyse frequency power and frequency phase response of the probe, a high precision AND 3525 Dual Channel Fast Fourier Signal Analyser was used. Three excitation gauges, d_1, d_2 and d_3, shown in Figure 6.1, were driven in sequence by a random signal in order to obtain the frequency response of the whole system. Corresponding pick-up sensors were p_1, p_2, and p_3 (Figure 6.1). The frequency range of the random signal was set between 1 and 100 kHz with an amplitude of $3V_{0\text{-}p}$.

Figure 6.3. shows a typical frequency spectrum of the system. The active pair was d_1-p_1 PZT mechanism.

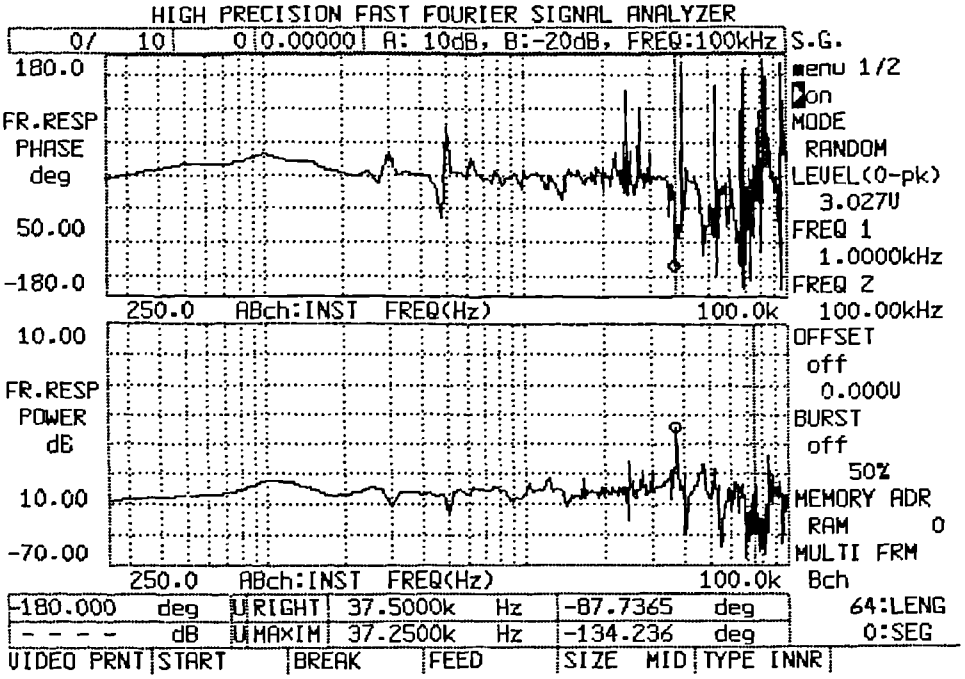

Figure 6.3. Typical frequency spectrum of the system when activated by d_1-p_1 driving-pick up piezoelectric mechanism

It was observed that the frequency response of the probe was almost the same, regardless of which pair of PZTs was activated. In all three cases, resonance frequency was around 38kHz with phase shift around -90 degrees.

The probe response was also analysed when the driving and pick up mechanisms were adjacent (d_1-p_2, d_1-p_3, d_2-p_1, etc.). Figure 6.4. shows such response with pair d_2-p_1 being active. The resonance frequency of the probe was around 90 kHz. In this case the probe exhibited very low sensitivity which would not prove satisfactory in practical applications.

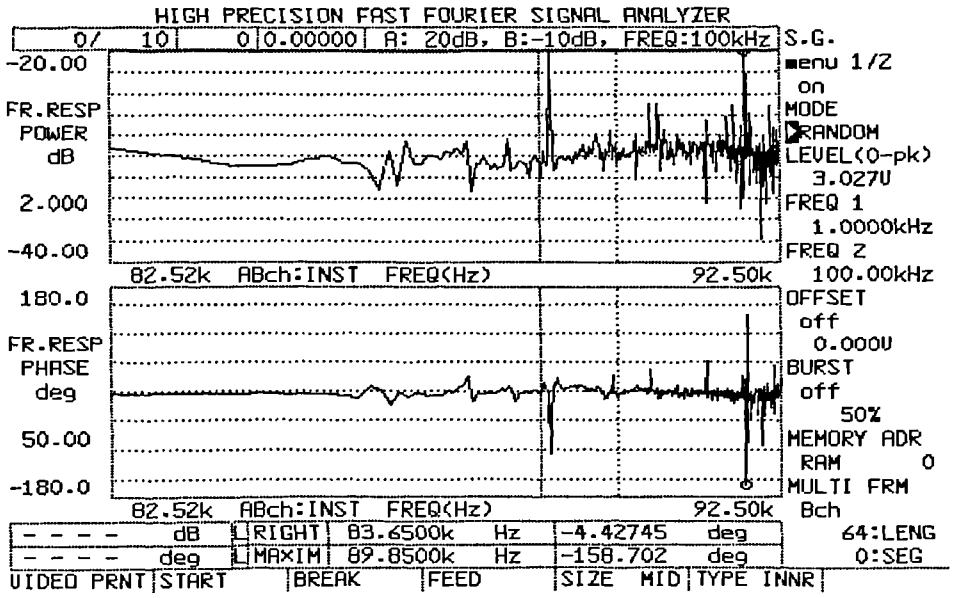

Figure 6.4. Frequency spectrum of the system when pair d_2-p_1 was acting as a driving - pick up mechanism.

The frequency response tests showed that the probe exhibited very similar sensitivity regardless of the piezoelectric drive used as long as the corresponding pick-up was one symmetrically placed with respect to the vertical axes of the probe (i.e. d_1-p_1, d_2-p_2, d_3-p_3 in Figure 6.1). The probe also exhibited marked directional sensitivities when forces were applied radially which suggested possible applications of the sensor not just as a probe on coordinate measuring machines and device for detecting material properties, but also as a vector probe which will be discussed in due course. However, the resonance frequency of the probe, and therefore its sensitivity, strongly depends on its mounting arrangement due to variations of the interface stiffness at the clamped end. Typical frequencies for the new sensor were in the region of 38 kHz and the whole system exhibited a second order response. During some experiments, the second harmonic (56.06 kHz) was chosen for operation because the probe showed high sensitivity when in contact with both soft and hard materials while the phase response was close to -90 degrees.

6.2. Observations of contact measurements with engineering surfaces

Chapter 5. has outlined the importance of understanding the mechanics of contact phenomena between two objects and the necessity to examine effects such as stiffness, mass and damping when the probe is in contact with different materials. It has also described a systematic theoretical study of the contact mechanisms between a resonator sensor and a broad range of engineering surfaces. This section describes the experimental investigation conducted using the resonator sensor described above. To assess the interaction between a probe tip and typical engineering surfaces, the complete resonator was mounted onto an electromagnetic linear motion actuator for fine positioning of the probe, whilst the specimen was placed on a special mount of a cantilever beam on which two strain gauges were mounted and arranged in a half Wheatstone bridge to detect the normal load. In subsequent experimentation, a 5mm sapphire sphere, typically used for coordinate measuring machine probes, was employed as the tip. The sensor could be operated in two modes:

1. Monitoring frequency at constant phase (mode I)
2. Monitoring phase at constant frequency (mode II)

To this end, a variety of materials were assessed, ranging from rough rubber to polished, hardened steel and surfaces covered by liquid films having viscosity ranging from 0.20 to 10 Pa s. A broad range of phenomena was observed both 'prior to' and 'at' the contact with the surface. Characteristics of added mass, stiffness and damping were observed and these are illustrated with selected results from a large number of tests [137,138].

6.2.1. Instrumentation and experimental set up

Two types of surfaces were assessed in these experiments:

1. A solid glass surface covered with a thick layer of oil;
2. Clean solid surfaces of different engineering materials.

In order to assess the interaction between a probe tip and the above surfaces, two simple test rigs were used. Figure 6.5 shows the schematic diagram of the first which was used to assess the response of the probe when contacting a solid glass surface covered with a thick layer of oil. A microscope slide was used as a glass surface.

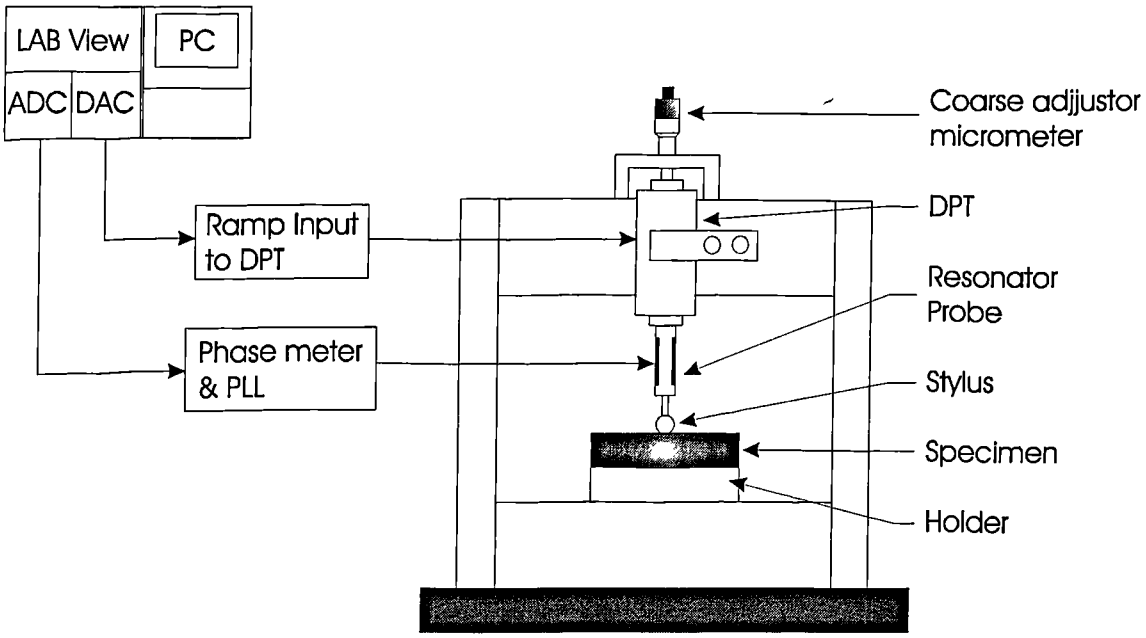

Figure 6.5. Schematic diagram of the test rig used to monitor the contact between resonator probe and solid glass surface covered with a thick layer of oil

The resonator probe was mounted onto a Queensgate Instruments AX100 Digital Piezoelectric Transducer (DPT), for fine positioning. This in turn was mounted at the end of differential micrometer for coarse adjustment. The whole assembly was then mounted in a fixed bridge type frame with its axis vertical, the probe tip pointing downward. The specimen was rigidly secured in a special fixture beneath the probe. During these experiments, the change in phase were recorded as the probe approached (using coarse adjuster) and contacted first the oil film then the solid surface. The system was controlled and data acquired using National Instruments LABView software.

The second test rig, shown in Figure 6.6, was used to assess the response of the probe when it contacted clean solid surfaces.

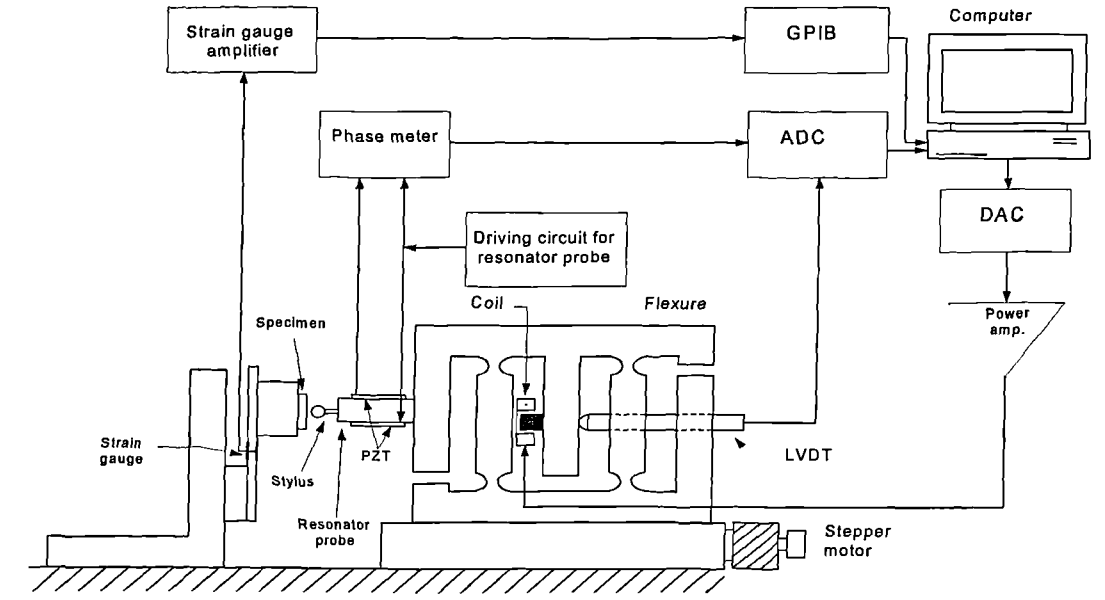

Figure 6.6. Schematic diagram of the test rig used for monitoring the contact between resonator probe and solid surfaces.

In this the resonator probe was mounted onto a simple linear flexure translation stage for fine positioning, (see section 5.2.1). Displacement of the flexure was continuously monitored by an LVDT which was periodically calibrated against a Hewlett Packard laser interferometer system (HP 5528A). The LVDT used was D5/00G8, with a linear

range of ±0.2 mm and with 0.15 % of linearity. The conversion rate of the LVDT output was 13 μm/V (Appendix E.2). The whole assembly was mounted onto a linear x-stage driven by a stepper motor to provide coarse adjustment. This was then positioned horizontally in line with a stationary specimen. Two strain gauges in a half bridge arrangement were used to monitor the contact force between the probe tip and the specimen. These were fixed on the opposite sides of a cantilever which holds the specimen at its free end. A digital strain gauge indicator P-350A (Vishy Instruments), with a range of ±50,000 με (microstrain) and accuracy of ±0.1 % or 5 με was used. The calibration factor of the strain gauge amplifier output was 325.369 g/V (3.25 NV^{-1}) (Appendix E.1).

Two sets of tests were conducted. In the first (mode II), the probe was oscillated at a fixed frequency, and the change in phase, using a Phase meter, was monitored as the probe approached the surface. In the second (mode I), the phase angle was locked at near 90° using analogue phase locked loop (PLL) circuitry, and the change in frequency was monitored as the probe contacted the surface of the specimen. The calibration factor for the PLL at 56.06 kHz was k=2.767 kHz/V or k=0.3614 V/kHz (Appendix E.3). Tests were repeated over a broad range of materials ranging from rough rubber to polished and hardened steel.

The PLL output voltage (mode I), Phase meter output voltage (mode II), LVDT output voltage, and solenoid input voltage were recorded and analysed. Data collection was done by an IBM compatible PC via an ADC data acquisition board (Amplicon Liveline Instruments PC 74 16 I/O board with 12 bit resolution). The strain gauge amplifier readings were recorded via a standard GPIB (General purpose interface bus) interface. A program written in turbo Pascal 7.0 was used to acquire the data into the computer while the analysis was done using Microsoft Excel and Matlab application programs.

6.2.2. Experimental method

6.2.2.1. Contact characteristics of thick oil films

In the first set of experiments, two types of oil were used. The oil layer was produced by applying a few drops of oil onto a standard 1 mm thick microscope cover-slide. For both types used, the thickness of resultant layer settled to a value of approximately 1 mm. In the first set of experiments, the probe was contacted with the oil layer by incremental adjustment of the manual micrometer. This displacement was continued until solid contact of the underlying substrate was detected as a rapid increase in the effective stiffness of the system. Each experiment took approximately five minutes with approximately 200 increments of approximately 10 μm towards and away from the surface. It was found that consistent and repeatable results could only be obtained when the probe was cleaned (with ethyl alcohol) before each individual contact experiment.

6.2.2.2. Contact characteristics of clean solid surfaces

Contacting solid surfaces required considerably finer control of the displacement of the probe towards the specimen surfaces. Two separate tests were conducted. In the first, the specimen and the strain gauge were mounted onto the same assembly. In order to bring the probe into contact with the surface, flexure was driven via an electro-magnetic actuator on the flexure in 700 increments of 0.002 V (8.5 nm) with a time delay between increments of 100 μs. Therefore, the total displacement produced was approximately 3 μm towards and away from the specimen. The maximum load, which was measured simultaneously, corresponds to approximately 15 mN. Contacting soft surfaces was much more complicated due to the high compliance of rubber-like materials resulting in low values for the derivatives in equations (5.39) and (5.40). A force of approximately 200 mN had to be applied onto the specimen via the probe in order to produce significant phase or frequency shift. The stage was

driven via the stepper motor to generate larger displacements, and therefore large deflections, of the cantilever. Prior to each experiment the stylus and specimen surfaces were cleaned thoroughly using acetone.

6.2.3. Experimental results

A large number of experiments was performed to observe the contact phenomenon between the probe tip and engineering surfaces and this discussion represents an overview of typical observations. For significant oil films, characteristics of the approach extended over 1 -2 mm while, for solid contacts, significant effects could only be observed over a range of a few micrometers. For this reason these results are discussed separately.

6.2.3.1. Contact with a relatively thick oil layer on a smooth glass surface

Figure 6.7. a) shows a typical plot of the phase shift of the probe from a free value lag of 81 degrees. In the first series of tests, a thick layer of silicone oil[1] having a viscosity of approximately 10 Pa s was used.

[1] L-45 Polydimethylsiloxane, Union Carbide, Danbury CT 06817-0001, USA

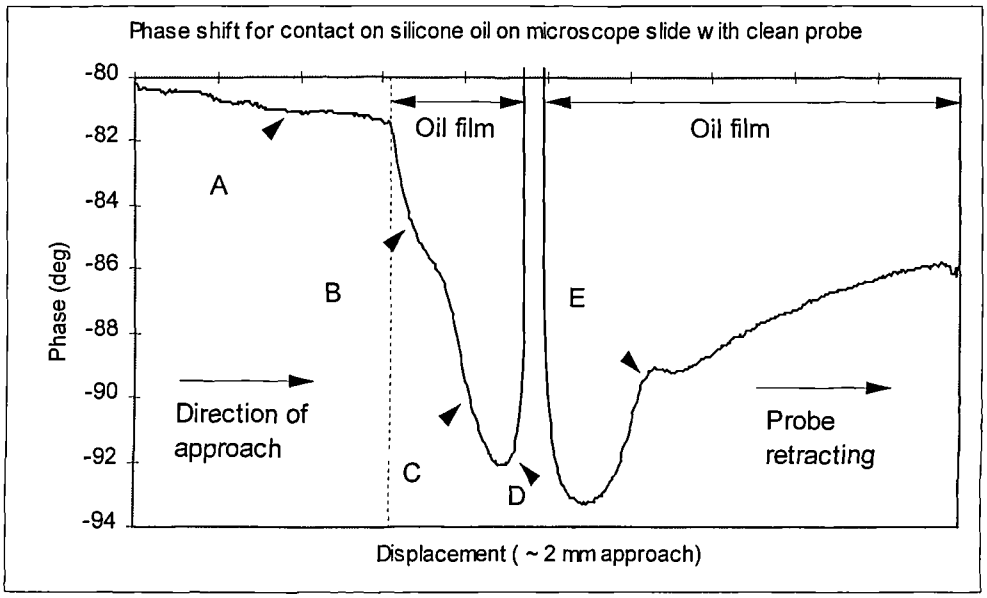

a)

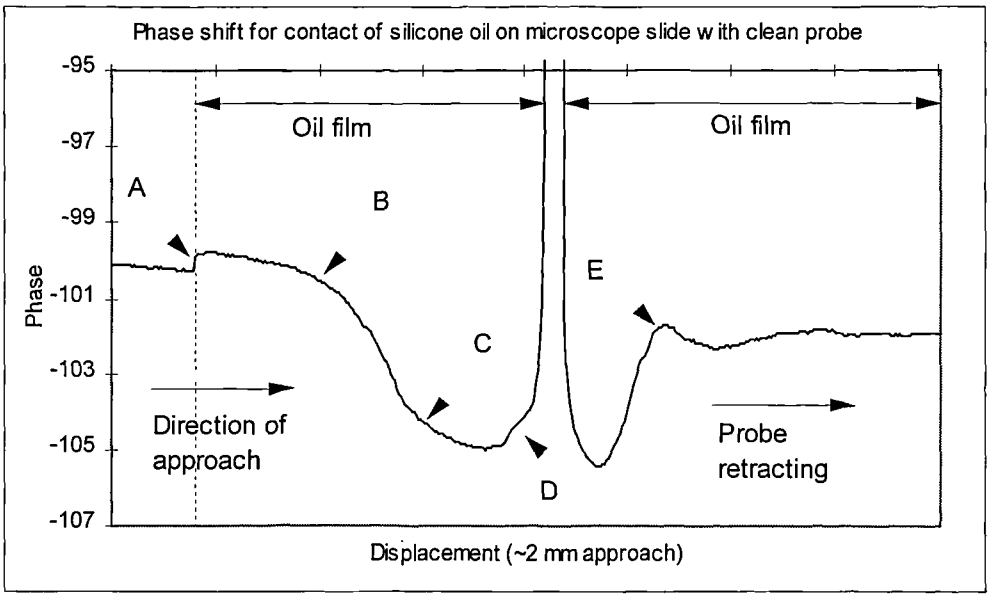

b)

Figure 6.7. Typical plot showing contact characteristics of thick oil film on glass microscope slide for free value phase shift of (a) -81 degrees; (b) -100 degrees and (c) -70 degrees.

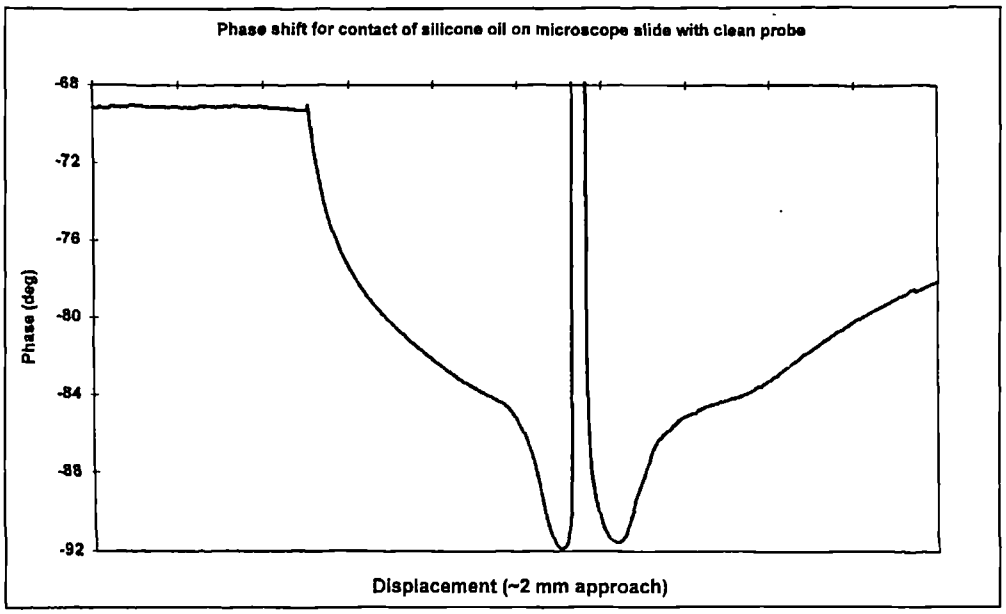

c)

Figure 6.7. (Continued)

There are a number of distinct regions visible in the graph and these have been labelled accordingly. Region A corresponds to displacement of the probe tip towards the oil surface prior to physical contact. In practice, the point of contact is relatively easy to identify as the capillary forces cause an easily visible meniscus to form around the probe. At this point there is a relatively large increase in phase lag. Referring to Table 2 (Chapter 5.), this would be the result of either an additional mass or an additional damping within the system. This increase continues into region B until there is another transition to a third region C. As the probe nears the surface the phase has crossed over -90 degrees at which point an additional damping would result in a *reduction* of the phase lag. Such a reduction occurs prior to mechanical contact, after which the phase very rapidly increases which is characteristic of a relatively large increase in effective stiffness. Retracting the probe away from the surface, the phase shift of the probe mirrored the original approach curve with a similar characteristic at D and C only with a permanent offset of approximately -2 degrees. However, upon retraction, a transition can be seen, region E, which is close to the original point of inflection in the approach curve. At this point the phase appears to be increasing more rapidly. At this point it is observed that the meniscus is becoming elongated. Such a

rapid reduction in phase would be characteristic of an increase in either stiffness or damping or a reduction in mass. It is not clear which is a dominant effect at this stage. Eventually, the meniscus breaks leaving a small amount of oil on the tip of the probe and a permanent phase shift of approximately -5 degrees. Interestingly, subsequent cleaning of the tip resulted in a further reduction in phase of approximately 2 degrees which, in addition to the permanent shift observed after solid contact, would return the phase to the original free value of 81 degrees. In this, and most of the subsequent experiments, repeating the experiments resulted in nominally similar characteristics.

After cleaning the probe, the excitation frequency was increased to produce a phase shift of -100 degrees. The subsequent phase shift as a function of approach is shown in Figure 6.7. b). Again, prior to contact there is a reduction in the phase indicating an effective inertial force. This followed upon immediate contact with the oil by a reduction in phase. This is not present in Figure 6.7. a). It is possible to explain this as an effective damping which would add to the inertial effect with an opposite sign either side of the resonant frequency. Upon further displacement of the probe into the oil, the phase shift is observed to decrease with opposite curvature to that observed in Figure 6.7. a). This suggests that there are two predominant effects in this portion of the curve which are additive on the lower side of the resonance peak, and subtractive above it. Regions C and D show similar behaviour to that of Figure 6.7 a) which is not surprising since they are both on the same side of the resonant frequency. Interestingly, region E is observed upon retraction of the probe at the point where significant thinning of the meniscus is observed. Again cleaning of the probe after separation from the film resulted in a phase increase of approximately two degrees.

Noting the total phase shift in Figure 6.7. a) passed across the -90 degree point, this experiment was repeated with a substantially larger offset of -70 degrees. On this side of the resonance the damping and inertial phase shifts are additive. Figure 6.7. c) shows a similar characteristic only this time with an initial positive phase shift with separation showing a characteristic common to a first order system step response of

magnitude 16 degrees. This is considerably larger than that on the other side of the resonance curve which has a magnitude of approximately 6 degrees. Assuming simple superposition and a linear phase characteristic (see Chapter 4.), this would imply a contribution of 11 degrees due to the additional mass and 6 degrees from damping. Clearly, these are very rough assumptions but such analysis does indicate the relative magnitude of each effect.

6.2.3.2. Contact with a relatively thin oil layer on a smooth glass surface

Replacing the silicone oil with SAE 20W (viscosity 0.2 Pa s) the above experiments were repeated. Having comparable density but with a viscosity 50 times lower than that of the previous experiment, resulted in considerably different contact characteristics as shown by Figure 6.8 a) and b).

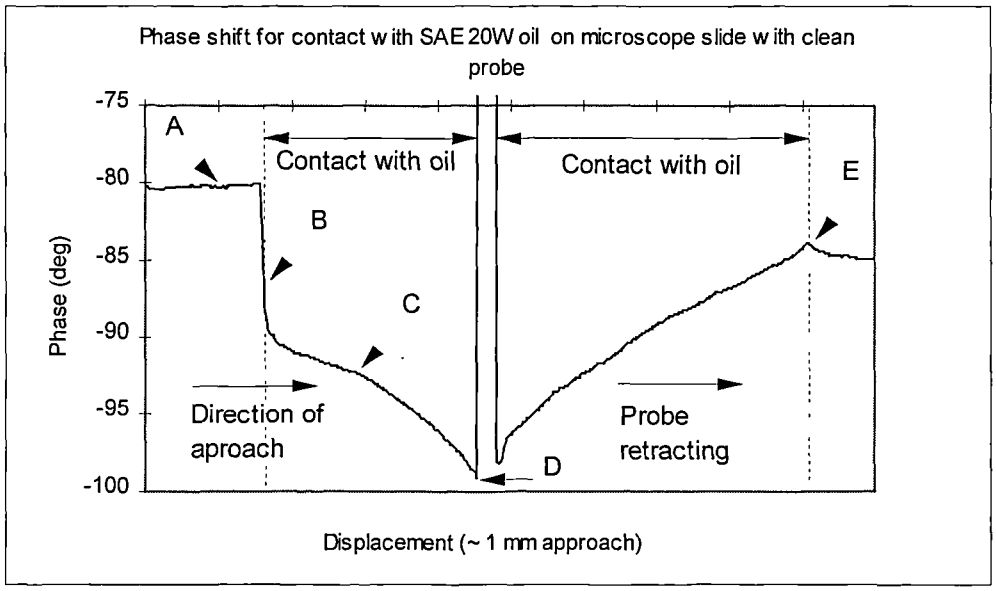

a)

Figure 6.8. Typical plot showing contact characteristics of thin oil film on glass microscope slide for free value phase shift (a) -80 degrees and (b) -100 degrees

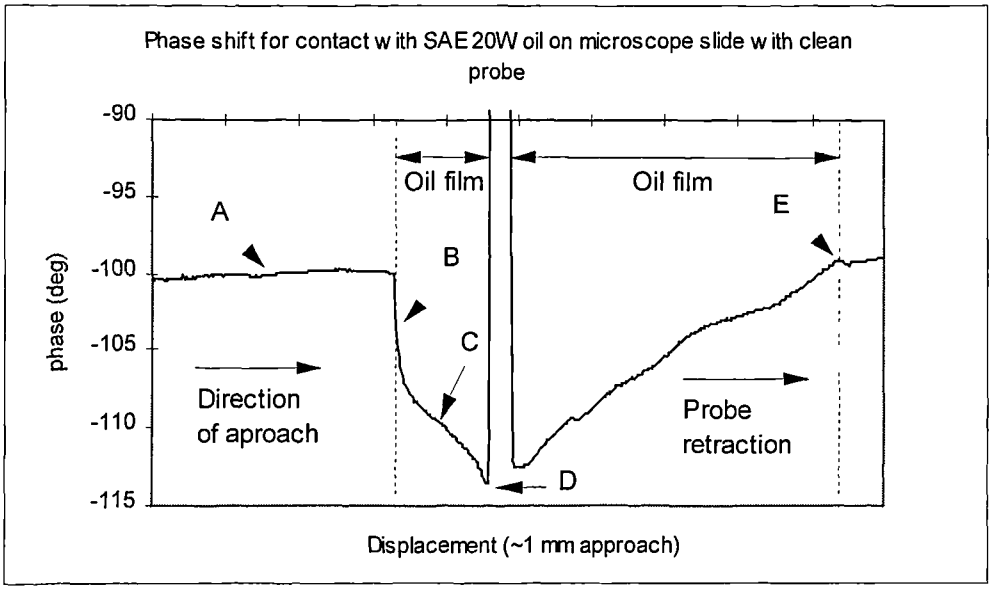

b)

Figure 6.8. (Continued)

Again there is a slight reduction of the phase lag prior to contact in both cases indicating that the air acts as an acoustic coupling. Upon initial contact with the oil film, rapid increases in phase lag of approximately 9 and 7 degrees on the lower and upper sides of the resonance curve are observed. This implies a significant addition of mass plus perhaps, a relatively small additional damping. Further motion of the probe into the film produces a slow increase in phase lag in both plots until contact is observed at D. The sharp transition at this point implies that the viscosity of the film is responsible for the negative phase effects in the previous experiments. Upon retraction of the probe, a similar marked difference in phase is observed as the meniscus is at its limit of extension at E. Again cleaning of the probe tip resulted in a further increase in phase of approximately 1 - 2 degrees.

6.2.3.3. Contact of solid surfaces

A number of experiments were conducted on different types of materials: PTFE (Poly TetraFluoro Ethylene), aluminium, copper, steel, glass and two types of rubber in order to experimentally support the theoretical model developed in Chapter 5. Each

specimen was cube-shaped: 10mm long; 10mm wide, and 4mm thick. Rapid Araldite was used to bond them onto the specimen holder at least 24 hours before experimentation took place. Prior to, and after each experiment the specimen's surface , as well as the probe, was thoroughly cleaned using acetone. Figure 6.9. shows a typical plot of a probe's phase shift when contacted with these solid surfaces.

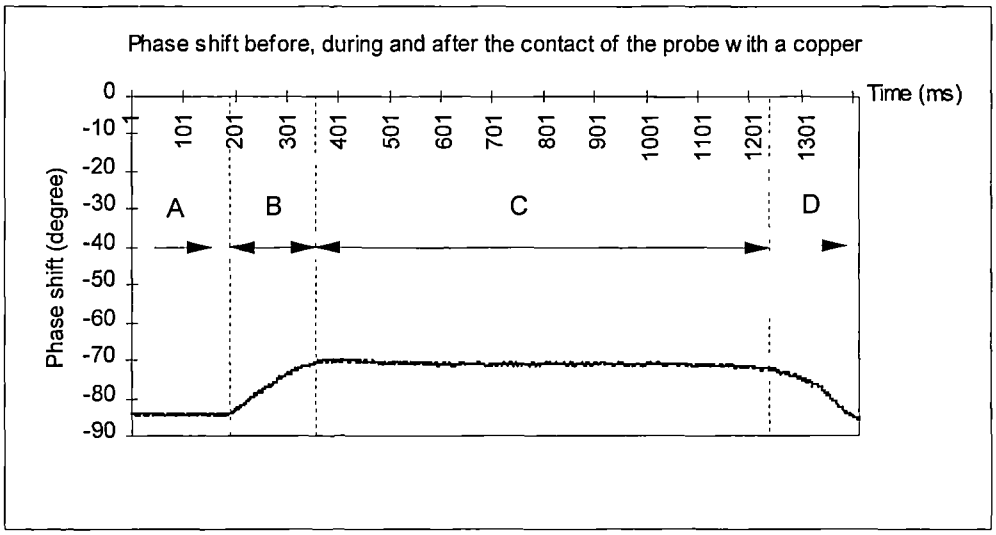

Figure 6.9. Typical plot showing contact of the probe with solid surfaces

The above figure represents phase shift versus time showing that whole experiment could be divided in four sections. Section A represents the start of experiment during which probe is driven towards the specimen but not in contact with it. Section B shows the probe in contact with the surface during which phase shift increases as applied force and displacement of the flexure, on which probe is mounted, increase. Region C is the region of saturation where the probe is in solid contact with the surface and maximum load is applied. Finally, section D is the region of the probe retracting from the specimen with phase shift returning to its original value. The most important region is region B during which the phase shift changes from its free to its maximum value. A further analysis will be based on data acquired during this period.

Figure 6.10 *(a)* and *(b)* shows the typical results of the experiments when the free value phase shift was set at -85 and -100 degrees, respectively.

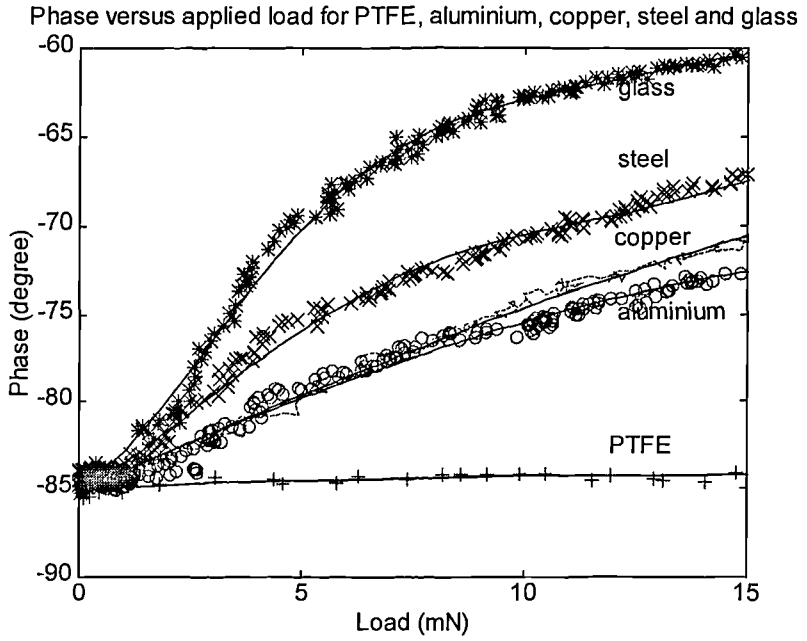

(a)

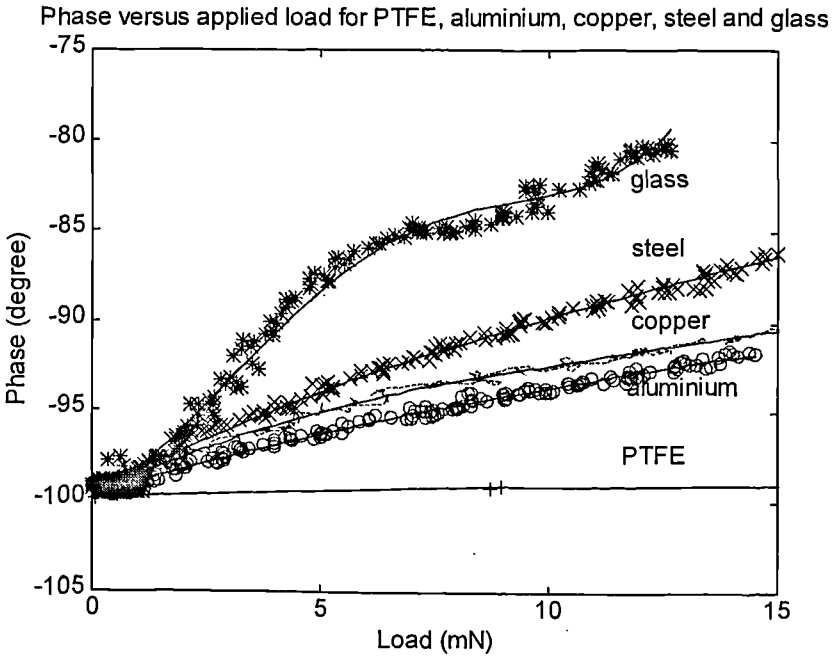

(b)

Figure 6.10. Plot showing phase shift when probe contacts solid engineering surface for free value phase shift of a) -85 degrees and b) -100 degrees.

In both cases, phase shift was monitored versus applied force. For PTFE, the phase shift starting at above -90 degrees was increased by less than one degree, whereas for the same contact force, on a glass surface, the increase in phase was more than 25 degrees. Phase shifts for aluminium, copper and steel fit in between these two values. Comparing the above results with classification scales for hardness and values for modulus of elasticity and density of materials used in these experiments which are shown in Table 6.1, an interesting conclusion could be assumed: phase shift favourably agrees with hardness scale leading to potential applications of the new probe in non-destructive hardness testing.

Material	Hardness (MPa)	Phase shift (degree)	E ($\times 10^9 Nm^{-2}$)	ρ ($\times 10^3$ kgm^{-3})	E/ρ
Glass	5200	25	70	2.7	26
Steel	1000	18	200	7.9	25.3
Copper	580	14	120	9.8	12.2
Aluminium	190	12	70	2.7	26
PTFE	75	1	3	2.5	1.2

Table 6.1. Hardness scale and values for phase shift, modulus of elasticity and density of different materials used in experiments

Furthermore, observing similar test as above, but for phase shift starting below -90, (Figure 6.10 b) it could be seen that testing materials like PTFE resulted in more or less similar increase in phase of less than one degree whereas for the glass the increase was about 20 degrees. This means that the phase shift has lower increase rate when free value of the phase shift is set bellow -90 degrees. Close comparison with other materials tested indicates that, on average, the difference in the phase shift for the same material is about 5 degrees when the phase is both below and above -90 degrees. This is illustrated in Figure 6.11 for a copper specimen and in Appendix F.1 for other materials.

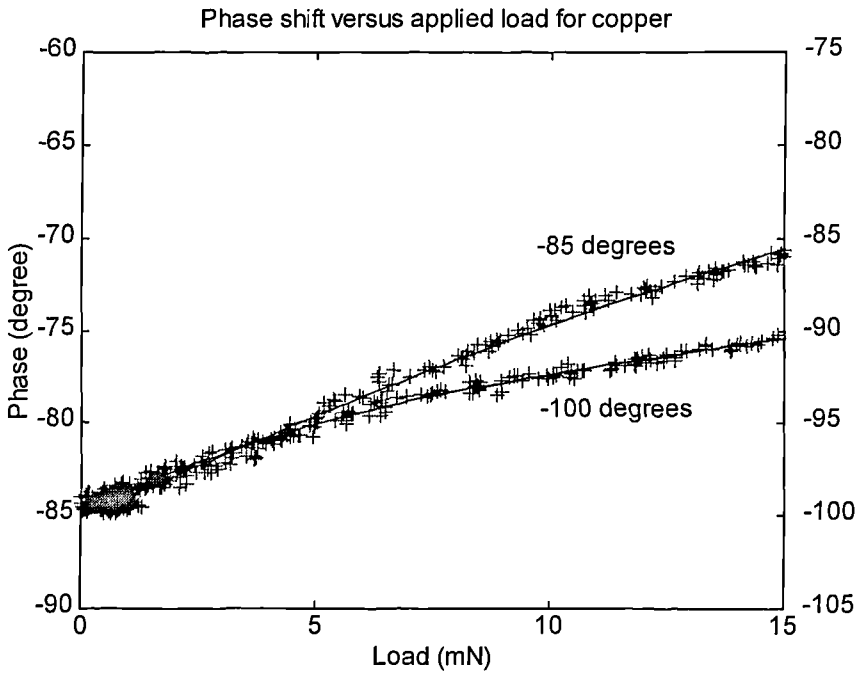

Figure 6.11. Plot showing phase shift difference for the copper for free value phase shift at -85 (left y axis) and 100 degrees (right y axis)

Again, referring to Table 5.2. suggests that the reason for behaviour described above is due to the contribution of the added damping in the system although these large phase shifts may include other non symmetric factors. As predicted (Equation 5.36), all the materials tested and shown in Figure 6.10 exhibit a reduction in phase lag, but at different rates, which indicates that added stiffness is the predominant effect. Figure 6.12 shows a favourable comparison of theoretical models, developed in Chapter 5, and experimental results for steel. Figures for other materials can be found in Appendix F.2.

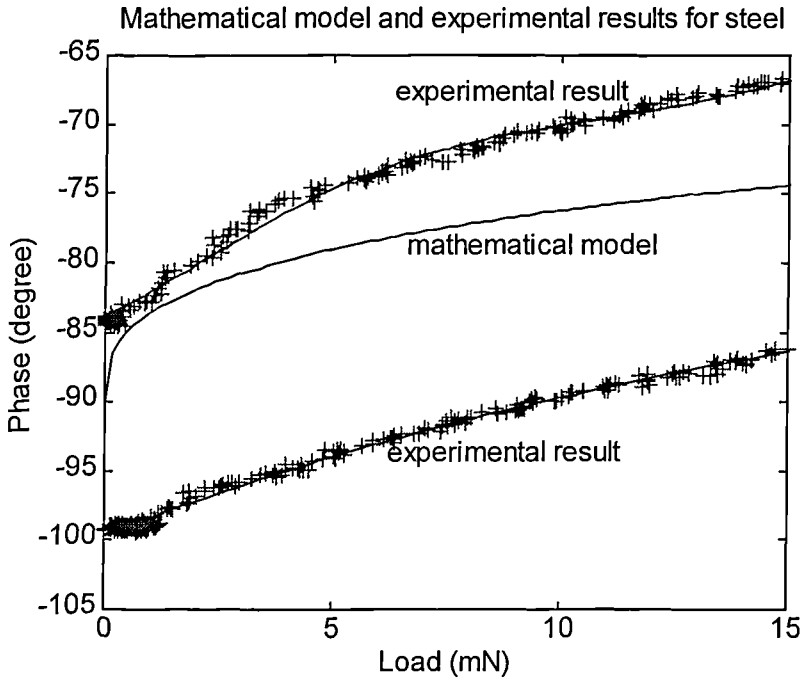

Figure 6.12. Typical plot showing mathematical model and experimental results for steel

The experimental results do not exhibit sudden changes in phase shift lag as in the case of the theoretical model. The reason for this is the way the experiments were conducted. As was explained in section 6.2.2.2, the probe was brought in contact with the surface via the flexure mechanism which was driven in 700 increments of 8.5 nm with the settling time of 100μs between each step. The sampling rate was also set up at 1ms. This means that there was no sudden contact between the probe and the specimen, and that the force applied by the probe onto the surface had a very slow increase during this time. Hence no sudden change in phase shift occurred.

Another, similar, set of experiments was conducted on rubber-like materials. Figure 6.13 shows typical test results for two types of rubber with different hardness (softness). The specimens were of the same shape and size as the specimens used during the experiments conducted on solid surfaces (10x10x4mm).

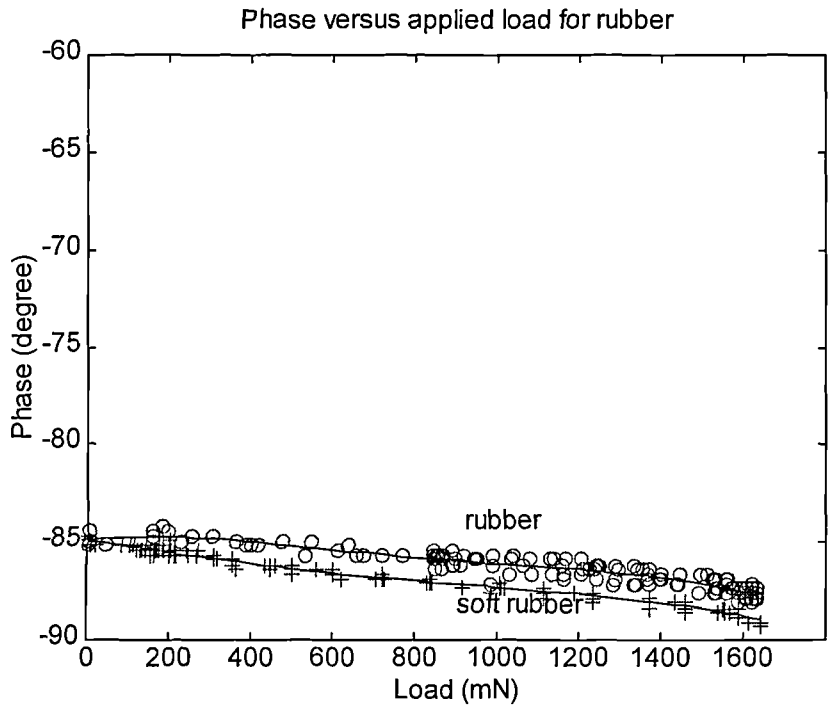

Figure 6.13. Typical plot showing phase shift when probe contacts rubber-like materials

As can be seen from the above results, a substantial amount of contact force had to be applied onto the specimen in order to achieve a significant change in phase shift of about -3°/1600 mN. The force applied was approximately 100 times the force applied on solid surfaces. On the contrary to the experiments on solid materials, these test have shown an increase in absolute value of the phase lag. Softer materials, register higher increase, indicating the predominant effect of added mass as the result of relatively high density and low elastic modulus. Figure 6.14 represents a comparison of the theoretical model, developed in Chapter 4, and experimental results for rubber showing favourable agreement between test results and mathematical model.

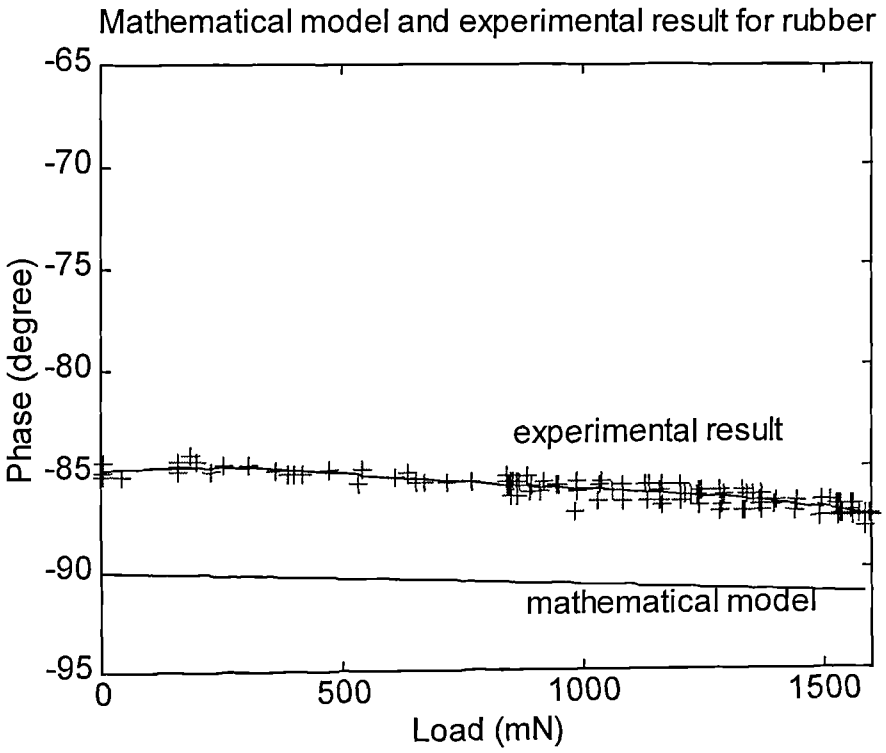

Figure 6.14. Typical plot showing mathematical model and experimental result for rubber

All above experiments were done in mode II monitoring a phase shift versus applied load when the probe was driven by VCO (voltage controlled oscillator) at constant frequency. Referring to the section B of the Figure 6.9 which shows contact of the probe with the surface during which phase shift increases as applied force and displacement of the flexure, on which probe is mounted, increase, it could be observed that changes in phase lag could also be monitored versus displacement of the probe tip in the contact region. Some typical results of this analysis could be found in Appendix F.3.

Finally, the set of experiments was conducted in mode I in which changes in frequency were monitored as the probe contacted specimens, while the phase was locked at near -90 degrees. Figure 6.15 shows a typical plot of frequency shift of the probe as it contacts various solid surfaces.

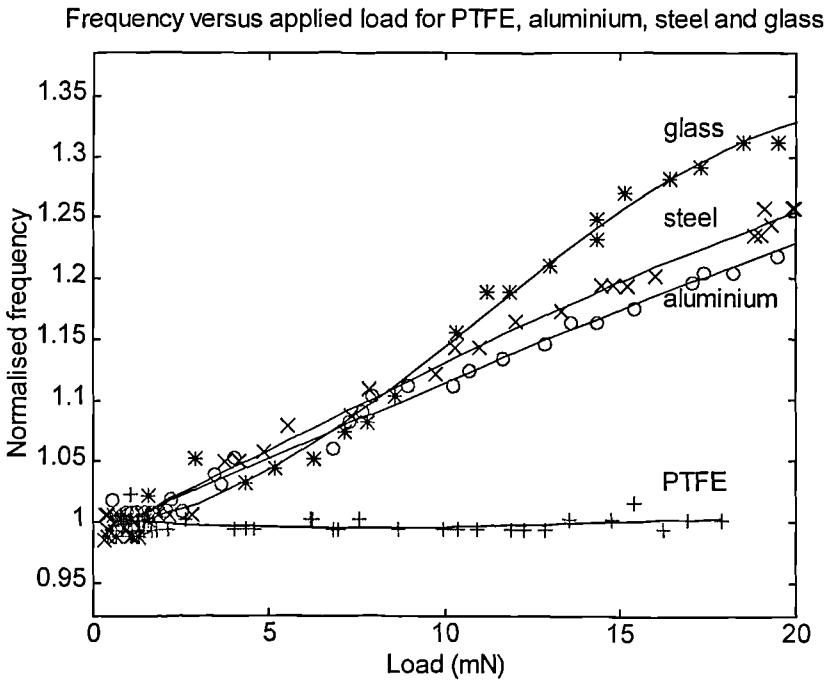

Figure 6.15. Plot showing frequency shift when probe contacts solid surfaces

The results of these tests conform with the theoretical model (Figure 5.5) which predicts an increase in frequency shift when the probe contacts solid surfaces. PTFE, aluminium, steel, copper and glass were used as experimental specimens and increase in frequency confirms that the added stiffness was the dominant factor. All materials, except PTFE, exhibited higher frequency shift than the mathematical model predicted, which was attributed to the high sensitivity of the probe. Also, effects of the strain gauges and stiffness of the cantilever beam probably had some significant contribution.

Rubber-like materials were also investigated using the same set up of the probe in mode II. A typical plot of frequency shift when the probe is in contact with rubber-like materials is shown in Figure 6.16.

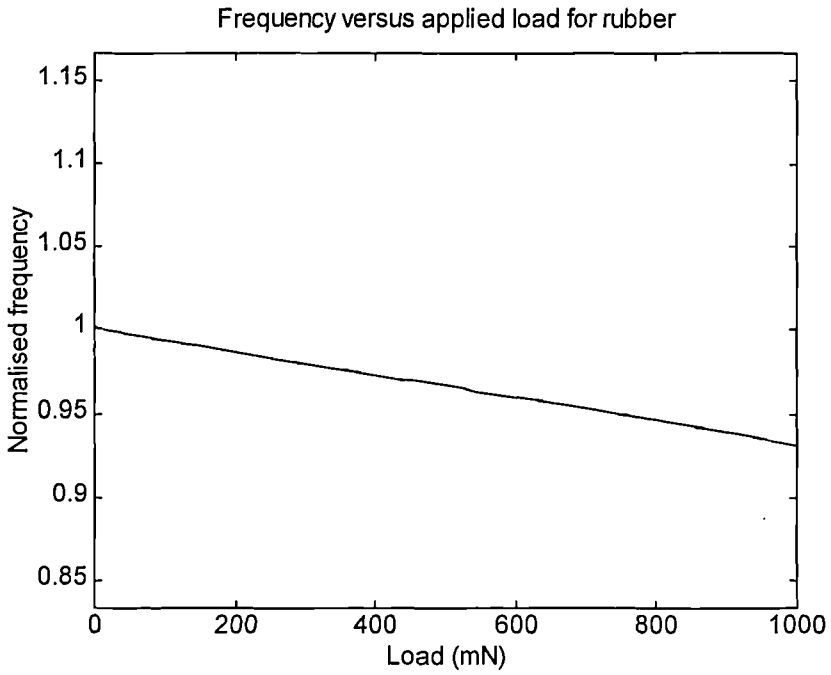

Figure 6.16. Typical plot showing frequency shift when probe contacts rubber-like materials

In the case of rubber-like materials there is an obvious decrease in resonant frequency. Referring to Figure 5.3, experimental results conform with the mathematical model. Such behaviour is, again, due to the relatively high density and low modulus of elasticity of the rubber.

In all the above experiments, it has been shown that the dynamics of the resonant probe sensor, as it approaches typical engineering surfaces, is subjected to a complex variety of forces leading to the observation of characteristic effects of added inertial, stiffness and damping forces. However, it has been shown that observation of dynamic characteristics on either side of resonant frequency of the probe can be used to identify the predominant effect. Also, the analysis of the experimental results in contact with solid surfaces and comparison with corresponding hardness scales could lead to potential applications in non-destructive hardness testing.

6.3. Probe application as 3D vector sensor

Section 6.2. has described potential applications of the new touch sensor regarding the observations of contact measurements between a sensor and a broad range of engineering surfaces. It was concluded that sensitivities of the probe were the same for each piezoelectric sensor - actuator pair along the axes of the probe but exhibited marked directional sensitivities when forces were applied radially. These, so called, directional sensitivities, led to the experimentation in order to investigate possibilities to reveal information related to both the magnitude of exerted pressure as well as the direction of approach. This would make a significant contribution in scanning and measuring applications as it would provide more accurate surface profile measurement and prediction of the workpiece orientation.

6.3.1. Instrumentation and experimental set up

To assess the interaction between the probe tip and the workpiece and possible directional sensitivities when contact force has a radial component a simple test rig was designed. Figure 6.17 shows its schematic representation together with the top view of the mechanical set-up.

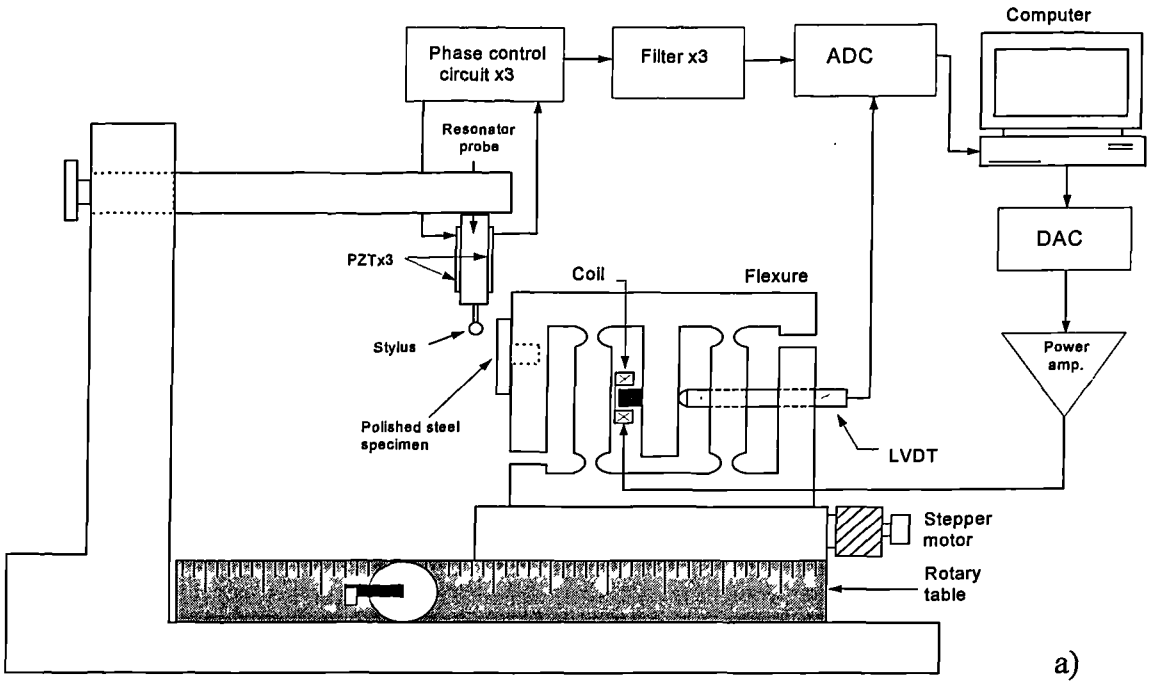

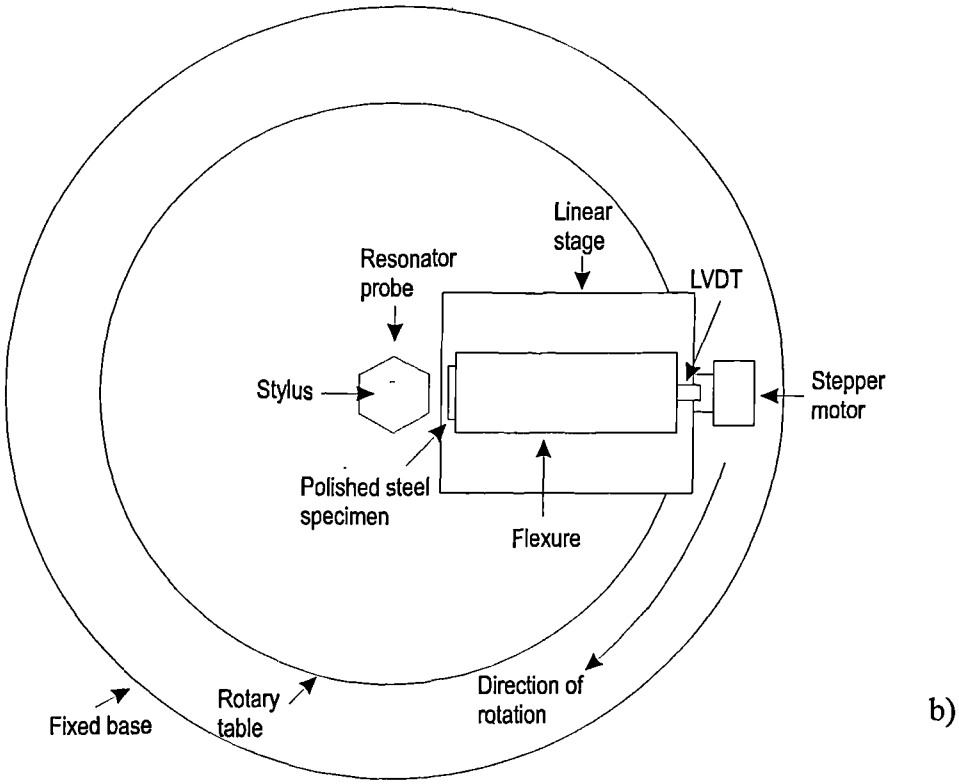

Figure 6.17. Schematic diagram of the test rig used to assess directional sensitivities when contact force between the probe and the workpiece had a radial component a) and top view of the test rig including the main mechanical components b). Drawings are not to scale.

The resonator touch probe was vertically mounted on a cantilever holder which was part of the assembly comprising a rotary table. Care was taken to ensure very rigid mounting of the probe in order to minimise influence of the stiffness at the mounting point. The probe was also centred along the axis of the rotation of the rotary table. In order to establish contact between the probe and workpiece a polished flat surface steel specimen was mounted onto the front side of the flexure mechanism. This linear flexure translation stage (flexure described in section 5.2.1.) was used for fine positioning of the specimen. Displacement of the flexure was continuously monitored by an LVDT. The flexure was mounted onto a linear stage and positioned in line with the probe tip. The flexure mechanism was in turn driven by a stepper motor for coarse adjustment in order to bring the specimen to very close proximity to the probe. Finally, the linear stage was assembled radially onto the rotary table with one degree resolution over full 360 degrees range. This allowed coarse angular positioning of the specimen relative to the probe tip.

In this set up all three piezoelectric sensor - actuator pairs (p_1-d_1, p_2-d_2 and p_3-d_3 in Figure 6.1) were used and their signals monitored; therefore three phase locked loop circuitry's (Chapter 4) were required. Analogue output signals from all three circuits were recorded as the probe was contacted from different radial directions against polished steel specimen. Simultaneously, the displacement of the flexure measured via an LVDT was also recorded. The system was controlled and data acquired using a PC 74 data acquisition card and program written in Turbo Pascal 7.0. Figure 6.18 shows a photograph of the system comprising of the three PLL circuitry's.

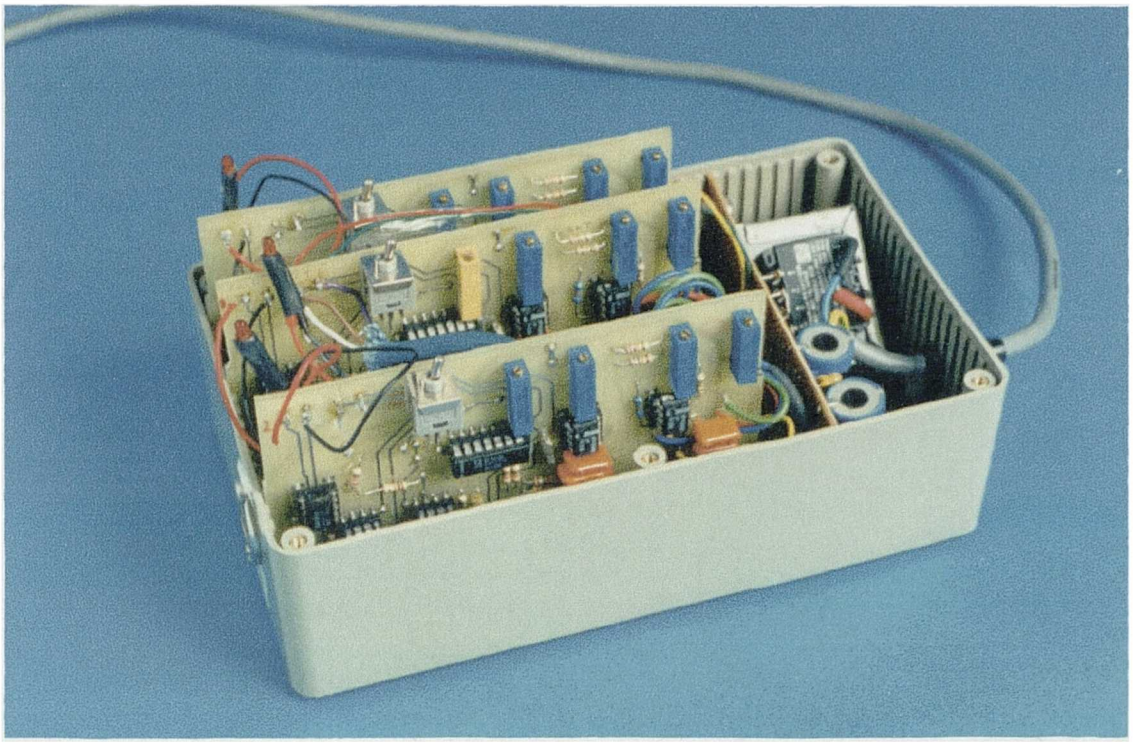

Figure 6.18. Photograph of the electronics comprising of three PLL circuits

6.3.2. Experimental method

Analysing a frequency spectrum of the touch sensor (Section 6.1, Figure 6.2) it was observed that its resonant frequency was about 38 kHz, while the other harmonics were recorded in regions of 56, 75, 96 and 120 kHz. The system exhibited different sensitivities at different harmonics, having the highest sensitivity at 38 kHz. A second harmonic at 56 kHz has already been successfully exploited (Section 6.2) which led to the conclusion that there was the possibility of tuning the sensor to different frequencies according to the application. Initial experiments using only one pair of PZT mechanisms showed that the probe exhibited some directional sensitivities when forces were applied radially. An idea had emerged that redesigning the shape of the probe, in the way described earlier in this chapter (Figure 6.1), would allow the application of the new sensor as a 3D vector probe in order to reveal the direction of the contact between the probe and the workpiece. Namely, positioning the three pairs

of the PZT drive - pick-up mechanisms in the way described, and tuning them at the different harmonics of the system, there was the possibility that each pick-up sensors would react differently and show different sensitivity to the force applied radialy to the probe tip. Also, there was an expectancy, based on previous tests, that output signals from each sensor will not only differ between each other but will also be very dependant on the angle of the contact approach itself. Applying contact force radialy from different angles, monitoring signal outputs from three pick-up sensors and comparing them could possibly be a way to reveal information related to the direction of the approach.

Tuning each sensor-actuator pair to a different harmonic was achieved using three PLL circuits and matching the free running frequencies of corresponding VCOs with these harmonics. Consequently, monitoring outputs from three pick-up sensors was again achieved by monitoring output voltage signals from the PLL circuits. Figure 6.19 represents the top view of the touch sensor showing the arrangement of piezoelectric plates and their position relative to the probe holder.

In order to bring a polished steel specimen in contact with the probe, the flexure was driven via a DAC and via an electro-magnetic actuator in 60 or 120 increments of 0.033 μm producing a total displacement of 2μm towards and away from the probe. The time delay between increments was 1s. Prior to each test, an angle of approach was set using the rotary table starting at the position marked 0 degrees on Figure 6.19, and than rotating clockwise in increments of 10 degrees or greater. The stepper motor was used for coarse positioning before and after each set of measurements was taken.

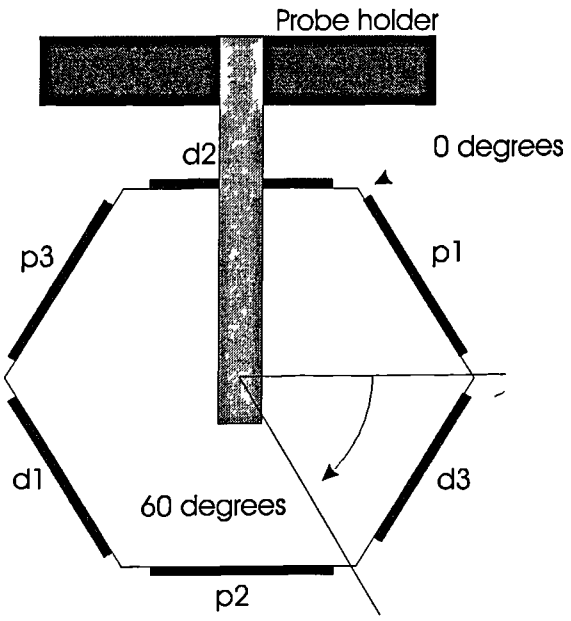

Figure 6.19. A top view of the touch probe showing arrangement of piezoelectric sensor -actuator pairs and their position relative to the probe holder

Setting the VCOs at different free running frequencies appeared to be time consuming due to the difficulties in controlling six variables: three different frequencies and three driving signals amplitudes. Any altering of the frequency at the same time alters the amplitude of the signal. Interference between signals was significant and it was almost impossible to achieve any stability when the probe was driven using all three drivers because of the way signals propagate and influence each other through the body of the probe. According to Benes *et al.* [94] in sensor applications of piezoelectric oscillators, the entire frequency spectrum usually has to be considered. This is because the influence of the measurand on different frequencies varies considerably. As a consequence, neighbouring resonance frequencies may cross each other with the changing measurement quantity. This causes mode coupling which may not only produces significant deviations from linearity, but sometimes even produces frequency jumps and activity dips in the frequency versus measurand curve. To overcome this problem, it was decided to use VCO output from only one PLL circuit to drive the system and to disconnect the other two, but still use three circuits

to detect three different pick up signals. The PZT driver 2 on Figure 6.19 was set to be active while 1 and 3 were passive. Disconnecting drivers 1 and 3 meant not using the VCO output of the PLL to drive the probe but having it set at an appropriate free running frequency and using the rest of the circuitry as per usual practice. It was experimentally found that the best stability, sensitivity and repeatability could be achieved if the VCOs of corresponding circuits were set far apart from each other using only odd harmonics [94]. The frequencies of circuits 1, 2 and 3 were set at 75.420 kHz, 40.115 kHz and 120.349 kHz, respectively. The PLL outputs were calibrated for each frequency, although that was not necessary since the voltage output can provide all the necessary information needed at this stage of the research.

6.3.3. Experimental results

Figure 6. 20 shows typical voltage outputs from the three PLL circuits at 0, 160 and 240 degrees, respectively relative to the 0 degrees position.

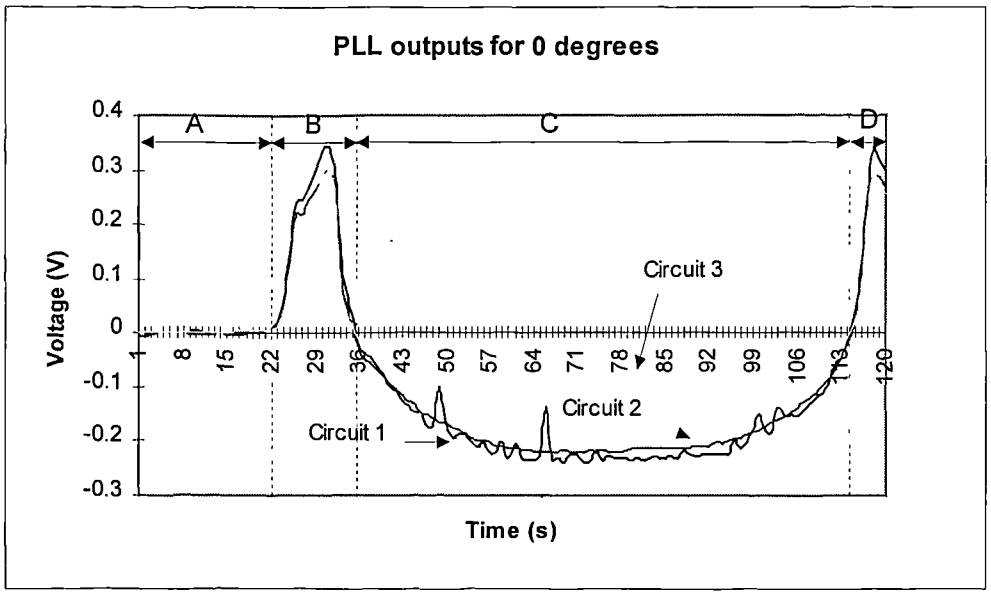

a)

Figure 6.20. Typical plot of PLL voltage outputs for circuits 1, 2 and 3 at a)0 degrees, b) 160 degrees and c) 240 degrees relative to the 0 position.

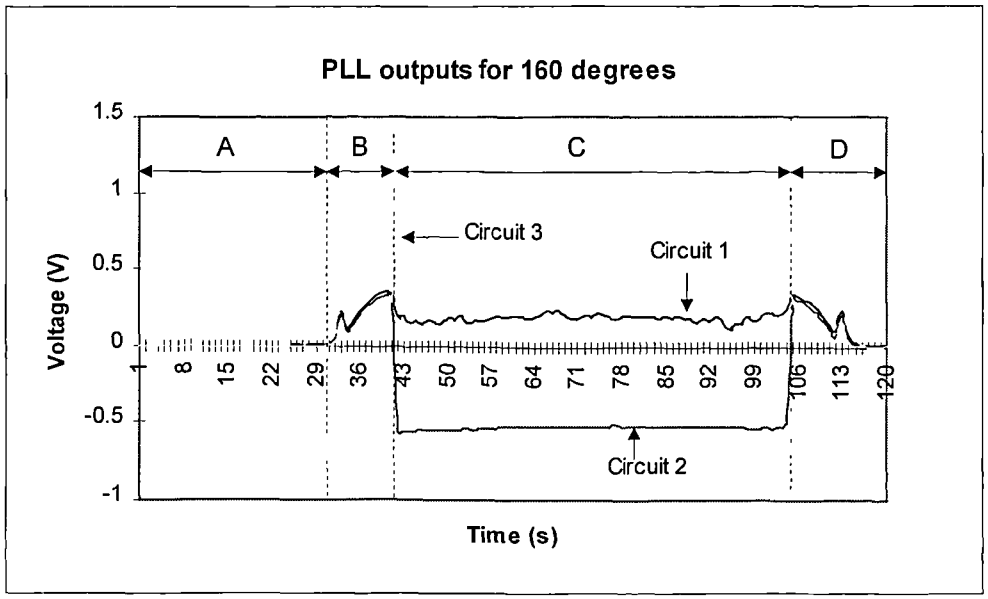

b)

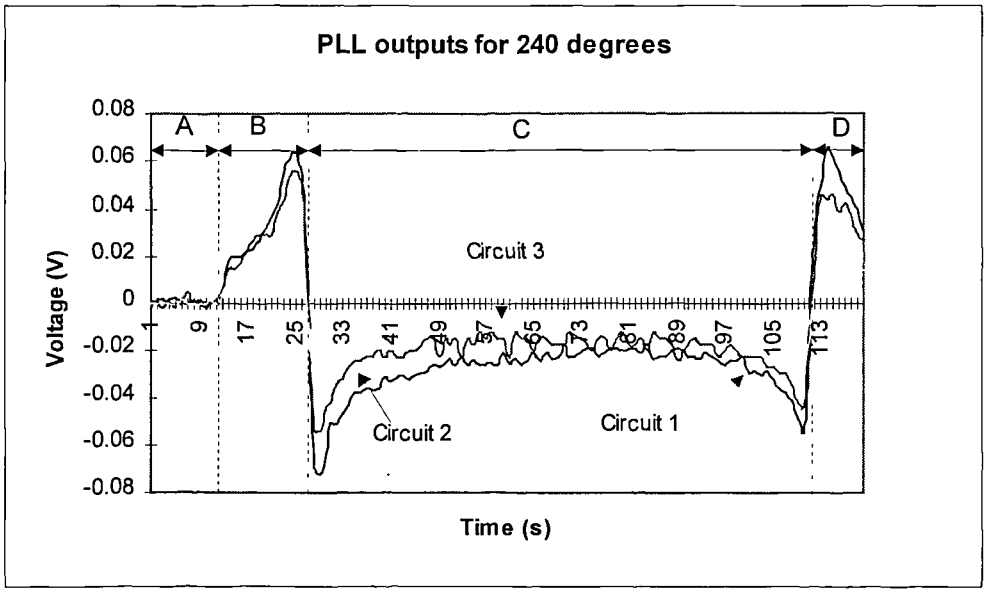

c)

Figure 6.20. (Continued) Typical plot of PLL voltage outputs for circuits 1, 2 and 3 at a)0 degrees, b) 160 degrees and c) 240 degrees relative to the 0 position.

From the above figure it is clear that the three PZT pick-up sensors respond differently with different sensitivity at different angles of approach. Moreover, the system exhibits an interesting behaviour regarding the load applied while contact

takes place and distinguishing regions are labelled on the above graphs. Section A represents the start of measurements during which the specimen is driven via the flexure towards the probe but not in contact with it. Section B shows a period during which probe is in contact with the steel specimen and exhibits changes in resonance frequency (voltage) due to the increase in flexure displacement and therefore an increase in radial force applied to the probe tip. During this time some jumps in frequency occur because of the coupling [94]. Region C is the region of saturation were the probe is in solid contact with the specimen with maximum load of 88.5 mN and and maximum indentation of 1.5 μm. Frequencies (voltages) settle on certain values until the moment of the probe retracting (Region D) when they exhibit behaviour symmetrical to the one in region B.

To assess the system behaviour around a full probing plane of 360 degrees a set of experiments was conducted using the above described test rig and taking a measurement in increments of 30 degrees, at first instance, starting from the relative zero position. Figure 6.21 shows typical plots of voltage outputs from three PLL circuits at various angles of radial contact. Plots are shown for two different amounts of probe indentation into the specimen's surface of 0.7 and 1.5 μm which could be in turn related to the applied force of 41.3 and 88.5 mN, respectively.

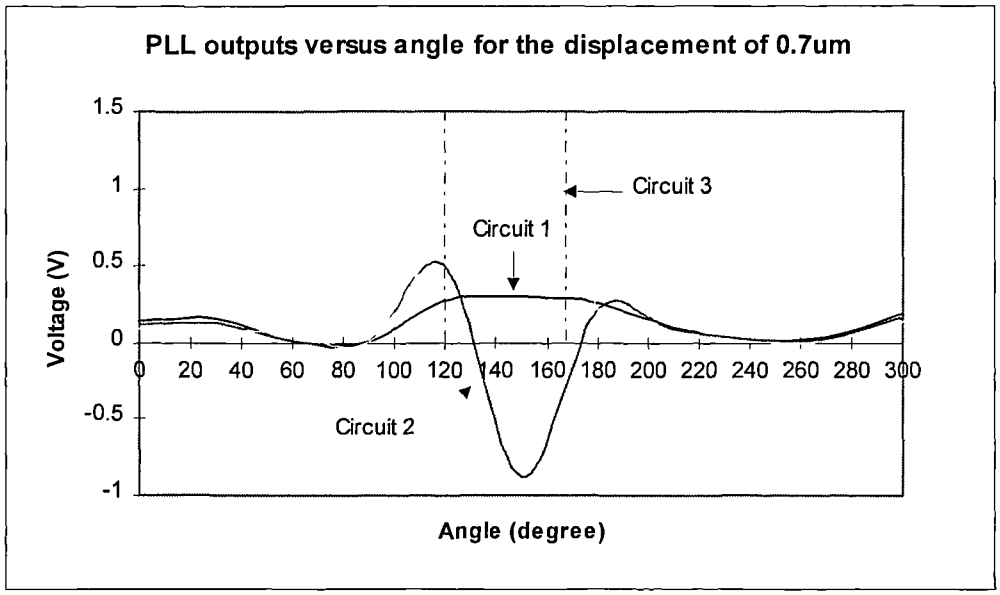

a)

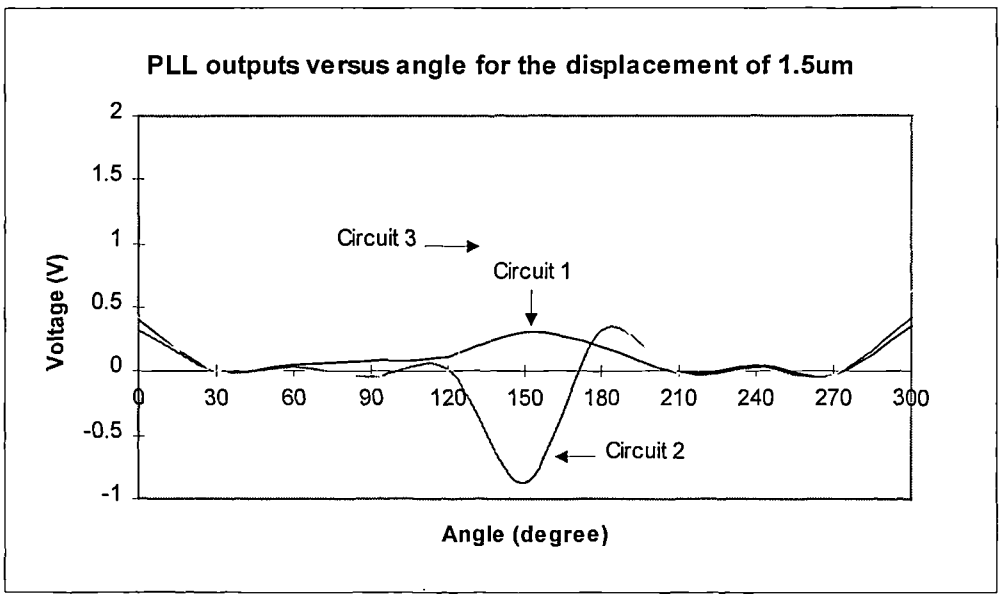

b)

Figure 6.21. Typical plots of voltage outputs from three PLL circuits against the angle of radial contact for the probe indentation of a) 0.7μm and b) 1.5μm.

Figure 6.21 shows variation of frequency shift as a function of angular approach for all three pick up sensors when the probe is contacted radialy within a full circle in increments of 30 degrees. It is apparent that the system exhibits the maximum sensitivity between 100 and 200 degrees and least sensitivity within regions around 90

and 240 degrees. A slight difference in the response of the system to the applied forces of 41.3 and 88.5 mN could be observed but the actual trend is very similar and once in firm contact (contact force of about 60 mN or greater) the probe has the same response regardless of the force applied. To give a better vision of how this compares with the relative position of the probe, Figure 6.22 shows Figure 6.21 a) presented in a form of radar chart (a) alongside with the top view of the probe (b).

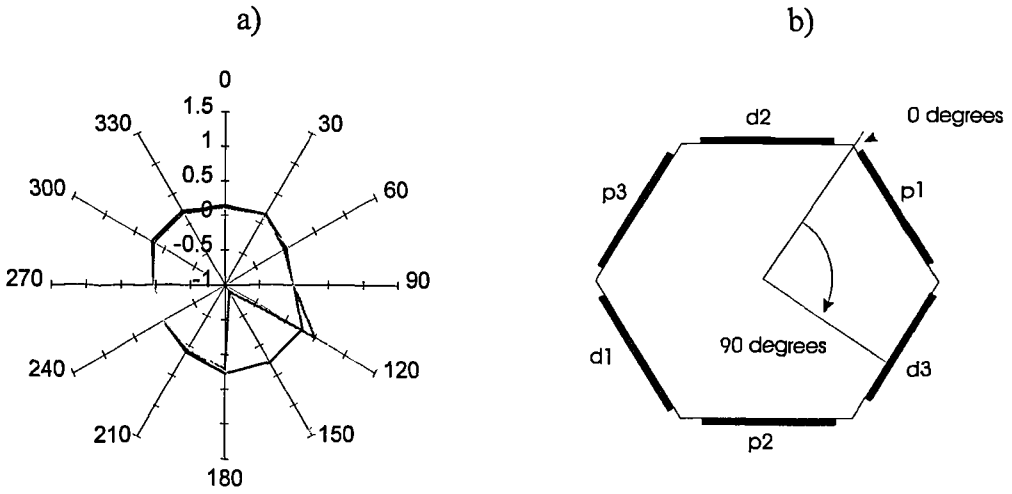

Figure 6.22. a) Radar chart presentation of voltage outputs from three PLL circuits against angle of radial contact; **b)** a top view of the touch probe and relative 0 degrees starting measurement position

The sensors exhibit the highest sensitivity when probe is radialy contacted from the direction directly opposite to the active PZT actuator which is expected because of signal propagation from the driver through the body of the probe. There is an increase in sensitivity in region between 0 and 300 degrees which is most likely because of the close proximity of the active driver. Although there is a high sensitivity in the middle of the range examined there is no symmetry involved, which in a way acts in the favour of the argument to reveal useful information regarding the direction of the approach. Analysing Figure 6.21 it is clear that each direction of approach has its

own, corresponding unique combination of three output signals from three pick-up sensors. It is possible to find two or more angles of approach where response of one sensor has the same values, but at the same time combination of all three of them is different at these points. For example at the approach angles of 120 and 167 degrees (Figure 6.21), the output voltage of sensor 3 is registered as 0.8 V. For the same directions of approach of 120 and 167 degrees sensor 2 has outputs of 0.5 V and -0.25 V, respectively, while the values for sensor 1 were 0.28 V and 0.3 V at these two points. Therefore the combination of three output signals for the angle of approach of 120 degrees is (0.28 V, 0.5 V, 0.8 V) while the combination for 167 degrees is (0.3 V, -0.25 V, 0.8 V). It is apparent that these two points have their own unique signal combinations regardless of the fact that one of the sensors had the same output values in both cases. The same analysis can be applied for any angle, and such method could give enough information to reveal the direction of approach.

The above discussion is valid within a range of a full circle but for an increment of 30 degrees. In order to examine the angular sensitivity of the system, similar tests were conducted but with smaller angular increments. The area of interest was the range between 90 and 210 degrees where the sensors exhibited highest sensitivity. Within this range, measurements were taken in increments of 10 degrees while in the two other areas, between 0 and 90 degrees and 210 and 300 degrees, signals were recorded in increments of 30 degrees. Figure 6.23 shows a typical plot of voltage outputs from the three PLL circuits versus the angular contact.

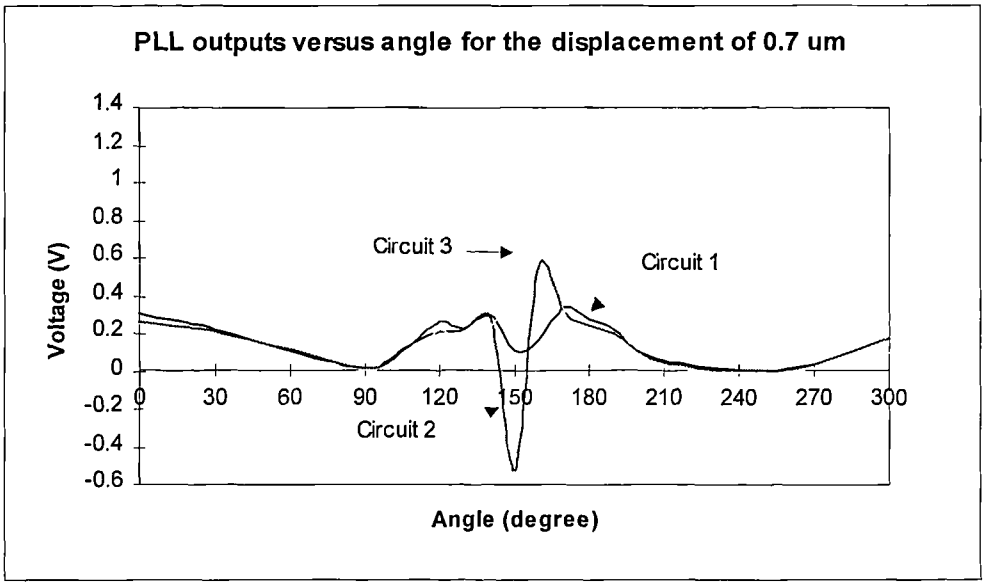

Figure 6.23. Typical plot of voltage outputs from three PLL circuits against angle of radial contact for the indentation of 0.7μm

Comparison between Figure 6.23 and Figure 6.21 a) shows that the main difference exists in the region between 90 and 210 degrees. Taking measurements in smaller increments of 10 degrees allowed more information to be revealed in this more sensitive area. It could be noticed that there are slight changes in frequency variation around approach angles of 130 and 180 degrees compared to the one on Figure 6.21 a). All three sensors show reduced sensitivity in these regions. Figure 6.22 b) indicates that these two areas are aligned with two sharp 60 degrees angles of the hexagonal body of the probe. This reduced sensitivity in these regions is to be expected bearing in mind that the sensors, being made out of piezoelectric material, have a sensitivity that is directly related to the stress distribution of the system. Referring to the Figure 6.1 and observing the position of pick-up sensors it can be predicted that they will exhibit the lowest sensitivity when the stylus is contacted from the direction which is in line with the area between two PZT plates.

The same conclusion about the unique combination of the three sensor outputs at any direction of approach is also applicable for Figure 6.23. In order to specify the

angular sensitivity of the probe a small section of 20 degrees has been extracted out of the whole angular approach range of 360 degrees. Figure 6.24 shows the fragment between 130 and 150 degrees which coincides with the area of reduced sensitivity around 130 and the area of high sensitivity around 150 degrees. As it was stated above, measurements within this region were taken in increments of 10 degrees. From the Figure 6.24 it is apparent that the angular sensitivity of the new resonant probe is much higher then this incremental value. Namely, applying the method of interpolation in the area between 140 and 150 degrees the unique combination of three output signals can be clearly discriminated for each 0.5 degrees of angular approach, thus setting the angular sensitivity of the probe to at least 0.5 degrees. In the region around 130 degrees, this sensitivity is significantly reduced to about 2 degrees. Applying the same interpolation method in the rest of the full circle range, the angular sensitivity of the new probe could be estimated at about 0.5 degrees in the high sensitivity area around 150 degrees and at about 2 degrees in the rest of the region. It has to be emphasised that these are just approximations of angular sensitivity and that only one plane of contact was considered in this first instance of research.

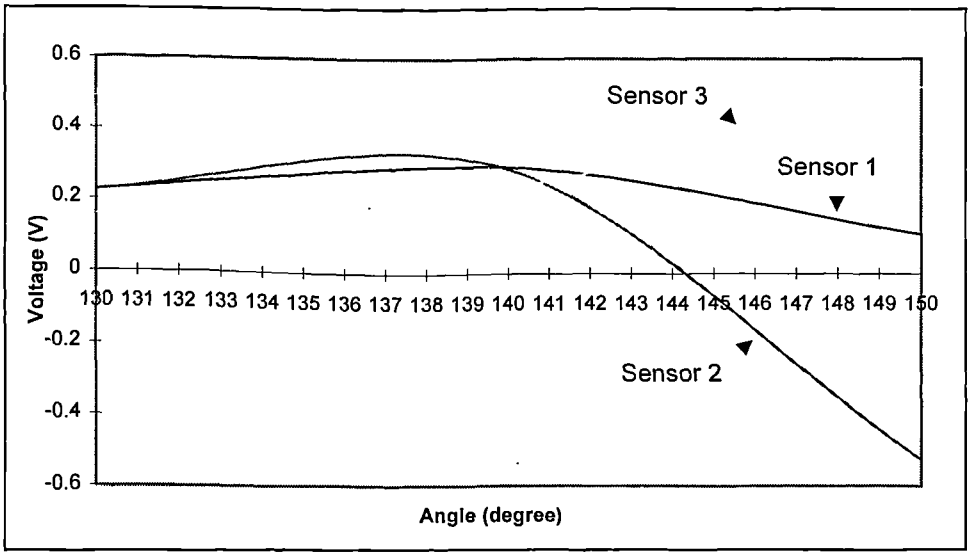

Figure 6.24. Typical plot of voltage outputs from three pick-up sensors for angular approach between 130 and 150 degrees.

How could the above results be implemented in the practical application of the new resonant sensor as a vector probe? Firstly, the probe would be contacted by a specimen of a specific material in increments of two or more degrees around a full probing plane of 360 degrees and results from three pick-up sensors stored in an appropriate form (i.e. look-up table, voltage -angle graph etc.). When the probe is contacted from an unknown direction of approach, measurement would be recorded and compared with the stored results until the nearest combination is found. In the case where measured values lie between two stored contact angles, a method of interpolation could be employed to determine the nearest direction of approach.

The preliminary experiments in exploring the possible application of the new touch sensor as a vector probe in order to detect position and direction of approach have proven to be feasible, although refinement of this work is necessary. The validity of the above results covering one plane of contact has to be checked and confirmed in other probing planes. Also, reduced sensitivity in certain regions of the range has to be improved significantly, having the driver in such a position that would avoid undesirable coupling. An idea which may occur from above results is to have an actuator of tubular shape centred inside the body of the probe which would maintain uniform signal propagation in all directions. It has to be mentioned that such alterations in the design are unlikely to affect employment of the probe in contact measurements discussed in section 6.2. The use of three circuits has been proven to be very appropriate in the proposed vector probe application allowing comparison between output signals from three separate sensors. An adequate algorithm could be developed to execute storage of contact combinations of sensors outputs around the full probing plane. The same algorithm could also be further expanded to carry out comparisons between unknown contact combinations and stored results in order to retrieve information regarding the position and direction of approach. One of the obvious possibilities would be to use a neural network algorithm or generic algorithm. Further refinement of this work including the development of adequate software could

lead to the design of an instrument which could make a significant contribution in measuring applications.

6.4. Performance evaluations of the resonant sensor as a touch trigger probe

Sections 6.2 and 6.3 discussed redesign of the touch trigger probe, proposed in Chapter 5, and its possible applications in the observation of contact measurements and as a vector probe in detecting position and direction of approach. To explore further the versatility of such a probe some characterisation measurements were conducted on a coordinate measuring (CMM) machine. These measurements had a purpose to investigate the sensitivity of the probe to touch (when only a marginal force was applied) in all directions and pre-travel variation of the probe. It was also necessary to compare performance of the new sensor design with a commercially available probe. Tests were conducted on a KEMCO E600 CNC CMM (600×500×500 mm) machine. The probe used for comparison purposes was a Renishaw TP6. The measurements included calibration of the new probe using a Renishaw 4mm stylus, measuring of diameter and coordinates of a 25.4mm calibration ball and recording the coordinates and inside diameter of a master ring gauge. Also, part of the solid marble surface of the CMM was scanned using both the new sensor and TP6 probe and accuracy in z direction was compared.

6.4.1. Measurement results

6.4.1.1. Probe calibration

The first set of measurements was conducted to calibrate the new probe using a Renishaw 4mm stylus tip. The probe was mounted onto Renishaw's TP1 probe head to ensure a kinematic mounting. Calibration was carried out against a 25.4mm

calibration ball using KEMCO PC-3D (V 3.00) measuring software. Five points were probed around the sphere to cover the largest possible area (Figure 6.25).

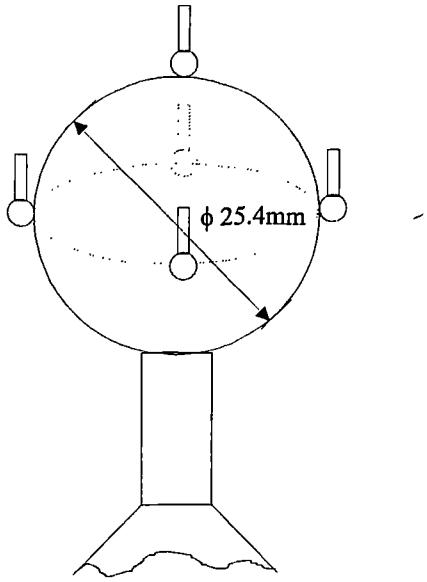

Figure 6.25. Calibration of the new resonance based touch sensor

One PLL circuit (Chapter 4) was used to detect triggering points while the working frequency of the probe was set at 39.001 kHz. The value was set just above the resonant frequency (on the slope of the peak) in order to slightly reduce the very high sensitivity which tends to bring the probe into saturation when contacted with the metal surface of the calibration sphere. For reasons of simplicity (refer to the section 6.1 of this Chapter) and easier monitoring and analysing measurements, only one driving-pick up piezoelectric pair (d_1-p_1) was used. Moreover, due to the high sensitivity, the travelling speed of the CMM between measuring points was restricted to 20 mm/s. The measuring speed, which is the speed that probe moves at just before probing takes place is recommended by CMM manufacturers to be relatively small to maintain accuracy. Renishaw recommends a value of 8 mm/s as a maximum for their probes and for new resonator probe this value was set at 2 mm/s. Calibration of the probe was performed a number of times and Table 6.2 shows some of the results

alongside the error of form and the error for each of five points taken during calibration.

Probe diameter (mm)	The error of the form (mm)	Error for each point (mm)
4.0048	0.004	01) -0.002 02) +0.000 03) -0.000 04) -0.000 05) +0.002
3.9929	0.001	01) +0.000 02) -0.001 03) +0.000 04) -0.000 05) +0.001
3.9982	0.001	01) -0.000 02) +0.000 03) -0.000 04) +0.000 05) -0.000

Table 6.2. Calibration results for the new probe using Renishaw 4mm diameter stylus as a probe tip

Using the above calibration results, the probe was engaged in measuring diameter and coordinates of a 25.4mm calibration ball. The speed of the CMM and the measuring speed were kept as set during calibration. In order to measure the sphere, the KEMCO PC-3D software prompts for 5 contact points, but this could be changed to a maximum of 99 points. Table 6.3 shows some of the results obtained when the sphere was probed 5 and 9 times. The points were spread as far apart as possible.

Sphere diameter (mm)	The error of the form (mm)	Error for each point (mm)
25.388	0.005	01) -0.000 02) -0.002 03) +0.002 04) -0.002 05) +0.002
25.392	0.003	01) +0.000 02) +0.002 03) -0.001 04) +0.001 05) -0.002
25.396	0.010	01) -0.000 02) -0.002 03) +0.006 04) -0.004 05) -0.000 06) -0.000 07) +0.002 08) -0.002 09) +0.001

Table 6.3. Measurement results on 25.4 diameter sphere using the new touch sensor

From the above two tables it could be observed that the new touch probe exhibits high accuracy, favourably comparable to the commercially available probes (TP6). The measurement errors were well within the resolution of the CMM (±5μm).

6.4.1.2. Pre-travel variation in X-Y probing plane

A set of measurements was conducted in order to observe variation in pre-travel of the new probe in X-Y plane. This, so called lobing effect depends on the direction of probing and it is caused by variations in triggering force (Sections 2.2.8). A master ring gauge with a diameter of 38.1mm (1.5 inch) and the same set up shown in Figure 4.13 was used for these purposes. The method was adopted in order to obtain maximum pre-travel variation and was based on obtaining a number of points along the circle by probing radially the inside surface of the master ring gauge. For the given set of points a best-fit circle could be found. Calculating the radius for each

point and comparing it to the radius of the best-fit circle the range of pre-travel variation can be found.

During the measurements, the inside surface of the ring gauge was probed a number of times ranging from 18 to 32 points. This obtained enough data to determine the best-fit circle with its radius R and centre (X0, Y0). Figure 6.26 shows measurement points together with the mathematically determined best-fit circle.

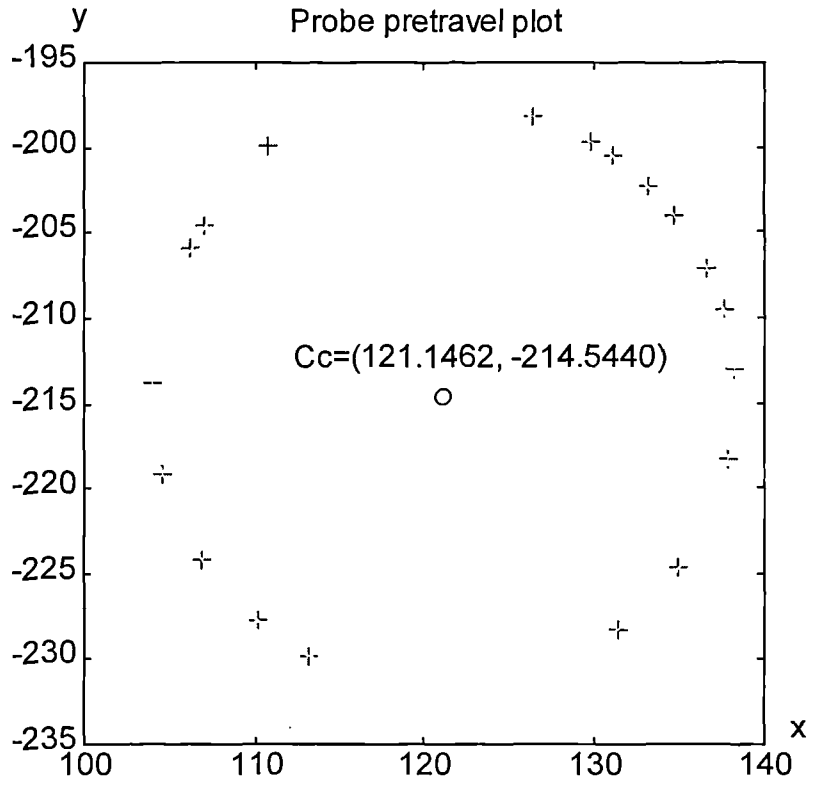

Figure 6.26. Typical pre-travel plot showing points measured along the inside surface of the master ring gauge (+) and calculated best-fit circle (full line). Scale in mm.

A Brute Force Approach was used to fit a circle through a given number of points. The concept of this approach is to minimise by least squares the root-mean-squared error of the radius in the equation for a circle (Appendix G). A simple Matlab

program was written to implement this idea. As a result it was found that the radius of the best fit circle was in the range of 17.19 to 17.20 mm. It has to be noted that CMM measuring software was not used to calculate the diameter of the circle and therefore the 4mm diameter of the probe was not taken into account to compensate for. In the particular case shown on the Figure 6.26 best fit circle had the centre at X0 = 121.1462, Y0 = -214.5440 with the radius R = 17.1917 mm. Calculating the radius, r, for each point and comparing it to the value of R it could be observed that there are four regions roughly 90 degrees apart in a 360 degrees probing plane where the probe exhibits different pre-travel variation. Assuming that 0 degrees region is the region alongside the active PZT driver and 180 degrees region alongside the corresponding PZT pick up sensor (Figure 6.27 a) calculated square values for (r - R) within these areas are in the range of 0.01 μm to 0.5 μm. Regions around 90 and 270 degrees, relative to the 0 degrees, are regions of increased triggering force. The pre-travel variations within these areas are increased with the square values of (r - R) in range of 1 μm to 3.5 μm.

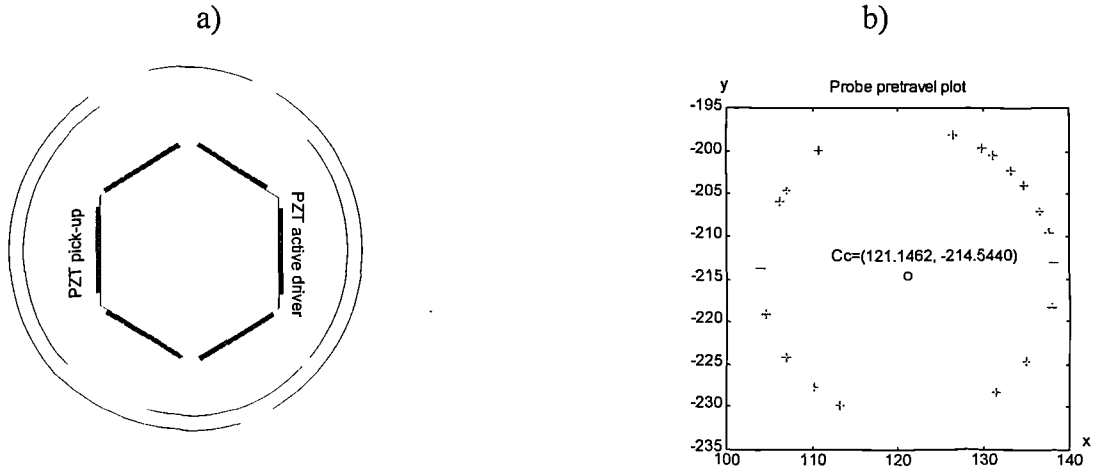

Figure 6.27. a) A top view of the touch probe and its position relative to the ring gauge (not to scale); **b)** pre-travel plot showing points measured along the inside surface of the master ring gauge

The lower sensitivity within the regions of 90 and 270 degrees (relative to the 0 position) and therefore increased triggering force were expected because of the shape

of the new sensor and the arrangement of piezoelectric plates. These regions align with two 60 degrees angles of the probe's hexagonal shape and, as it was stated in Section 6.3.3, it is predictable that the pick-up sensor will exhibit lowest sensitivity when the stylus is contacted from the direction which is in line with the area between two PZT plates. Although the new probe exhibits some pre-travel variations it is possible to reduce the errors by changing the position of piezoelectric actuator. Again, probably the most suitable solutions could be to have a tubular actuator centred inside the body of the probe

6.4.1.3. Accuracy of the probe in Z direction

The above measurements have been conducted in order to observe variation in pre-travel of the new probe in X-Y direction within a 360 degrees probing plane. To examine the accuracy of the probe in the Z direction, a simple program was written for the CMM to digitise the square segment of the marble surface. The measurements were repeated several times. 79 points were taken within the marked square area and for comparison reasons, the same measurements were conducted using the Renishaw TP6 probe. Figure 6.28 shows typical measurement results using the TP6 a) and new touch probe b).

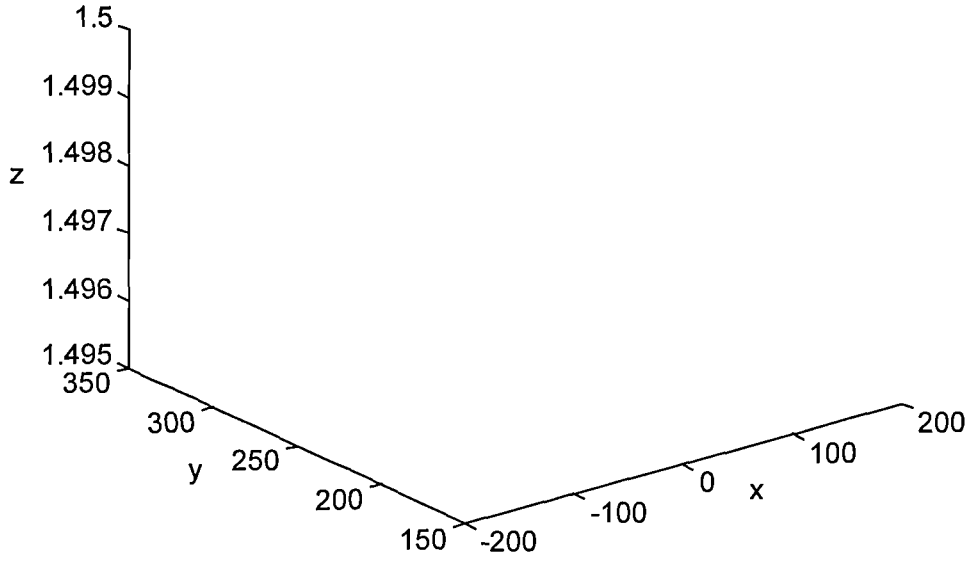

a)

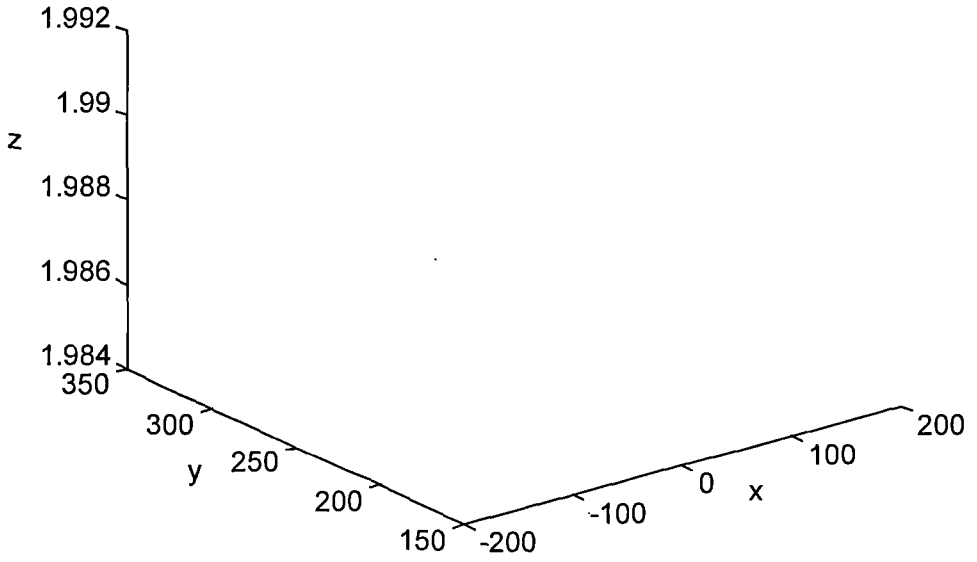

b)

Figure 6.28. Typical results of digitising the marked square area using **a)** Renishaw's TP6 probe and **b)** using new touch sensor (all dimensions are in mm)

The number of measurements performed on the marked square area using a Renishaw touch trigger probe, have shown that TP6 has an accuracy in the Z direction between 4 and 5μm while the accuracy of the new tactile sensor was between 4 and 7μm.

6.4.1.4. Pre-travel variation in X-Y-Z probing plane

The measurements performed to observe variation in pre-travel of the new probe in the X-Y plane and accuracy in Z direction have shown the good performance of the new resonant sensor as a touch trigger probe. It has to be noted that, during all tests, either a vertical or radial component of the force was applied to the probe tip but not the combination thereof. Therefore a final set of measurements on the CMM was performed on the 50.8 mm (1.5 inch) precision metal sphere in order to observe overall accuracy and variation in pre-travel of the new tactile probe in X-Y-Z probing plane. Measurements were taken manually and the surface was probed at 118 points forming five concentric circles around the top hemisphere of the ball. Points around the middle of the sphere, forming the first circle, were recorded with fixed z axis. Prior to each successive measurement the probe was slightly moved in z the direction, the z axis fixed again and the sphere probed along the next concentric circle. Figure 6.29 shows a typical test result together with five best fit concentric circles through the set of recorded points.

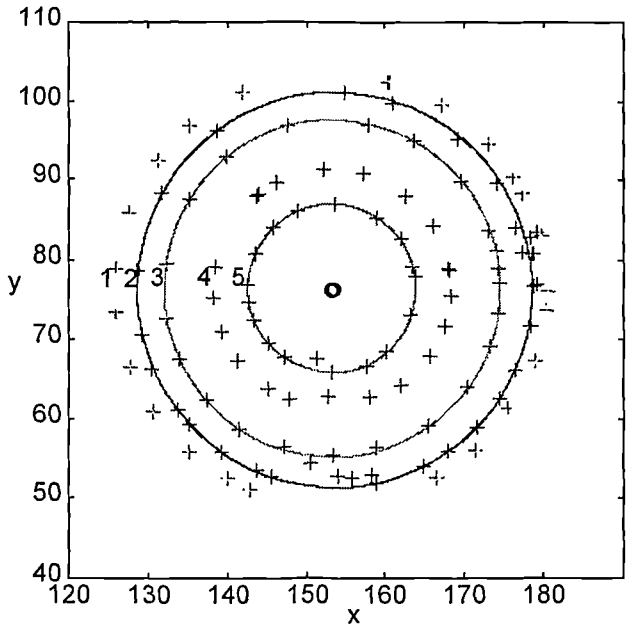

Figure 6.29. Typical plot showing X-Y coordinates of the points measured around the top hemisphere of the calibration ball (+) and calculated best-fit circles (full line). Scale in mm.

As was described above, points along each concentric circle were taken with locked movement in Z direction. Although, theoretically Z dimension was constant, the CMM introduced an error which could not be neglected especially around larger circles. The error introduced in the Z direction between the first and last point taken along the circle 1 was 4.117 mm; along the circle 2 - 3.333 mm; along the circle 3 - 0.209 mm; along the circle 4 - 0.078 mm; and finally along the circle 5 it was 0 mm. The error in the z direction had a large influence on the calculation of variation in pre-travel of the new probe in X-Y-Z probing plane. As the error in the Z direction increases from 0.078mm to 4.117mm calculated maximum variation in pre-travel also increases from 9.3μm to 563.9μm which cannot be accepted as an accurate value. Bearing in mind the error in the Z dimension, the points were not actually taken along the circle but along the helix, therefore the best-fit circle approach could not be accurately applied. Only for the circle 5, where such error was non-existent, variation in pre-travel could be determined and calculated, square values for (r - R) were in the

range from 0 to 0.8μm with an exception of two points with the values of 3.8μm and 2.3235mm. Figure 6.29 shows X-Y coordinates of the points measured around the top hemisphere of the calibration ball and best fitted circles through them. This figure does not represent actual pre-travel variation because of the induced error in the z direction. However, the area of increased triggering force is evident (triangular area delineated by the centre of the sphere and by the points between 140 and 160 mm on the x axis). Again it is aligned with the 60 degrees angle of the probe's hexagonal shape. Expected second area of reduced sensitivity which usually appears parallel with the first one, in this case coincides with the region of increased error in z direction and therefore it becomes very difficult to identify.

Points obtained during the measurements on the 50.8mm calibration ball were imported into Surfacer software (Imageware, USA) in order to determine the best-fit sphere through the given number of points. Figure 6.30 shows a 2D presentation of a typical result with a colour plot representation of deviations from the best fit values. Points in the largest area (green) have deviations from the best fit value between 2 and 20 μm. Two (yellow) areas have deviations between 50 and 75 μm, while four points in the area of increased triggering force (blue) have deviations up to 750 μm.

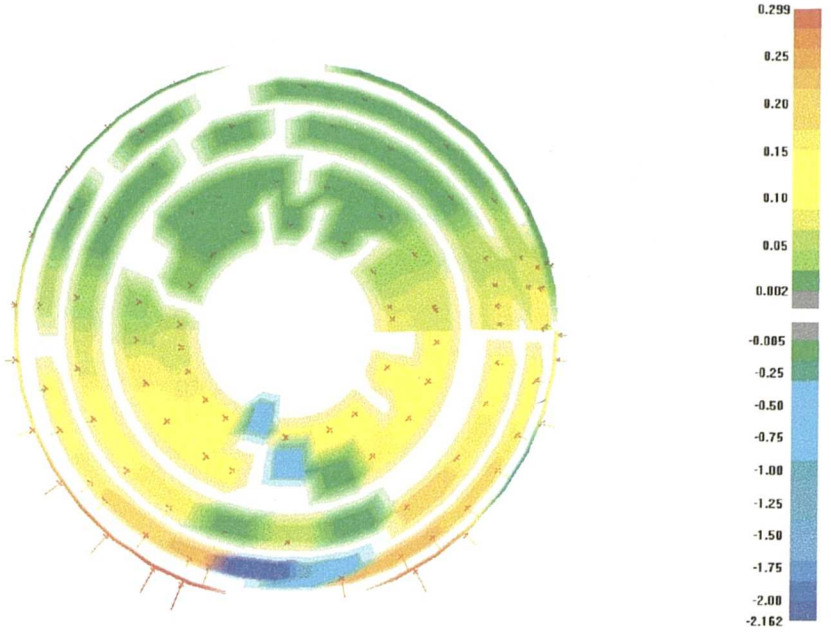

Figure 6.30. Schematic of a three-dimensional probe performance test to determine pre-travel variation measuring a 50.8mm precision sphere (values for deviations are in mm).

All the above measurements, conducted on the CMM machine, have shown good accuracy of the new sensor determining its possible use in coordinate metrology applications. The accuracy of the probe in the Z direction in the range of 4 μm could also suggest its utilisation as a digitising and furthermore scanning probe. Exploration of variation in pre-travel of the new probe has been shown as very promising, although areas of increased triggering force still exist in a regions of 90 and 270 degrees in a 360 degrees probing plane (Figure 6.25 and 6.30) with a maximum square value for (r - R) of 3.5μm. This 'lobing' effect could be eliminated re-arranging the position and orientation of piezoelectric elements, especially the piezoelectric actuator. Refinement of the present work could lead to the development of a very competitive multipurpose tactile probe.

6.5. Proposed application of the new resonator probe as a profilometer instrument

The possible application of the new resonator based probe developed at Coventry University has been exploited by Harb [148] at Precision Engineering Laboratory at UNC Charlotte, North Carolina proposing a simple 2-dimensional resonator profilometer. The resonator probe is used to monitor the interfacial forces between the stylus and a surface specimen along the z-axis by providing a feedback error signal into a digital piezoelectric translator (DPT) in order to maintain constant contact force. The scanned specimen is slid beneath the probe using high precision single degree of freedom polymer bearing slideways. As the specimen slides, the probe moves along the vertical axis in order to maintain a constant force.

6.5.1. Instrumentation and experimental set up

The proposed profilometer instrument is based on the initial design of a tactile sensitive probe originally designed for coordinate measuring machines (Chapter 4) [121,122]. It consists of an aluminium rod of rectangular shape oscillated using a pair of piezoelectric plates, one drive and one pick-up sensor mechanisms cemented on the opposite sides of the beam. The 4 mm ruby ball was replaced with a standard 2μm diamond tip stylus screwed into the free end of the rectangular rod.

The same PLL circuitry described in Chapter 4 (Figure 4.7) was used to oscillate the probe at its resonance frequency and monitor the frequency shift as the result of interfacial force variations. During these experiments, the phase shift between the drive and the strain signal was set near -90 degrees. As contact takes place change in resonance frequency occurs shifting the phase angle from its present value. Automatically the analog PLL NE 565 IC adjusts the driving signal frequency to null the change producing a proportional error signal with a conversion constant of

0.73mV/Hz. A typical relationship between the PLL output and interaction force of the probe/sample was shown on Figure 4.9.

Figure 6.31 shows a schematic representation of the proposed resonator profilometer set up.

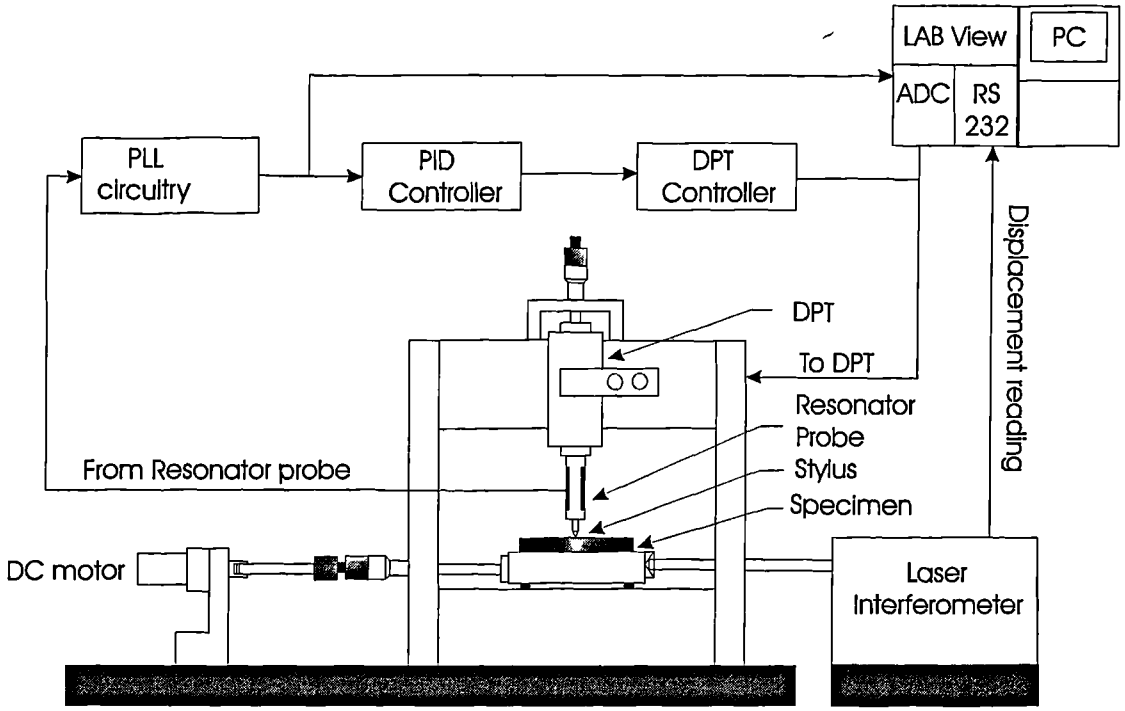

Figure 6.31. Schematic diagram of the resonator profilometer

The complete resonator has been mounted to the z translator, the underside of a vertical piezoelectric translator (QueensGate Instruments model S300 digital piezoelectric translator, DPT), the holder of which forms part of a z-axis coarse positioner. DPT consists of tubular piezoelectric actuator with a capacitance sensor along the central axis to monitor actual extension. The DPT translator has a linear extension range of 15μm with noise level of 0.6 nm rms at bandwidth of 1100Hz. The z axis was mounted into a rigid fixed bridge above a horizontal slideway.

The specimen was scanned beneath the probe using a high precision glass-ceramic (Zerodur) polymer bearing slideway. The carriage is actuated by a DC motor through a transmission system consisting of a micrometer and hysteretic coupling. Horizontal displacement of the carriage was monitored using a Michelson based laser interferometer system.

To obtain a trace of the surface, the specimen was secured onto an aluminium carriage, and then aligned parallel to the slideway surface using an angular adjustment mechanism attached to the carriage. The probe is then brought into close contact with the surface until the PLL output registers a value corresponding to the static force at which the control loop is closed. The height and physical properties such as elastic modulus and density variations of a surface create interfacial force variations affecting the dynamic characteristics of the probe and causing a shift in its resonant frequency (Chapters 4 and section 6.2 in Chapter 6). The shift is detected by the PLL which produces an output voltage proportional to the surface profile and variations in some of its physical properties. After being filtered and amplified this signal is fed into a proportional-integrator-differentiator (PID) controller. As the carriage moves, at approximately 1mm/sec, the PID error signal is then in turn fed into the DPT to maintain the interfacial force between the stylus tip and specimen at a fairly constant level (the set static force). The PID error signals are recorded into an IBM-compatible PC, via an ADC data acquisition board. The readings of the laser interferometer system were recorded via a standard RS232 interface. The system was controlled and data recorded via the LabVEW software (National Instruments) while the analysing of the data was facilitated using the Microsoft Excel application program.

6.5.2. Performance and experimental results

Traces over reasonably flat engineering surfaces ranging from ground and lapped steel to flat glass and silicon surfaces, some partially coated with aluminium and gold were tested and analysed.

Figure 6.32 shows a typical resonator profile over a scratched glass microscope slide surface. In this more than eight traces in uni-direction were recorded over the same line and the results were fairly consistent and reproducible.

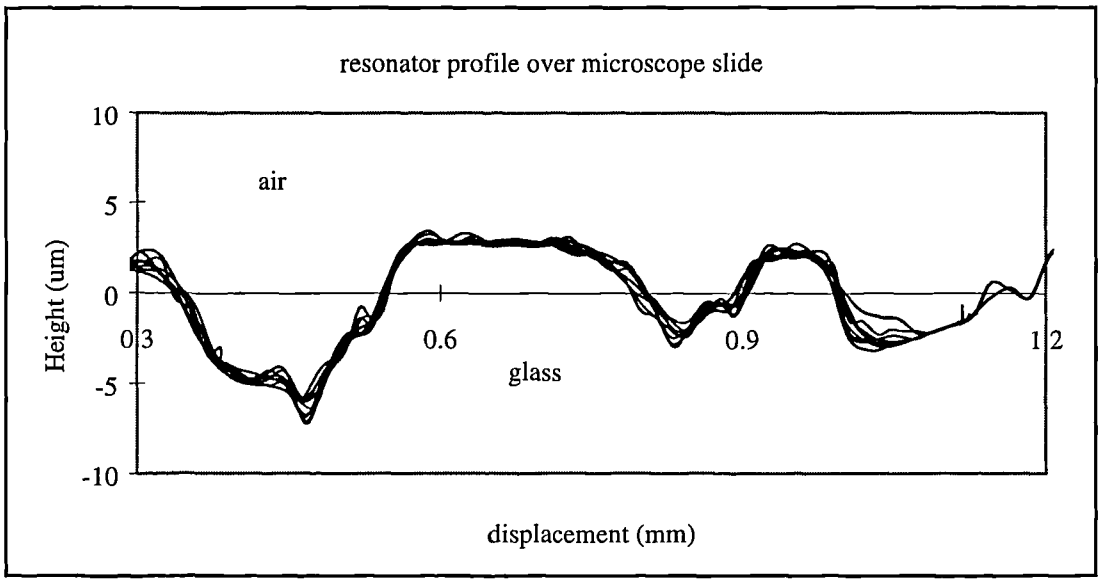

Figure 6.32. Typical traces over scratched microscope slide glass surface

Figure 6.33 shows a typical resonator profiles over a microscopic slide partially coated with thin film of aluminium, nominally 50nm. Measurement was set when the probe was in contact with the glass surface, traversed over the aluminium film and then moved back to the starting point. Again, several traces were recorded indicating the consistency of the measurement. In the Figure 6.33 the specific behaviour of the probe when it encounters different surfaces should be noted. At the cross over region, the probe exhibits rapid changes in resonant frequency which do not correspond to the actual surface level variations but more likely are due to sudden changes in the physical properties of the surface. This forced the controller to exaggerate the probe's height displacement about 4.5 μm in order to compensate for these changes. This favourably agrees with the mathematical model of the probe developed in Chapter 4, and experimental results described in section 6.2 of this chapter. After the probe

crosses over onto the aluminium surface the controller settles down and the variations in profile can be attributed mainly to the surface topography.

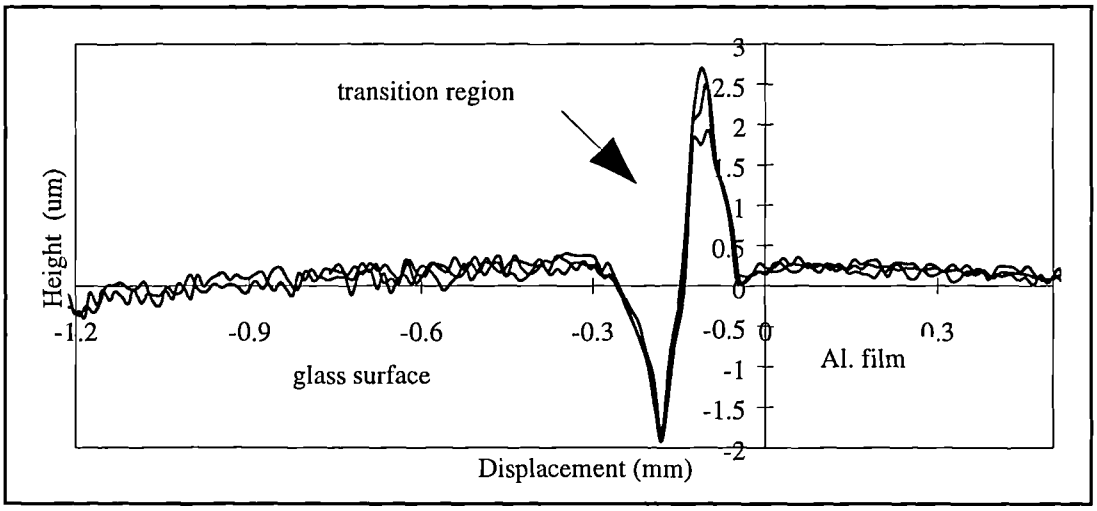

Figure 6.33. Profiles over a microscopic slide partially coated with 50nm film of aluminium

The above results indicate the probe's response to the surface topography and surface property variations (of particular interest are the variation in Young's modulus and density). Such response was evident when multi-surfaces were scanned. The instrument also shows high sensitivity in detecting the edge point (i.e. the transition between two surfaces). This work has potential to be extended into the design of a 3-dimensional surface characterisation instrument which would be able to correlate generated profiles to some useful surface properties. This however, may require incorporating such an instrument with a conventional stylus measuring device in order to differentiate topography from the physical properties.

6.6. Summary and conclusions

The new resonant sensor, consisting of hexagonal beryllium-copper rod with three pairs of piezoelectric drive and pick-up mechanism bonded to its surface and a standard coordinate measuring machine tip holder, was designed and its practical engineering applications were described in this Chapter. The resonance frequency of the sensor was in the region of 38 kHz and whole system exhibited a second order response. Other harmonics were recorded in regions of 56, 75, 96 and 120 kHz. Typical applications considered for this new design were observations of contact mechanisms with engineering surfaces, probe utilisation as a 3D vector sensor and as profilometer instrument. The idea for the new design has its origins in touch trigger probe designs, therefore the performance evaluations of the new resonant sensor as a touch trigger probe were also conducted.

In the observations of contact mechanisms with engineering surfaces, the sensor was operated in two modes: monitoring frequency at constant phase and monitoring phase at constant frequency. In the first mode, the phase angle was locked at near 90 degrees using PLL circuitry, and the change in frequency was monitored as the probe contacted the surface of the specimen. The harmonic of 56.06 kHz was chosen to be operated at because at this frequency the sensor had shown high sensitivity when contacted with both soft and hard materials. For this frequency the calibration factor for the PLL was 2.767 kHz/V. In the second mode, the probe was oscillated at a fixed frequency, and the change in phase was monitored as the probe approached the surface. A variety of materials ranging from rough rubber to polished, hardened steel, and surfaces covered by liquid films having viscosity between 0.20 and 10 Pa s were assessed. The characteristics of added mass, stiffness and damping were observed. The obtained results were compared with the theoretical model developed in Chapter 4 to predict the causes of parametric changes 'at near' and 'at' contact conditions between the two surfaces.

In the contacts with relatively thick or thin oil layers on smooth glass surfaces variation in phase was monitored and a number of distinct regions in the phase graph were observed 'prior to', 'at' and 'after' the contact. In this it was demonstrated that the dynamics of the resonant sensor as it approaches typical engineering surfaces is subjected to a complex variety of added inertial, stiffness and damping forces leading to the observation of their characteristic effects. The experiments had confirmed theoretical prediction (Chapter 5) that monitoring of dynamic characteristics at either side of resonant frequency can be used to identify the predominant effect. Namely it was observed that in the interfacial zone, prior to mechanical contact, an additional damping would result in reduction of the phase lag, and that after mechanical contact the phase very rapidly increases which is characteristic of a relatively large increase in effective stiffness. The experiments were conducted for free value phase shift of -81, -100 and -70 degrees.

In order to experimentally support the mathematical model developed in Chapter 5 for mechanical contact of solid surfaces, a number of experiments were conducted on different type of materials such as PTFE, aluminium, copper, steel and glass. Also sets of tests were conducted on two types of rubber. In these experiments the phase shift of the probe when contacted with solid surfaces was monitored versus applied load. The free value phase shift was set at both -85 and -100 degrees. In the first case, at -85 degrees, an increase in phase shift of less than one degree was detected for the PTFE with applied force of 15 mN, whereas for the same contact force, on a glass surface, the increase in phase was more than 25 degrees. Phase shifts for aluminium, copper and steel fit in between these values. The obtained results were compared with classification scales for hardness, values for modulus of elasticity and the density of materials used. It was observed that the phase shift favourably agrees with hardness scale which could lead to potential applications of the new probe in non destructive hardness testing. All materials tested exhibited reductions in phase lag, at different rates, indicating added stiffness as the predominant effect and therefore confirming predictions established by Equation 5.36 from the developed mathematical model.

For phase shift starting at -100 degrees results were similar except that it was noticed that phase shift had a lower increase rate at about 5 degrees for all materials except PTFE. Referring to the mathematical model it was concluded that such behaviour was due to the contribution of the added damping in the system. During the experiments on rubber-like materials an increase in absolute value of the phase lag was observed. This indicated the predominant effect of added mass as the result of relatively high density and low elastic modulus, again showing favourable agreement between the test results and mathematical model.

A set of experiments was also conducted monitoring the changes in frequency for constant phase as the probe contacted different samples. An increase in frequency shift was registered when the probe contacted solid surfaces confirming that the added stiffness was dominant factor. In the case of rubber-like materials, there was an obvious decrease in resonant frequency as a result of added mass. In both cases all materials, except PTFE caused a higher frequency shift of the probe then the mathematical model predicted. This was attributed to the high sensitivity of the probe, and also to the effects of the strain gauges and stiffness of the cantilever beam on which samples were mounted. Apart from showing higher frequency shifts, experimental results again favourably agree with the mathematical model.

It can be concluded that experiments conducted in observations of contact measurements with engineering surfaces had a significant contribution in understanding the mechanics of contact phenomenon between two objects. In conjunction with a systematic theoretical study these practical results could be used to identify the predominant effect in the observations of effects characteristics of added inertial, stiffness and damping forces. They also represent the first steps towards possible quantitative measurements of physical properties of different materials.

In investigating probe application as a 3D vector sensor, a special test rig was designed to allow radial application of contact force to the probe tip at different angles

of approach in order to reveal the direction of contact. In this all three piezoelectric sensor-actuator pairs were used, output signals from three pick-up sensors were monitored and their values recorded and stored for comparison purposes. Three phase locked loop circuitry's were required and their free running frequencies were set at different harmonics of the probe system with values of 40.115, 75.420 and 120.349 kHz. Only one actuator was used to drive the probe. The idea behind this design and potential application was that tuning PZT sensor-actuator mechanisms at different harmonics, each pick-up sensor would react differently and show a different sensitivity to the force applied radialy to the probe tip. Also it was expected that output signals from each sensor would not only differ between each other but would also be very dependant on the angle of the contact approach. Therefore it was believed that applying contact force radialy from different angles, monitoring signal outputs from three pick-up sensors and comparing them could reveal the direction of the contact between the probe and workpiece. To assess the system behaviour around a full probing plane of 360 degrees measurements were taken in increments of 30 degrees. In this it was observed that the sensors exhibited the highest sensitivity when the probe was radialy contacted from the direction directly opposite to the active PZT actuator. This was expected because of signal propagation through the body of the probe which led to the conclusion that further redesign and rearrangement of piezoelectric plates would be necessary in order to achieve uniform sensitivity around the full probing plane. A set of measurements was conducted in increments of 10 degrees in the most sensitive area covering the range of 120 degrees. Analysing the response of the system when a constant force of 88.5 mN was applied to the probe tip at different angles it was apparent that each direction of approach had its own, corresponding unique combination of three output signals from three pick-up sensors. This phenomenon could be utilised by recording and storing these unique combinations around the full probing plane, in appropriate form (look-up table, etc.). When the probe is contacted from an unknown direction of approach, obtained measurement would be recorded and compared with the stored results. The angular sensitivity of the new resonant sensor was estimated to be around 0.5 degrees in the

high sensitive area while in the rest of the probing plane it was about 2 degrees. It has to be emphasised that these were just approximations of angular sensitivity and that only one plane of contact was considered in this first instance of research. Although further research and refinement of this work is necessary, the preliminary experiments in investigating the application of the new touch sensor as a 3D vector probe in order to detect position and direction of approach have been very promising. Improving sensitivity of the probe around the full circle of 360 degrees, investigating the validity of this preliminary research in other probing planes and development of the algorithm which could perform storage and data comparison could lead to the development of an instrument which would have a significant contribution in measuring applications.

Performance evaluations of the new resonant sensor as a touch trigger probe were also conducted. In these measurements a Renishaw 4mm stylus was used as a probe tip. Calibration was carried out against a 25.4 mm calibration ball and the maximum error of the form found in a large number of measurements was 4 μm. A set of tests was also conducted in order to observe variation in pre-travel of the new probe. The results were very promising, although areas of increased triggering force were found in regions of 90 and 270 degrees relative to the position of the PZT plate used as the excitation gauge. In a 360 degrees probing plane, a maximum square value for 'r-R', (r is the calculated radius of the circle at measured point and R is the radius of best fitted circle through the number of measured points), was 3.5 μm. The pre travel variation in X-Y-Z probing plane was very difficult to establish because of the errors introduced in the Z direction by the CMM machine. The actual accuracy of the probe in the Z direction was estimated to be around 4 μm which could suggest its possible application as a digitising and scanning probe. During the measurements conducted on the CMM machine the new resonant sensor has shown good accuracy determining its possible use in coordinate metrology applications. However, refinement of the present work is necessary in order to definitely eliminate the 'lobing' effect.

Finally an application of the new resonator probe as a profilometer instrument was suggested in this Chapter. The initial measurements were conducted at the Precision Engineering Laboratory at UNC Charlotte, North Carolina. The resonator probe was used to monitor the interfacial forces between the stylus and surface of a scanned specimen along the z-axis. The tests results indicated the probe's response to the surface topography and surface property variations. This response was evident when multi-surfaces were scanned. Of particular interest for further research will be the variation in Young's modulus and density. The probe has also shown high sensitivity in detecting an edge point such as the transition between two surfaces. The work carried out has good potential and could be extended into the design of a surface characterisation instrument.

It can be concluded that research conducted during the work on possible engineering applications of the new resonant sensor has shown very good potential and that its further refinement could lead to the development of a competitive multipurpose tactile sensitive probe.

Chapter 7

Conclusions and recommendations for future work

7.1. Conclusions

Extensive research conducted towards the design and development of a high precision resonator based tactile sensitive probe has been described in this thesis. Although an instrument for immediate commercial practice has not been constructed, initial probe design and tests carried out have shown high potential in engineering applications. Namely, during this research a novel design has been tested in contact measurements, coordinate metrology and also in scanning and surface topography. Several objectives set at the beginning of the research were achieved, contributing with some novel work to the area of resonant based sensors. The following text states the major conclusions of this thesis.

The first prototype of a novel tactile sensor was based on the design of a touch sensitive probe which utilises the piezoelectric effect and applies phase-locked loop frequency detection techniques. The design of the sensor exploits the fact that when a stiff element (probe), oscillating near or at it's resonance frequency, comes into contact with the surface of another body (workpiece), the frequency of vibrational resonance of the probe changes depending on the latter properties. The preliminary results gave great encouragement to the further development of the probe. The device had high sensitivity at both resonance frequency and when the second mode was selected. Also, it had showed a sensitivity to touch of less than 4 mN, and high triggering rate. Some initial tests were conducted on coordinate measuring machines. A possible novel application of the tactile sensitive probe in measuring the properties of different materials was demonstrated monitoring the hardening process of glass-fibre reinforced polyester laminate. Also, a typical relationship between the PLL output voltage and interaction force of the probe/sample has indicated the possible application of the probe in scanning systems by maintaining constant contact force.

In this research an ***analogue phase-locked loop (PLL) technique*** was adopted to track changes in frequency as well as in the phase of the resonant probe. A linear mathematical model was developed to evaluate static and dynamic behaviour of NE 565 PLL. Based on its Bode diagram, transient response and performed simulation, it was concluded that the characteristics of the NE 565 were satisfactory for implementation in this project.

*A **mathematical theory*** was developed in order to model contact mechanisms between resonator based sensor and engineering surfaces and to predict the effects characteristic of added mass, stiffness and damping. Combining Hertzian contact mechanics, Rayleigh's approximate energy method and Smith and Chetwynd's analysis of elastic contact of a sphere on a flat, a novel method was developed to analyse parametric changes induced on the resonant based sensor at contact and near contact conditions. The squeeze and surface film effects were also examined in this

model. It was considered that the dynamics of a resonant probe sensor, as it approaches typical engineering surfaces, are subjected to a complex variety of forces. The model predicts that the phase and frequency shift of a resonator based sensor can either increase or decrease depending on the dominant phenomena (added mass, stiffness and damping) in the contact region. Observation of dynamic characteristics at either side of the resonant frequency can be used to identify the predominant effect.

Preliminary results obtained with the first prototype probe, combined with the developed mathematical model, led to the ***further research and improvement of original design*** in order to achieve miniaturisation and greater versatility in engineering applications. The novel resonant sensor consisted of hexagonal beryllium-copper rod with three pairs of piezoelectric drive and pick-up mechanisms bonded to its surface and a standard coordinate machine tip holder. Typical applications considered for this new design were observations of contact mechanisms with engineering surfaces, probe utilisation in coordinate metrology as a 3D vector sensor and as a touch trigger probe, and in scanning applications as a profilometer instrument.

In ***the observations of contact mechanisms with engineering surfaces***, contacts with relatively thick and thin oil layers on smooth glass surfaces were monitored as well as contacts of solid materials. In this, effects characteristic of added mass, stifness and damping were examined. It was observed that in the interfacial zone, prior to mechanical contact, an additional damping would result in phase lag, and that after mechanical contact the phase very rapidly increases which is characteristic of a relatively large increase in effective stiffness. All solid materials tested exhibited reductions in phase lag, at different rates, indicating added stiffness as the predominant effect. During tests on rubber-like materials, an increase in the absolute value of the phase lag indicated the predominant effect of added mass as the result of relatively high density and low elastic modulus. The changes in phase shift of the probe in contact with different materials were recorded and obtained results compared

with classification scales for hardness, values for modulus of elasticity and density of materials used. It was noticed that change in phase shift agrees with the hardness scale. This could lead to the potential applications of the new probe in non destructive hardness testing. All experimental results have showed favourable agreement with the developed mathematical model. The experiment also confirmed the theoretical prediction that monitoring of dynamic characteristics at either side of resonant frequency can be used to identify the predominant effect.

Although further research and refinement of the work is necessary, the preliminary experiments in investigating the application of the new touch sensor as ***a 3D vector probe*** in order to detect position and direction of approach have been very promising. Analysing the response of the system when constant contact force was applied to the probe tip at different angles it was observed that each direction of approach had its own, unique combination of output signals from pick-up sensors used in the design. The angular sensitivity of the new resonant sensor was estimated to be around 0.5 degrees in the area of higher sensitivity, while in the rest of the probing plane it was about 2 degrees. It has to be emphasised that these were just approximations of angular sensitivity and that only one plane of contact was considered in this first instance of the research.

Performance evaluations of the new resonant sensor as ***a touch trigger probe*** have shown its high accuracy determining possible use in coordinate metrology applications. The results were very promising, although areas of increased triggering force were found in regions of 90 and 270 degrees relative to the position of the PZT plate used as excitation gauge. During calibration of the probe, maximum error of the form found in a large number of measurements was 4 μm. A high accuracy of the probe in the z direction, estimated to be also around 4 μm, suggested its possible application as a digitising and scanning probe. However, further refinement of the present work is necessary in order to eliminate pre-travel variation.

In an application as ***a profilometer instrument,*** the new resonator probe was used to monitor the interfacial forces between the stylus and the surface of the scanned specimen along the z-axis. The results of experiments have highlighted the capacity of the probe to respond to the surface topography and surface property variations. The probe has also shown high sensitivity in detecting the edge points such as the transition between two surfaces. The present work could be extended towards the design of a surface characterisation instrument.

In summary, it could be concluded that some important research has been described in this thesis. Some questions regarding the complexity of the interaction between a resonant sensor and typical engineering surfaces in less than ideal environments have been answered. It was never envisaged that this research will completely summarise such a complex mechanism but rather that will help to gain a better understanding. It also offers an understanding about problems that commercial exploitation of resonant sensors encounter in precision applications. The prototype design of the new resonator-based tactile sensor described in this thesis has been proven to be of significant importance in such applications. Initial research has shown that it has great potential in contact measurements where it can be used for quantitative assesment of physical properties of different materials and in non-destructive hardness testing. It can also find its application in coordinate metrology as a touch trigger probe and as a 3D vector probe. Moreover this design could be further improved towards a surface characterisation instrument. Therefore, the initial design could provide the basis for further development of a very competitive multipurpose tactile sensitive probe with significant importance in engineering applications as well as in research.

7.2. Recommendations for future work

Although a significant amount of work has been done, there is still scope for future work and improvement. The following recommendations might be advantageous.

- Further analysis of the position and vibrations of piezoelectric plates should be conducted in order to obtain best sensitivity of the resonator based probe. This would largely depend on particular applications.
- Ribbon cable which connects the probe with associated electronic circuitry should be replaced with flexible shielded cable so that noise and signal interference could be minimised.
- An active second order filter should be incorporated into the electronic circuitry in order to obtain cleaner output signals.

When used in contact measurement applications:

- The prototype design should be further extended towards the commercial servo controlled resonator profiler to map material surface properties such as the modulus of elasticity, density and energy dissipation and at the same time towards the instrument for non-destructive hardness testing.

In the case of the 3D vector probe:

- Priority should be given to the most suitable way of exciting the vibrations of the probe so that high sensitivity could be achieved around a full probing plane. One possibility could be to have an actuator of tubular shape centred inside the body of the probe which would maintain uniform signal propagation in all directions.
- Explore other probing planes to confirm the validity of results obtained in this research when the probe was contacted only in radial direction.
- Develop an adequate algorithm in order to practically finalise the idea of detecting position and direction of approach.

In the case of the touch trigger probe:

- Existing pre travel variation has to be minimised and, to that effect, further refinement of the shape of the probe and investigation into rearrangement of the piezoelectric plates, especially the PZT actuator, might be necessary.

When used as a profilometer:

- The design should be extended towards the servo controlled resonator profiler for surface topography (similar to conventional Atomic Force Microscopy). One particularly interesting application would be as an end-point detection device in the semiconductor manufacturing industry. Tests could be conducted on multi-phase polished and etched metalographic flat surfaces to investigate this potential application.

Finally, it can be concluded that the research described in this thesis will have made a significant contribution in the field of resonator based tactile probes, especially in achieving a better understanding of contact mechanisms. It will also provide the basis for some important further developments in this area and in commercial exploitation of resonant sensors for precision applications.

REFERENCES

[1] Butler, C. *An investigation into the performance of probes on coordinate measuring machines,* Industrial Metrology, Vol. 2, (1991), pp. 59-70.

[2] Butler, C. and Yang, Q. *A fibre-optic 3-D analog probe for component scanning on coordinate -measuring machines*, Sensors and Actuators A, Vol. 37-38,(1993), pp. 473-479.

[3] Haeusler, E. and Rech, V. *Touch Trigger Probe with PVDF Sensor*, Proceedings of the 6th Int. Symposium on Electrets (ISE) Oxford, Sept. 1-3 (1988), pp. 657-661.

[4] Aoyama, H., Kawai, M. and Kishinami, T. *A new Method for Detecting the Contact Point between a Touch Probe and Surface,* Annals of the CIRP, Vol. 38, (1989), pp. 517-520.

[5] Shinoda, T., Inasaki, I., Nacamura, T. *Development of a Tactile Sensing Probe Utilising Piezoelectric material for Coordinate Measuring Machines,* Transactions of Japan Society of Mechanical Engineers, Vol. 60,(1994),PT.C/580, pp. 4216-4221.

[6] Carl Zeiss *Coordinate Metrology - Technology and Application,* Verlag Moderne Industrie AG & Company, 1990.

[7] Renishaw *Probing Systems for Coordinate Measuring Machines*, 1994-1995 Renishaw plc, Ref. TS 5m 595 Part No. H-1000-5050-10-A.

[8] Langdon R.M. *Resonator sensors-a review*, J. Phys. E: Sci. Instrum., Vol. 18, (1985), pp. 103-115.

[9] Morten, B., De Cicco, G., Prudenenziati, M. *Resonant pressure sensor based on piezolectric properties of ferroelectric thick fillms,* Sensors and Actuators A, Vol. 31, (1992), pp. 153-158.

[10] Cheshmehdoost, A., Stroumboulis, S., O'Connor, B. and Jones, B.E. *Dynamic characteristics of a resonating force transducer,* Sensors and Actuators A, Vol. 41-42, (1994) pp. 74-77.

[11] Tansock, J. and Williams C.C. *Force measurement with a piezoelectric cantilever in a scanning force microscope,* Ultramicroscopy, Vol. 42-44, (1992) pp. 1464-1469.

[12] Olin, H. *Design of a scanning probe microscope,* Meas. Sci. Technol. Vol. 5, (1994) pp. 976-984.

[13] Kuk, Y. and Silverman, J. *Scanning tunneling microscope instrumentation,* Review article, Rev. Sci. Instrum. Vol. 60, (1989), pp. 165-180.

[14] Itoh, T. and Suga, T. *Development of a force sensor for atomic force microscopy using piezoelectric thin films,* Nanotechnology, Vol. 4, (1993), pp. 218-224.

[15] McMurtry, D.R., U.S. Patent 4,138,823 *Probe for Use in Measuring Apparatus,* Feb. 13, 1979.

[16] Carl Zeiss Jena GMBH *Probe Element for Coordinate Measurement Systems,* Internationale Patentklassifikation: G01B 7/00, 7. July 1994.

[17] Sigg, H, Viret, R. and Wegmann, H. *Contact Sensing Head,* United States Patent 4, 246,795, Jan. 27, 1981.

[18] Aoyama, H., Inasaki, I., Kishinami, T. and Yamazaki, K. *Measuring Methods of Shape Elements by Detecting Position Vectors and Unut Normal Vectors* Proceedings of Japan-USA Symposium on Flexible Automation, A Pacific Rim Conference, Kobe, Japan, July 1994, Vol. 2, pp.263-268.

[19] Butler, C. *Probes for High Precision Dimensional Measurement,* Sensor Review, Vol. 14, (1994), pp. 24-26.

[20] Shams , I. and Butler, C. *Performance of an opto-electronic probe used with*

coordinate measuring machines, SPIE Speciality Fiber Optic Systems for Mobile Platforms, Boston 5 Sept 1991, Vol.1589, pp. 120-125.

[21] Ni, J. *Accessory Elements,* Coordinate Measuring Machines and Systems, edited by J.A. Bosch, New York: Dekker, 1995.

[22] Renishaw, *TP200 A new concept in CMM probing technology,* Part No. H-1000-3180-01-A, (1994), Wotton-under-Edge, UK.

[23] Estler, W.T., Phillips, S.D., Borchardt, B., Hopp, T., Witzgall, C., Levenson, M., Eberhardat, K., McClain, M., Shen, Y. and Zhang, X. *Error Compesation for CMM Touch Trigger Probes,* Proceedings of American Society for Precision Engineering, Vol. 12, (1995), pp. 428-431.

[24] Renishaw *A new concept in probing technology,* Ref. TP200B 6m 993 Part No. H-1000-3180-01-A, (1993), Renishaw plc, Wotton-under-Edge, UK.

[25] Gast, T. *Sensors with oscillating elements*, J. Phys. E: Sci. Instrum., Vol. 18, (1985), pp. 783-789.

[26] Mulder B.J. *Simple piezoelectric microbalance based on a vibrating quartz wire*, J. Phys. E: Sci. Instrum., Vol. 17, (1984), pp. 119-121.

[27] Weinmann, M., Radius, R., Asmuss, F. *Measuring profile and position by means of vibrating quartz resonators used as tactile and nontactile sensors*, Sensors and Actuators A, Vol. 37-38 (1993), pp. 715-722.

[28] Binnig, G. Quate, C. F. and Gerber, C. *Atomic force microscopy*, Phys. Rev. Letts., Vol. 56, (1986), pp. 930-933.

[29] Martin, Y., Williams, C. C., Wickramasinghe, H. K. *Atomic force microscope-force mapping and profiling on a sub 100 A scale*, J. Appl. Phys. Vol. 61, (1987), pp. 4723-29.

[30] Itoh, T. and Suga, T. *Piezoelectric force sensor for scanning force microscopy,* Sensors and Actuators A, Vol. 43, (1994), pp. 305-310.

[31] Beeby, S. *Resonance: picking up good vibrations,* Sensor Review, Vol. 16, (1996), pp. 23-27.

[32] *Ferroelectricity and related phenomena, Vol 4: Piezoelectricity*, edited by Taylor, G.W., Gagnepain, J.J., Meeker, T.R., Nakamura, T. and Shuvalov, L.A., Gordon and Breach Science Publishers, 1985, pp. 93-103.

[33] Pointon, A.J., *Piezoelecttric Devices,* Proc. IEE, Vol. 129, Pt. A, (1982), pp. 285-307.

[34] Bintley, J.P. *Principles of measurement systems,* (2nd edn.), Longman Scientific & Technical, 1983, pp. 176-183.

[35] Sashida, T. and Kenjo, T. *An Introduction to Ultrasonic Motors,* Oxford University Press, 1993, pp. 48-83.

[36] IEEE Standard 176-1978, *IEEE Standard on Piezoelectricity.*

[37] Huston, A.R. and White, D.L. *Elastic wave propagation in piezoelectric semiconductors,* J. Appl. Phys., Vol. 33, (1962), pp. 40-47.

[38] Naillon, M. Coursant, R.H., Besnier, F. *Analysis of piezoelectric structures by a finite element method,* Acta Electronica, Vol. 25, (1983), pp. 341-362.

[39] McDearman, *The addition of piezoelectric properties to structural finite element programs by matrux manipulations,* J. Acoust. Soc. Am. Vol. 76, (1984), pp. 666-669.

[40] Tanaka, K. and Tanaka, M. *A Boundary Element Formulation in Linear Piezoelectric Problems,* Journal of Applied Mathematics and Physics, Vol. 31, (1980), pp. 568-580

[41] Tiersten, H.F. *Linear piezoelectric Plate Vibrations,* Plenum Press, New York, 1969.

[42] Zelenka, J. *Piezoelectric Resonators and their Applicatins*, Elsevier, 1986, pp. 64-94.

[43] Bottom, V. *Introduction to Quartz Crystal Unit Design*, Van Nostrand Reinhold Company, 1982, pp.63-100.

[44] Snowdon, J.C. *Vibration and shock in damped mechanical systems,* J. Wiley & Sons, London 1968, pp. 134-192.

[45] Holland, R. and EerNisse, E.P. *Design of Resonant Piezoelectric Devices,* The M.I.T. Press 1969.

[46] Jaffe, B., Cook, W.R. and Jaffe, H. *Piezoelectric ceramics,* Academic Press, London 1971, pp. 23-47.

[47] van Randeraat, J., Setterington, R.E. *Piezoelectric Ceramics,* Mullard Limited, London 1974.

[48] Challis, R.E. and Harrison, J. A. *Rapid solutions to the transient response of piezoelectric elements by z-transform technique,* J. Acoust. Soc. Am. Vol. 74, (1983), pp. 1673-1680.

[49] Aoyagi, R. and Tanaka, H. *Equivalent Circuit Analysis of Piezoelectric Bending Vibrations,* Japn. J. Appl. Phys. Vol 33 (1994) Pt.1, No. 5B, pp. 3010-3014.

[50] Hirose, S. *New Method for Measuring Mechanical Vibration Loss and Dielectric Loss of Piezoelectric Transducers under High-Power Excitation,* Japn. J. Appl. Phys. Vol. 33 (1994) Pt. 1, No. 5B, pp. 2945-2948.

[51] Yang, S. and Huang, W. *Dynamic Analysis of Piezoelectric element,* Rev. Sci. Instrum., Vol. 66, (1995), pp. 4157-4160.

[52] Crawley, E.F. and de Luis, J. *Use of piezoelectric Actuators as Elements of Intelligent Structures,* AIAA Journal, Vol. 25, (1987), pp. 1373-1385.

[53] Crawley, E.F. and Anderson, E.H. *Detailed Models of Piezoceramic Actuation of Beams,* J. of Intell. Mater. Syst. and Struct., Vol. 1, (1990), pp. 4-25.

[54] Bailey, T. and Hubbard Jr., J.E. *Distributed Piezoelectric - Polymer Active Vibration Control of a Cantilever Beam,* Journal of Guidance, Control And Dynamics, Vol. 8, (1985) pp. 605-611.

[55] Pan, J., Hansen, C.H. and Snyder, S.D. *A study of the response of a simply supported beam to excitation by a piezoelectric actuator,* Proc. of the Conf. On recent advances in active control of sound and vibrations, UK, (1991), pp. 39-49.

[56] Vaz, A.F. *Modeling piezoelectric behaviour for actuator and sensor applications,* Technical repoprt, Applied Computing Enterprises, February 1991.

[57] Banes, E., Groschl, M., Burger, M. and Schmid, M. *Sensors Based on Piezoelectric Resonators,* Sensors and Actuators, A, Vol. 48, (1995) pp. 1-21.

[58] Dokmeci, M.C. *Dynamic Applications of Piezoelectric Crystals; Part I: Fundamentals,* The Shock and Vibration Digest, 1983, Vol. 15, pp. 9-20.

[59] Dokmeci, M.C. *Dynamic Applications of Piezoelectric Crystals; Part II: Theoretical Studies,* The Shock and Vibration Digest, 1983, Vol. 15, pp. 15 - 26.

[60] Dokmeci, M.C. *Dynamic Applications of Piezoelectric Crystals; Part III: Experimental Studies,* The Shock and Vibration Digest, 1983, Vol. 15 (5), pp. 11 - 22.

[61] Dokmeci, M.C. *Recent advances in the dynamic Applications of Piezoelectric Crystals,* The Shock and Vibration Digest, 1989, Vol. 21, pp. 3-20.

[62] Soderkvist, J. *Activation and detection of mechanical vibrations in piezoelectric beams,* Sensors and Actuators A, Vol. 32 (1992) 567-571.

[63] Mecea, V.M. *Vibrating piezoelectric sensors,* Sensors and Actuators A, Vol. 41-42, (1994) pp.630-637.

[64] Wade, W.H. and Slutsky, L.J. *Quartz Crystal Thermometer,* Rev. Sci. Instrum. Vol. 33 (1962), pp. 212-213.

[65] Smith, W.L. and Spencer, W.J. *Quartz crystal thermometer for measuring temperature deviations in the 10^{-3} to 10^{-6} °C range,* Rev. Sci. Instrum., Vol. 34 (1963), pp. 268-270.

[66] Ueda, T., Koshaka, F., Iino, T. and Yamazaki, D. *Temperature sensor using quartz tuning fork resonator,* Proc. of 40th Ann. Freq. Control Symp., Philadelphia, PA, USA, 1986, pp. 224-229.

[67] EerNisse, E.P. and Wiggins, R.B. *A resonator temperature transducer with no activity dips,* Proc. 40th Ann. Freq. Control Symp., Philadelphia, PA, USA, 1986, pp. 216-223.

[68] Viens, M. and Cheeke, J.N. *Highly sensitive temperature sensor using SAW resonator oscillator,* Sensors and Actuators A, Vol. 24 (1990), pp. 209-211.

[69] Ballato, A.D. and Bechmann, R. *Effect of initial stress in vibrating quartz plates,* Proc. IRE, Vol. 48 (1960), pp. 261-262.

[70] Ratajski, J.M. *Force-frequency coefficient of singly rotated vibrating quartz plates,* IBM J., Vol. 12 (1968) pp. 92-99.

[71] Dauwalter, C.R. *The temperature dependence of the force sensitivity of AT-cut quartz crystals,* Proc. 26th Ann. Freq. Contr. Symp., Fort Monmouth, NJ, USA, 1972, pp. 108-112.

[72] Karrer, E. and Ward, R. *A low range quartz pressure transducer,* ISA Trans., Vol. 16 (1977), pp. 90-98.

[73] EerNisse, E.P. and Paros, J.M. *Practical considerations for miniature quartz resonator force transducers,* Proc. 37th Annual Frequency Control Symp., Philadelphia, PA, USA, 1983, pp. 225-260.

[74] Ono, M., Hirata, M, Kokubun, K.,Murakami, H., Hojo, H., Kawashima, H. and Kyogoku, H. *Quartz friction vacuum gauge for pressure range from 0.001 to 1000 torr,* J. Vac. Sci. Technol., A4 (1986), pp. 1728-1731.

[75] Morgan Matroc Ltd., *A guide to the use of PZT Piezoelectric strain, vibration and excitation gauges,* Bulletin 66022/c, Thornhill Southampton, England.

[75a] Morgan Matroc Ltd., *Piezoelectric ceramics: Data book for designers,* Morgan Matroc Ltd., Transducer Products Division, Thornhill Southampton, England.

[76] Ballato, A., EerNisse, E.P. and Lukaszek, T. *The force-frequency effect in dubly rotated quartz resonators,* Proc. 31st Ann. Freq. Contr. Symp., Fort Monmouth, NJ, USA, 1977, pp. 8-16.

[77] Janiaud, D., Nissim, L. and Gagnepian, J.J. *Analitical calculation of initial stress effects on anisotropic crystals: application to quartz resonators,* 32nd Ann. Freq. Contr. Symp., Atlantic City, NJ, USA, 1978, pp. 169-179.

[78] Karrer, H.E. and Leach, J.A. *A quartz resonator pressure transducer,* IEEE Trans. Industr. Electr. Control Instrum., IECI-16, (1969), pp. 44-50.

[79] Karrer, E. *Low range quartz resonator pressure transducer,* 1977, ISA Trans. Vol. 16, No. 2, pp.60-68.

[80] Paros, J.M. *Digital quartz transducers for absolute pressure measurement,* ISA 21st Int. Instrum. Symp. Philadelphia, USA, May 1975.

[81] Kirman, R.G. *A vibrating quartz force sensor,* Transducer Tempcon Conf. 14-16 June 1982, London.

[82] EerNisse, E.P. *Vacuum applications of quartz resonators,* J. Vac. Sci. Technol., , Vol. 12, (1975), pp. 564-568.

[83] Garratt, J.D. and Bottomley, S.C., Nanotechnology 1, (1990), 38.

[84] Takata, K. *Novel Method for Detecting Resonant Frequency Shift in Atomic Force Microscopy,* Jpn. J. Appl. Phys. Vol. 32 (1993) pp. 2455-2458.

[85] Binnig, G and Smith, D.P.E., Rev. Sci. Instrum. 57(8), August 1986.

[86] Ohara, T. and Youcef-Toumi *Dynamics and Control of Piezotube Actuators for Subnanometer Precision Applications,* Proceedings of the American Control Conference, Seattle, Washongton, June 1995, pp 3808- 3812.

[87] Hara, S., Iyoki, M., Kaneko, R., Matsuda, R. and Itao, K., *Development of a Micro-step XYθ Stage Using Piezoelectric Tube Actuators,* Jnl. of the Japan Society for Precision Engineering, Vol. 60, (1994), pp. 1736-1740.

[88] Jeon, D. and Willis, R.F. *Inchworm controller for fine approach in a scanning tunneling microscope,* J. Vac. Sci. Technol. A Vol. 9, (1991), 2418.

[89] Main, J.A., Garcia, E. and Newton, D.V. *Precision Position Control of Piezoelectric Actuators Using Charge Feedback,* J. of Guidance, Control and Dynamics, Vol. 18, (1995), pp. 1068-1073.

[90] Oiwa, T., Kaneko, K., Kaneko, T. and Kyusojin, A. *High-Rigidity Multi-Degrees-of-Freedom Fine Motion Mechanism using Piezoelectric Actuators,* Jnl. Of The Japan Society for Precision Engineering, Vol. 60, (1994), pp. 1355-1359.

[91] Chen, L., Zhang, H. and Rink, R. *Tactile Sensing of Point Contact,* Proc. of The IEEE Int. Conf. On Systems, Man and Cybernetics, Piscataway, NJ, USA, (1995), pp. 574-579.

[92] Yeung, S.K., Petriu, E.M., McMath, W.S. and Petriu, D.C. *High Sampling Resolution Tactile sensor for Object Recognition,* IEEE Transactions on Instrumentation and Measurement, Vol. 43, (1994), pp. 277-282.

[93] Charlton, S., Sikka, P. and Zhang, H. *Extracting Contact Parameters from Tactile Data Using Artificial Neural Networks,* Proc. of The IEEE Int. Conf. On Systems, Man and Cybernetics, Piscataway, NJ, USA, Vol. 5, (1995), pp. 3954-3959.

[94] Shida, K. and Li, D. *A Mono-Structural Thin Plate Touch Sensor with Four Sensing Functions for Discrimination of Material Properties,* Integrating Intelligent Instrumentation and Control IEEE Instr/Measurement Tech. Conf. IMTC Pro. Cat. No. 95CH35783, 1995, pp. 152-157.

[95] Shinoda, H., Morimoto, N. and Ando, S. *Tactile Sensing Using Tensor Cell,* Proc. IEEE Int. Conf. Robotics and Automation, Piscataway, NJ, USA, 1995, Vol. 1, pp. 825-830.

[96] Omata, S. and Terunama, Y. *Development of a new type tactile sensor for detecting hardnes and/or softness of an object like the human hand,* Transducers '91, Int. Conf. Solid State Sens. Actuators, 1991, pp. 868-871.

[97] Chonan, S., Jiang, Z, Mori, K. and Munekata, Y. *Development of Tribosensor System Using Neural Networks (Tribosensor Using Piezoelectric Ceramics),* Trans. of The Japan Society of Mechanical Engineers, Vol. 61, (1995), Pt.C/587, pp. 2996-3003.

[98] Albrecht, T.R., Grutter, P., Horne, D. and Rugar, D. *Frequency modulation detection using high-Q cantilevers for enhanced force microscope sensitivity,* J. Appl. Phys. Vol. 69, (1991), pp. 668-673.

[99] Proksch, R. and Dan Dahlberg, E. *A detection technique for scanning force microscopy,* Rev. Sci. Instrum. Vol. 64 (1993), pp. 912-916.

[100] Rodahl, M., HooK, F., Krozer, A, Brzezinski, P. and Kasemo, B. *Quartz crystal microbalance setup for frequency and Q-factor measurements in gaseous and liquid environments,* Rev. Sci. Instrum. Vol. 66, (1955), pp. 3924-3930.

[101] Spencer, W.J. and Smith, W.L. J. Appl. Phys. Vol. 37, (1966), 2557.

[102] Wajid, A. *Method and a simple apparatus for rapid simultaneous measurement of resonance frequency and Q factor of a quartz crystal,* Rev. Sci. Instrum.,Vol. 67, (1996), pp. 1961-1964.

[103] Bottom, V.E. *Introduction to Quartz Crytal Devices,* Van Nostrand, New York, (1982), p. 148.

[104] Rubin, L.G. *The new wave: Digital lock-in amplifiers,* Rev. Sci. Instrum. Vol. 59, (1988), pp. 514-515.

[105] Dixon, P.K. and Wu, L. *Broadband digital lock-in amplifier techniques,* Rev. Sci. Instrum. Vol. 60, (1989), pp. 3329-3336.

[106] Lee, S. and Kwun, S. *Digital frequency tripling circuit for third harmonic detection by lock-in amplifiers,* Rev. Sci. Instrum. Vol. 65, (1994), pp. 971-973.

[107] Mead, M.L. *Lock-in Amplifiers: Principles and Applications*, Peter Peregrinus, London, 1983.

[108] Holcomb, M.J. and Little, W.A. *Cascading lock-in amplification: Application to wavelength modulation spectroscopy,* Rev. Sci. Instrum. Vol. 63, (1992), pp. 5570-5575.

[109] Takata, K., Kushida, K., Torh, K. and Miki, H. *Strain Imaging of Lead-Zirconate-Titanate Thin Film by Tunneling Acoustic Microscopy,* Jpn. J. Appl. Phys. Vol. 33 (1994), pp. 3193-3196.

[110] Bridge, N.O. and Nagel, S.R. *Wide-frequency specific heat spectrometer,* Rev. Sci. Instrum. Vol. 58, (1987), pp. 1464-1470.

[111] Shakkottai, P., Kwack, E.Y. and Back, L.H. *Analog circuit for the measurement of phase difference between two noisy sine-wave signals,* Rev. Sci. Instrum. Vol. 60, (1989), pp. 3081-3083.

[112] Golnabi, H. and Ashrafi, A. *Phase-shift generation and monitoring by a simple circuit,* Rev. Sci. Instrum. Vol. 67, (1996), pp. 2017-2019.

[113] Gardner, F.M. *Phaselock Tecniques,* John Wiley, New York (1979).

[114] Kikukawa, A., Hosaka, S., Honda, Y. and Imura, R. *Phase-locked noncontact scanning force microscope* Rev. Sci. Instrum. Vol. 66, (1995), pp. 101-105.

[115] Best, R.E. *Phase-Locked Loop: theory, design and applications,* McGraw-Hill, New York, London, (1993).

[116] Kuo, B.C. *Automatic Control Systems,* Prentice-Hall, (1991).

[117] RS data, *Phase locked loops NE565 and 567,* (1992).

[118] Choudhury, D.R. *Linear integrated circuits*, John Wiley, New Delhi, India, (1991).

[119] McMenamin, J.M. *Linear integrated circuits,* Prentice-Hall,New Jersy, (1985).

[120] Neubert, H.K.P. *Instrument Transducers: An Introduction to their Performance and Design,* (2nd edn.), Oxford University Press, (1975), pp.237-238.

[121] Harb, S.M. and Vidic, M. *Resonator based touch sensitive probe,* Sensors and Actuators A, Vol. 50 (1995), pp. 23-29.

[122] Harb, S.M. and Vidic, M. *Characterisation of a resonator based touch sensitive probe,* 1st World Congress Inteligent Manu. Process & Sys., San Juan, Puerto Rico USA, Feb. 1995.

[123] Micro Materials, Measuring Nanotechnology, *Nano Test 600,* Product Catalogue, Micro Materials, Wrexham Technology Park, Wrexham, UK.

[124] Vidic, M. and Harb, S.M. *Verification of high precision touch sensitive probe,* 8th Inter. Conf. Precision Eng., Compiegne, France, May 1995.

[125] Deng, Y., Martin, G.C. *Analysis of the Cure-Dependent Dielectric Relaxation Behavior of an Epoxy Resin,* Journal of Polymer Science: Part B: Polymer Physics, Vol. 32, (1994), pp. 2115-2125.

[126] Rapra, *Technical products, Scanning Vibrating Needle Curemeter,* Rapra.net web site (http://www.rapra.net/svnc.htm)(see Appendix H).

[127] Johnson, K.L. *Contact Mechanics*, Cambridge University Press, Cambridge (1985), pp. 56-106.

[128] Thomson, W.T. *Theory of Vibration with Applications*, Prentice Hall, (1988), pp.17-76.

[129] Elings, V. and Gurley, J. US *Patent No. 5,266,801.*

[130] Zong, Q., Innis D., Kjoller, K. and Elings, V. B. *Fractured polymer/silica fibre surface studied by tapping mode atomic force microscopy,* Surf. Sci. Letts., Vol. 290,(1993), L688.

[131] Gross, W.A. *Gas Film Lubrication,* John Wiley and Sons, New York, (1962), pp. 38-44, 307-327.

[132] Grigg, D.A., Russell, P.E. and Griffith, J.E. *Tip-sample forces in scanning probe microscopy in air and vacum,* J. Vac. Sci. Technol., Vol. A10, (1992), pp. 680-683.

[133] McFarlane, J.S. and Tabor, D. *Adhesion of solids and the effects of surface films,* Proc. R. Soc. Lond., Vol. A202, (1950), pp. 224-243.

[134] Smith, S.T. and Chetwynd, D.G. *Foundation of Ultraprecision Mechanism Design,* Gordon and Breach Science Publishers, Chemin de la Sallaz, Switzerland, (1992).

[135] Wert, C.A. *Internal friction in solids*, J. Appl. Phys. Vol. 60, (1986), pp. 1888-1895.

[136] Steidel, R.F. *An Introduction to Mechanical Vibrations*, John Wiley and Sons, New York, (1989), pp. 164-226.

[137] Vidic, M., Harb, S. M. and Smith, S. T. *Observations of contact measurements using a resonance based touch sensor,* Precision Engineering, Vol. 22, (1998), pp. 19-36.

[138] Vidic, M., Harb, S. M. and Smith, S. T. *Observations of contact measurements using a resonance based touch sensor,* Proceedings of 1996 ASPE (American Society for Precision Engineering) Annual meeting, California, USA. Nov. 1996, Vol. 14, pp. 41-46.

[139] Harb, S.M., Vidic, M. and Smith, S.T. *Resonator based Profilometer Instrument,* Proceedings of Laser Metrology and Machine Performance Conference, 1997, Huddersfield, UK.

Appendix A

Schematic diagram and PCB lay out of an analogue Phase Lock Loop (PLL) circuitry

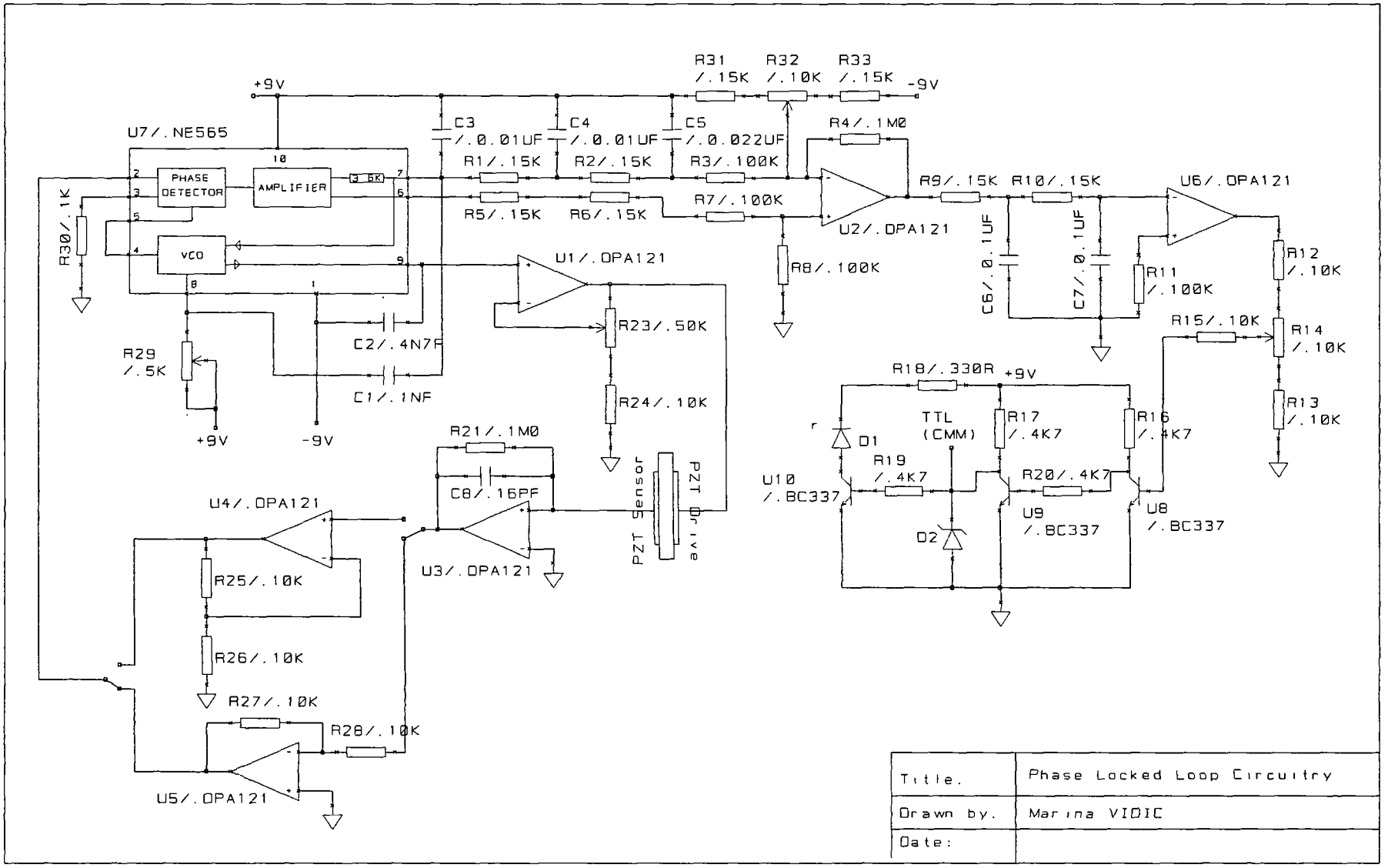
+9V
R31 /.15K
R32 /.10K
R33 /.15K
-9V
U7/.NE565
PHASE DETECTOR
AMPLIFIER
VCO
C3 /.0.01UF
C4 /.0.01UF
C5 /.0.022UF
R4/.1M0
R1/.15K
R2/.15K
R3/.100K
R5/.15K
R6/.15K
R7/.100K
R8/.100K
U2/.OPA121
R9/.15K
R10/.15K
U6/.OPA121
C6/.0.1UF
C7/.0.1UF
R11 /.100K
R12 /.10K
R14 /.10K
R13 /.10K
R15/.10K
R30/.1K
U1/.OPA121
R23/.50K
R24/.10K
C2/.4N7F
C1/.1NF
R29 /.5K
R18/.330R
R17 /.4K7
R16 /.4K7
TTL (CMM)
D1
R19 /.4K7
R20/.4K7
U10 /.BC337
U9 /.BC337
U8 /.BC337
D2
R21/.1M0
C8/.16PF
U3/.OPA121
PZT Sensor
PZT Drive
U4/.OPA121
R25/.10K
R26/.10K
R27/.10K
R28/.10K
U5/.OPA121
Title. Phase Locked Loop Circuitry
Drawn by. Marina VIDIC
Date:

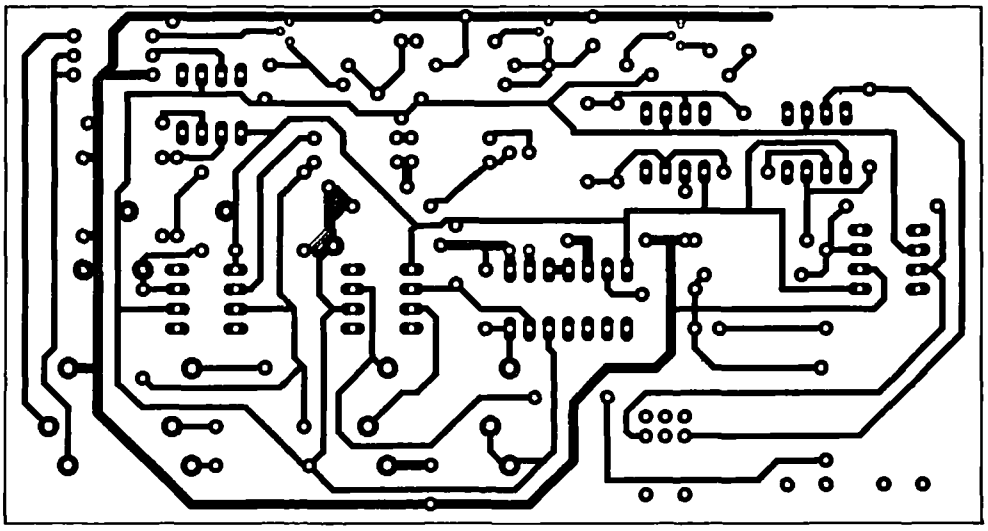

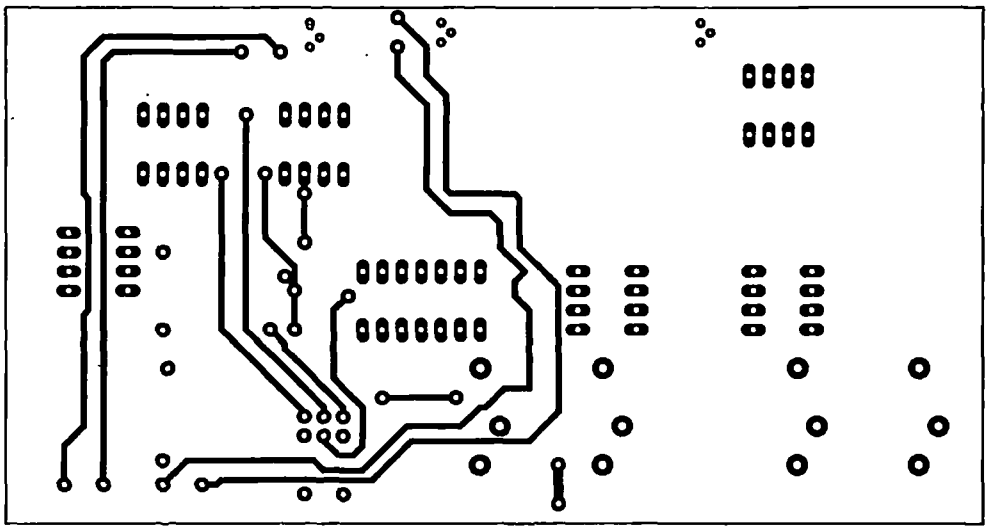

Appendix B

Program written in Turbo Pascal 7.0 to control data acquisition

```
{


}

Program HardTst;
Uses
 CRT,pc74,Dos;

const
badd          =  $218;
var
 F,gpib       : text;
 Filename     : string;
 i            : integer;
 ch           : char;
 s_real       :real;
 cde          :integer;
 status,s1,ss  :string[20];
 time_delay    :word;
 Maxpoint      :integer;
 tt0           :LongInt;
 h,mn,s,hund   :Word;

Procedure Read_DVM;
 var
  iii   :integer;
begin
   Rewrite(gpib);
   Writeln(gpib,'ENTER 11');
```

```
    Reset(gpib);
    Readln(gpib,ss);
    for iii:=1 to 14 do
     begin
        s1[iii]:=ss[iii+2];
        write(F,s1[iii]);
     end;
    write
    (F,' ');
{    val(s1,S_real,cde);}

   {Read data directly into string }
end;

Procedure Read_Data;
var
  in_val0,in_val1,j,ch0,ch1,ch2,ch3,m        : Integer;
  sumval0,sumval1,sumval,sumval2,sumval3     : real;

  tt                                :Longint;
begin
   sumval:=0;
   ch0:=0;
   ch1:=1;
   ch2:=2;
   ch3:=3;
   m:=Ad_in(ch0,in_val0);
   sumval := sumval + in_val0;
   sumval0 := (sumval - $800)*5/$800;
   sumval:=0;
   m:=Ad_in(ch1,in_val1);
   sumval := sumval + in_val1;
   sumval1 := (sumval - $800)*5/$800;
   sumval:=0;
   m:=Ad_in(ch2,in_val0);
   sumval := sumval + in_val0;
   sumval2 := (sumval - $800)*5/$800;
   sumval:=0;
   m:=Ad_in(ch3,in_val1);
   sumval := sumval + in_val1;
   sumval3 := (sumval - $800)*5/$800;
{  GetTime(h,mn,s,hund);
  tt:=h*3600+mn*60+s;
  tt:=tt-tt0;}
  writeln(' LVDT : ',sumval0:6:3,'  ',sumval1:6:3,'  ',sumval2:6:3,'  ',sumval3:6:3);
```

```
    write(F,sumval0:6:3,',',sumval1:6:3,',',sumval2:6:3,',',sumval3:6:3,',');
    Read_DVM;

 end;
 {Read DVM Meter through gpib board}
 Procedure Reset_GPIB_PC;
  Begin
     Writeln(gpib, 'ABORT');
     Writeln(gpib, 'RESET');
  end;


 Procedure DVM_Status;
 begin
   Rewrite(gpib);
   Writeln(gpib,'TRIGGER 11');
   writeln(gpib,'STATUS');
   Reset(gpib);
   Readln(gpib,Status);
   Writeln('Status :',Status);
   Readln;
 end;
 Procedure Write_DVM;
 begin
   Rewrite(gpib);


   Writeln(gpib, 'TRIGGER 11');
   Writeln(gpib,'OUTPUT 11; FNC FRQ,RNG A,RSL 3,MSP 2,OUT N14');
   Reset(gpib);
   Readln(gpib,s);
   Writeln('output from write_DVM VL Value =',s);
 end;
   {Check version for PC74 data aquistion board}
 procedure ver_chk;
 var
  quit_f: boolean;
  r:  real;
  ii:  integer;
 begin
   ii := version;
   r := hi(ii) + lo(ii)/100;
   clrscr;
   GotoXY(25, 2);
   write('PC-74 Driver version ', r:4:2);
```

```
  quit_f := false;

  if diag <> 0 then begin
     writeln;
     writeln('PC-74 dignostics report A/D not installed or other fault.');
     quit_f := true;
  end;
end;
     { End ver-chk}

var
 ii,da,val,d_ch,k,l   :integer;
 dac_v,dacv,del_dacv    :real;


Begin
{ Open device GPIB0 }

  Assign(gpib,'gpib0');
  Rewrite(gpib);
  Reset_GPIB_PC;
  Write_DVM;
  DVM_Status;

 Write('Enter data file name  <filen name.ext>  : ');
 Readln(filename);
 Assign(F,filename);

 Rewrite(F);
 Writeln;
 Write('Enter Delay time (Msecond)');
 Readln(Time_delay);
 Write('Enter Number of point <3600>');
 Readln(Maxpoint);

 base_74 := badd;
   for ii := 0 to 15 do gain_74[ii] := 0;
  ver_chk;

  da:=Round(4095/2);
  val := da_out(d_ch, da);
  writeln('Gain of channel 0 := ',Get_gain(0));
  readln;
  d_ch:=0;
{  Write('Input Coil voltage <V> :');
```

```
  Readln(dacv);
}  d_ch:=0;
  Write('Enter Coil increment voltage <V> :');
  Readln(Del_dacv);
  dacv:=0;
for l:=1 to 3 do
 begin
      { Forward motion }

 for i:=1 to Maxpoint do
  begin
  dacv:=dacv+del_dacv;
  dac_v := (dacv + 5)*409.5;
   if dac_v < 0 then dac_v := 0
        else if dac_v > 4095 then dac_v := 4095;
   da := round(dac_v);
   val := da_out(d_ch, da);
  for k:=1 to 1 do
   begin
    Read_Data;
   delay(time_delay);
   end;
 end;
    { Reverse motion }
for i:=1 to Maxpoint do
  begin

  dacv:=dacv-del_dacv;
  dac_v := (dacv + 5)*409.5;
   if dac_v < 0 then dac_v := 0
        else if dac_v > 4095 then dac_v := 4095;
   da := round(dac_v);
   val := da_out(d_ch, da);
   for k:=1 to 1 do
    begin
      Read_Data;
      delay(time_delay);
    end;
 end;
end;
  da:=Round(4095/2);
  val := da_out(d_ch, da);
  Close(F);
  Close(gpib);
End.
```

Appendix C

Making a Laminate

1. Cut two squares of film to a size larger than the required laminate size;
2. Put one sheet on a flat surface and tape down each corner;
3. Cut a square of glass equal to the required laminate size;
4. Weigh the glass (density should be approximately 450 g/m^2);
5. Place the glass mat on the film and mark the position of each corner of the film;
6. Using a ratio of resin to glass of 2.3 to 1 (this gives a 33% laminate) weigh the resin;
7. To get a gel point of approximately 5 mins use .25% of acceleator, BYK and pigment;
8. Mix thoroughly;
9. Add 2% of catalyst and mix in (this should give a gel point of approximately 5-6 mins. If a longer time is needed cut the catalyst to 1% to give 10-11 mins time);
10. Pour about 1/3 by volume of the mixture into the area marked by crosses;
11. Put the glass mat on the top;
12. Dab it in to wet it out;
13. Pour the remaining resin on the top of the mat to give an equal distribution;
14. Put the other nylon sheet on the top;
15. Smooth over with a steel rule to remove trapped air./

Appendix D

Theoretical representation of the shift in resonance frequency and phase shift for selection of different materials (Matlab programs)

```
R=0.002;
area=3.464*0.00364*0.00364;
Leng=0.020;
E_BeCu=128*10^9;
D_BeCu=7800;
K=area*E_BeCu/Leng;
M=D_BeCu*area*Leng;
om02=K/M;
t1=str2mat('PTFE','Alu','Cu','Steel','glass');
t2=str2mat('N_Rubber','Balsa','Nylon');
t3=str2mat('Concrete','E_resin','gold','Graphite','Lead');
Tname=str2mat(t1,t2,t3);
E=[0.4 80.1 147 200 72 0.1 3.5 3 40 2 95.3 170 18];
Row=[2200 2800 8800 8000 2540 900 140 250 1140 1100 19300 1500 1130];
apcelum=[0.03 0.0098 0.0126 0.0113 0.0038 0.07 0.1 0.5 0.1 0.3 0.018 0.1 0.1];
 for j=1:13
  for i=1:100
        P(i)=(i-1)*0.00016;
        a=(3*P(i)*R/(4*E(j)*10^9))^0.3333;
        del=(9*P(i)*P(i)/(16*R*E(j)*10^9*E(j)*10^9))^0.3333;
        Me=Row(j)*pi*pi*P(i)/(2*E(j)*10^9);
        Keq=(6*(E(j)*10^9)^2*P(i)*R)^0.3333;
        mass=Me/(3*M);
        Omega(i,j)=sqrt(om02*(1+Keq/K)*(1-mass+mass^2-mass^3+mass^4-mass^5));
        Omega(i,j)=Omega(i,j)/sqrt(om02);
        if Omega(i,j)==1.0
```

```
            phase(i,j)=-90;

        elseif Omega(i,j)<1
            phase(i,j)=atan(2*apcelum(j)*Omega(i,j)/(1-Omega(i,j)^2))*360/(2*pi);
            phase(i,j)=phase(i,j)-180;
            amplitude(i,j)=1/sqrt((1-
Omega(i,j)^2)^2+4*(apcelum(j))^2*Omega(i,j)^2);
        else
            phase(i,j)=atan(2*apcelum(j)*Omega(i,j)/(1-Omega(i,j)^2))*360/(2*pi);

            amplitude(i,j)=1/sqrt((1-
Omega(i,j)^2)^2+4*(apcelum(j))^2*Omega(i,j)^2);
        end
        P(i)=P(i)*1000;
    end;
  end;
%plot(P,Omega(:,1:5), 'w');
plot(P,phase(:,1:5),'w')
axis([0 15 -95 -65])
xlabel('Load (mN)'), ylabel('Phase (degree)')
%xlabel('Load (mN)'), ylabel('w/w_n')
gtext ('PTFE')
gtext ('aluminium')
gtext ('copper')
gtext ('steel')
gtext ('glass')



R=0.002;
area=3.464*0.00364*0.00364;
Leng=0.020;
E_BeCu=128*10^9;
D_BeCu=7800;
K=area*E_BeCu/Leng;
M=D_BeCu*area*Leng;
om02=K/M;
t1=str2mat('PTFE','Alu','Cu','Steel','glass');
t2=str2mat('N_Rubber','Balsa','Nylon');
t3=str2mat('Concrete','E_resin','gold','Graphite','Lead');
Tname=str2mat(t1,t2,t3);
E=[0.4 80.1 147 200 72 0.1 3.5 3 40 2 95.3 170 18];
Row=[2200 2800 8800 8000 2540 900 140 250 1140 1100 19300 1500 1130];
apcelum=[0.03 0.0098 0.0126 0.0113 0.0038 0.07 0.1 0.5 0.1 0.3 0.018 0.1 0.1];
 for j=1:13
```

```
  for i=1:100
        P(i)=(i-1)*0.016;
        a=(3*P(i)*R/(4*E(j)*10^9))^0.3333;
        del=(9*P(i)*P(i)/(16*R*E(j)*10^9*E(j)*10^9))^0.3333;
        Me=Row(j)*pi*pi*P(i)/(2*E(j)*10^9);
        Keq=(6*(E(j)*10^9)^2*P(i)*R)^0.3333;
        mass=Me/(3*M);
        Omega(i,j)=sqrt(om02*(1+Keq/K)*(1-mass+mass^2-mass^3+mass^4-mass^5));
        Omega(i,j)=Omega(i,j)/sqrt(om02);
        if Omega(i,j)==1.0
              phase(i,j)=-90;

        elseif Omega(i,j)<1
              phase(i,j)=atan(2*apcelum(j)*Omega(i,j)/(1-Omega(i,j)^2))*360/(2*pi);
              phase(i,j)=phase(i,j)-180;
              amplitude(i,j)=1/sqrt((1-
Omega(i,j)^2)^2+4*(apcelum(j))^2*Omega(i,j)^2);
        else
              phase(i,j)=atan(2*apcelum(j)*Omega(i,j)/(1-Omega(i,j)^2))*360/(2*pi);

              amplitude(i,j)=1/sqrt((1-
Omega(i,j)^2)^2+4*(apcelum(j))^2*Omega(i,j)^2);
        end
        P(i)=P(i)*1000;
    end;
  end;
 %plot(P,Omega);
plot(P,phase(:,6),'w')
axis([0 1600 -95 -65])
xlabel('Load (mN)'), ylabel('Phase (degree)')
gtext ('rubber')
```

Appendix E

Calibration figures

E.1. Strain Gauge Calibration

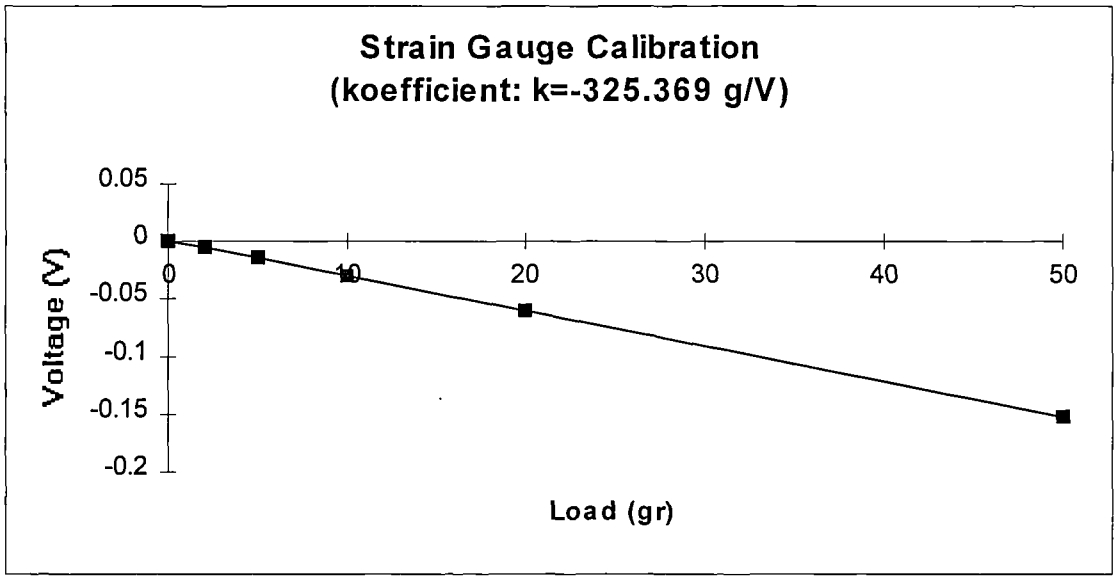

E.2. LVDT Calibration

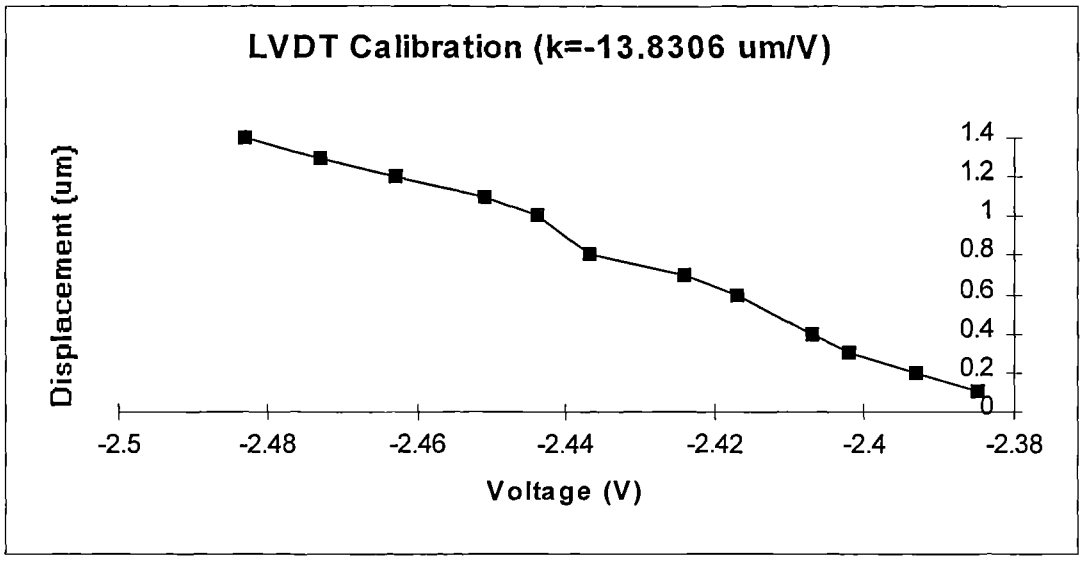

E.3. PLL Calibration (for 56.06 kHz resonance frequency)

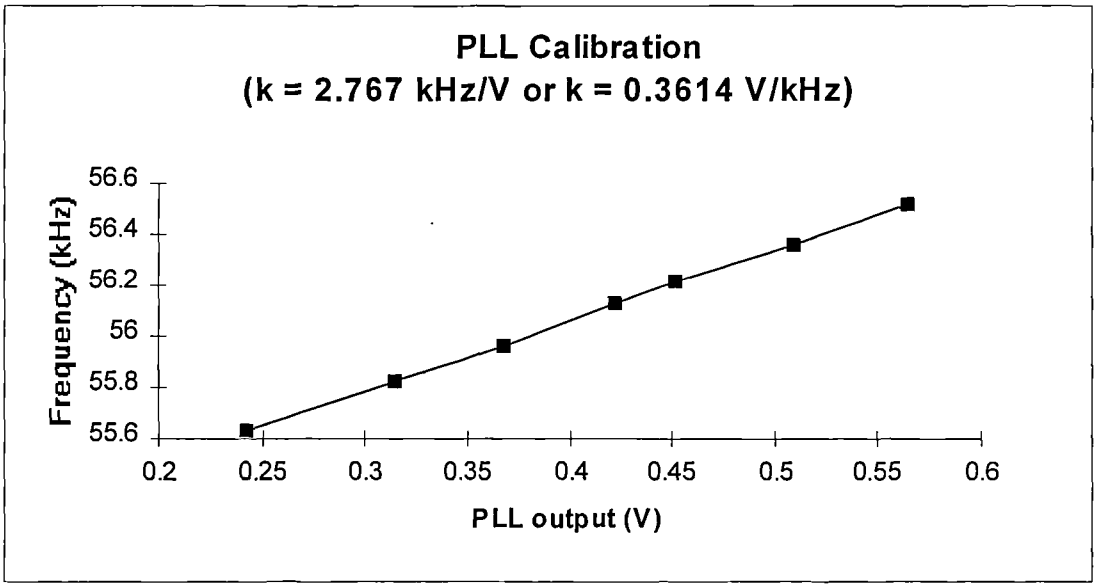

Appendix F

Contact measurements

F.1. The difference in the phase shift for free value phase shift set at -85 and -100 degrees

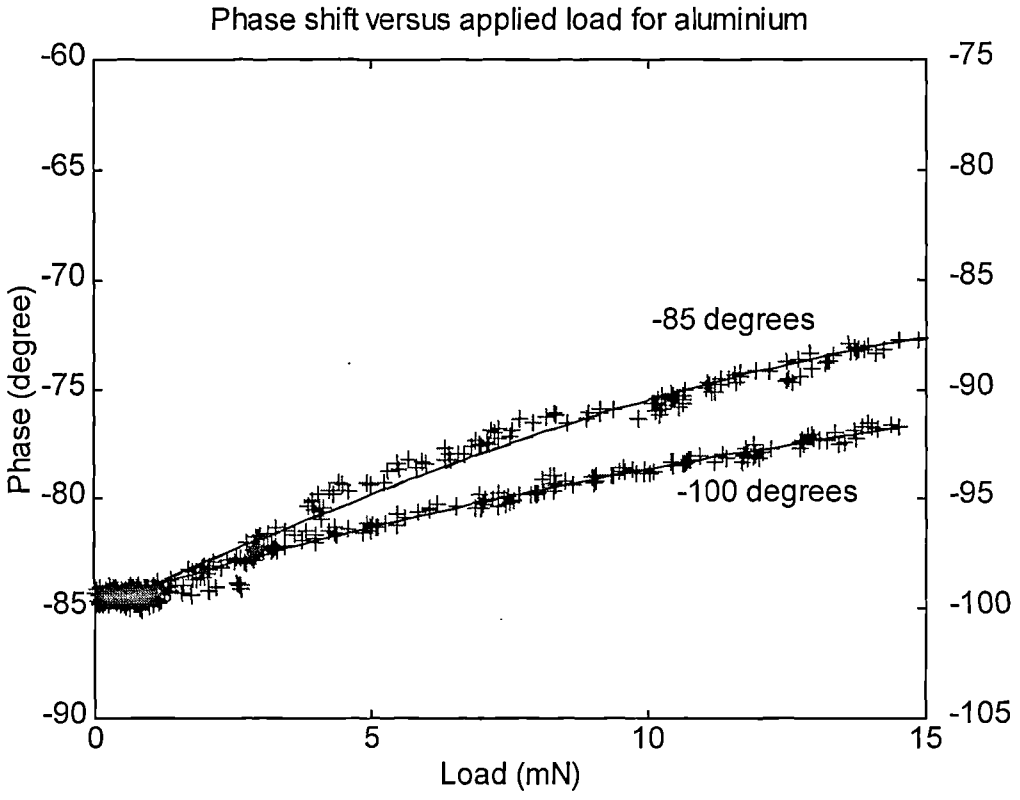

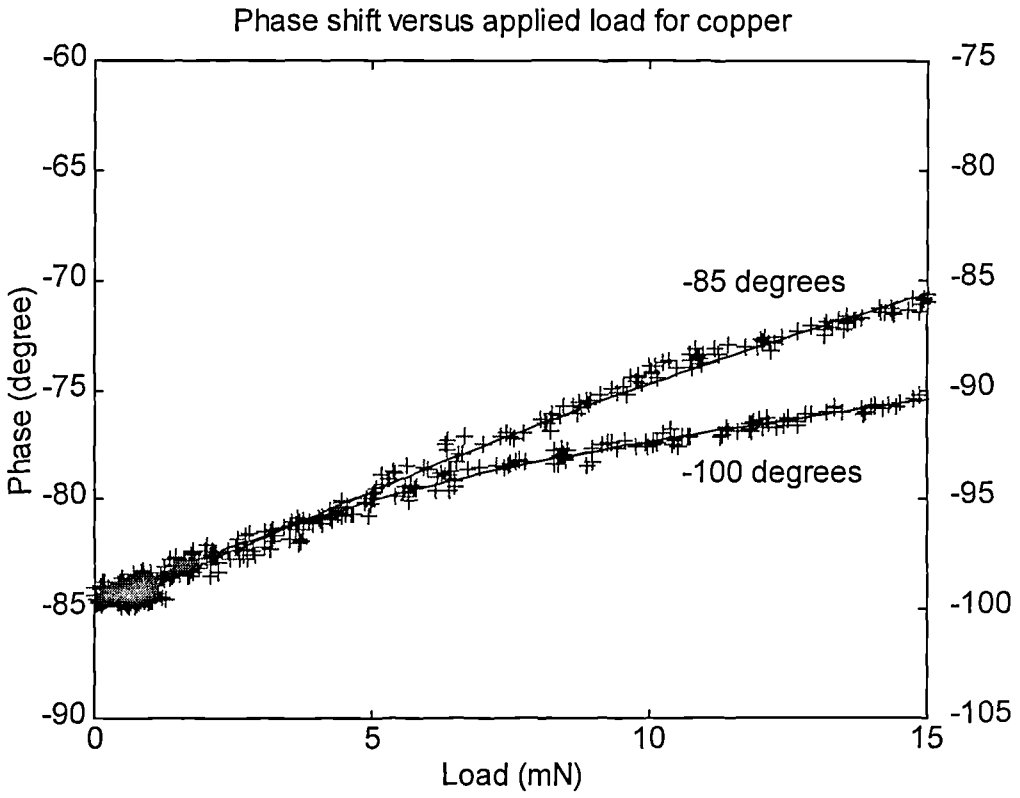
Phase shift versus applied load for copper
-60
-65
-70
-75
-80
-90
-75
-80
-85
-90
-95
-100
-105
0
5
10
15
Phase (degree)
Load (mN)
-85 degrees
-100 degrees

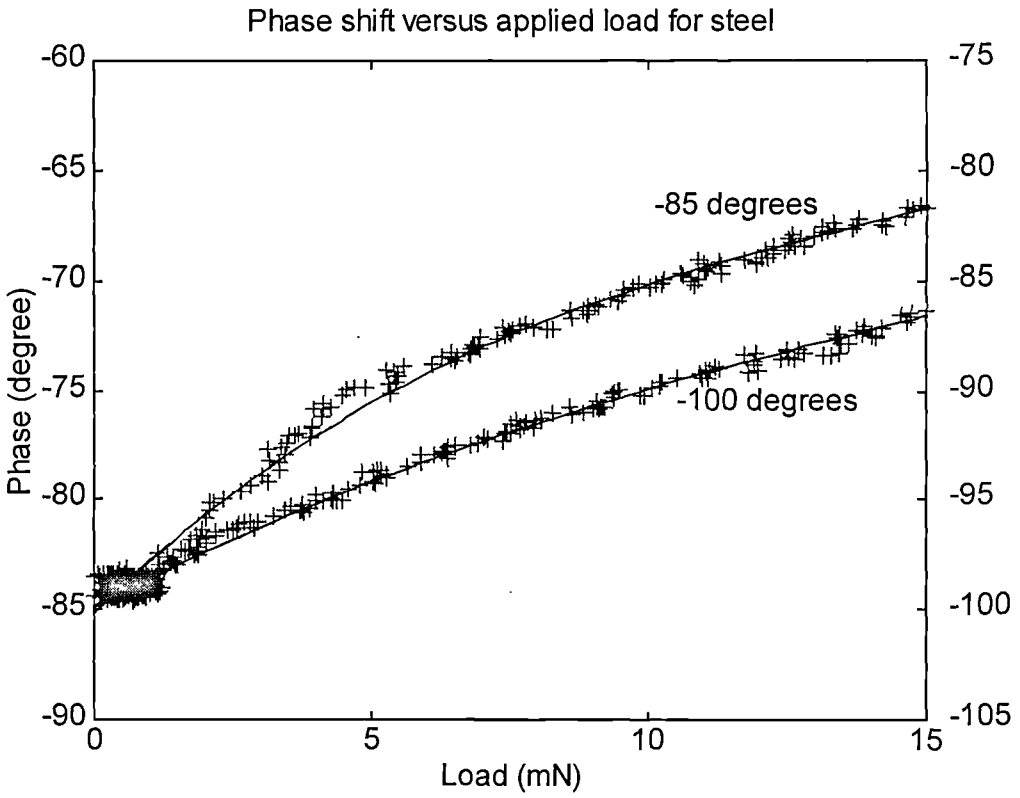
Phase shift versus applied load for steel
-60
-65
-70
-75
-80
-90
-75
-80
-85
-90
-95
-100
-105
0
5
10
15
Phase (degree)
Load (mN)
-85 degrees
-100 degrees

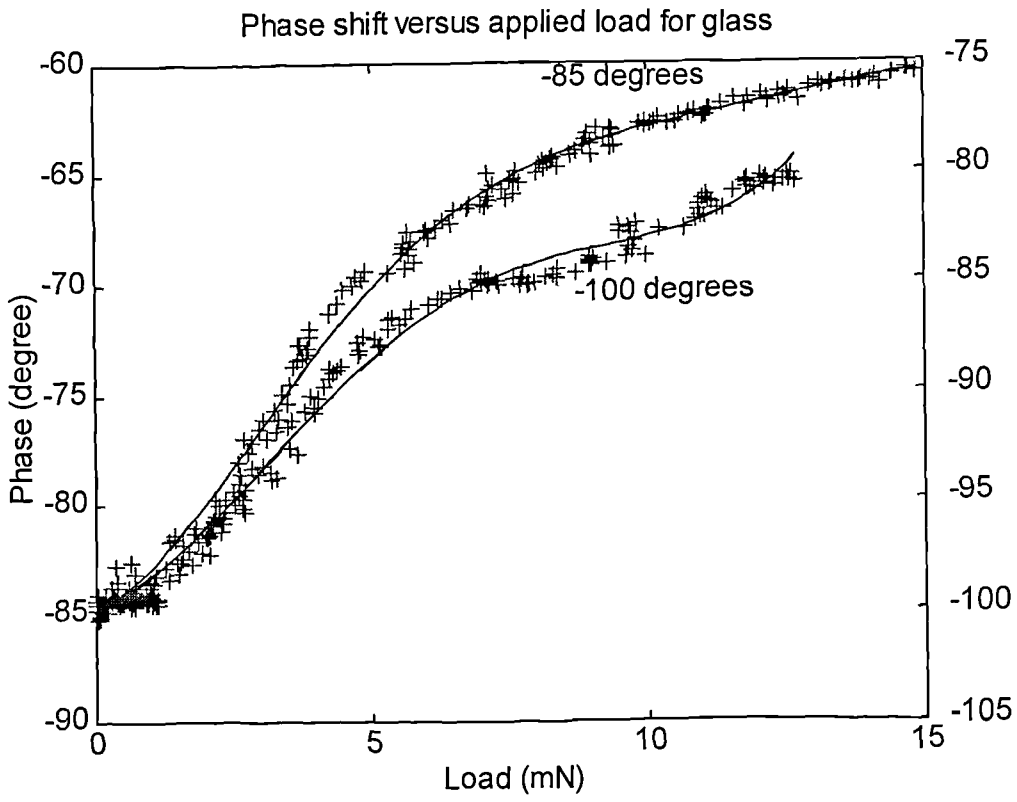

F.2. Comparison of mathematical model and experimental results for different materials

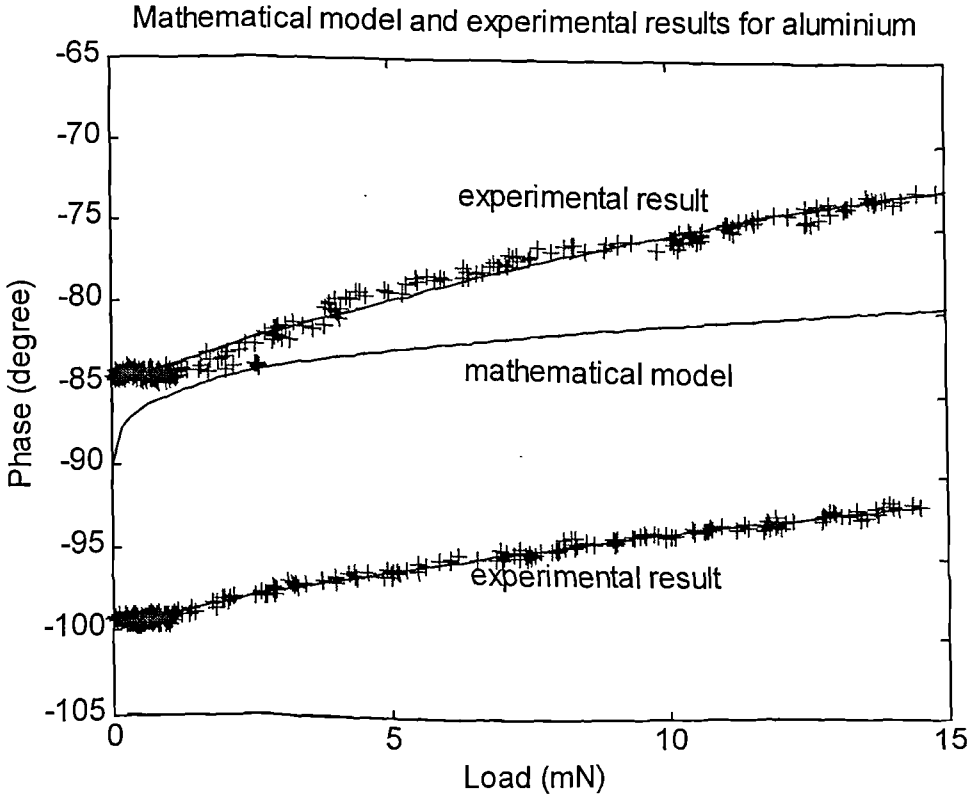

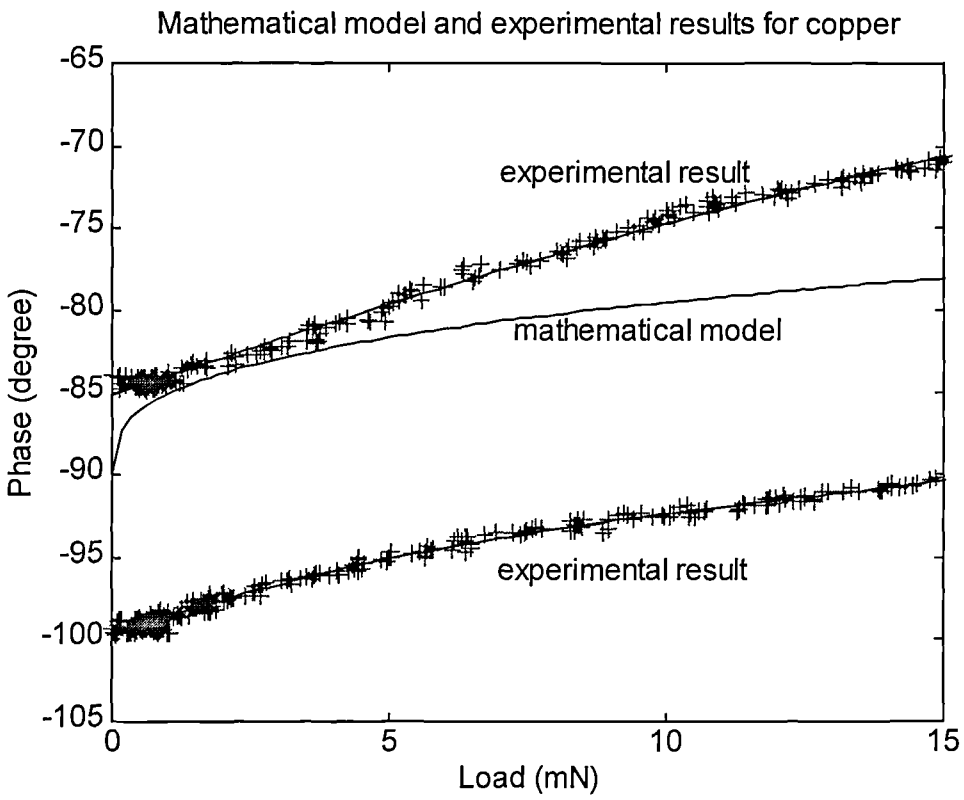
Mathematical model and experimental results for copper
-65
-70
-75
-80
-85
-90
-95
-100
-105
Phase (degree)
experimental result
mathematical model
experimental result
0
5
10
15
Load (mN)

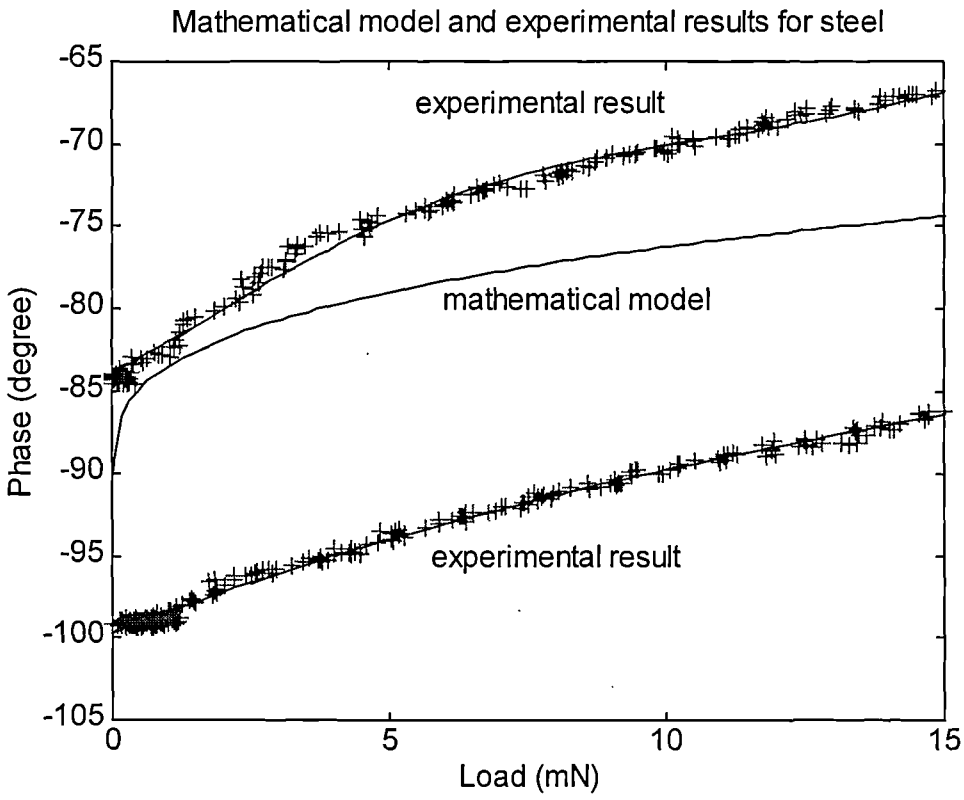
Mathematical model and experimental results for steel
-65
-70
-75
-80
-85
-90
-95
-100
-105
Phase (degree)
experimental result
mathematical model
experimental result
0
5
10
15
Load (mN)

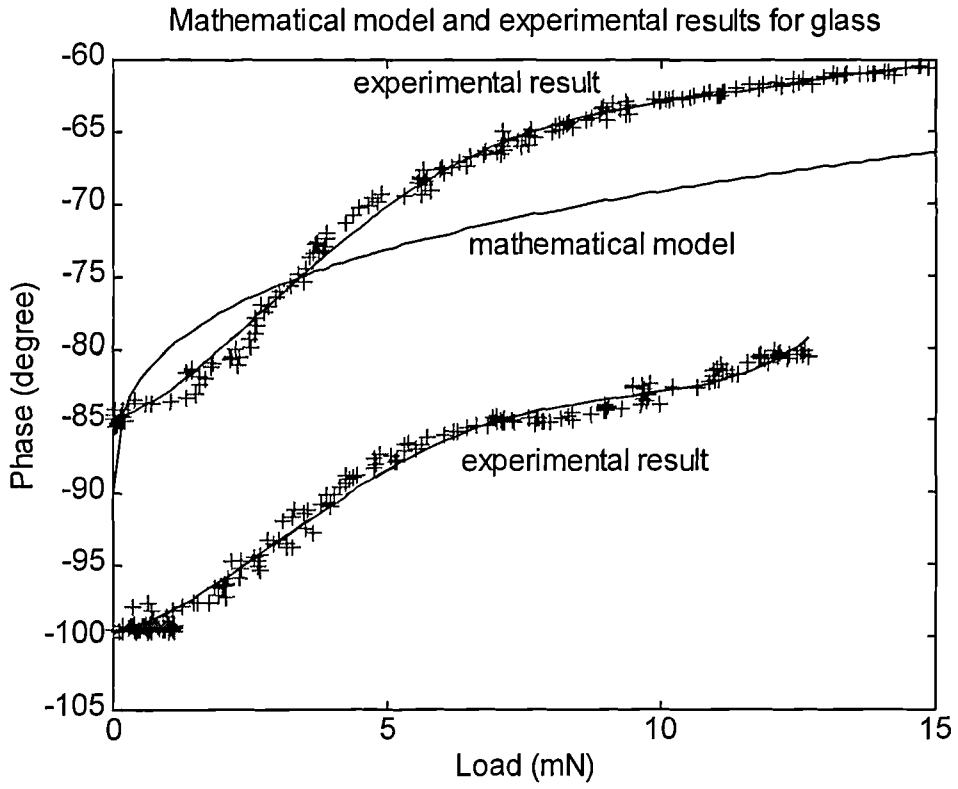
Mathematical model and experimental results for glass
experimental result
mathematical model
experimental result
Phase (degree)
Load (mN)
-60
-65
-70
-75
-80
-85
-90
-95
-100
-105
0
5
10
15

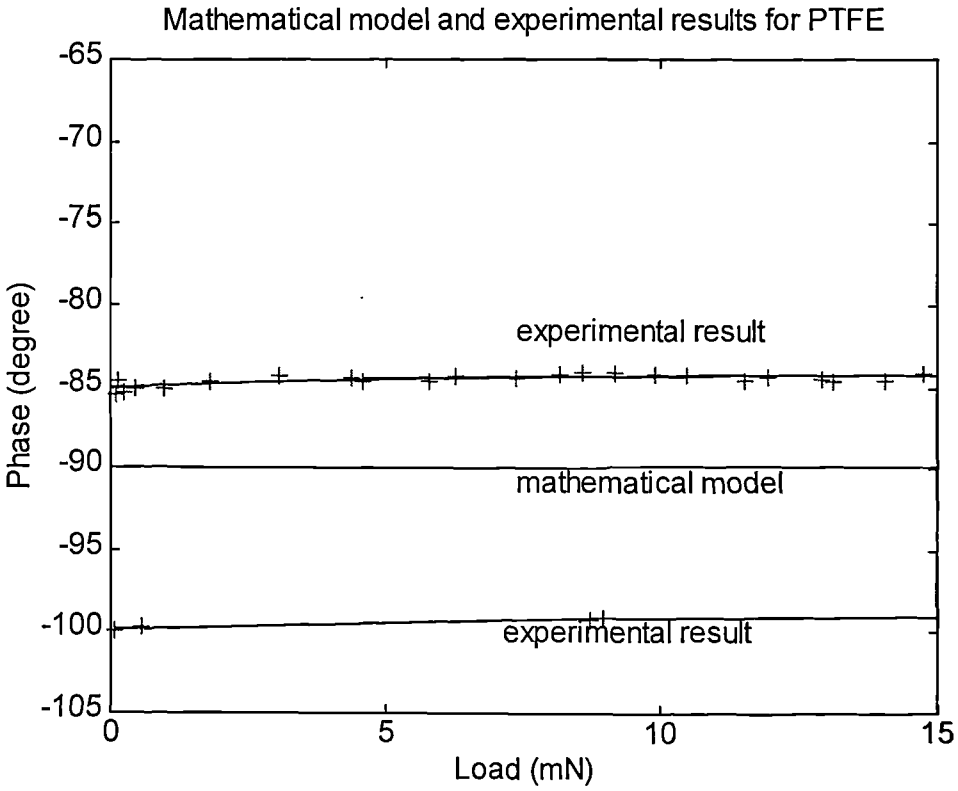
Mathematical model and experimental results for PTFE
experimental result
mathematical model
experimental result
Phase (degree)
Load (mN)
-65
-70
-75
-80
-85
-90
-95
-100
-105
0
5
10
15

F.3. Plots showing phase shift versus probe displacement for different materials

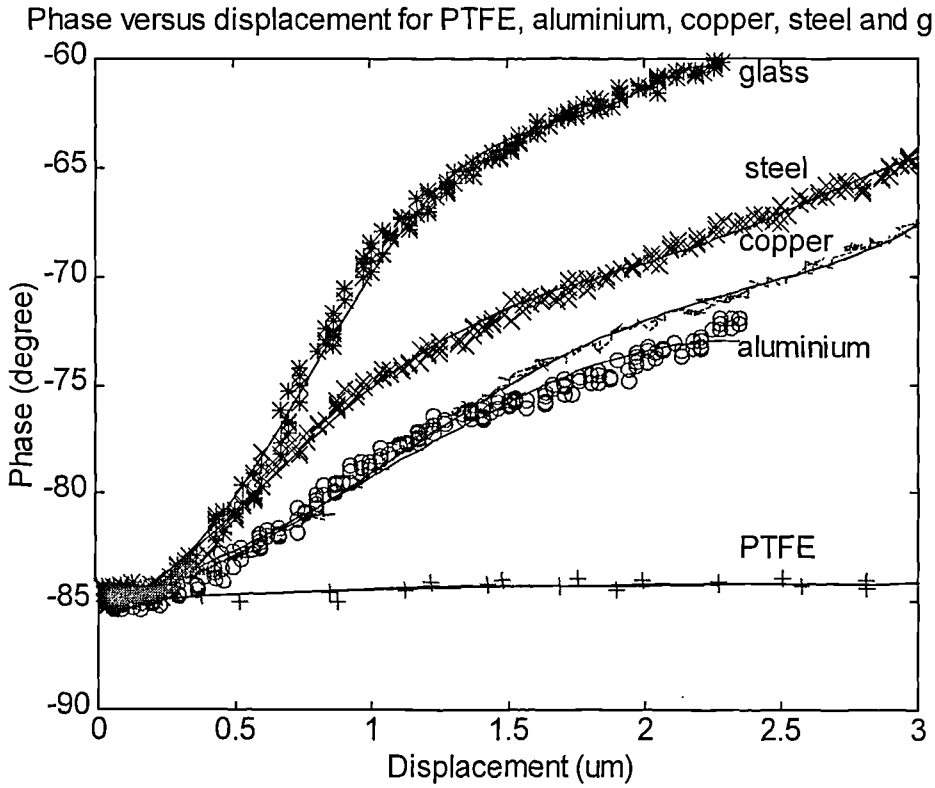

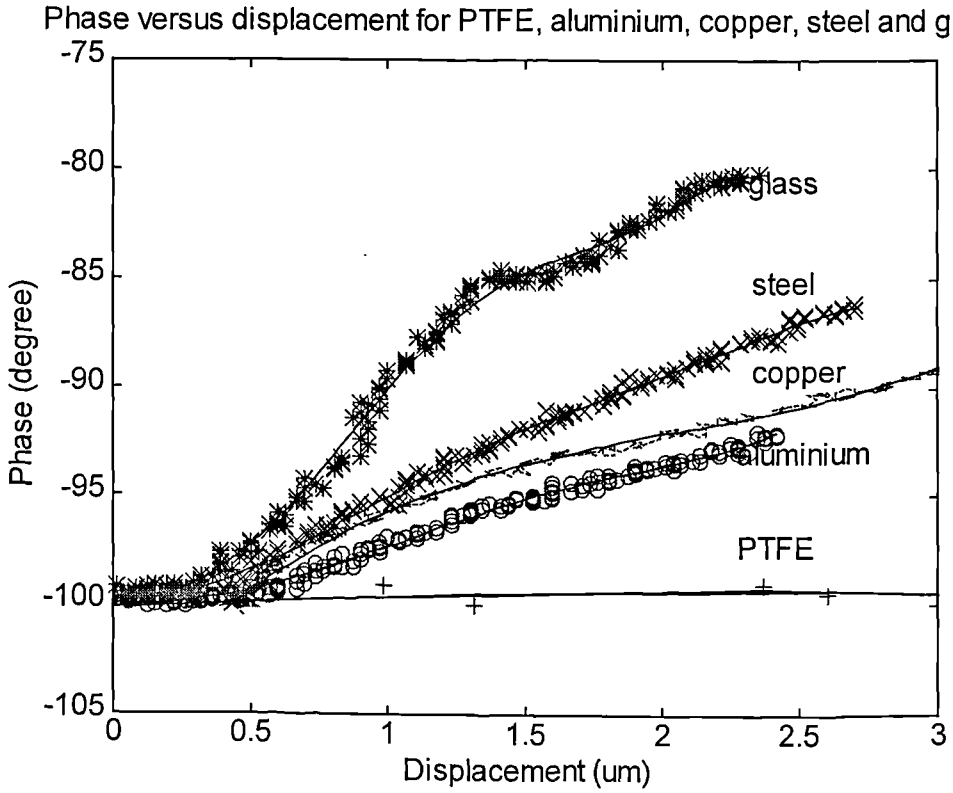

Appendix G

Fitting a circle through a set of points

Fitting a circle to a set of points

Problem: Given N Points: (x1,y1); (x2,y2).. (xN,yN), we want to find for best-fit circle: (X0,Y0), R. (Note: for fitting an *ellipse*, substitute the equation for an ellipse for the equation for a circle in the "Brute Force Approach").

Brute Force Approach (leads to a non-linear system): [Amara Graps]

Idea: Minimize by least squares the root-mean-squared error of the radius in the equation for a circle. In this method, one minimizes the sum of the squares of the *length* differences, which gives you a non-linear problem with all the associated pitfalls.

(x-X0)^2 + (y-Y0)^2 = R^2 Equation for a circle
R = SQRT[(x-X0)^2 + (y-Y0)^2)] Radius of the circle

where:

(X0,Y0) = center of circle
(x,y) = point coordinates
R = radius

1) Get first estimate for (X0,Y0,R).

(Details: Find some points to make first estimates- either solve the circle exactly (3 equations, 3 unknowns) to get a first estimate of the center and radius, or just do a kind of centroid calculation on all points- to get a rough estimate of the center and radius.)

2) Calculate r (r1, r2,.. rN) for each of your N points from the equation for a radius of a circle.

3) Calculate the root-mean-squared error For example, for 5 given points on the circle:

RMS error = SQRT[[(r1-R)^2 + (r2-R)^2 + (r3-R)^2 + (r4-R)^2

+ (r5-R)^2] / 3]

(dividing by "3" because we have 3 free parameters.)

4) Change (X0,Y0,R) slightly in your minimization algorithm to try a new (X0,Y0,R).

(Details: Because minimization algorithms can get very computationally intensive, if one's problem is a simple one, I would look for a "canned" minimization routine. Some commercial computer programs for plotting and spreadsheets do this sort of thing. For example, the Excel spreadsheet has a built-in "solver" that will perform minimzation. Other possibilties for software: Matlab with the optimization toolbox, MACSYMA, ODRPACK from Netlib, and the recent L-BFGS-B package which allows you to specify bounds on the variables, from:
L-BFGS-B

5) Calculate r (r1, r2 etc.) again from new (X0,Y0,R) above.

6) Calculate RMS error again.

7) Compare current RMS error with previous RMS error. If it doesn't vary by more some small amount, say 10^{-3} then you're done, otherwise continue steps 4 -- 7.

Other References:
Berman & Somlo: "Efficient procedures for fitting circles..." IEEE Instrum & Meast., IM-35, no.1, pp. 31-35, 1986. [Peter Somlo]

Other (more elegant) approaches that reduce to a linear system.

If you choose to minimize the squares of the *area* differences, you get a linear problem, which is a much safer way. [Pawel Gora, Zdislav V. Kovarik, Daniel Pfenniger, Condensed by Amara Graps]

1. Function to minimize is (sum of the area differences):

Q = Sum { [(xi - X0)^2 + (yi -Y0)^2 - R^2]^2 , i=1..N }

2. A necessary condition is the system of 3 equations with 3 unknowns

X0, Y0, R. Calculate the partial derivatives of Q, with respect to
X0, Y0, R. (all d's are partial)

dQ / dX0 = 0
dQ / dY0 = 0
dQ / dR = 0

3. Developing we get the linear least-squares problem:

```
| x1 y1 1 | | a | | -x1^2-y1^2 |
| x2 y2 1 | | b | =~ | -x2^2-y2^2 |
| x3 y3 1 | | c | | -x3^2-y3^2 |
| x4 y4 1 | | -x4^2-y4^2 |
| x5 y5 1 | | -x5^2-y5^2 |
..... .....
```
(for example, for 5 points)

where a = -2 X0; b = -2 Y0 ; c = X0^2 + Y0^2 - R^2. Take any good least-squares algorithm to solve it, yielding a,b,c. So the final circle solution will be given with X0 = -a/2; Y0 = -b/2; R^2 = X0^2+Y0^2 - c.

By the way, with 5 points you can also find the unique quadratic form (ellipse, hyperbola) which passes exactly through 5 points. With more than 5 points one can do a linear least-squares as well. The problem is then to minimize:

```
| x1^2-y1^2 x1y1 x1 y1 1 | | a | | -x1^2-y1^2 |
| x2^2-y2^2 x2y2 x2 y2 1 | | b | =~ | -x2^2-y2^2 |
| x3^2-y3^2 x3y3 x3 y3 1 | | c | | -x3^2-y3^2 |
| x4^2-y4^2 x4y4 x4 y4 1 | | e | | -x4^2-y4^2 |
| x5^2-y5^2 x5y5 x5 y5 1 | | f | | -x5^2-y5^2 |
..... .....
```

There are Fortran programs fcircle.f, fellipse.f and the Lawson & Hanson least-squares routines ls.f showing how to implement these least-squares problems at:
Circle Programs

The robust or L1 or least-first-power approximation [Zdislav V. Kovarik].

If you try to minimize

W(a,b,r) = SUM(j=1:N) ABS (((x_j-a)^2 + (y_j-b)^2)^(1/2) - r)

all you have to do is set up the 10 (i.e. if 5, choose 3) circles passing through every choice of 3 of 5 points, calculate W(a,b,r) for each of them and pick the minimizing circle. The extra feature is that this procedure separates and discards points which are conspicuously far from the majority trend. (Of course, it becomes increasingly time-consuming when the number of given points increases.)

[Amara Graps] This method of determining the minimum bounding circle from a set of _circles_ is solved, and with code available at:
Sky Coyote

Return to Numerical Analysis FAQ Home Page

Updated: Mon Aug 31 20:27:00 1998

Appendix H

Rapra: Technical products

Rapra.net

Technical products

The Rapra Scanning Vibrating Needle Curemeter (SVNC)

Rapra's SVNC is a simple, versatile and relatively inexpensive instrument for monitoring cures in liquid formulations as in, for example, cast elastomers, sealants, polyurethanes foams and thermosetting resins. A second instrument, the Rapra Foam SVNC, has recently been launched. This has specifically been designed to monitor the cure of foam samples ranging from 2 to 25 litres.

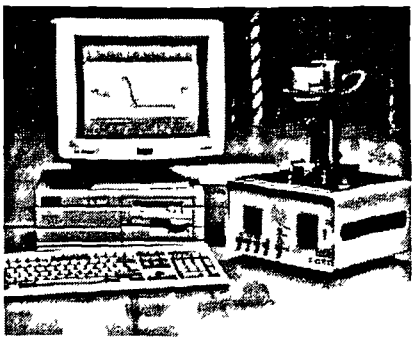

The standard instrument (pictured above) provides a continuous record of cure progression - even through gel point - providing a profile of both pre-gelation and post-gelation stages. The fully automatic stand allows the needle to be positioned to within 10 microns in the heat stage giving accurate and fast positioning which is important for providing reproducible results. The SVNC is an invaluable tool for those engaged in troubleshooting, quality control or product development with liquid curing systems for either rubbers or plastics. The precise needle positioning extends the scope of the instrument to surface coatings, paints and resins. A separate monitoring position is easily accessed for small (upto 200 millilitre) foam samples.

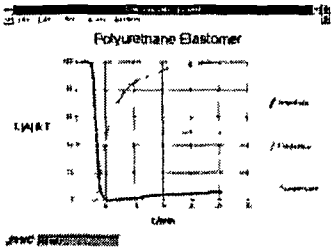

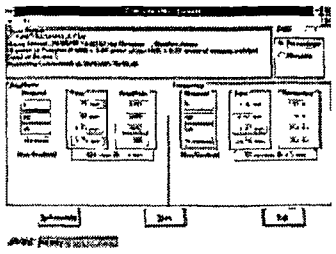

The above figure shows the two SVNC traces, resonance frequency and amplitude, and the cure temperature which was 50°C. Both the frequency and amplitude traces are given as a percentage change. Prior to the gel point, the amplitude trace indicates the change in the viscosity of the formulation, the resonance amplitude decreasing as the viscosity increases. Later in the cure, after the gel point, the amplitude starts to increase again. This indicates that the damping in the curing material is decreasing due to the development of resilience as the cure progresses and the polymer network becomes more complete. The gel point is indicated by the initial shift in the resonance frequency. The continued increase in the resonance frequency indicates the increase in the storage modulus as the cure progresses beyond the gel point.

More

Home | E-mail

Rapra.net

Technical products

The Rapra Scanning Vibrating Needle Curemeter (SVNC)

The Foam SVNC provides the continuous recording of the cure profiles (resonance frequency and amplitude) as with the standard instrument. In addition further data is recorded relating the development of exotherm and the rate of rise for the foam sample to those of cure. As the materials react the interaction of the exotherm, blowing, and cure can be seen in real time. The instrument has been designed to cater for all reactive foam samples ranging from 2 to 25 litres. However sizes outside this range could be easily be used.

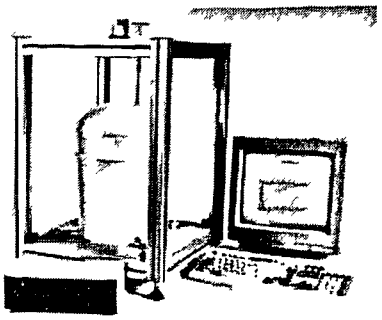

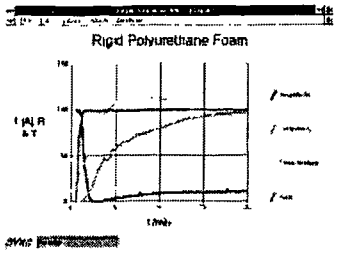

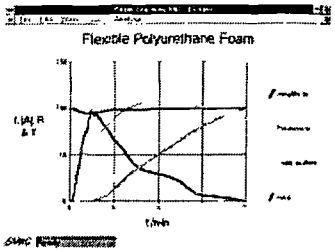

The above figure shows a typical set of traces generated from rigid and flexible polyurethane foams. The four separate responses for amplitude, frequency, temperature and rise can be seen. The amplitude, frequency and rise plots have been normalised (i.e. max. value =100). The temperature is shown in °C, and reaches 113°C after 7 min 50 sec. The fact that the frequency continues to increase beyond this point shows that the cure reactions are still progressing - even after the mix begins to cool. This indicates that the point where the mix begins to cool is not the end of the chemical sequence, but merely the point where the heat generated by continued reaction is not sufficient to maintain the elevated temperature against heat losses.

The cream time of a foam is the point at which gas bubbles begin to form within the reacting liquid. This corresponds with the initial increase in the rise profile after 30 seconds. The sharp decrease that is seen in the amplitude trace at 65 seconds is due to a fast increase in the viscosity of the foam material. This point has been seen to be indicative of the string time for the material.

The rise time is shown to be 85 seconds for this cure, fractionally before gelation as determined by the +5% frequency shift. This close timing is not unexpected, as it is undoubtedly a feature of stable foam formation. In this case the stability of the resultant foam is indicated by maintenance of a steady height through and beyond the exotherm peak. Examining this data gives a clear 'finger print' of the reaction identifying previously unknown criteria.

Other features and benefits of the SVNC and Foam SVNC include:

- No requirement for sophisticated torque measuring devices or displacement transducers
- Provision of a continuous record of cure progression
- Monitoring through the transition from viscous to elastic
- Ability to work with free-flowing liquid starting materials
- Ability to profile chain extension with crosslinking - 'finger printing' the reaction
- Ability to work without damage to systems which set hard

- Availability of software for storage, retrieval and comparison of data

For more information please contact Keith Scott on:

Tel: +44 (0)1939 250383
Fax: +44 (0)1939 251118 or ➢e-mail

Home | E-mail

Appendix I

Publications from this thesis

Reprinted from

SENSORS AND ACTUATORS A PHYSICAL

Sensors and Actuators A 50 (1995) 23–29

Resonator-based touch-sensitive probe

S.M. Harb, M. Vidic

Coventry University, School of Engineering, Priory Street, Coventry CV1 5FB, UK

Received 11 November 1994; in revised form 23 May 1995; accepted 8 September 1995

ELSEVIER

ELSEVIER

Sensors and Actuators A 50 (1995) 23–29

SENSORS AND ACTUATORS A PHYSICAL

Resonator-based touch-sensitive probe

S.M. Harb, M. Vidic

Coventry University, School of Engineering, Priory Street, Coventry CV1 5FB, UK

Received 11 November 1994; in revised form 23 May 1995; accepted 8 September 1995

Abstract

This paper presents a design of a simple low-cost resonator-based touch-sensitive probe. The design exploits the fact that when a stiff element (probe) oscillating near the resonance frequency comes into physical contact with the surface of another body (workpiece), the frequency of vibrational resonance of the probe changes depending on the latter's stiffness. This change can be detected by monitoring the variations in the phase shift between the probe driving force and the resulting strain, which consequently prompts the trigger signal. Standard phase-lock-loop oscillator circuitry is used to adjust the drive frequency to maintain a pre-set phase difference between the input and output signals, thus ensuring that the oscillator remains locked at the probe resonance frequency as contact takes place. A prototype probe has been designed and tested. The probe is excited to resonate at its fundamental frequency by employing piezoelectric drive and pick-up arrangements. The operating frequency of the probe is set at 25.179 kHz (second-mode frequency), which seems to be an adequate choice for excellent static and dynamic characteristics. The shift in the natural frequency as the contact force progresses follows a non-linear trend before it saturates. The maximum frequency shift measured is about 2 kHz, which corresponds to 140 mN contact force in the axial direction, whilst the minimum detectable trigger force is 3.8 mN.

Keywords: Resonator-based sensors; Touch-sensitive probes

1. Introduction

There is an increasing need for high-sensitivity high-speed touch-sensitive probes (TSPs). This requirement is necessary to meet the ever-growing demand for high-precision coordinate-measuring machines. Current development of a touch trigger probe is based on circuit breaking as the result of probe deflection due to a difference in contact resistance [1]. Due to the inherent design principle, lobbing effects and variations in the triggering forces of these probes have limited their reliability at sub-micron level accuracy. In addition, the slow dynamic performance has restricted their high-speed measurements.

This paper highlights the design and characterization of a high-sensitivity resonator-based TSP. Resonator-based sensors have been proposed and used successfully in a wide range of applications, including sensors for liquid or gas density and viscosity [2,3], liquid level, mass, microbalances [4], and also for sensing stresses, pressure and mechanical forces [5,6]. Resonator sensors of some sort have also been very popular in the design of scanning probe microscopy (SPM), which is used for high-resolution imaging of surface structures and surface electron spectroscopy [7–9].

In this paper, a similar principle will be adopted for the design of a high-sensitivity TSP. The probe consists of a stiff cantilever beam vibrated longitudinally by a PZT layer cemented onto one side; another layer of PZT, acting as a pick-up element, is cemented on the other side of the beam. The design principle exploits the fact that when a rigid element (probe) is oscillated at near it resonance frequency and comes into physical contact with the surface of another body (workpiece), there is an increase in the force gradient acting on the probe tip regardless of the rigidity of the workpiece. This increase gives rise to a shift in the frequency of vibrational resonance, Δf, of the probe. By detecting this frequency shift, a threshold circuit can be used to provide a 'trigger signal' for the controller to record the current position of the probe in space with respect to the machine coordinate system.

Various frequency-shift detection techniques have been proposed and used, including the slope detection method [10] in which the oscillation amplitude is measured when the probe is driven at a frequency slightly off resonance. A change in the force gradient causes the resonance frequency to shift, which results in a change in the steady-state amplitude. Other direct measurements of changes in the resonance frequency employ the frequency modulation (FM) method [11]. An impedance sensing method has also been reported as a means of detecting the change in load conditions [12].

In this article, the frequency-shift measurement is based on a standard phase-lock-loop (PLL) technique [13]. It

SSDI 0924-4247(95)01046-6

involves an oscillator circuit that adjusts the drive frequency to maintain a pre-set phase difference between the input and output signals, thus ensuring that the oscillator remains locked at the probe resonance frequency. The PLL provides an output signal (d.c. level) proportional to the shift in resonance frequency.

2. Theory

The wave equation governing the longitudinal vibration of an isotropic bar is given in terms of displacement by [14]

$$\frac{\partial^2 U}{\partial x^2} = \frac{1}{c^2}\frac{\partial^2 U}{\partial t^2} \tag{1}$$

where c is the velocity of propagation of longitudinal waves in a solid body and is given by

$$c = (E/\rho)^{1/2} \tag{2}$$

E is Young's modulus and ρ is the density of the material, from which the general vibration solution, $U(x)$, for a longitudinal bar can be written as

$$U(x) = B_1 \sin(\omega/c)x + B_2 \cos(\omega/c)x \tag{3}$$

ω is the angular frequency and B_1 and B_2 are constants and can be determined from the boundary conditions. For a fixed–free bar, the boundary conditions are

$x=0$ displacement $U(0)=0$
$x=l$ strain $(\mathrm{d}U(l)/\mathrm{d}x)=0$

After considering the boundary conditions, the resonance frequency for the unloaded case becomes

$$\omega_i = \frac{(2i-1)\pi}{2l}(E/\rho)^{1/2} \quad (i=1, 2, 3, \ldots) \tag{4}$$

The lowest natural frequency of a bar of length l in the longitudinal mode is

$$\omega_1 = \frac{\pi}{2l}\left(\frac{E}{\rho}\right)^{1/2} \tag{5}$$

and the corresponding normal mode shape $\phi(x)$ is given by

$$\phi(x) = \sin\left(\frac{\pi}{2}\right)\frac{x}{l} \tag{6}$$

When the free end of the bar is loaded with some kind of mechanical impedance, the resonance (low-impedance) mode of vibration shifts depending on the nature of the load. It decreases if the load is mass-like and increases if it is spring-like. However, the shift does not exceed the original frequency separation of the particular resonant mode and the next anti-resonance frequency of the unloaded condition [14].

In this particular case, the probe is mainly employed as a high-precision tactile sensor, where the load is likely to be of spring type (repulsive load). Furthermore, the effective spring constant due to the interaction of the probe and specimen can be estimated using the Hertz equation of contact between two elastic bodies [15]. The equation models the indentation of the probe, δ, into the specimen using the following relationship:

$$\delta = \left(\frac{9P_0^2}{16RE^{*2}}\right)^{1/3} \tag{7}$$

where

$$\frac{1}{E^*} = \frac{(1-\nu_1^2)}{E_1} + \frac{(1-\nu_2^2)}{E_2}$$

R denotes the probe radius, P_0 the contact force and E and ν represent the modulus of elasticity and Poisson's ratio of the two contacting materials. The normal stiffness K_{eff} of the probe/specimen interface is the inverse of the compliance, defined as the derivative of deflection with respect to the applied load, that is [16]

$$K_{\mathrm{eff}} = \frac{\partial F_{\mathrm{m}}}{\partial \delta} = (6E^{*2}P_0R)^{1/3} \tag{8}$$

Here ∂F_{m} denotes the modulated force of the probe acting on the specimen.

A simple model of a probe consisting of a bar with cross-sectional area A and length l and in contact with a workpiece demonstrates that the resonance frequency and the effective spring constant (K_{eff}) of the probe/workpiece interaction are related by a transcendental equation

$$K_{\mathrm{eff}} = \frac{AE}{l}\frac{(\pi/2l)(E/\rho)^{1/2}}{\tan[\pi/2l)(E/\rho)^{1/2}]} = \frac{AE}{l}\frac{\omega_0}{\tan(\omega_0)} \tag{9}$$

Plotting the above relationship reveals that the shift in resonance frequency is more sensitive when the effective stiffness is close to the stiffness of the probe.

3. Construction of the resonator TSP

The basic body structure of the resonance TSP and its control system are shown in Fig. 1. The probe consists of an aluminium bar (4 mm×8 mm×30 mm) with both ends threaded. One end was fixed into a platform, which can in turn be mounted kinematically into the probe head rigidly attached to the machine quill, whilst on the other end of the probe an M2 thread stylus, with a 4 mm diameter sapphire ball, was mounted. Two rectangular plates of piezoelectric materials (PZT-5H) [16] were cemented on to the bar. One drives the probe (excitation gauge BEG/1-6) and the other picks up the generated strain signal (strain gauge BSG/1-6).

The voltage applied to the PZT layer will induce axial stresses along the length of the probe, with some bending moment proportional to the lateral offset between the centre line of the probe and the PZT plane. An experimental test was performed to establish the vibrational modes of the tactile probe, by sweeping the frequency of a sinewave with constant

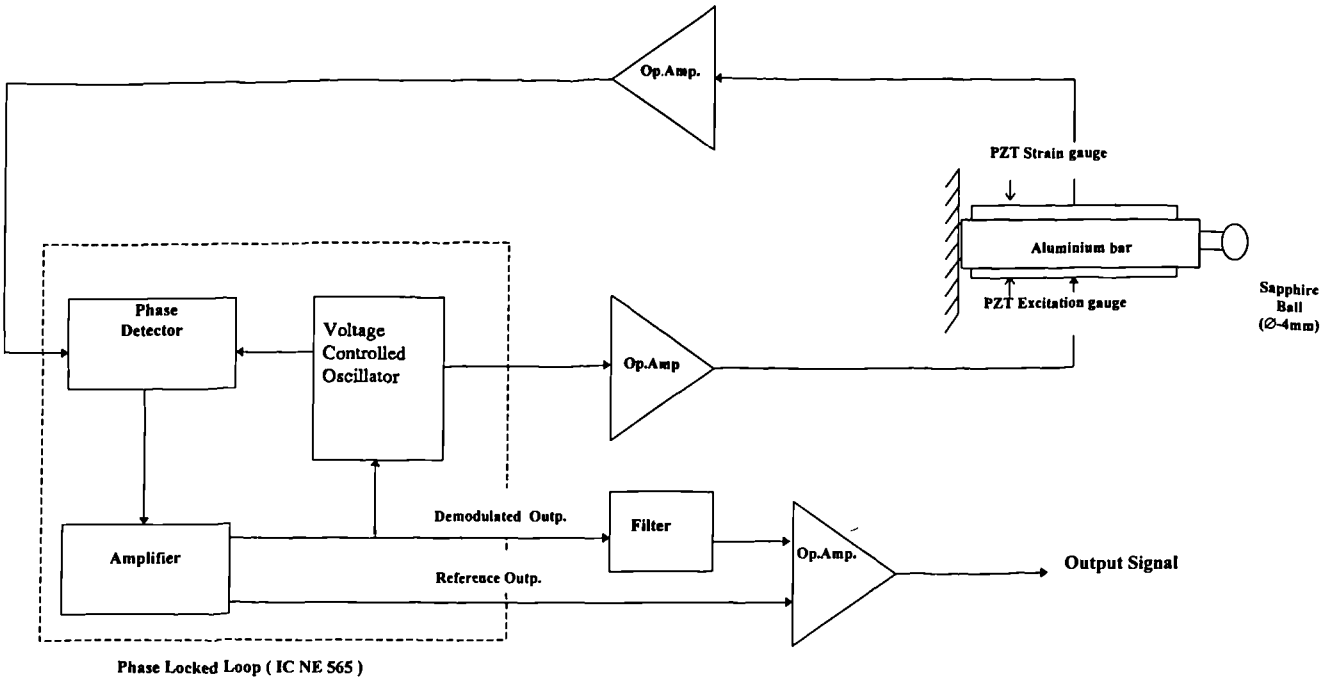

Fig. 1. Schematic diagram of the resonator-based touch-sensitive probe.

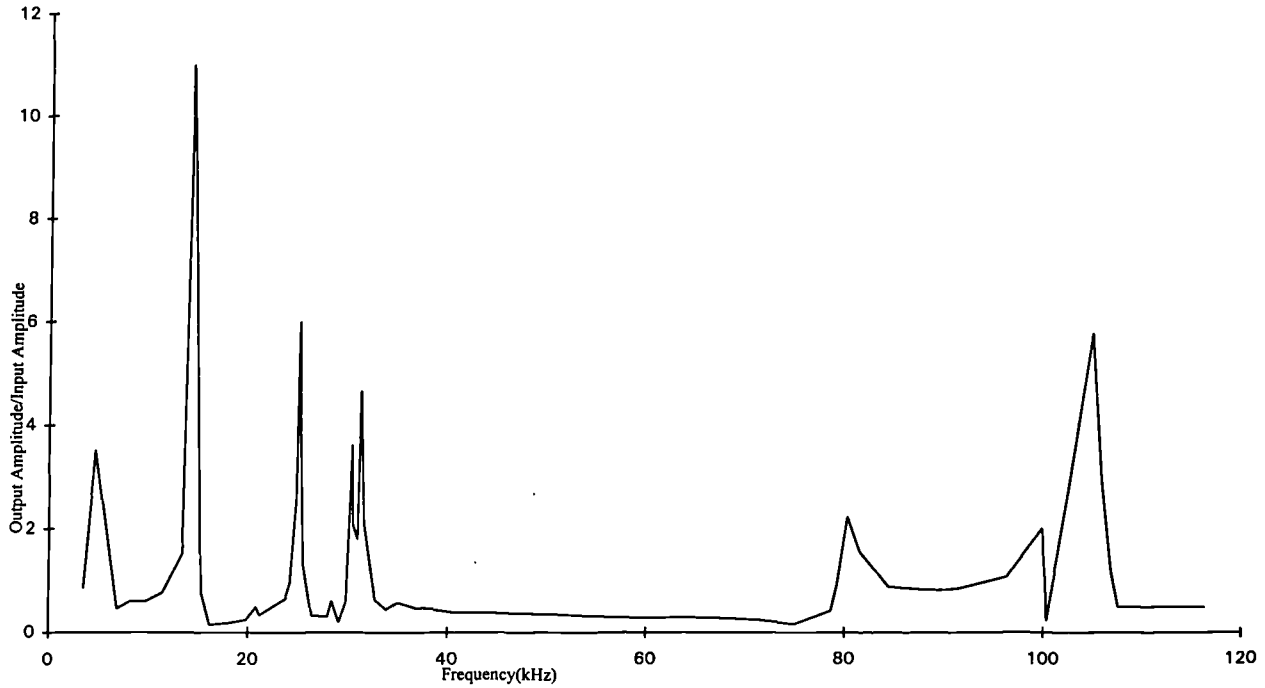

Fig. 2. A.c. voltage generated in strain gauge element at various frequencies.

amplitude driving the excitation gauge of the PZT, and measuring the r.m.s. piezoelectric voltage of the strain gauge. Fig. 2 presents the result of the vibrational mode spectrum. Although the fundamental resonance frequency occurs at 14.3 kHz (± 5 Hz), the second mode at 25.179 kHz was selected simply to eliminate audible noise. This has proved to be an adequate choice for good static and dynamic performance.

An analog PLL circuit was used to drive and monitor the shift in resonance frequency. Fig. 1 shows the block diagram of an electronic circuit that implement the PLL technique. A voltage-controlled oscillator (VCO) provides the driving signal (highly stable triangular wave), feeding the drive plate after amplification to 10 V peak-to-peak. The longitudinal strain generated in the probe is detected by the strain-gauge PZT plate. The phase shift between the drive and the strain

signal at the near-resonance frequency is set at 180°. As contact takes place, the changes in the resonance frequency shift the phase angle from its preset value. Instantly, the PLL technique adjusts the driving signal frequency to null the change in the phase angle. An NE 565 integrated circuit was used to implement the PLL technique. It consists of a phase comparator and VCO. The comparator provides an analogue signal proportional to the phase difference between the VCO signal and the strain signal, which feeds the VCO to adjust the input frequency to restore the preset phase relation, hence maintaining the vibration of the mechanical system at the new resonance frequency. The output of the PLL (d.c. level) is proportional to the changes in the resonance frequency, with a conversion rate of 0.73 mV Hz^{-1}. This output is then fed into an open gain op-amp to generate the OFF/ON trigger signal.

4. Experimental set-up

To evaluate fully the performance of the probe, a dedicated test rig was constructed. Fig. 3 shows the set-up used. The trigger force of the probe was generated by a simple linear flexure translation stage machined from an aluminium monolith and driven by an electromagnetic force actuator (solenoid and magnet). A samarium cobalt permanent magnet is rigidly cemented to the moving platform of the state and surrounded, but not touched, by a uniformly wound circular cylindrical solenoid coil. Current through the coil produces a magnetic field, inducing a force on the magnet that bends the flexure springs. The coil was controlled by a Darlington pair current driver. The flexure has a spring constant of 59 N mm^{-1} and the actuator has an overall gain of 8.2 μm V^{-1}. Displacement of the flexure was continuously monitored by a linear variable differential transducer (LVDT) which was periodically calibrated against a Hewlett–Packard laser interferometer system (HP 5528A). The conversion rate of the LVDT output was 20 μm V^{-1}. To coarse position the actuator with respect to the probe, the flexure was mounted onto a three degrees of freedom (X, Y, θ) manually operated micropositioning table. The probe meanwhile was attached onto a steel bracket, which in turn can be rotated about the longitudinal axis of the probe to form the fourth degree of freedom. Both the flexure and the probe were aligned horizontally in the same plane and placed at very close proximity.

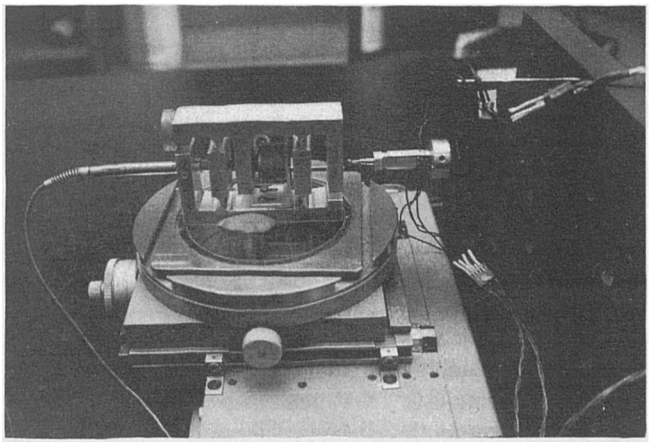

Fig. 3. Photograph of the prototype probe together with the test rig.

Prior to each test, a gap separation of around 0.1 mm was set between the probe's tip and the moving platform. The contact force vector is always aligned along the coil's centre line, while the contact arrangement is in the form of a sphere on a flat surface.

Recording and analysing the analogue signals from the PLL, the triggering signal, the LVDT and the input voltage to the solenoid coil were facilitated by the use of an IBM-compatible PC (Viglen 486 PC), via an ADC data-acquisition board (Amplicon Liveline Instruments PC74 16 I/O board with standard 12-bit resolution). Laser readings were recorded via a standard GPIB interface. The room in which these experiments were conducted is housed within a humidity- and temperature-controlled laboratory (a diurnal of approximately ± 2 °C was maintained).

5. Results and discussion

Calibration of the probe was performed by commanding the coil drive in a ramp to contact its tip. Triangular and sinewave inputs with various amplitudes (0.1–1.2 V) and frequencies (0.1–700 Hz) were tried. Simultaneously, the output from the PLL together with the flexure displacement were measured and recorded.

Fig. 4 shows a typical plot presenting the input sinewave driving the coil (a), the flexure deflection measured via the LVDT (b), the output voltage from the PLL (c) and the trigger signal (d). The amplitude of the input signal (1.2 V p–p at 0.5 Hz) corresponds to a maximum flexure deflection of 10 μm for a free run (contact free). The displacement of the LVDT was used here to detect the point at which contact takes place and also to measure the amount of indentation (Fig. 4(e)), from which the contact force exerted at the probe can be evaluated. The force, F, was estimated as the product of the indentation, δ, and the spring constant of the flexure, k ($F = \delta k$). The actual contact point was deduced from the trace of the LVDT signal as the point when the output starts to slow down compared to that of free run. Fig. 4(e) shows the amount of indentation, which was derived by subtracting the contact-free trace from trace (b). On the other hand, the probe triggers the moment the PLL output has an incremental increase of about 10 mV (corresponding to a shift of 14.5 Hz) from its pre-set value (just below 0 V).

Fig. 5 presents the relationship between the PLL output (Hz) and the probe/sample interaction. Although the graph shows a global non-linearity over its full range, two linear regions can be assumed: one up to 50 mN contact force with a gradient of 7.3 Hz mN^{-1} followed by a small jump and

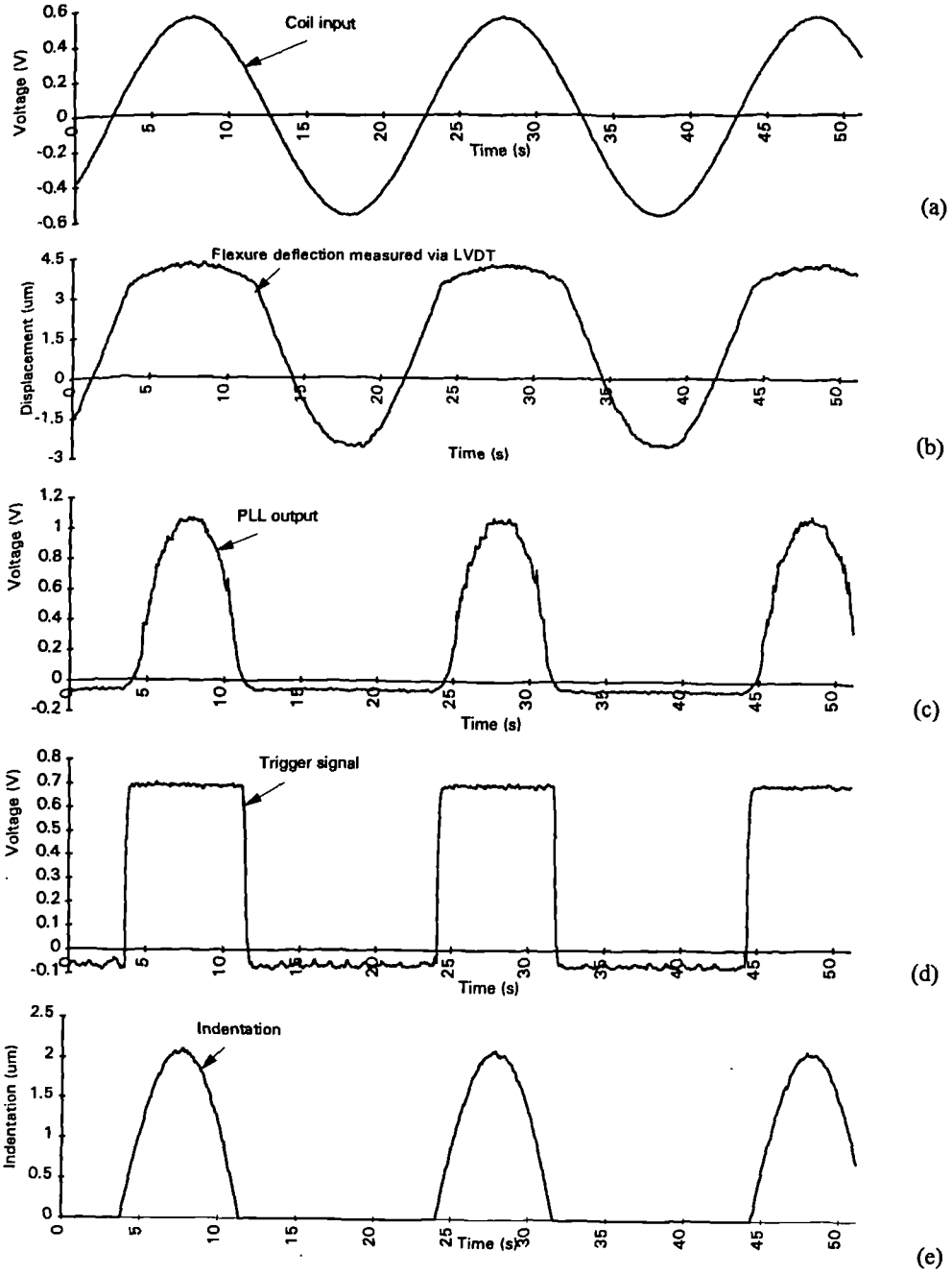

Fig. 4. Typical plot showing input sinewave (a), flexure deflection (b), PLL output (c), trigger signal (d) and amount of indentation (e).

another linear trend up to 140 mN with a gradient of 12.8 Hz mN^{-1}.

A repeatability test was conducted by driving the coil in steps of 0.4 μm over a 3 μm ramp. At each position the average of five readings of the PLL output was recorded. This was repeated over five cycles. Here the repeatability at each position was defined as the uncertainty band $\pm 2\sigma$ (4σ) from the mean value. Fig. 6 presents the mean value of the five cycles together with the $\pm 2\sigma$ from the mean. At the trigger point a repeatability of 40 Hz was estimated but as the indentation progressed the deviation was ± 200 Hz. The minimum force required to trigger the probe was set at about 4 mN. This compares favourably with most commercially available TSPs.

Fig. 7 shows the drift test of the PLL plotted together with the LVDT over a period of one hour. It demonstrates the stability and fidelity of the probe to slight variations in contact pressure compared with the LVDT reading.

Dynamic performance was defined as the maximum possible triggering rate. This, however, was limited by the bandwidth of the flexure mechanism to 700 Hz, at which the probe was still able to provide sufficient signals.

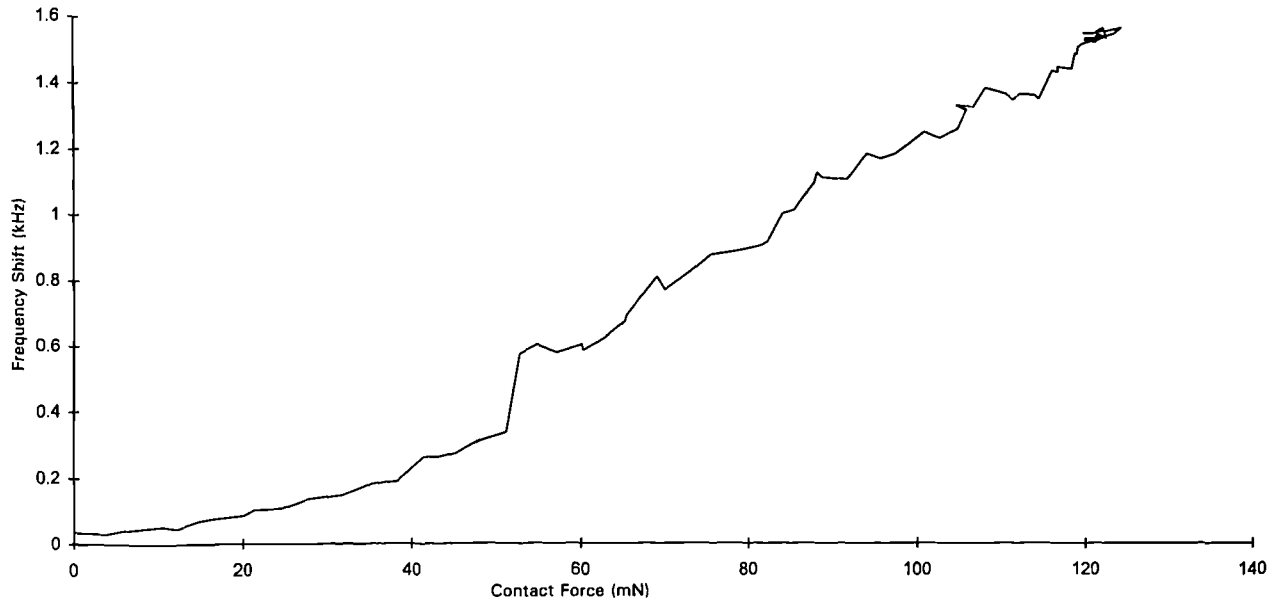

Fig. 5. Frequency shift (kHz) vs. applied contact force (mN).

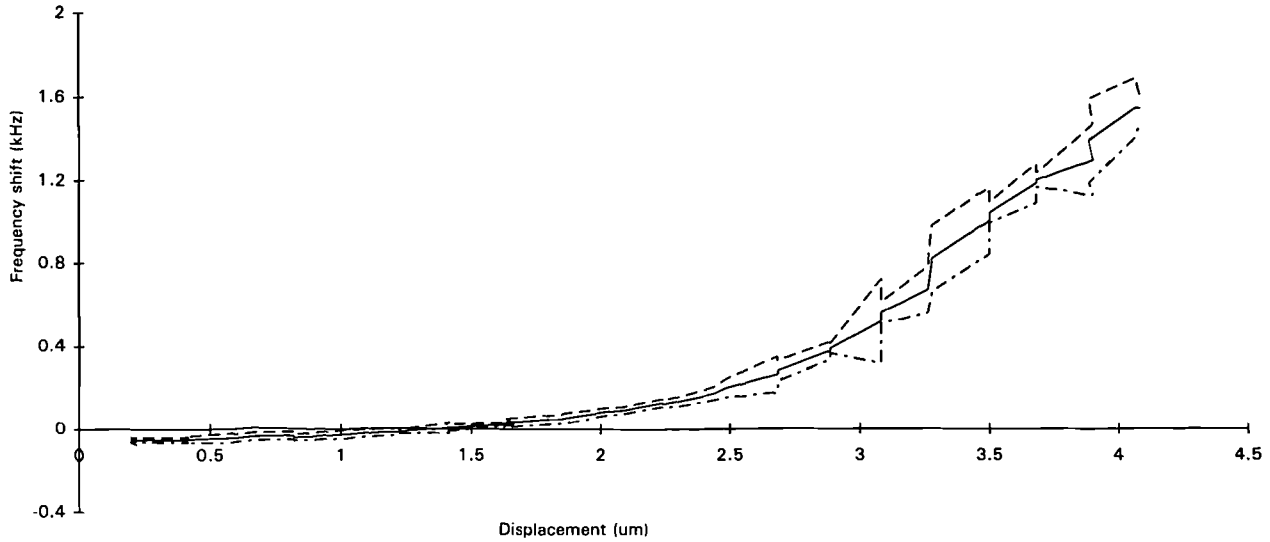

Fig. 6. The mean value of five cycles together with the deviation $\pm 2\sigma$ from the mean value.

Further tests are currently underway to examine the maximum permissible speed and to provide a more constructive comparison with commercially available touch trigger probes. The findings will be presented in future publications.

6. Conclusions

A simple low-cost resonator-based touch-sensitive probe is proposed for applications that involve coordinate measuring machines and high-precision machine tools, where high sensitivity, good repeatability and accuracy are of paramount importance. The design aims at improving the static and dynamic performance of currently used probes. A phase-locked-loop technique was utilized to detect any shift in the probe resonance frequency. To illustrate the potential of this approach, a prototype probe was designed and tested on a dedicated rig. The result of the tests reveals high sensitivity, a repeatability of ± 20 Hz (± 4 mN) and a trigger force of less than 4 mN, which can be easily adjusted depending on applications. It also demonstrates a triggering rate of more than 700 Hz.

Moreover, the probe is potentially attractive in applications that involve scanning the geometry of the workpiece. Here, the probe might act as a nulling device, feeding the force signal to the controller of the machine to maintain a constant interaction pressure.

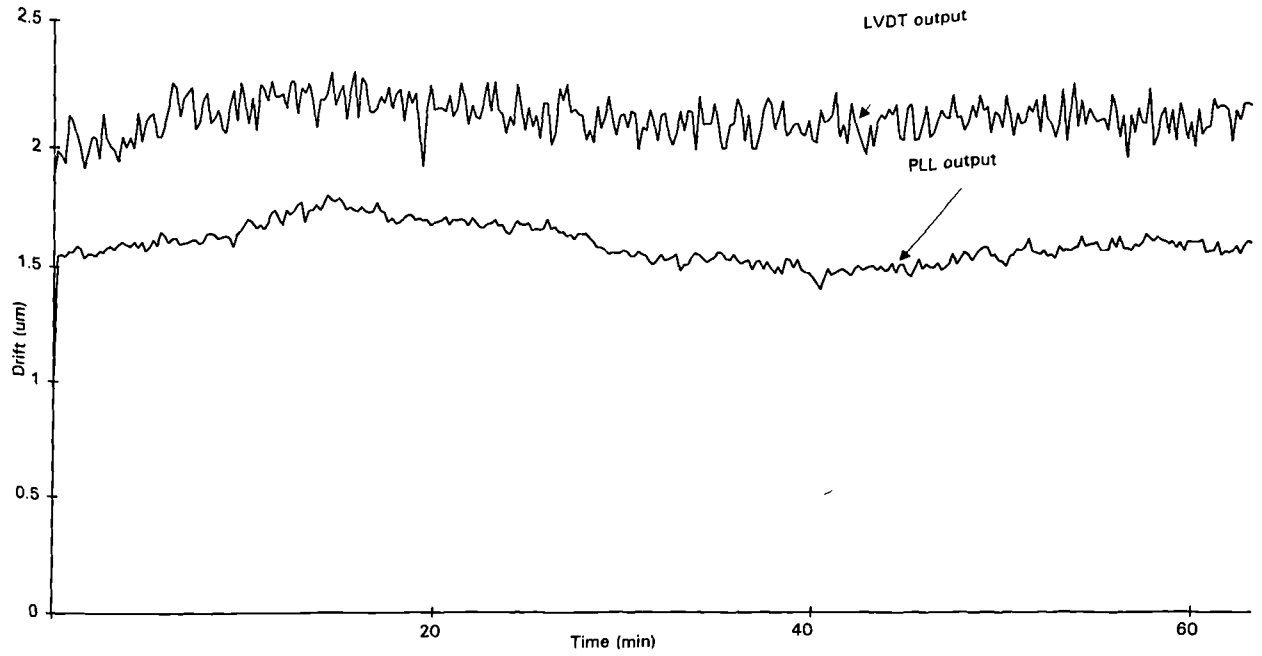

Fig. 7. Drift test of the PLL and LVDT over a period of 1 h.

Acknowledgements

The authors are grateful to both Coventry University School of Engineering and the Nuffield Foundation for supporting this research. Also we would like to thank Dr S.T. Smith for useful discussions and Mr P. Brennan and Mr B. Pittaway for technical assistance.

References

[1] Renishaw CMM Product Group 'General Product', Renishaw Precision Metrology and Insp. Equip., *Bulletin No. 4*, February 1992.
[2] R.M. Langdon, Resonator sensors – a review, *J. Phys. E: Sci. Instrum., 18* (1985) 103–115.
[3] T. Gast, Sensors with oscillating elements, *J. Phys. E: Sci. Instrum., 18* (1985) 783–789.
[4] B.J. Mulder, Simple piezoelectric microbalance based on a vibrating quartz wire, *J. Phys. E: Sci. Instrum., 17* (1984) 119–121.
[5] B. Morten, G. De Cicco and M. Prudenenziati, Resonant pressure sensor based on piezoelectric properties of ferroelectric thick films, *Sensors and Actuators A, 31* (1992) 153–158.
[6] A. Cheshmehdoost, S. Stroumboulis, B. O'Connor and B.E. Jones, Dynamic characteristics of a resonating force transducer, *Sensors and Actuators A, 41–42* (1994) 74–77.
[7] G. Binnig, C.F. Quate and C. Gerber, Atomic force microscope, *Phys. Rev. Lett., 56* (1986) 930–933.
[8] Y. Martin, C.C. Williams and H.K. Wickramasinghe, Atomic force microscope – force mapping and profiling on a sub 100 Å scale, *J. Appl. Phys., 61* (1987) 4723–4729.
[9] M. Wienmann, R. Radius and F. Assmus, Measuring profile and position by means of vibrating quartz resonators used as tactile and nontactile sensors, *Sensors and Actuators A, 37–38* (1993) 715–722.
[10] T.P. Albrecht, P. Grutter, D. Horne and D. Rugar, Frequency modulation detection using high-Q cantilevers for enhanced force microscope sensitivity, *J. Appl. Phys., 69* (1991) 668–673.
[11] R. Proksch and E.D. Dahlberg, A detection technique for scanning force microscopy, *Rev. Sci. Instrum., 64* (1993) 912–916.
[12] K. Takata, Novel method for detecting resonant frequency shift in atomic force microscopy, *Jpn. J. Appl. Phys., 32* (1993) 2455–2458.
[13] National Linear Data Book, *Application Note on LM 565 'Phase Locked Loop', National PLL.*
[14] J.C. Snowden, *Vibration and Shock in Damped Mechanical Systems*, John Wiley, London, 1968, pp. 134–192.
[15] S.T. Smith and D.G. Chetwynd, *Foundation of Ultraprecision Mechanism Design*, Gordon and Breach, UK, 1992.
[16] Morgan Matroc Ltd, A guide to the use of PZT piezoelectric strain, vibration and excitation gauges, *Bulletin 66022/c*, Thornhill, Southampton, UK.

Biographies

Salam M. Harb received the B.Sc. degree in 1983 and the M.Sc. in 1985 from the Middle East Technical University, Ankara, Turkey, and the Ph.D. degree in 1989 from the University of Manchester Institute of Science and Technology.

From 1989 to 1992 he was working with the Nanotechnology Group at the University of Warwick. He is currently a senior lecturer in the School of Engineering at Coventry University.

His present research interests are in high-precision sensors and instrumentation, mechanical metrology and inspection. He is a member of the ASPE.

Marina Vidic was born in 1964 in Yugoslavia. She received her B.Sc. degree in electrical engineering in 1988 from the University of Titograd, Yugoslavia. She spent four years in the Aluminum Factory, Podgorica, Yugoslavia, working as an engineer for planning and operative affairs. She is currently working for her Ph.D. at the School of Engineering, Coventry University, UK, where she is doing research on the design and application of a resonator-based probes.

Precision Engineering: The Journal of the American Society for Precision Engineering covers all subjects related to the design, manufacture, and application of precision machines and components. International news, reviews, conference reports, informed comment, and a calendar of forthcoming events complete the spectrum of coverage designed to keep readers abreast with a fast-moving technology.

All papers are refereed, and no page charges are levied by this journal.

Precision Engineering is published four times a year in January, April, August, and December by Elsevier Science Inc., 655 Avenue of the Americas, New York, NY 10010. Subscription rate: For customers in Europe, The CIS and Japan: Institutional rate NLG 983.00. For customers in all other countries: Institutional rate US$ 565.00. For customer service phone (212) 633-3950; TOLL-FREE for customers in the USA and Canada: 1-888-4ES-INFO (1-888-437-4636), fax (212) 633-3680, or e-mail: usinfo-f@elsevier.com. Claims for missing issues can be honored only up to three months for domestic addresses, six months for foreign addresses. Duplicate copies will not be sent to replace one undelivered through failure to notify Elsevier of change of address. Single copy and back volume information available upon request.

POSTMASTER: Send address changes to *Precision Engineering*, Elsevier Science Inc., 655 Avenue of the Americas, New York, NY 10010.

For Advertising Orders & Inquiries: North & South America: Tino DeCarlo, Elsevier Science Inc., 655 Avenue of the Americas, New York, NY 10010, Tel: (212) 633-3815, Fax: (212) 633-3820. International: Advertising Department, Elsevier Science, The Boulevard, Langford Lane, Kidlington, Oxford OX5 1GB, United Kingdom, Tel: (+44) (0) 1865 843565, Fax: (44) (0) 1865 843976. (e-mail: media@elsevier.co.uk). Japan: Advertising Department, Elsevier Science Japan, Tel: (81) (3) 5561 5033, Fax: (81) (3) 5561 5047.

PRECISION ENGINEERING

JOURNAL OF THE AMERICAN SOCIETY FOR PRECISION ENGINEERING

Volume 22 Number 1 January 1998

ORIGINAL ARTICLES

0141-6359(199801)22:1;1-X

ELSEVIER

Observations of contact measurements using a resonance-based touch sensor

M. Vidic and S. M. Harb
Coventry University, Coventry, UK

S. T. Smith
Precision Engineering Laboratory, University of North Carolina at Charlotte, Charlotte, NC, USA

A study of the contact mechanisms between a resonator probe sensor and a broad range of engineering surfaces is presented. The resonator-based touch sensor used in these studies consists of a prismatic beam clamped at one end with a spherical probe attached at the other. Pairs of piezoelectric (PZT) elements cemented at either side of the beam along its axis are employed; one to actuate and the other to pick up the strain signals. Over a band of frequencies near to a resonance, the sensor behaves like second-order system. When oscillated near to its resonant frequency, interactions between the probe tip and specimen are detected by monitoring phase or frequency shifts using phase-locking techniques. As the probe approaches and contacts a surface, a range of phenomena are observed. Approximate theoretical models have been developed to predict the effects characteristic of added mass, stiffness, and damping (i.e., kinetic, potential and dissipative energy transfer) for contacts between clean solids and when contaminant films are present. These models predict that phase and frequency shifts can either increase or decrease depending upon the dominant phenomena in the contact region. For example, when a solid surface is contacted by a clean probe, the resonant frequency can either increase or decrease depending upon the ratio of elastic modulus to density, and this is demonstrated with contact measurements made on metals and rubbers. A systematic method for the identification of the dominant effect (if there is one) based on observations of frequency or phase shifts using either constant phase or constant frequency monitoring is presented.

Keywords: resonator probe; touch sensor; contact force measurement; piezoelectric sensors

Introduction

Resonator-based sensors have been proposed and used successfully in wide range of applications, including measuring liquid or gas density, viscosity, and liquid level,[1] and sensing stress, pressure, and mechanical forces.[2] Other applications, including coordinate measuring machine (CMM) probes, stylus transducers, friction measurement, and surface mechanical probes (i.e., elastic modulus, density, and energy dissipation). One particularly promising application is for monitoring

Address reprint requests to Dr. S. M. Harb, Coventry University, School of Engineering, Priory Street, Coventry CV1 5FB, UK. E-mail: s.harb@cov.ac.uk

Precision Engineering 22:19–36, 1998

655 Avenue of the Americas, New York, NY 10010

0141-6359/98/$19.00
PII S0141-6359(97)00088-3

contact conditions or for dynamic control of interface forces. Although much work has been carried out on the development of resonant touch sensors for scanned probe microscopy,[3–5] commercial exploitation for precision applications have not been particularly successful. One reason for this is the complexity of the interaction between a resonant sensor and typical surfaces in less than ideal environments. Implementation of such systems requires an understanding of the nature of interaction between the resonating probe and a broad variety of surfaces. The experimental investigations in this study were conducted using resonator sensors already constructed.[6] The sensor consists of a cantilever beam vibrated by a piezoelectric (PZT) layer cemented onto one side; another layer of PZT is cemented onto the opposite side, which acts as a pick up sensor. Consequently, the frequency and phase of both drive and response signals can be readily monitored using standard phase-locking circuits.

To assess the interaction between a probe tip and typical engineering surfaces, the complete resonator was mounted onto an electromagnetic linear motion actuator for fine positioning of the probe, and the specimen was placed on a special mount of cantilever beam on which two strain gauges were mounted and arranged in a half Wheatstone bridge to detect the normal load. In subsequent experimentation, a 5-mm sapphire sphere typically used for CMM probes was employed as the tip.

For many applications, it is desired to know the nature of the contact. To this end, a variety of materials were assessed ranging from rough rubber to polished, hardened steel and surfaces covered by liquid films having viscosities ranging from 0.20 to 10 Pa s. A broad range of phenomena were observed both "before" and "at" contact with the surface. Characteristics of added mass, stiffness, and damping were observed, and these are illustrated with selected results from a large number of tests. This paper also presents approximate theoretical models for the prediction of such contact and near-contact effects as stiffness, mass, squeeze film, and surface film damping.

Theoretical model of the resonator sensor

In general, any changes in force at the end of the probe will effect the dynamics of the system. One particularly problematic aspect of theoretical modeling is attributable to changes in boundary conditions. For example, if the probe is undergoing lateral vibration, a "rigid" contact would change the end condition from "free" to either "sprung" or "hinged" or combinations thereof, the magnitude of which is difficult to predict. Adopting a system undergoing longitudinal vibrations could simplify modeling of the interaction between oscillating probe and contacting surfaces. The essential feature of this assumption is that the resonance can be considered to be a consequence of reflections of elastic waves from either end of the probe. Upon contact, it might be assumed that a physical barrier in the form of a change in velocity of elastic waves will occur. Consequently, such a process can be modeled as a simple longitudinal oscillator of length L, with the boundary conditions of added mass, stiffness, and damping at the free end. Applying Rayleigh's method to such a system, a natural frequency can be determined from the approximate equation

$$\omega_n \approx \sqrt{\frac{k_c + k_e}{M + m_e/3}} \tag{1}$$

where k_c, M, k_e, and m_e are the equivalent stiffness and mass of the probe and the effective added stiffness and mass during contact, respectively.

Commonly, two modes of contact detection are used for resonant sensors:

1. monitoring frequency at constant phase, hereafter called mode I; and
2. monitoring phase at constant frequency, mode II.

In both of these modes, modeling is considerably simplified if small variations about a 90° phase shift are considered. However, in reality, this is not easy to achieve, and there is almost always a shift away from this ideal condition. Therefore, it is necessary to consider the general effects of variations of the end condition on a second-order system over a band of frequencies around the undamped resonance (not the same as the damped resonance).

It will be assumed that superposition applies, and, therefore, in this discussion, the effects of added mass, stiffness, and damping are considered separately. If any one of these dominates, it will also be shown that the effect can be systematically extracted from a series of three measurements. For example, consider the simple case of added stiffness that will result in an increase of the resonant frequency. Clearly, in mode I, an increase in frequency would result irrespective of the locking phase; whereas, in mode II, there will always be a decrease in phase for a given frequency. Adding damping is not so straightforward. For a system originally (i.e., far from the specimen surface) at the resonant frequency, there will be no phase or

Table 1 Direction of frequency shift for mode I operation of resonant sensor

Dominant factor	Phase angle in noncontact state (constant phase) $\lvert\phi\rvert < \lvert-90\rvert$	$\lvert\phi\rvert = \lvert-90\rvert$	$\lvert\phi\rvert > \lvert-90\rvert$
Mass	Decrease	Decrease	Decrease
Stiffness	Increase	Increase	Increase
Damping	Decrease	0	Increase

Table 2 Direction of phase shift for mode II operation of resonant sensor

Dominant factor	Phase angle in noncontact state (constant frequency) $\lvert\phi\rvert < \lvert-90\rvert$	$\lvert\phi\rvert = \lvert-90\rvert$	$\lvert\phi\rvert > \lvert-90\rvert$
Mass	Increase	Increase	Increase
Stiffness	Decrease	Decrease	Decrease
Damping	Increase	0	Decrease

frequency shifts in either mode, reflecting the immunity of this sensor to changes in amplitude. If, however, the probe is originally offset to a frequency slightly below the undamped resonance, additional damping will result in an increased phase lag in mode II and a reduction in frequency in mode I. With the sensor originally oscillating on the other side of the undamped resonance, the effects will be the opposite. Finally, it can be readily verified that the effect of added mass is opposite to that of added stiffness.

To visualize this *Tables 1* and *2* and *Figure 1* show the direction of the output from the phase lock-in amplifier for different types of loading on the sensor. In a number of cases, it is possible that two of the three influences will be insignificant. Under such conditions, it is desirable to identify the dominant effect. This can be systematically measured by monitoring changes in output with the probe set at either side of and at the resonant frequency. To see how this can be achieved, consider the generalized relationship between the output from the sensor and the end conditions

$$\phi = f(k_e, m_e, \xi_e)$$
$$\omega = g(k_e, m_e, \xi_e) \tag{2}$$

For small changes, the above can be differentiated to give the equation, for mode I

$$d\omega = \frac{\partial \omega}{\partial k_e} dk_e + \frac{\partial \omega}{\partial m_e} dm_e + \frac{\partial \omega}{\partial \xi_e} d\xi_e \tag{3}$$

or for mode II

$$d\phi = \frac{\partial \phi}{\partial k_e} dk_e + \frac{\partial \phi}{\partial m_e} dm_e + \frac{\partial \phi}{\partial \xi_e} d\xi_e \tag{4}$$

Assuming a single degree of freedom, second-order model, the partial derivatives in the above equations are fixed functions of the probe system and, for small perturbations, can be considered constants representing the sensitivity of the system to changes in these parameters. Consequently, the above equations can be rewritten as

$$d\omega = \Psi_{\omega k} dk_e + \Psi_{\omega m} dm_e + \Psi_{\omega \xi} d\xi_e \tag{5}$$

$$d\phi = \Psi_{\phi k} dk_e + \Psi_{\phi m} dm_e + \Psi_{\phi \xi} d\xi_e \tag{6}$$

The above constants will be a function of the initial, or "free," excitation frequency relative to the undamped resonance. The constant for the damping coefficient will reverse the sign passing through zero at the undamped resonant frequency; whereas, the sign of the other two coefficients will remain unaltered. To determine a single dominant factor, changes in ϕ or ω can be monitored as a function of the change in contact. The only restriction on the change is that it be small and repeatable for different settings of frequency and phase. For example, in the subsequent experiments it was possible either to measure the strain in the cantilever, and therefore by implication, the displacement x of the probe or the force F applied to the end of the probe. For small changes in these parameters, Equations (5) and (6) can be expressed in the forms

$$\frac{d\omega}{dF} = \Psi_{\omega k} \frac{dk_e}{dF} + \Psi_{\omega m} \frac{dm_e}{dF} + \Psi_{\omega \xi} \frac{d\xi_e}{dF}$$
$$\frac{d\omega}{dx} = \Psi_{\omega k} \frac{dk_e}{dx} + \Psi_{\omega m} \frac{dm_e}{dx} + \Psi_{\omega \xi} \frac{d\xi_e}{dx} \tag{7}$$
$$\frac{d\phi}{dF} = \Psi_{\phi k} \frac{dk_e}{dF} + \Psi_{\phi m} \frac{dm_e}{dF} + \Psi_{\phi \xi} \frac{d\xi_e}{dF}$$
$$\frac{d\phi}{dx} = \Psi_{\phi k} \frac{dk_e}{dx} + \Psi_{\phi m} \frac{dm_e}{dx} + \Psi_{\phi \xi} \frac{d\xi_e}{dx} \tag{8}$$

It is important to realize that the constants represent values whose magnitude and sign depend upon the nominal values of phase and frequency. Each derivative on the right side of Equations (7) and (8) represent the change in the system attributable to effects of the probe to specimen interaction. From this arise three important points.

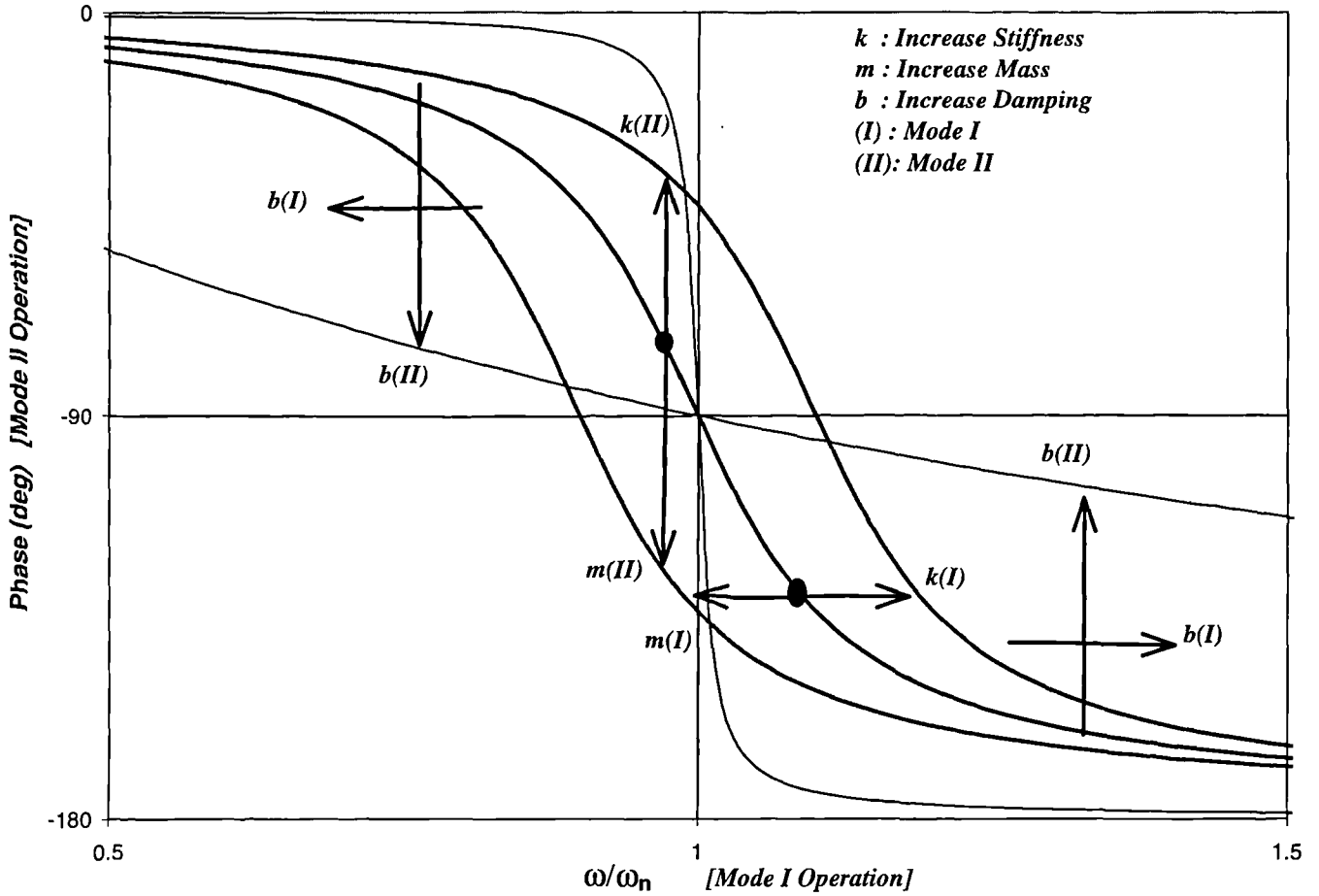

Figure 1 Direction of frequency shift for mode I and phase shift for mode II operation of resonant frequency

1. The constants ψ remain so only for small perturbations about a given frequency or phase shift. A change in the initial, or "free," phase or frequency will result in a change in the values of these "constants."
2. Change in the constants will be nearly *symmetric* about the resonant frequency.
3. The derivatives on the right-hand side of Equations (7) and (8) are function of the contact and are, therefore, *independent* of changes in the initial phase or frequency of the sensor.

Consequently, it is possible to set up a test to determine which of the contact phenomena dominate. However, before outlining the test procedure it will be informative to examine some of the reasons for the dominance of different effects with different materials.

Causes of parametric changes on resonant sensors

To simplify this discussion, only relatively large radius probes attached to a relatively stiff oscillator mount are considered for two touch regimes:

1. near surface phenomena; and
2. continuous mechanical contact.

Intermediate contact conditions characteristic of "tapping"[7,8] or "bouncing" types of sensor are outside of the scope of this paper.

Near-surface phenomena

As a resonating touch sensor approaches a surface, a number of effects that introduce a mechanical force are present. Such forces, and their gradients, will effect the frequency response characteristics of the probe. For nonmagnetic, clean materials in vacuum, the only interactive forces will be those attributable to retarded and nonretarded van der Waals forces and electrostatic forces from surface charge. As evidenced by the rapid growth of the atomic force microscopy (AFM) industry, such effects can be significant for extremely compliant and sensitive probes. In our investigations, such effects are considered ignorable relative to the effects present during measurement of engineering surfaces in air. Under these conditions, it is likely that the dominant near-surface forces will be those attributable to squeeze film damping and/or contaminant films on the probe and/or the specimen surface.

Squeeze film effects. In modeling squeeze film damping effect on the sphere, it must be remembered that for nanometer-size oscillations, the velocity between probe and specimen is extremely small. Consequently, the Reynolds number (ratio of inertial to viscous force) is low, and therefore, this process can be modeled as an incompressible fluid undergoing laminar flow. A solution for the normal force F between a sphere and a flat surface separated at distance x can be obtained by integrating Reynolds equation, relating pressure, density, surface velocities, and film thickness. Neglecting wedge effects and compressibility terms, the Reynolds equation is

$$\Delta^2 p = \frac{12\mu}{h^3}\frac{dh}{dt} \tag{9}$$

$V = dh/dt$ is the squeeze velocity in cylindrical polar coordinates, for constant density and viscosity, when axial symmetry exists, and the pressure is a function only of the radius. Assuming the gravitational and inertial forces (i.e., Reynolds number) are low, and the thickness of film is small as compared to other dimensions (i.e., the minimum film thickness $h_o \ll R$), the appropriate Reynolds equation can be expressed as

$$\frac{d}{dr}\left(rh^3\frac{dp}{dr}\right) = -12\mu r\frac{dh}{dt} \tag{10}$$

where h is the film thickness, and for spherical surface and a plane where $h \ll R$, h can be approximated as $h = h_0 + r^2/2R$, integrating once gives

$$\frac{dp}{dr} = \frac{-6\mu rV}{h^3} + \frac{A}{rh^3} \tag{11}$$

Making use of boundary condition that $dp/dr = 0$ when $r = 0$ results in $A = 0$. Integrating again gives

$$p = -6\mu V\int \frac{rdr}{h_0\left[1 + \left(\frac{r_2}{2h_0}\right)R\right]^3} \tag{12}$$

or

$$p = -\frac{6\mu VR}{h_0^2}\int\frac{du}{u^3} = \frac{-6\mu VR}{h_0^2}\left[\frac{-1}{2\left(1 + \frac{r^2}{2h_0R}\right)^2} + C\right] \tag{13}$$

The boundary condition is that $p = 0$ when $r = R$; therefore,

$$p = \frac{3\mu VR}{h_0^2}\left[\frac{1}{\left(1 + \frac{r^2}{2h_0R}\right)^2} - \frac{1}{\left(1 + \frac{R^2}{2h_0R}\right)^2}\right] \tag{14}$$

The normal load (squeeze film load) component can be written as

$$F = \int_0^R 2\pi rpdr$$

$$F = \frac{3\mu VR}{h_0^2}\int_0^R\left\{\frac{rdr}{\left[1 + \left(\frac{r^2}{2h_0}\right)R\right]^2} - \frac{rdr}{\left[1 + \left(\frac{R^2}{2h_0R}\right)^2\right]}\right\} \tag{15}$$

letting $R_1 = R^2/2h_0R$

Integrating the above produces

$$F = -\frac{3\pi\mu VR}{h_0^2R_1^4(1 + R_1^2)^2} \tag{16}$$

where μ is the viscosity of the medium between sphere and flat.

It can be seen that the force is both proportional to the velocity and inversely as the square of the separation between two surfaces. For oscillation amplitudes much smaller than the probe-to-specimen separation, there will be a rapid increase in the velocity-dependent force as the probe approaches the surface. However, surface finish is likely to have a significant effect on the characteristic of squeeze film forces at very small separations.

Effectively, this will add damping in the interfacial zone without adding significant mass (i.e., low air density) or stiffness (high sound velocity). However, as the squeeze film forces increase, these must be resisted by the surfaces of probe and specimen. Subsequent distortions will add an effective stiffness and mass to the system.

Surface films. The surfaces considered above are assumed to be perfectly clean and contaminant free. This is far from the case for many engineering surfaces in their typical environments. Commonly, surfaces will be covered by a condensed moisture film. As a consequence, when contacted, there will be a surface tension force resulting in capillary action. Grigg *et al.*[9] speculate that this leads to attractive forces on the order of tens of nanoNewtons with a force P that can be calculated from following the equation:

$$P = \frac{4AR\gamma \cos(\theta)}{(1 + x/d)} \quad (17)$$

where θ is the contact angle, d is the film thickness on both probe and specimen (assumed equal), γ is the free surface energy (72 mJ m ^{2} for water), A and R are the contact area and probe's radius, respectively.

Being proportional to the probe radius, for a separation distance of 15 nm with a 7.5-nm water film on both probe and surface will result in an attractive force of approximately 9R/30, which for a 10-mm radius probe, gives a force in the region of 3 mN upon initial contact and a residual attractive force of 1 mN after the probe has physically contacted the surface. After contact has been made, there is likely to be a hysteresis on retraction of the probe because of the necking of the meniscus layer. A potential method for discrimination of this mechanism from true van der Waals forces is to retract the probe before contact and monitor for any hysteresis. This should not be observed for true van der Waals attraction or repeated contacts if Coulomb forces are present. Simple calculations based on Hertzian contact indicate that for thin films of thickness less than the radius of the contact, there will be relatively low induced stress because of capillary action between two typical solids.

The effect of surface films on the adhesion between a sphere and flat was studied by McFarlane and Tabor.[10] In this, a sphere was suspended from a thin wire to form a simple pendulum and contacted with a flat plate. The adhesion force was then determined by moving the flat away from the sphere and measuring the maximum angular deflection of the pendulum from the vertical position before separation occurred. For very small separations, the denominator of Equation (17) becomes unity, and a linear relationship between the adhesion and radius is both predicted and confirmed by experiment. Using this modified equation, a rather high force of 9 mN is predicted for a 10-μm radius probe irrespective of material. It was also found in these studies that glass was particularly susceptible to the formation of water layers, with effects being readily observed at relative humidities of the order 50% or more. These adhesion effects could be reduced by abrading the surface, suggesting that asperities would be capable of protruding from the layer and would not accumulate any films. However, this roughness will also increase the net separation between solids and, thus, increase the denominator in Equation (17). Viscous effects were also observed, and these were predominant with castor oil. For metallic materials, adhesion was reduced by both exposure to atmosphere and with increasing hardness (which, for metals, is a measure of the elastic recovery after indentation), with aluminum showing no measurable effect and indium having high adhesion. The coefficient of adhesion was found to reduce after time, with that for lead becoming too low to measure after about 8 hours; whereas, indium reduced its adhesion strength by approximately half. The softness and adhesive properties of indium are what make it a well-known cold solder material. Application of a fatty acid monolayer again reduced adhesion to below instrument resolution, and this could only be observed after a load sufficient to rupture the film and enable metal-to-metal contact. The effects of adhesion as an energy dissipation mechanism are discussed more fully in the Additional damping mechanisms subsection.

Mechanical contact

Effective stiffness. From Hertzian analysis, it is relatively straightforward to show that the local stiffness for an elastic contact is given by the familiar equation,[11]

$$k_e = (6E^2F_oR)^{1/3} \quad (18)$$

where E and F_o are Young's modulus and applied normal load.

Effective mass. Upon physical contact, the material in the region of the interface must be moving at the same frequency as the motion of the probe tip and thus, will, add an inertial load. Clearly, this will extend into the specimen with diminishing amplitude. To assess the effective added mass, it is assumed that the specimen is smooth and flat, and the probe is also smooth and spherical. For velocities of the probe much less than those of stress waves, it is reasonable to assume that the strain field is the same as that derived from Hertz analysis. Consequently, for a harmonic motion of the probe at an amplitude X and frequency ω, the vertical component of inertial force on an element in a hemispherical contact zone beneath the probe is

$$dP = \rho dV\ddot{u}_r(z) \quad (19)$$

where ρ is the density of the specimen, dV is the volume element and $u_r(z)$ is the z-axis component of strain in the hemispherical region under the probe.

It is believed that displacements outside this zone will not contribute significantly to the inertial forces. Assuming that the radial distribution at the contact extends in a like manner radially into the

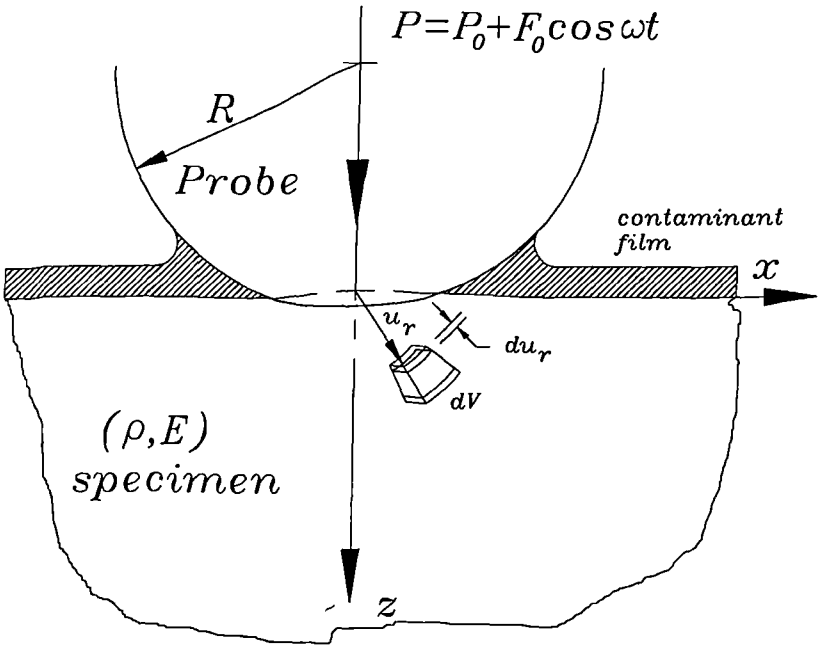

Figure 2 Simple model of spherical probe in contact with half space contaminated surface

surface, it is possible to determine u in terms of the mutual approach of distant points δ between the probe and surface as a function of the applied, or nominal, force F_o. Although not precise, this assumption will attribute excessive mass within this region, but it is expected that this error will be compensated for, at least in part, by the ignored components of strain outside of the contact zone and those in the other two axes. Based on these assumptions it is possible to use the Equations[12]

$$u_r(z) = \frac{(1-\nu^2)}{E}\frac{\pi p_o}{4a}(2a^2 - r^2)$$

and

$$p_0 = \frac{3F_0}{2\pi a^2}$$

$$a = \left(\frac{3F_0R}{4E^*}\right)^{1/3}$$

$$\delta = \frac{a^2}{R} \qquad (20)$$

To visualize the origin of the inertial force consider the elemental volume of *Figure 2* undergoing a small displacement du because of a fluctuating force of magnitude F_o. The conditions of total load P and displacement u can then be expressed by the equations

$$P = F_o + F_o\cos(\omega t)$$

$$u = u_o + du \qquad (21)$$

Consequently, the inertial reaction ΔF_i of an elemental volume to the applied load is given by the following equation:

$$\Delta F_i = \rho dV\frac{d^2u}{dt^2} \qquad (22)$$

where

$$\frac{d^2u}{dt^2} = \frac{1-\nu^2}{E}\frac{3(2a^2-r^2)}{8a^3}\frac{d^2P}{dt^2}$$

$$= \frac{1-\nu^2}{E}\frac{3(2a^2-r^2)}{8a^3}F_0\omega^2\cos(\omega t) \qquad (23)$$

Combining Equation (20) with Equations (21) through (22) and integrating throughout the three-dimensional (3-D) region gives the total inertial force

$$F = \rho F_o\omega^2\iiint_V u_r(z)\,r^2 dr d\phi d\theta\cos(\omega t)$$

$$= \frac{21F_0^2\pi^2\omega^2a^2(1-\nu^2)\rho}{60E}\cos(\omega t)$$

$$= m_e\omega^2 du(0)\cos(\omega t) \qquad (24)$$

For a probe having an elastic modulus of considerably higher value than that of the specimen, we can reasonably replace the elastic modulus used in Equations (19)–(24) by the value for the specimen. Additionally, the ratio of the fluctuating force to change in deflection at the surface $du(0)$ is the probe–specimen interactive stiffness given in

Equation (18). Substituting these into Equation (24) gives the effective mass

$$m_e = \frac{21\pi^2 a^2(1-\upsilon^2)\rho(6E^2F_0R)^{1/3}}{60E} \quad (25)$$

or, from Equation (20)

$$m_e \approx \frac{\pi^2 F_0 R}{2E}(1-\upsilon^2)\rho \quad (26)$$

This equation indicates that the added mass becomes significant for materials with high density and low modulus of elasticity; e.g., natural rubber and possibly some biological matter.

Additional damping mechanisms. Upon repulsive contact, the squeeze film effect will be confined to the region within the meniscus and the circle of contact. The authors are unaware of any studies in this field; therefore, it is difficult even to comment on the magnitude of such an effect. However, there will also be the effects of cyclic stresses within the strained zone of the contact, and this has been well analyzed over the last 60 some years. However, this has not resulted in any simple generalized models, and a large number of physical mechanisms that will result in energy dissipation under the action of a cyclic stress are recognized.[13] It is beyond the scope of this text to discuss these in any detail. Most prominent among these for metals and ceramics are:

1. thermal currents and atomic diffusion;
2. the Snoek effect;
3. Zener relaxation;
4. dislocation damping; and
5. dielectric relaxation.

For most metals and ceramics, this results in losses corresponding to Q values measured in thousands and are unlikely to be significant in our measurements.

More compliant materials, such as rubbers and plastics, can be characterized as hysteretic. Mathematically, for steady-state frequency response, this can be modeled as either a frequency-independent factor $h\dot{x}/\omega$, or, equivalently, as a complex stiffness (often referred to as structural damping). Choosing the latter approach, a second-order system with hysteresis damping subject to a sinusoidal input can be characterized by the following equation:

$$m\ddot{x} + k(1 + ih/k)\,x = F_0 e^{i\omega t} \quad (27)$$

Assuming a solution of the form $Xe^{i\omega t}$, the frequency response is given by

$$\frac{X}{F_0/k} = \frac{1}{\left[\left(1 - \frac{\omega^2}{\omega_n^2}\right) + i\,\frac{h}{k}\right]} \quad (28)$$

Clearly, the gain and phase of such a system can be obtained from

$$\left|\frac{X}{F_0/k}\right| = \frac{1}{\left[\left(1 - \frac{\omega^2}{\omega_n^2}\right)^2 + \left(\frac{h}{k}\right)^2\right]^{1/2}} \quad (29)$$

$$\phi = -\tan^{-1}\left(\frac{h/k}{1 - \frac{\omega^2}{\omega_n^2}}\right) \quad (30)$$

The frequency independence of the dissipation term leads to an amplitude and phase offset at low frequency. Fortunately, the general characteristics of hysteretic damping near to the resonant frequency follow similar trends to viscously damped systems for relatively low values of damping. Consequently, identification of the dominant frequency response influences in contact using *Tables 1* and *2* are also valid for this mechanism.

Another potential dissipation mechanism is that attributable to variation of surface energy upon contact. Consider two surfaces in Hertzian contact. Before contact, each solid surface will have an associated surface energy. Upon contact, the interface can be considered a newly created solid region with a different interfacial energy. If the two surfaces undergo no bonding or modification then the total energy is simply that of the two separate surfaces. On the other hand, if the surfaces were to form a perfect bond, then there will be no interface energy. This energy change can be represented by the Dupré equation

$$\gamma_{12} = \gamma_1 + \gamma_2 - \gamma_{int} \quad (31)$$

where γ_{int} is the surface energy of the interface (often referred to as the work of adhesion). The value of Equation (31) represents the work per unit area required to separate the two surfaces. For simple oscillating contact, there will not be complete separation, but there will be a change in the contact area. Therefore, the fractional amount of this work per cycle is given by

$$W = \gamma_{12}A\frac{\Delta A}{A} = \gamma_{12}\pi\left(\frac{3R}{4E}\right)^{2/3}(k_c\Delta x)^{2/3} \quad (32)$$

where Δx is the probe's oscillation amplitude.

The power dissipated P is the product of work done per cycle and frequency (Hz) of excitation

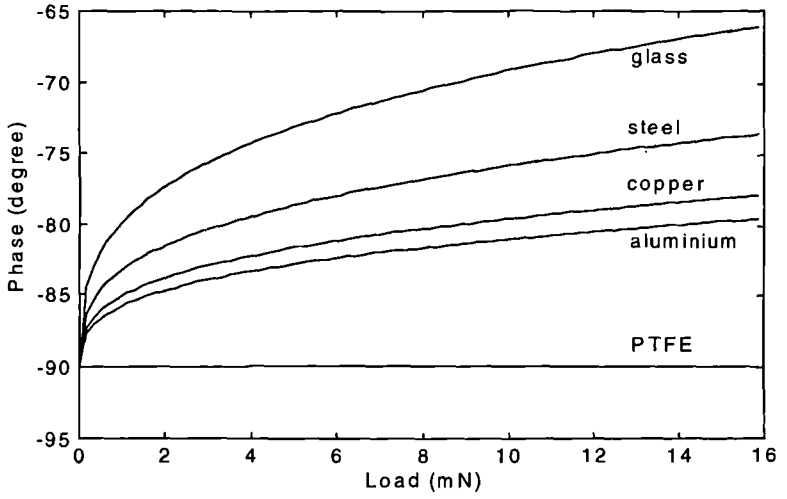

(a)

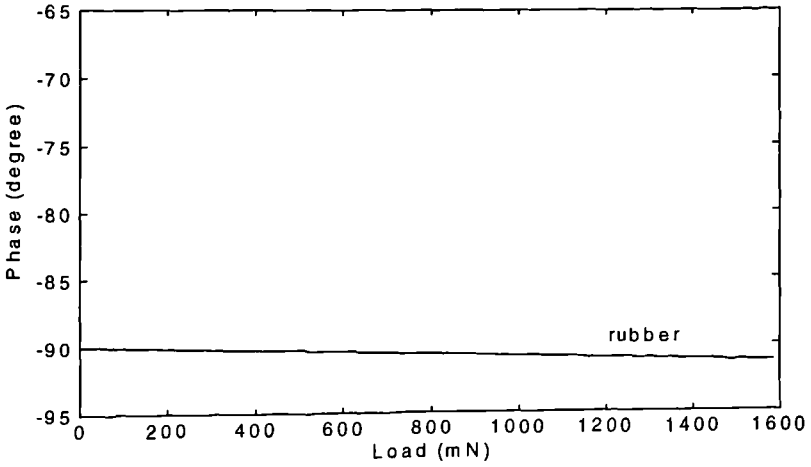

(b)

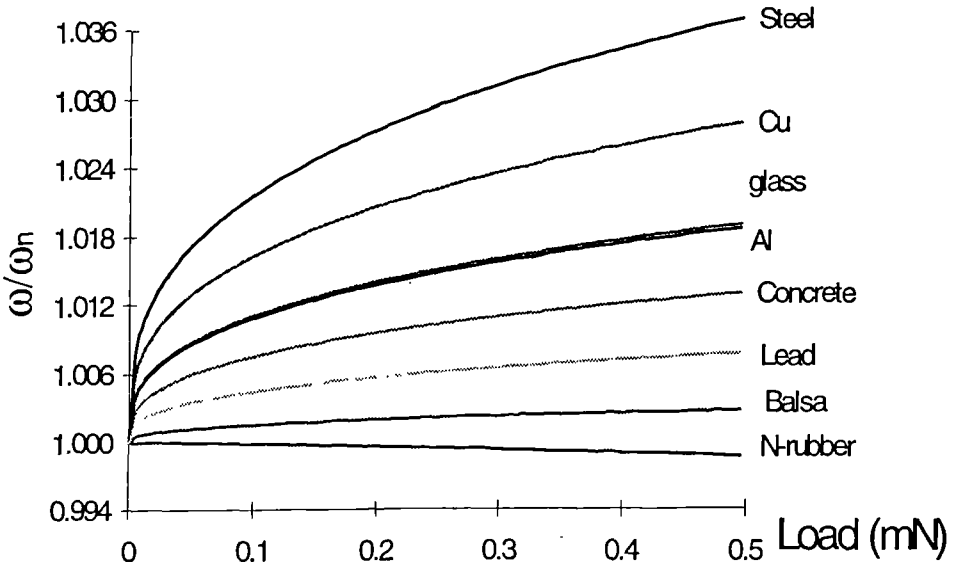

(c)

Estimated values for Damping and Coupling Loss factor (ζ)

Aluminum : 0.009
Copper : 0.012
Steel : 0.011
Glass : 0.004
PTFE : 0.03
Rubber : 0.07

Figure 3 Mathematical results representing (*a*) and (*b*) the phase shift and (*c*) shift in resonant frequency for a selection of different materials as a function of applied load and for given probe geometry

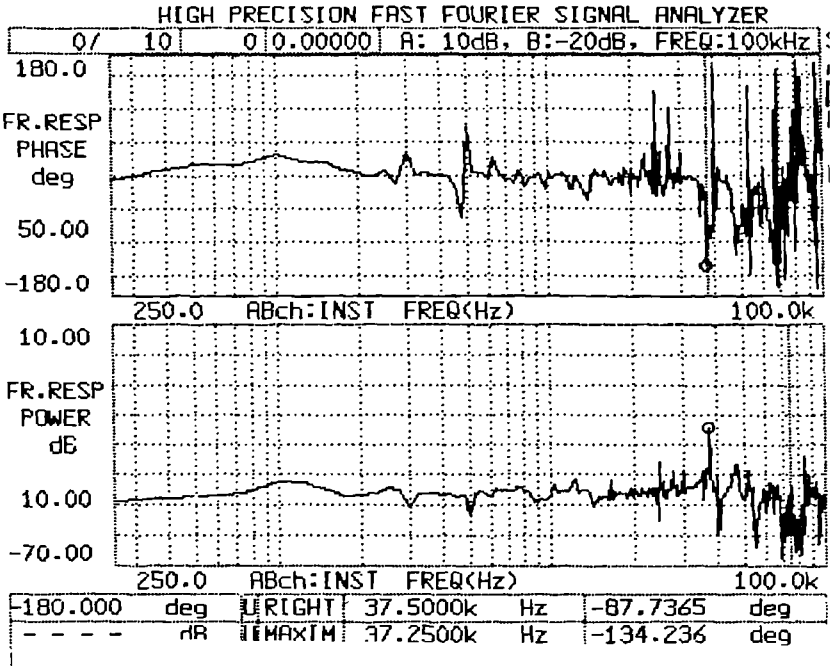

Figure 4 Typical frequency spectrum of the resonator probe. The fundamental frequency for this arrangement is set at 37.5 kHz

$$\underline{P} = \frac{\omega\gamma_{12}}{2}\left(\frac{3R}{4E}\right)^{2/3}(k_e\Delta x)^{2\ 3} \tag{33}$$

To equate this energy dissipation to an equivalent damping ratio for a viscously damped system, we can make use of the ratio of energies.[14]

$$\frac{\Delta U}{U} = 4\pi\xi x^{m-2} \tag{34}$$

Consequently, substituting Equation (32) into the left-hand side of Equation (34) and dividing through by $k_e(\Delta x)^2/2$ yields

$$4\pi\xi x^{m\ 2} = \gamma_{12}\pi\left(\frac{3R}{4E}\right)^{2/3}\frac{2}{(\Delta x)^{4\ 3}k_e^{1/3}} \tag{35}$$

from which it can be seen that

$$m = 2/3$$

$$\xi = \gamma_{12}\left(\frac{3R}{4E}\right)^{2\ 3}\frac{1}{2(\Delta x)^{4\ 3}k_e^{1/3}} \tag{36}$$

also

$$\xi = \frac{h}{2k_e} \tag{37}$$

Substituting Equations (18) and (37) into Equation (36) and solving for h yields:

$$h = 1.23\gamma_{12}\left[\frac{R^1P}{E\Delta x^6}\right]^{2\ 9} \tag{38}$$

Figures 3a and *b* show the theoretical phase shift and frequency shift of a resonant probe for a selection of different materials under various loads. These were calculated using Equations (1), (18), and (26) and some estimated values for damping and coupling loss factor ξ.

Experimentation

Apparatus for solid contact sensing

The multipurpose probe used for experimentation consisted of a beryllium copper (BeCu) rod of hexagonal section (6 × 3.5 mm; l = 20 mm) with three pairs of piezoelectric drive actuator and pick up sensors mechanisms bonded on its surface using M-BOND 200 adhesive (M-BOND 200 adhesive, Measurement Groups UK, Basingstoke, Hants, UK). Rectangular plates made of piezoelectric lead–zirconate–titanate (PZT) ceramic were used. The probe itself consists of a standard coordinate measuring machine (CMM) tip holder screwed into the free end of the hexagonal rod. Because the frequency response of the probe was the same, regardless of which pair of PZTs were activated, in these experiments, only one pair of piezoelectric plates were used. Also, because the sensitivities were the same for each pair along the axis of the probe but exhibited marked directional sensitivities when forces were applied radially, the specimen surface was aligned normal with this axis. Consequently, in these studies, the probe sensitivity was not dependent upon the actuator/sensor pair used. However, the resonance frequency of the device strongly depends upon its mounting arrangement, probably because of variations of the stiffness of the interface at the

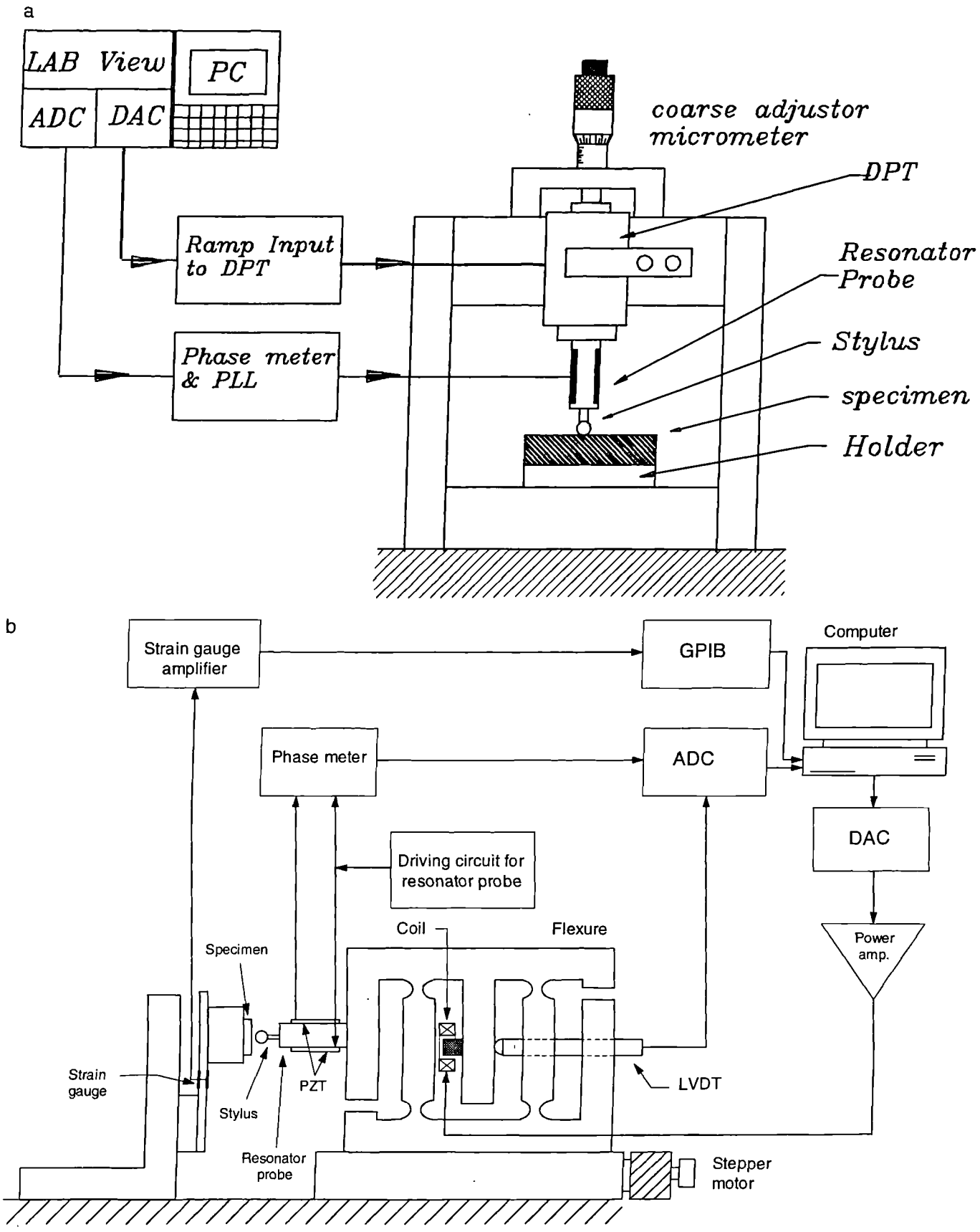

Figure 5 Schematic diagram of the test rig used to monitor the contact mechanism between resonator probe and (*a*) solid glass covered with thick layer of oil, (*b*) clean solid engineering surfaces

a

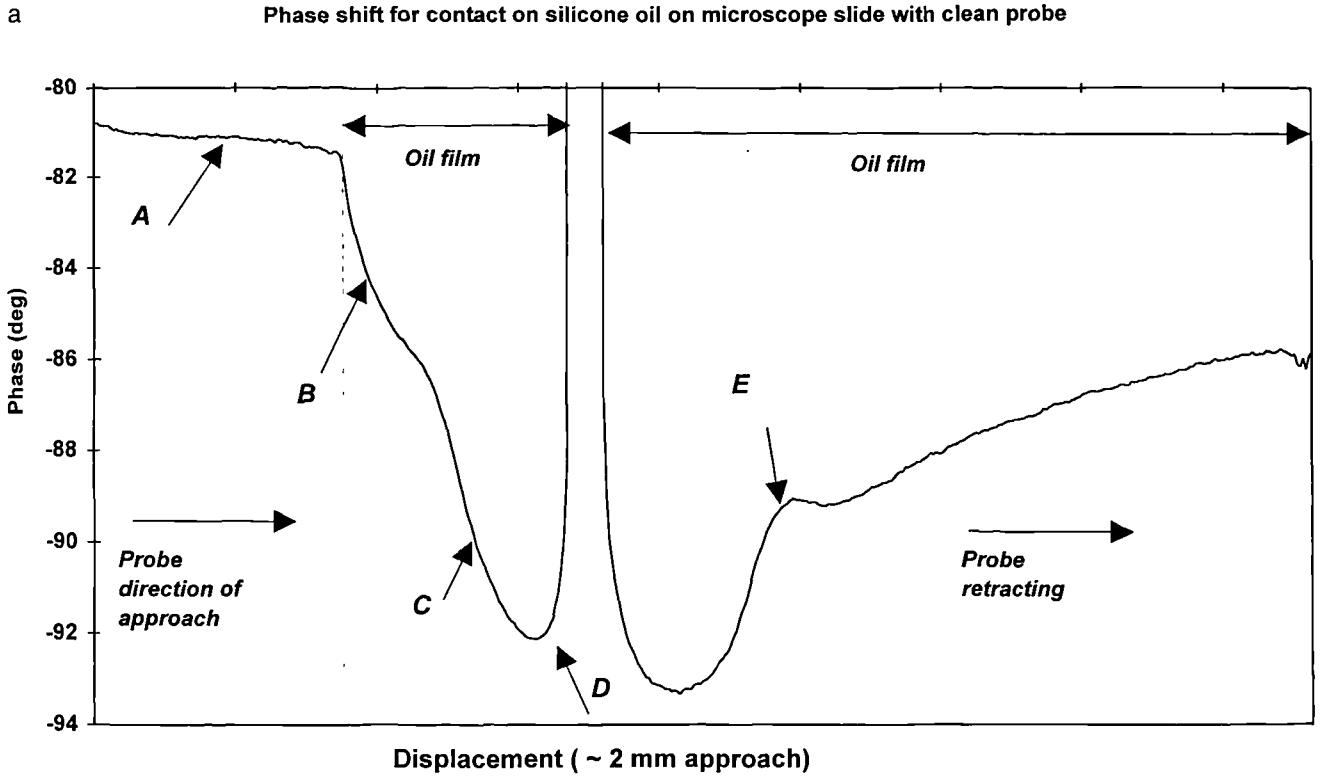

b

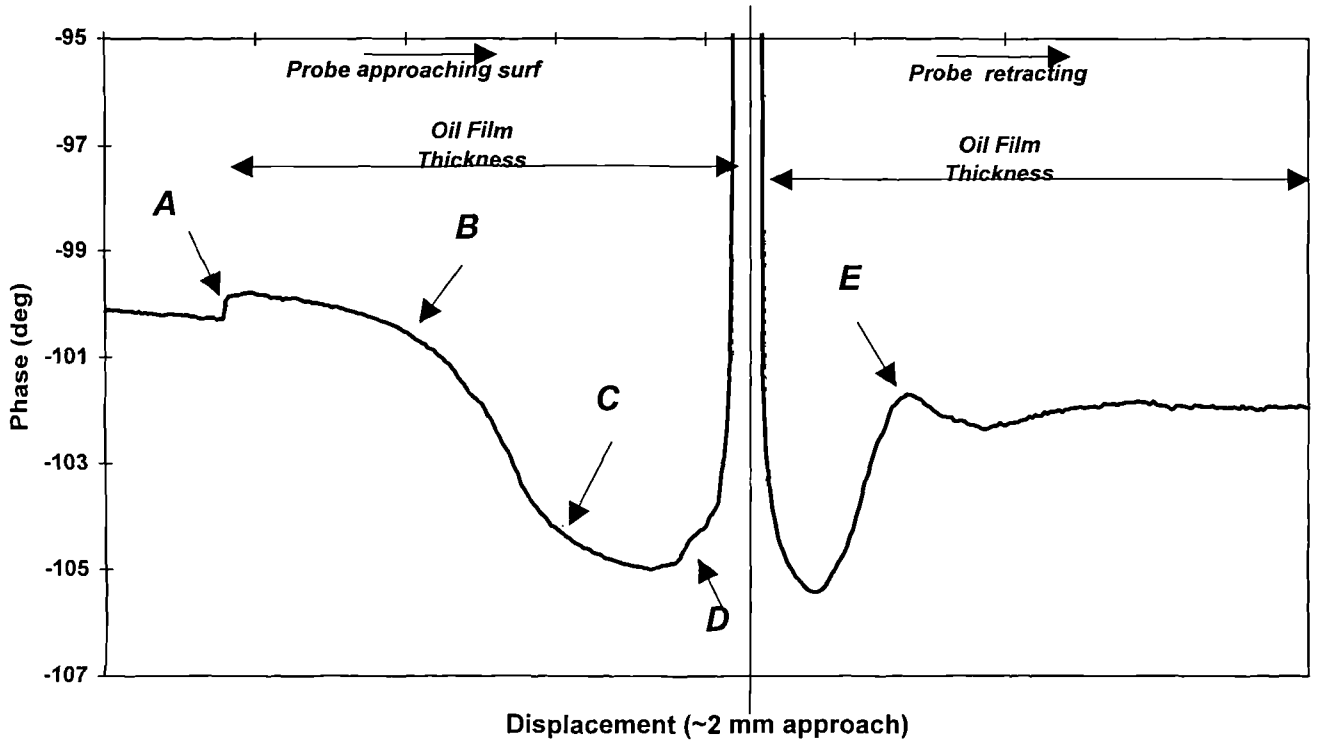

Figure 6 Typical plot showing contact characteristics of thick oil film on glass microscope slide for free-value phase shift of (*a*) −81°; (*b*) −100°; and (*c*) −70°

clamped end. Typical fundamental frequencies for this device were in the region of 38 kHz, with behavior characteristic of a second-order system. During these experiments, the first harmonic (56.06kHz) was usually chosen because of the high sensitivity when contacted with both soft and hard

c

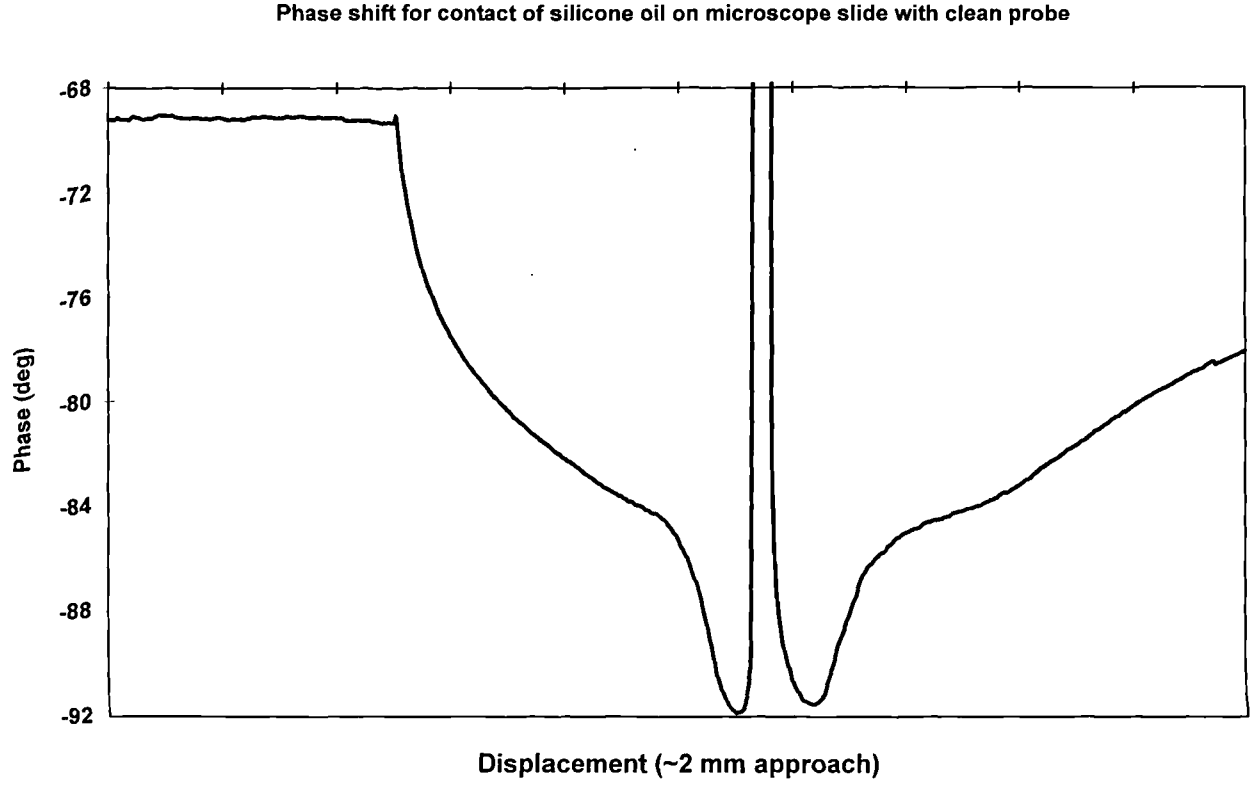

Figure 6 (*Continued*)

materials. *Figure 4* shows a typical frequency spectrum of the resonator probe.

To assess the interaction between a probe tip and typical engineering surfaces two simple test rigs were used. *Figure 5a* shows the schematic diagram of the first rig that was used to assess the response of the probe when contacting solid glass surface (microscope slide) covered with a thick layer of oil. The resonator probe in this was mounted into a Queensgate Instruments AX100 digital piezoelectric transducer (DPT), for fine positioning. This, in turn, is mounted at the end of differential micrometer for coarse adjustment. The whole assembly was then mounted in a fixed bridge-type frame with its axis vertical, the probe tip pointing downward. The specimen was rigidly secured in a special fixture beneath the probe. During these experiments, the changes in phase were recorded as the probe approached (using coarse adjuster) and contacted first the oil film then the solid surface. The second test rig, however, (*Figure 5b*) was used to assess the response of probe to clean solid surfaces of different engineering materials. In this, the resonator touch probe was mounted into simple linear flexure translation stage for fine positioning.[6] Displacement of the flexure was continuously monitored by an linear variable differential transformer (LVDT) which was periodically calibrated against a Hewlett-Packard laser interferometer system (HP 5528A). The whole assembly was mounted onto a linear stage driven by a stepper motor for coarse adjustment. This was then positioned horizontally in line with a stationary specimen. Two strain gauges in half-bridge arrangement were used to monitor the contact force between the probe tip and the specimen. These were fixed on the opposite sides of a cantilever beam that holds the specimen at its free end. Digital strain gauge indicator had range of $\pm 50{,}000\ \mu\epsilon$ (microstrain) with accuracy of $\pm 0.1\%$ or $5\ \mu\epsilon$. The calibration factor of the load cell was $3.25\ \mathrm{N\ V^{-1}}$. The load cell will add stiffness, mass, and damping to the probe in addition to that of the workpiece when contacted, which undoubtedly will affect the overall results, but because the measurements are of comparative nature, its effect is minimized and is ignored in this discussion.

Two sets of tests were conducted. In the first (mode II), the probe was oscillated at a fixed frequency, and the change in phase was monitored as the probe approached the surface. In the second (mode I), the phase angle was locked near $-90°$ using a phase-locked loop (PLL),[6] and the changes in frequency were monitored as the probe contacted the surface of the specimen. Tests were repeated over a broad range of materials ranging from rough rubber to polished, hard-

ened steel. Two types of surface were assessed in these experiments:

1. a solid glass surface covered with a thick layer of oil; and
2. clean surfaces of brass, steel, glass, and rubber.

Contact characteristics of thick oil films

In the first set of experiments, a few drops of oil were applied to a standard 1-mm thick microscope cover-slide. For both oils used, the thickness of the resultant layer settled to a value of approximately 1 mm. In the first set of experiments, the probe was contacted with the oil layer by incremental adjustment of the manual micrometer. This displacement was continued until solid contact of the underlying substrate was detected as a rapid increase in the effective stiffness of the system. Each experiment took approximately 5 minutes with approximately 200 increments of approximately 10 μm toward and away from the surface. It was found that consistent and repeatable results could only be obtained when the probe was cleaned (with ethyl alcohol) before each individual contact experiment.

Contact characteristics of solid surface

Contacting solid surfaces required considerably finer control of the displacement of the probe toward the specimen surfaces. Two separate tests were conducted. In the first, the specimen and the strain gauge were mounted onto the same assembly. To bring the probe in contact with the surface, the flexure was driven via an electromagnetic actuator in 700 increments of 2 mV; the time delay between increments was 100 μs, producing a total displacement of approximately 3 μm toward and away from the specimen. The maximum load, which was measured simultaneously, corresponds to approximately 15 mN. Contacting soft surfaces was much more complicated because of the high compliance of rubber-like materials resulting in low values for the derivatives in Equations (7) and (8). Force of approximately 200 mN had to be applied onto the specimen via the probe to achieve significant interaction forces. This was achieved by driving the stage via the stepper motor to generate larger displacements, and, therefore, deflections of the cantilever. Before each test, the stylus and the specimen surfaces were cleaned with acetone.

Results

Subsequent experimental results and discussions represent an overview of many observations. For significant oil films, characteristics of the approach extended over 1–2 mm; whereas, for solid contacts, significant effects could only be observed over a range of a few micrometers. For this reason, these are discussed separately below.

Contact with a relatively thick oil layer on a smooth glass surface

Figure 6a shows a typical plot of the phase shift of the probe from a free value lag of 81°. In the first series of test, a thick layer of silicone oil (L-45 polydimethylsiloxane, Union Carbide, Danbury, CT, USA) having a viscosity of approximately 10 Pa s was used. A number of distinct regions are visible in the graph, and these are labeled accordingly. Region *A* corresponds to displacement of the probe tip toward the oil surface before physical contact. In practice, the point of contact is relatively easy to identify, because the capillary forces cause an easily visible meniscus to form around the probe. At this point, there is a relatively large increase in phase lag. Referring to *Table 2*, this would be the result of either an additional mass or an additional damping within the system. This continues into region *B* until there is another transition to a third region *C*. As the probe nears the surface, the phase has crossed over −90°, at which point an additional damping would result in a *reduction* of the phase lag. Such a reduction occurs before mechanical contact, after which the phase very rapidly increases, which is characteristic of a relatively large increase in effective stiffness. Retracting the probe away from the surface, the phase shift of the probe mirrored the original approach curve, with a similar characteristic at *D* and *C* but with a permanent offset of approximately −2°. However, upon retraction, a transition can be seen; region *E*, which is close to the original point of inflection in the approach curve. At this point, the phase seems to be increasing more rapidly, and it is observed that the meniscus is becoming elongated. Such a rapid increase in phase would be characteristic of an increase in either stiffness or damping or a reduction in mass. It is not clear which is a dominant effect at this stage. Eventually, the meniscus breaks leaving a small amount of oil on the tip of the probe and a permanent phase shift of approximately −5°. Interestingly, subsequent cleaning of the tip resulted in a further increase in phase of approximately 2° which, in addition to the permanent shift observed after solid contact, would return the phase to the original free value of −81°. In this, and most of the subsequent experiments, repeating the experiments resulted in nominally similar characteristics.

After cleaning the probe, the excitation fre-

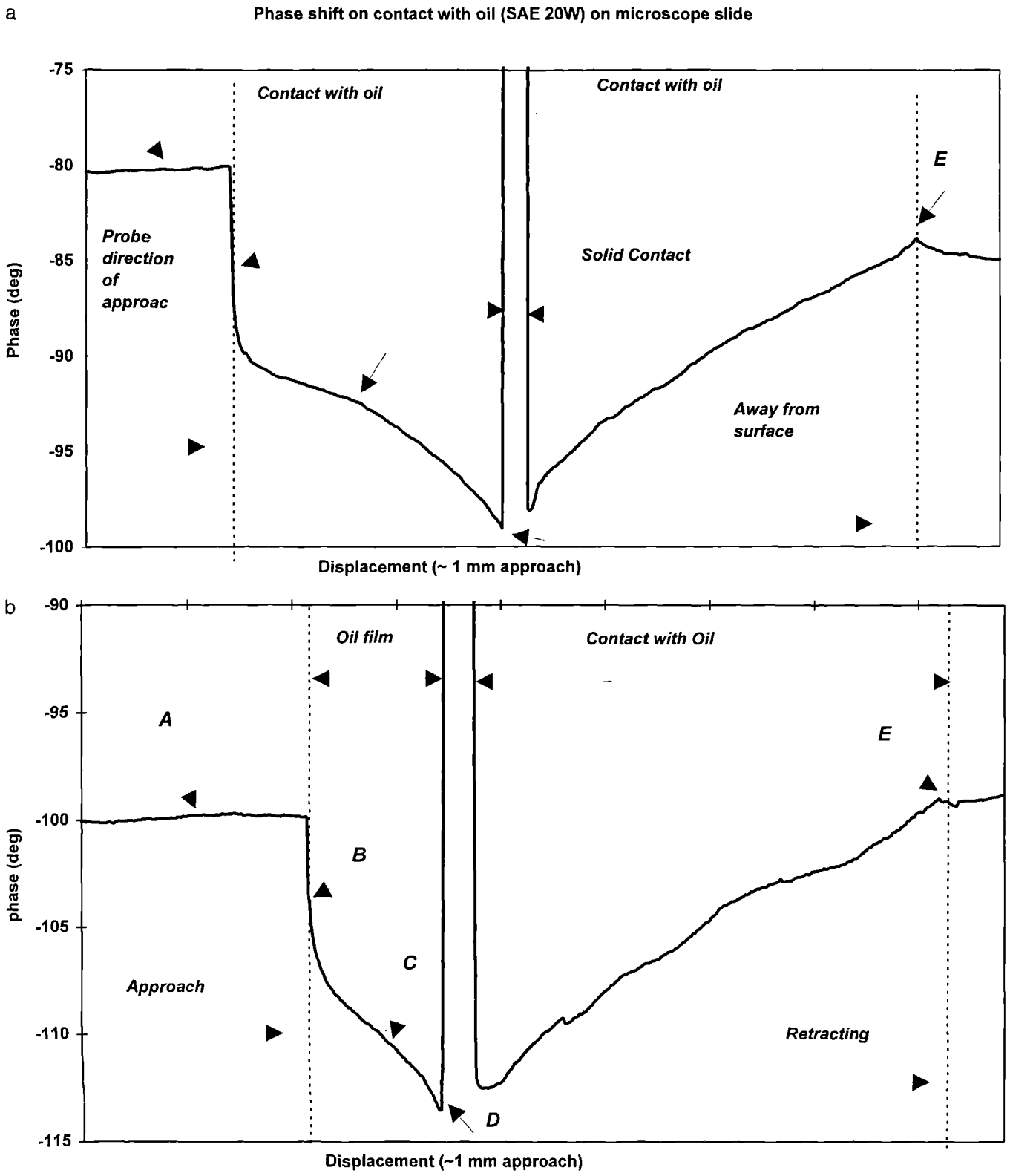

Figure 7 Typical plot showing contact characteristics of thin oil film on glass microscope slide for free value phase shift (*a*) −80°; and (*b*) −100°

quency was increased to produce a phase shift of −100°. The subsequent phase shift as a function of approach is shown in *Figure 6b*. Again, before contact, there is a reduction in the phase, indicating an effective inertial force. This followed upon immediate contact with the oil by a reduction in phase. This is not present in *Figure 6a*. It is possible to explain this as an effective damping that would

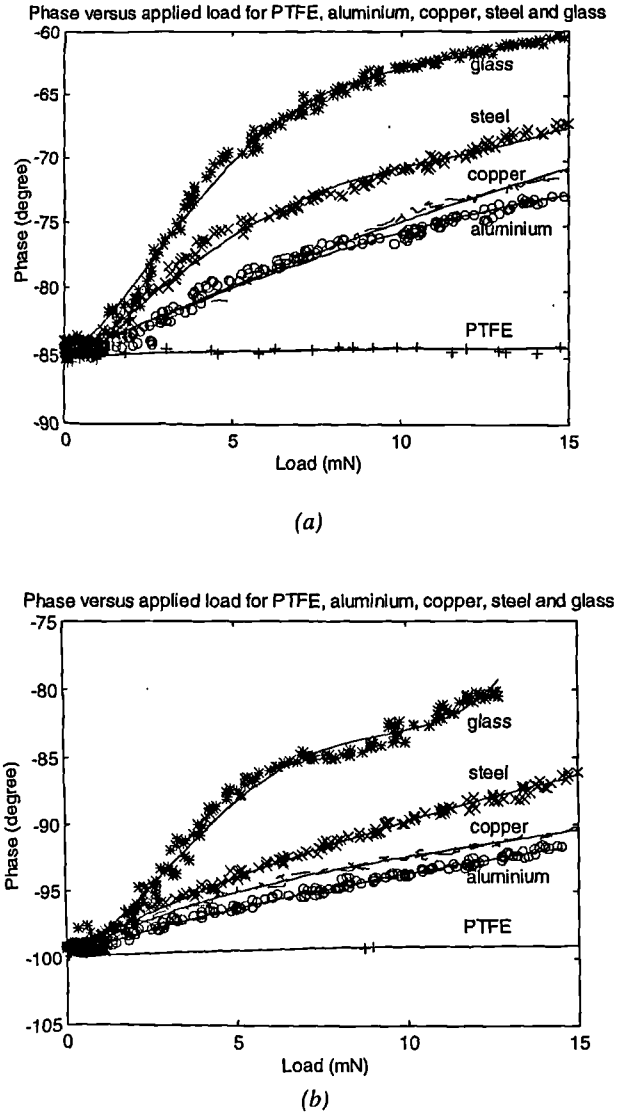

Figure 8 Plot showing phase shift when probe contacts solid engineering surface s for free value phase shift (*a*) −85°; and (*b*) −100°

add to the inertial effect with opposite sign either side of the resonant frequency. Upon further displacement of the probe into the oil, the phase shift is observed to decrease with opposite curvature to that observed in *Figure 5a*. This suggests that there are two predominant effects in this portion of the curve that are additive on the lower side of the resonance peak and subtract above it. Regions *C* and *D* show behavior similar to that of *Figure 6a*, which is not surprising, because they are both on the same side of the resonant frequency. Interestingly, region *E* is observed upon retraction of the probe at the point where significant thinning of the meniscus is observed. Again, cleaning the probe after separation from the film resulted in a phase increase of approximately 2°.

Noting the total phase shift in *Figure 6a* passed

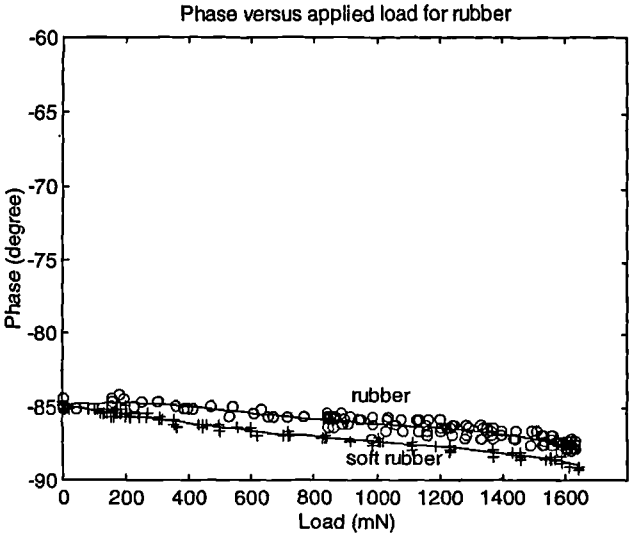

Figure 9 Plot showing phase shift when probe contacts rubber-like materials

across the −90° point, this experiment was repeated with a substantially larger offset of −70°. On this side of the resonance, the damping and inertial phase shifts are additive. *Figure 6c* shows a similar characteristic, but this time with an initial positive phase shift, with separation showing a characteristic common to a first-order system step response of magnitude 16°. This is considerably larger than that on the other side of the resonance curve, which has a magnitude of approximately 6°. Assuming simple superposition and a linear phase characteristic (see the Theoretical Model of the Resonator Sensor subsection), this would imply a contribution of 11° attributable to the additional mass and 6° from damping. Clearly, these are very rough assumptions, but such analysis does indicate the relative magnitude of each effect.

Contact with a relatively thin oil layer on a smooth glass surface

Replacing the silicone oil with SAE 20W (viscosity 0.2 Pa s) the experiments above were repeated. Having comparable density but with a viscosity 50 times lower than that of the previous experiment, resulted in a considerably different contact characteristics, as shown by *Figure 7a* and *b*. Again, there is a slight reduction of the phase lag before contact in both cases, indicating that the air acts as an acoustic coupling. Upon initial contact with the oil film, increases in phase lag of approximately 9 and 7° on the lower and upper sides of the resonance curve are observed. This implies a significant addition of mass plus, perhaps, a relatively small additional damping. Further motion of the probe into the film produces a slow increase in phase lag in both plots until

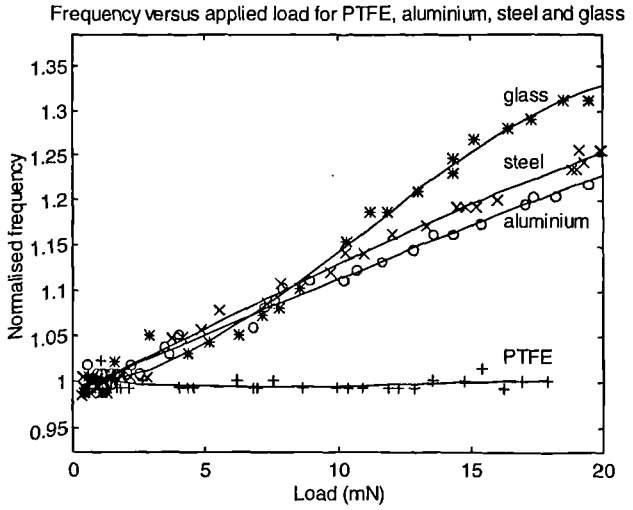

(a)

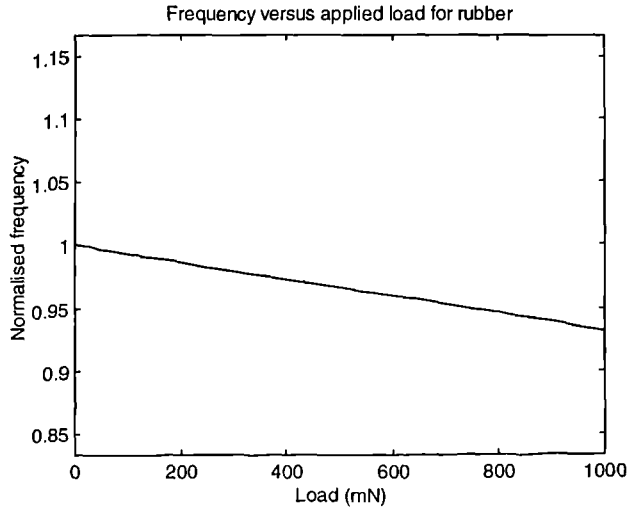

(b)

Figure 10 Shift in frequency when probe contacts (*a*) solid surfaces and (*b*) rubber-like materials

contact is observed at *D*. The sharp transition at this point implies that the viscosity of the film is responsible for the phase effects in the previous experiments. Upon retraction of the probe, a similar marked difference in phase is observed as the meniscus is at its limit of extension at *E*. Again, cleaning the probe tip resulted in a further increase in phase of approximately 1–2°.

Contact of solid surfaces

A number of experiments were conducted on different type of materials: PTFE, aluminum, copper, steel, glass, and two types of rubber. *Figure 8* shows a typical plot of a probe's phase shift when contacted with these solid surfaces. Before each experiment, the surfaces were thoroughly cleaned. In *Figure 8a*, and *b* the free-value phase shift was set at −85 and −100°, respectively. For PTFE, the phase shift starting at just above −90°, was increased by less than 1°; whereas, for the same contact force, on a glass surface, the increase in phase was more than 25°. When this is compared with similar test but for phase starting below −90°, materials such as PTFE resulted in a more or less similar increase in phase of less than 1°; whereas, for glass, the increase was about 20°. Close comparison with other materials tested indicates that, on average, the difference in the phase shift for the same material is about 5° when the phase is both below and above −90°. Again, referring to *Table 2*, this suggests that this is the contribution of the added damping in the system, although these large phase shifts may include other nonsymmetric factors. As predicted, all materials tested in *Figure 8* show a reduction in phase lag, but at different rates, which indicates that added stiffness is the predominant effect. Similar tests conducted on rubber-like surfaces (see *Figure 9*), show an increase in phase lag, which indicates the predominance of the added mass as the result of relatively high density and low elastic modulus.

Figures 10a and *b* show a typical plot of frequency shift (mode I) of the probe in contact with solid surfaces. Again, the results of these tests conform with the theoretical model, which predicts an increase in frequency shift when the probe is contacted such solid surfaces as PTFE, aluminum, steel, copper, and glass. In these, added stiffness is the dominant factor. However, in case of rubber-like materials, the dominant added mass results in negative frequency shift as predicted in *Figure 3b*.

Discussion and conclusion

It has been shown that the dynamics of a resonant probe sensor as it approaches typical engineering surfaces is subject to a complex variety of forces, leading to the observation of effects characteristic of added inertial, stiffness, and damping forces. These characteristics will superpose, making the separation of individual terms rather complex. However, it has been shown that observation of dynamic characteristics on either side of the resonant frequency can be used to identify the predominant effect. This has been shown theoretically and experimentally on both the contact of thick oil films and a variety of solid surfaces.

The analysis of experimental results in contact with solid surfaces and comparison with corresponding hardness scales could lead to potential applications in nondestructive hardness testing.

During these experiments, a reduction or increase in resonant frequency was observed for a variety of materials. The shift in the resonant frequency (or phase shift) depends on such specimen materials properties as the elastic modulus, hardness, density, and damping. It is envisaged that refinement of this work will make it possible to perform quantitative measurements of a number of physical properties.

Acknowledgments

The authors are grateful to Coventry University, the Nuffield Foundation, and the Royal Academy for Engineers for supporting this research. We also thank R. E. Johnson for his useful comments, and G. Singh and R. Edgeworth of the Precision Engineering group at UNCC Charlotte for their help and support.

References

1 Langdon, R. M. "Resonator sensors—A review," *J Phys E: Sci Instrum*, 1985, **18**, 103–115
2 Morten, B., De Cicco, G. and Prudenenziati, M. "Resonant pressure sensor based on piezoelectric properties of ferroelectric thick films," *Sensors Actuators A*, 1992, **31**, 153–158
3 Omata, S., Asano, H. and Ozaki, S. "New type tactile sensor for detecting the hardness of objects like human hand," *Tissue Eng BED*, 1989, **14**, 99–102
4 Shinoda, T., Inasaki, I. and Nacamura, T. "Development of a tactile sensing probe utilizing piezoelectric material for coordinate measuring machines," *Japan Soc Mech Eng I, 1994*, **60**, 4216–4221
5 Wienmann, M. Raduis, R. and Assmus, F. "Measuring profile and position by means of vibrating quartz resonators used as a tactile and nontactile sensors," *Sensors Actuators A*, 1993, **37–38**, 715–722
6 Harb, S. M. and Vidic, M. "Resonator-based touch-sensitive probe," *Sensors Actuators A*, 1995, **50**, 23–29
7 Elings, V. and Gurley, J., US Patent 5,266,801
8 Zong, Q., Innis, D., Kjoller, K. and Elings, V. B. "Fractured polymer/silica fiber surface studied by tapping mode atomic force microscopy," *Surf Sci Letts*, 1993, **290**, L688
9 Grigg, D. A., Russell, P. E. and Griffith, J. E. Tip-sample forces in scanning probe microscopy in air and vacuum," *J Vac Sci Technol* 1992, **A10**, 680–683
10 McFarlane, J. S. and Tabor, D. "Adhesion of solids and the effects of surface films," *Proc Royal Soc Lond* 1950, **A202**, 224–243
11 Smith, S. T. and Chetwynd, D. G. *Foundations of Ultraprecision Mechanism Design*, New York: Gordon & Breach, 1992
12 Johnson, K. L. *Contact Mechanics*. Cambridge, UK: Cambridge University Press, 1985, pp. 56–106
13 Wert, C. A. "Internal friction in solids," *J Appl Phys*, 1986, **60**, 1888–1895
14 Steidel, R. F. *An Introduction to Mechanical Vibrations*. New York: Wiley, 1989, 164–226

Verification Of A High Precision Touch Sensitive Probe

M. Vidic , S. M. Harb
School Of Engineering, Coventry University, COVENTRY, CV1 5FB UK

Introduction

Resonator based sensors have been proposed and used successfully in a wide range of applications. These include sensing the density and viscosity, fluid level, stresses, pressure and mechanical forces, as well as some material properties [1-4]. Resonator sensors of some sort have also been very popular in the design of scanning probe microscopy (SPM) [5].

In high precision coordinate measurement; resonator based touch sensitive probe offers some significant advantages over other alternative designs. These include the high 3-dimensional sensitivity and response, simplicity, ability for miniaturisation, low production cost, but more importantly, is the stability against false triggering.

This paper presents the verification of a resonator based touch sensitive probe. The design principle is based on the fact that when a rigid element (probe) vibrating at near resonance frequency, f_0 , is loaded with some kind of mechanical impedance, the resonance mode of vibration shifts depending on the nature of the load. It decreases if the load is mass-like and increases if spring-like. In this application, the contact pressure behaves like repulsive spring load that increases the force gradient acting on the probe tip. This increase gives rise to a shift in the vibrational resonance, Δf. A simple model of a probe consisting of a longitudinally resonating cantilever bar with cross sectional area ,A, young modulus of elasticity E, length l, and in contact with a workpiece, demonstrates that the resonance frequency and the effective spring constant (K_{eff}) of the interaction of probe/workpiece are related by transcendental equation given by

$$K_{eff} = \frac{AE}{l}\frac{(\pi/2l\sqrt{E/\rho})}{\tan(\pi/2l\sqrt{E/\rho})} = \frac{AE}{l}\frac{f_0}{\tan(f_0)} \qquad (1)$$

Plotting the above relationship, shows that the shift in resonance frequency depends on the young's modulus of elasticity of the materials, contact area, and applied pressure. However, this shift reaches its maximum sensitivity, when the effective stiffness is close to that of the probe.

Probe Construction

The basic body structure of the probe and its control system is shown in Figure 1. The probe consists of an aluminium bar oscillated longitudinally at its near resonance by a rectangular plate of piezoelectric based materials (PZT-5H) cemented onto one face of the bar. The generated strain signal was picked up by another PZT plate cemented on the opposite face. The probe was rigidly fixed at one end while on the other end a Φ 4 mm sapphire ball acting as probe tip was mounted. The oscillated frequency of the probe was set near its first fundamental vibrational modes, 16.350 kHz. The shift in the resonance frequency was detected using phase lock-loop (PLL) technique. This was implemented by an integrated circuit NE 565. The conversion factor of the PLL was 1.04 mV/Hz.

Performance evaluation and results

The performance of the probe was evaluated using a dedicated test rig [6]. The probe was mounted onto a simple flexure mechanism stage driven by an electromagnetic solenoid actuator. The actuator was driven to press the probe tip against a stationary high precision load cell. Meanwhile, the output of the PLL, LVDT monitoring the flexure displacement, load cell, and the input current were continuously recorded. Figure 2 shows a typical output plot. The probe triggers, the moment the PLL output has an incremental increase of about 10 mV (that is 10 Hz shift) from its pre-set value. Most of these tests were conducted on flat aluminium workpiece mounted into the load cell.

The relationship between the PLL output (Hz) and the interaction force of the probe/sample measured by the load cell is presented in figure 3. This shows a sensitivity of 12.8 Hz/mN, over an operating range in longitudinal direction of 130 mN, above which it saturates.

Figure 4 shows the uncertainty band of $\pm 2\sigma$ from the mean value as probe pressed against workpiece. At the trigger point, repeatability of ±20 Hz (±1.5 mN) was estimated but deviates to a maximum of ±200 Hz as indentation progress.

Dynamic performance was defined as the maximum possible triggering rate. This however, was limited by the bandwidth of the flexure mechanism 700 Hz at which the probe was still able to provide sufficient triggering signals. Figure 5 compares the PLL and the LVDT when exposed to slight variation in contact pressure as the result of thermal drift. It is clearly shown a sensitivity in submicrometre region.

Further tests were conducted on CNC CMM (Kemco E400) The probe was used to record the coordinates of the inside diameter of a master ring gauge. This was repeated over fifty times and the error in measurement was well within the resolution limit of the CMM (±1 μm).

Conclusion

The performance of a simple, relatively low cost, resonator-based touch-sensitive probe proposed for applications, which involve high precision coordinate measurement where high sensitivity and good repeatability are of paramount importance, has been evaluated. The results of the verification show that 3-dimensional sensitivity at mN contact force has been achieved. Triggering repeatability of ± 1.5 mN and triggering rate of more than 700 Hz have been demonstrated. Further development is currently under way using more than one sensor in the probe in an attempt to detect both the magnitude and direction of the contact force vector

Acknowledgement

The authors are grateful for support from both Coventry University School of Engineering and Nuffield foundation for supporting this research.

References

[1] Langdom R.M.', *J. Phys. E: Sci. Instrum., Vol. 18, 1985, pp 103-115*
[2] Gast, T., *J. Phys. E: Sci. Instrum., Vol. 18, 1985, pp 783-789*
[3] Mulder B. J., *J. Phys. E: Sci. Instrum, Vol. 17, 1984, pp 119-121*
[4] Binnig, G., Quate C.F. and Gerber C., , *Phys. Rev. Letts., Vol. 56, No. 9, pp. 930-933.*
[5] Martin, Y., Williams C.C. Wickramasinghe H.K, *J. Appl. Phys. 61 (10), 1987 pp 4723-29.*
[6] Harb S, Vidic M. *'to be published.*

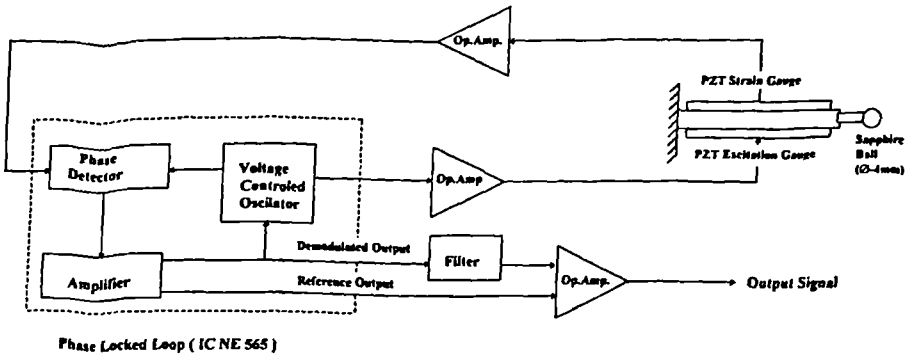

Figure 1. Schematic diagram of the touch sensitive probe

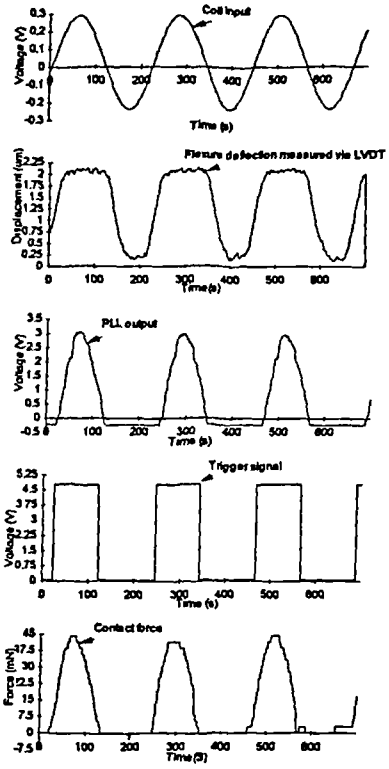

Figure 2. Typical plot showing Input sinewave, Flexure deflection, PLL output, and Trigger signal & Contact force

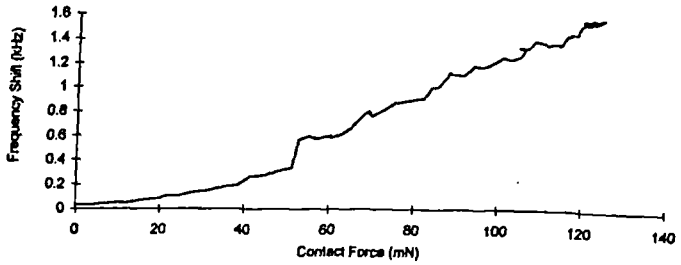

Figure 3. Frequency shift (kHz) versus applied contact force (mN)

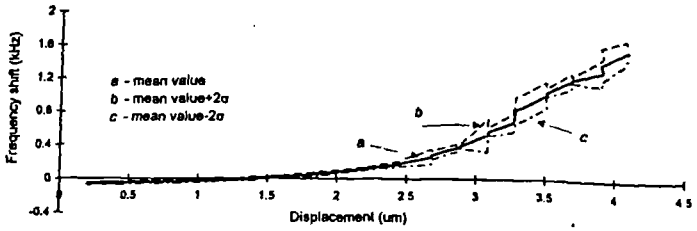

Figure 4. The mean value of the five cycles together with the ±2σ from the mean value

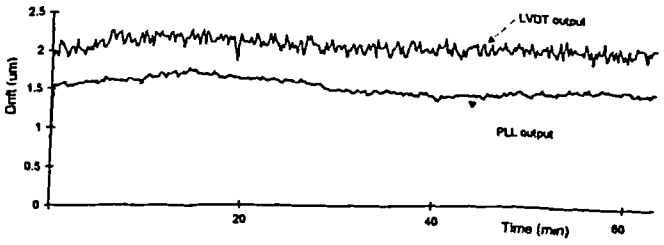

Figure 5. Drift test of the PLL and LVDT over a period of 1 hour

Proceedings of:

The Eleventh Annual Meeting

The American Society for Precision Engineering

November 9-14, 1996

Monterey Conference Center and Doubletree Hotel at Fisherman's Wharf

Monterey, California

The American Society for Precision Engineering (ASPE) is a multidisciplinary professional and technical society concerned with research and development, design, manufacture and measurement of high accuracy components and systems. ASPE activities encompass relevant aspects of mechanical, electronic, optical and production engineering, physics, chemistry, and computer and materials science. Membership is open to anyone interested in any aspect of precision engineering.

Founded in 1986, ASPE provides a new focus for a diverse but important community. Other professional organizations have covered aspects of precision engineering, always as a sideline to their principal goals. ASPE is based on the core of generic concepts necessary to achieve precision in any application; independent of discipline, ASPE intends to be the focus for precision technology — and to represent all facets from research to application.

ASPE — The American Society for Precision Engineering
401 Oberlin Road, Suite 108
P.O. Box 10826
Raleigh, NC 27605-0826
Phone (919) 839-8444 Fax (919) 839-8039

Observations of Contact Measurements Using a Resonance Based Touch Sensor

Marina Vidic, Salam M. Harb
School of Engineering, Coventry University, Coventry, UK
and
Stuart T. Smith
Precision Engineering Laboratory, UNC Charlotte, Charlotte, NC 28223

Introduction

Resonator based sensors have been proposed and used successfully in wide range of applications [1-3], which include measuring density and viscosity of gases or liquids, liquid level, sensing stress, pressure and mechanical forces. Although a considerable amount of work has been devoted towards the development of resonant touch sensors for scanned probe microscopy, commercial exploitation for precision applications has not been particularly successful. One of the reasons for this is due to the complexity of the interaction between a resonant sensor and typical surfaces in less than ideal environments. In this paper, a systematic study of the contact mechanisms between a resonator sensor and broad range of engineering surfaces are described. To do so, a resonator-based touch-sensor has been designed and manufactured and consists of a simple cantilever with actuators and sensors using PZT piezoelectric materials. Contact is detected by oscillating the sensor, which behaves like a second order system, near to its resonance frequency and monitoring the phase shift using phase locking techniques as the tip of the cantilever is approached towards a surface. The sensor could be employed for a broad range of applications including coordinate measuring machine probes, stylus transducers, friction measurement and surface mechanical probes (i.e. elastic modulus, density and energy dissipation). One particularly promising application is for monitoring changes in contact conditions or for the dynamic control of interface forces.

Sensor design and theoretical model

The resonator sensor used in the present investigation consists of a simple tip holder attached to one end of hexagonal BeCu rod (6x3.5 mm; l= 20 mm) and this is, in turn, mounted to a rigid base at the other. Mid way along the axis of the rod and symmetrically disposed are six piezoelectric elements. These form three pairs, each consisting of one actuator and one sensor on the opposing side. Consequently, drive and response signals can be monitored in terms of frequency and phase using standard phase locking circuits. In general any changes in force at the probe tip will effect the dynamics of the system. Such process can be modeled as a simple longitudinal oscillator of length, L, with the boundary conditions of added mass, stiffness and damping at the free end. Applying Rayleigh's approximate method to this system it is possible to derive a simple second order model with an undamped natural frequency given by

$$n = \sqrt{\frac{k_c + k_e}{M + m_e / 3}} \qquad (1)$$

where k_c, M, k_e, and m_e are the equivalent stiffness and mass of probe and the effective added stiffness and mass during contact, respectively.

In this discussion we shall separately consider the effects of added mass, stiffness and damping and assume that superposition applies. If any one of these dominates, it will also be shown that the effect can be systematically extracted from a series of three measurements. To visualize this Tables -I and II show the direction of the output from a phase locking amplifier for different types of loading (inertial, compliant or dissipative) on the sensor. In some cases, it is possible that two of the three influences will be insignificant. Under such conditions, it is desirable to identify the dominant effect. This can be deduced by systematically monitoring the changes in output with the probe set either side of. and at, the resonant frequency. Here, we shall consider two modes of detection commonly used for resonant sensors.

1. Monitoring frequency at constant phase shift between driver and sensor, hereafter called mode I
2. Monitoring phase at constant frequency, hereafter called mode II

In both of these modes, modeling is considerably simplified if small variations about a 90 degree phase shift are considered. In reality this is not easy to achieve and there is almost always a shift away from this ideal condition. Therefore it is necessary to consider the general effects of variations of the end condition on a second order system over a band of frequencies centered around the undamped resonance.

Table I: Direction of frequency shift for mode I operation of resonant sensor

Dominant factor	Phase angle in non contact state		
	$\|\phi\| < \|90\|$	$\|\phi\| = \|90\|$	$\|\phi\| > \|90\|$
Mass	Increase	Increase	Increase
Stiffness	Decrease	Decrease	Decrease
Damping	Increase	0	Decrease

Table II: Direction of phase shift for mode II operation of resonant sensor

Dominant factor	Phase angle in non contact state		
	$\|\phi\| < \|90\|$	$\|\phi\| = \|90\|$	$\|\phi\| > \|90\|$
Mass	Decrease	Decrease	Decrease
Stiffness	Increase	Increase	Increase
Damping	Decrease	0	Increase

Causes of parametric changes on resonant sensors

To simplify this discussion, only relatively large radius probes attached to a relatively stiff oscillator mount will be considered for two touch regimes, these being

1. Near surface phenomena
2. Mechanical contact

Near surface phenomena

As a resonating touch sensor approaches a surface a number of effects will be present which introduce a mechanical force. Such forces and their gradients will effect the frequency response characteristics of the probe. For non magnetic, clean materials in vacuum the only interactive forces will be those due to retarded and non retarded Van der Waals forces and electrostatic forces from surface charges. As evidenced by the rapid growth of the AFM industry, these effects can be significant for extremely compliant and sensitive probes. In our investigations such effects are considered negligible in relation to others that will be present during measurement of engineering surfaces in air. Under these conditions, it is likely that the dominant *near* surface forces will be those due to squeeze film damping and contaminant films on either the probe and/or the surface.

Surface films

The surfaces considered above are assumed to be perfectly clean and contaminant free. This is far from the case for many engineering surfaces and their typical environments. Commonly, surfaces will become covered by a condensed moisture film. As a consequence, there will be a surface tension force resulting in capillary action. It is speculated by Grigg *et al.* [4], that this leads to long range attractive forces of the order of tens of nanoNewtons and once the meniscus has been contacted will result in a force that can be calculated from the equation

$$F = \frac{4AR\,\gamma\cos(\theta)}{(1 + x/d)} \qquad (2)$$

where θ is the contact angle, d is the film thickness on both probe and specimen (assumed equal) and γ is the free surface energy (72 mJ m^{-2} for water).

Squeeze film damping between a sphere and a flat

For relatively low velocities, as is the case for small oscillations at the frequencies used in the following experiments, the normal force, F, between a sphere and a flat surface separated a distance x is given by the equation [4],

$$F = \frac{3\pi\mu}{x^2 p_a r^3 (1+r^2)^2} \frac{dx}{dt} \tag{3}$$

where, μ is the viscosity of the medium between sphere and flat, p_a is the ambient pressure and r is radius of sphere.

It should be noted that the force is both proportional to the velocity and inversely as the square of the separation between the two surfaces

Mechanical contact

In all of the following, it will be assumed that the oscillation amplitude is sufficiently small that 'bouncing' does not occur. In practice, this will only occur if there is a sufficient load at the contact. This load can be a combination of both the applied and self generated (i.e meniscus and adhesion forces) components.

Effective stiffness (k_e)

From Hertzian analysis, it is relatively straightforward to show that the local stiffness for small oscillations of an elastic contact is given by the familiar equation [6],

$$k_e = (6E^2 PR)^{1/3} \tag{4}$$

where E, P *and* R are Young's modulus, contact force and probe radius, respectively.

Effective mass (m_e)

Upon physical contact with a material the region of the interface must be moving at the same frequency as the motion of the probe tip and will thus add an inertial load. Clearly, this will extend into the specimen with diminishing amplitude. To assess the effective added mass, it will be assumed that the specimen is smooth and flat and the probe is also smooth, has an effective radius, R. For velocities of the probe much less than those of stress waves in the contact materials, it is reasonable to assume that the strain field is the same as that derived from Hertz analysis. For a probe having an elastic modulus of considerably higher value than that of the specimen, the effective mass for small oscillations can be approximated as

$$m_e \approx \frac{\pi^2 PR}{2E}(1-\upsilon^2)\rho \tag{5}$$

where ν and ρ are Poisson's ratio and density of the material, respectively.

This equation indicates that the added mass becomes significant for materials with high density and low modulus of elasticity e.g. natural rubber. Fig.1, shows the theoretical phase shift in the resonant probe for a selection of different materials under various loads, which was calculated using equations (1), (4) and (5) and estimated values for damping and coupling loss factor (ζ).

Effective damping (h_e)

Most compliant materials such as rubber and plastics can be characterized as exhibiting dissipation characteristic of hysteretic damping. Mathematically, this can be modeled as complex stiffness (often referred to as structural damping). A second order system with hysteresis damping, h_e, subject to sinusoidal input can be characterized by the equation:

$$m\ddot{x} + k(1 + ih/k)x = F_0 e^{i\omega t} \tag{6}$$

Assuming a solution of the form $Xe^{i\omega t}$, and also that the hysteresis is predominantly due to the cyclic adhesion between the two surfaces, h_e can be solved to give:

$$h_e = 1.23\gamma_{12}\left[\frac{R^4 P}{E\Delta x^6}\right]^{2/9} \tag{7}$$

where, γ_{12} and Δx are the interfacial energy characterized by the Dupré equation and amplitude displacement of the probe at the interface respectively.

Experimental results

To assess the interaction between a probe tip and typical engineering surface the resonator touch probe was mounted onto a simple linear flexure stage for fine positioning, Fig.2. This was then positioned horizontally, in line with a stationary specimen. The contact force between the probe tip and a specimen was monitored using two strain gauges in a half bridge arrangement, mounted onto the specimen. During these experiments, the phase shift in mode I operation (or frequency shift for mode II operation) and applied forces were recorded as the probe approached and contacted the surface.

Contact characteristics of thick oil film

Experiments were conducted to assess the influence of a thick oil film with the reference frequency or phase set to each side of the free resonance. Fig.3 shows a typical plot of the probe's phase shift from the free value (non contact) set to-81 degrees, Fig. 3*a*., and -100 degrees, Fig. 3*b*, as it was contacted with a thick layer of silicone oil having a relatively high viscosity of approximately 10 Pa s. A number of distinct regions could be seen on the graphs. The first region corresponds to approach of the probe tip towards the oil surface prior to physical contact where there is an increase in phase in both figures which from table II indicates a predominant inertial force. The immediate contact with the oil results in the reduction in phase in Fig. 3*b*, which is not present in Fig. 3*a*. Referring again to Table II, it is possible to explain this as an effective damping which would add to the inertial effect with opposite sign either side of the resonant frequency. Upon further displacement of the probe into the oil the phase shift increases and it could be observed that in Fig. 3*a*, it has opposite curvature to the one in, Fig. 3*b*, but at a faster rate for phase less then -90 degrees. Referring to the Table II. this suggests that if the free value is below resonance, the two predominant effects, mass and damping, are summed, while the value above the free resonance results in their difference. As the probe approaches the surface the phase increases to a value above |90| degrees at which point an additional damping results in a reduction of the phase. When mechanical contact takes place, phase rapidly reduces as a result of a large increase in effective stiffness. Retracting the probe away from the surface, the phase shift mirrors the original approach curve although there is a permanent offset of +2 degrees. Cleaning of the probe after separation from the film returned the phase to the original free value of -81 degrees, or -100 degrees.

Contact of solid surfaces

A number of experiments were conducted on different type of materials: PTFE, aluminum, copper, steel, glass and two types of rubber. Fig. 4 shows a typical plot of a probe's phase shift in mode II operation when contacted with these solid surfaces. Prior to each experiment the surface were thoroughly cleaned using acetone. In Fig. 4*a*, and 4*b* the free value phase shift was set at -85 degrees and -100 degrees, respectively. For PTFE, the phase shift starting at less than |90| degrees was decreased of less than one degree, whereas for glass it was decreased of more than 25 degrees, for the same contact force. When this compared with similar test but for phase shift starting from above |90|, materials like PTFE resulted in more or less similar decrease in phase of less than one degree whereas for glass it was decreased about 20 degrees. Close comparison with other materials tested indicates that, on average, the difference in the phase shift for the same material is about 5 degrees when the phase is below and above |90| degree. Again, referring to Table I. this suggests that this is the contribution of the added damping in the system although these large phase shifts may include other non symmetric factors. As predicted, all the materials tested in Fig. 4 show a reduction in phase, but at different rates, which indicates that added stiffness is the predominant effect. In contrasst, similar tests conducted with rubber show an increase in phase which indicates the relatively high density and low elastic modulus results in added mass being the predominant effect, Fig.5.

Discussion and conclusion

It has been shown that the dynamics of a resonant probe sensor as it approaches typical engineering surfaces is subject to a complex variety of forces leading to the observation of effects characteristic of inertial, stiffness and damping forces. These characteristics will superpose making the separation of individual terms rather complex. However, it has been shown that observation of dynamic characteristics either side of the resonant frequency may provide a systematic method to identify the predominant effect. Preliminary theoretical and experimental investigations on both contact of thick oil films and solid surfaces provide encouraging results.

It is also speculated that further analysis of oscillatory contact with solid surfaces and comparison with corresponding hardness scales could lead to potential applications in non-destructive hardness testing. That the shift in the resonant frequency (or phase shift) depends on near surface properties such as the elastic modulus, hardness, density and internal damping makes the quantitative measurements of a number of physical properties an exciting possibility.

Acknowledgments

The authors are grateful to Coventry University and the Nuffield Foundation for supporting this research.

References:

[1] Langdon R.M. Resonator sensors-a review, *J. Phys. E: Sci.Inst.*, **18** (1985), 103-115.

[2] Morten, B., De Cicco, G., Prudenenziati, M. Resonant pressure sensor based on piezoelectric properties of ferroelectric thick films, *Sensors and Actuators A*, **31** (1992), 153-158.

[3] Omata, S. and Terunama, Y. Development of a new type tactile sensor for detecting hardness and/or softness of an object like the human hand, IEEE, 1991, 868-971.

[4] Gross W. A., 1962, *Gas Film Lubrication*, John Wiley and Sons, NY, p325

[5] Grigg D.A., Russell P.E. Griffith J.E. Tip-sample forces in scanning probe microscopy in air and vacuum *J.Vac.Sci. Technol.*, **A10**(4) 680-683.

[6] Smith, S.T. Chetwynd D.G. *Foundations of Ultraprecision Mechanism Design*, Gordon and Breach, 1992, NY.

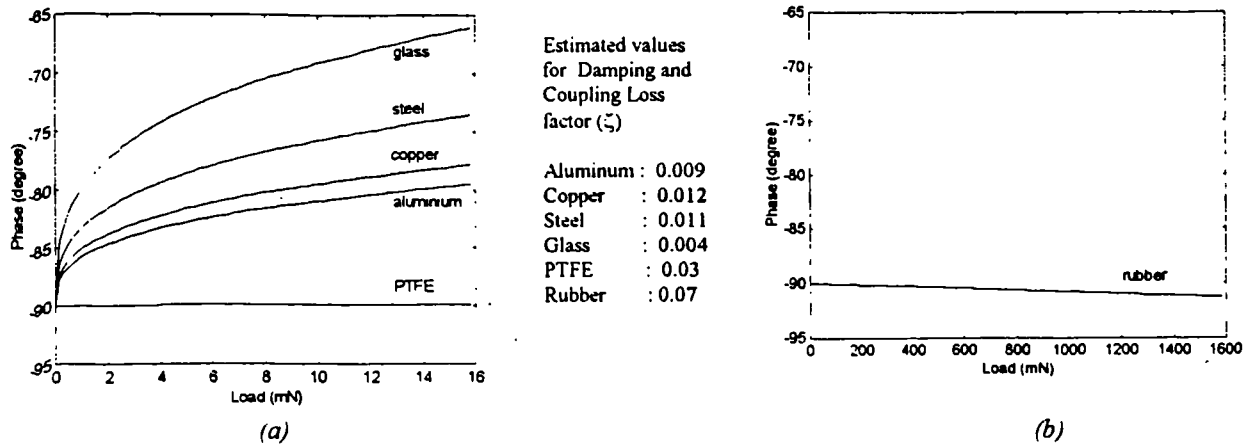

Figure 1. Mathematical results representing the phase shift in a resonant probe for a selection of different materials as a function of applied load and for given probe geometry.

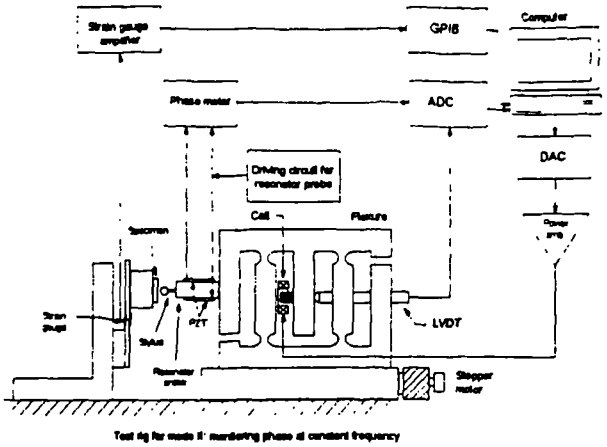

Figure 2. Schematic diagram of the test rig used to monitor the contact between resonator probe and solid surfaces

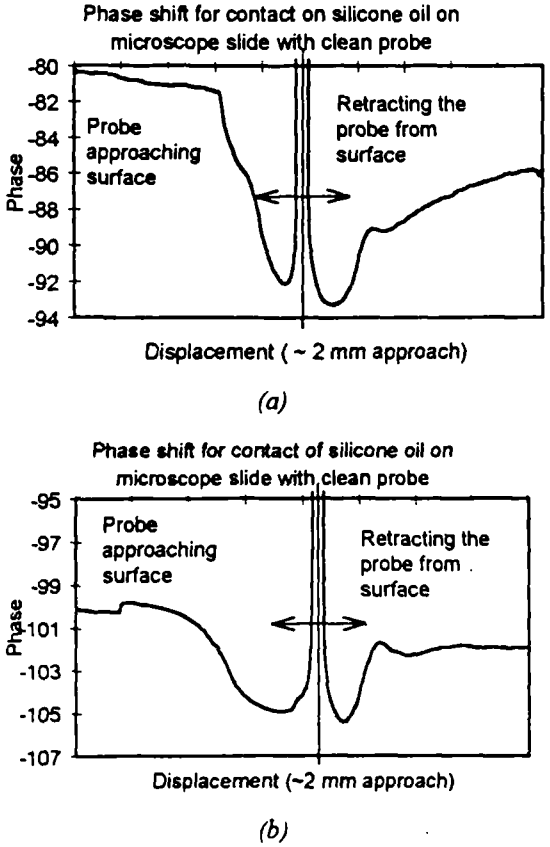

Figure 3. Plot showing contact characteristics of thick oil film for phase shift of *a*) -81 degrees and *b*) -100 degrees

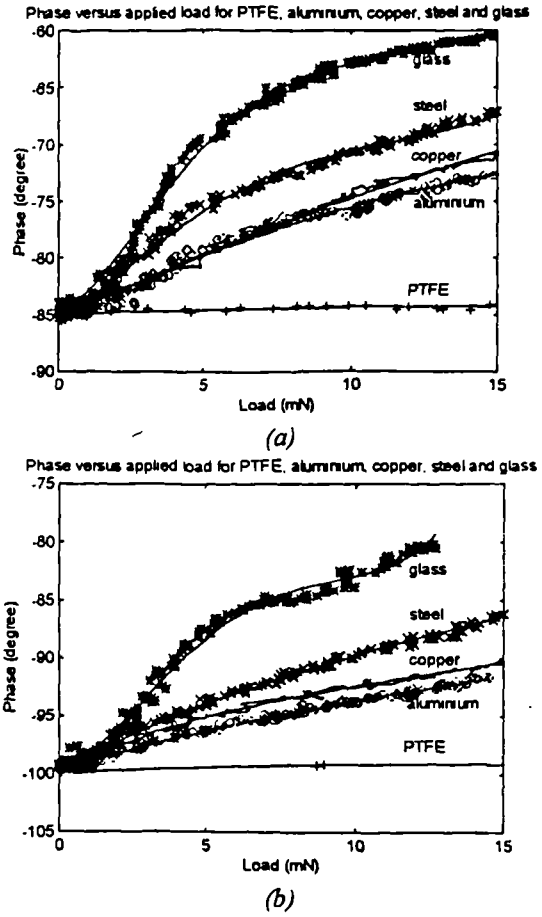

Figure 4. Plot showing phase shift when probe contacts solid surface for free shift of *a*) -85 degrees and, *b)* -100 degrees.

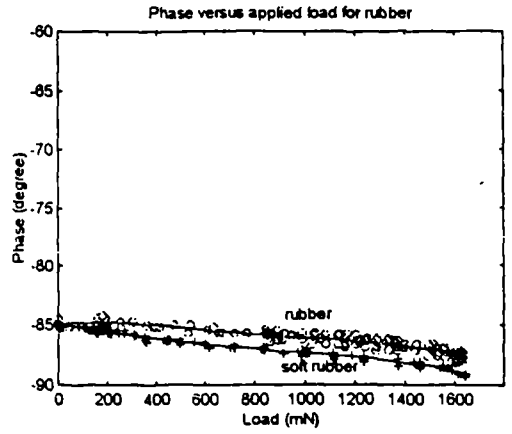

Figure 5. Plot showing phase shift when probe contacts rubber like materials

Resonator Based Profilometer Instrument

S.M. Harb, MSc. PhD., M. Vidic, MPhil, and S.T. Smith*, PhD.
Coventry University, Coventry, CV1 5FB, UK
** Precision Engineering Laboratory, UNC Charlotte, Charlotte, NC 28223*
E-mail : s.harb@coventry.ac.uk

Abstract

The design of a simple 2-dimensional resonator profilometer is presented. This instrument provides useful information of engineering surfaces such as height variations, edge point detection and some surface properties variations mainly elastic modulus and density. In this design the resonator probe is used to monitor the interfacial forces between stylus and a surface specimen along *the* z-axis and provides a feedback error signal into a digital piezoelectric translator (DPT) in order to maintain constant contact force. The specimen is scanned beneath the probe using a high precision single degree of freedom polymer bearing slideways monitored by a laser interferometer system. As the specimen is traversed, the probe 'feels' the contact force, and moves up and down to maintain constant force. Specimens ranging from thin metallic films to flat glass surfaces are used to illustrate its metrological capability.

1. Introduction

Resonator probes have been used for several decades in a broad range of applications which required high precision sensors. These includes sensors for liquid or gas density and viscosity, liquid level, mass, and microbalance [1,2]. They have also been very popular in the design of scanning probe microscopy [3]. The principle operation of these sensors is based on the fact that when a mechanical element oscillated at one of its resonance frequency comes into near-contact or contact with another object it alters the stiffness, mass or shape of the resonator consequently causing changes in the resonant frequencies. This can be detected by monitoring the phase, the amplitude or the impedance of the signal. These sensors are designed such that the resonator's natural frequency is a function of the measurand.

This paper presents the design and results of a simple resonator profilometer using a probe initially designed as an analogue touch sensitive

sensor for coordinate measuring machines [4]. In this design the resonator probe is oscillated using a pair of PZT plates one to drive and the other to pick-up the generated strain signal. The signal is fed into a phase locked loop (PLL) analogue circuitry which drives and detects the shift in resonance frequency. In this application, the probe is used merely as a nulling device in closed loop system to profile a range of different substrates with different material properties. The signal of the PLL, after passing through a PID controller, is appropriately amplified and used as a closed loop error signal to feed a digital piezoelectric translator (DPT), which in turn is used to control the vertical displacement of the probe at nanometer resolution. A 2 μm diamond tip stylus was used. The specimen is manipulated underneath the probe using a high precision single degree of freedom polymer bearing slideway. As the specimen is scanned, the probe feels the contact force, and moves up and down in order to maintain constant force at the stylus/ specimen interface. The vertical displacement is used to provide height, edge point detection and properties variations of the surface. Resonator traces over reasonably flat multi-surfaces are presented

When traces were compared with similar ones obtained using Taylor Hobson Talystep, noticeable discrepancies between both readings were apparent, particularly when different materials were encountered during a scan. This has instigated a more thorough investigation into the contact mechanism between the probe and specimen surface, Vidic [6].

2. Probe design and Theory

The experimental investigation of this study was conducted using a resonator sensor consisting of a cantilever beam that is vibrating longitudinally. For such system the resonance frequencies of an unloaded (no contact) probe are given by [5]:

$$\omega_i = \frac{(2i-1)\pi}{2l}\sqrt{E/\rho} \qquad (1)$$

$(i=1,2,3, ...)$

where, E, ρ , and l are Young's modulus, density and probe length, respectively.

In general any changes in forces at the end of the probe will affect the dynamic characteristics of the system and hence its resonance frequencies. The interaction between an oscillating probe and contacting surfaces can be modelled as a simple longitudinal oscillator of length l, with boundary conditions of added mass m_e, stiffness, k_e, and damping, h_e at the free end. Applying Rayleigh's approximate method, it is possible to derive a simple second order model with a natural frequency given by :

$$\omega_n \approx \sqrt{\frac{k_c + k_e}{M + m_e/3}} \qquad (2)$$

where k_e and m_e are given by [6]

$$k_e = (6E^2 P_o R)^{1/3} \tag{3}$$

$$m_e \approx \frac{\pi^2 P_o R}{2E}(1-\upsilon^2)\rho \tag{4}$$

Above relations indicate the dependency of the resonance frequency on normal load P_0 , elastic modulus E, poisson ration υ and density ρ for a given probe raduis.

3. Profilometer Instrument

The profilometer probe used consists of an aluminum rod of rectangular shape (5x5x10 mm) oscillated using a pair of piezoelectric plates, one drive actuator and one pick-up sensor mechanism, cemented on the opposite sides of the beam. The probe itself consists of a standard 2 μm diamond tip stylus screwed into the free end of the rectangular rod.

Although the resonance frequency of the device strongly depends on its mounting arrangement, it is typically in the region of 18.5 kHz with behavior characteristic of a second order system. An analogue phase lock loop (PLL) NE 565 integrated circuit is used to oscillate the probe at one of its resonance frequencies and monitor the frequency shift as the result of interfacial force variations. Figure 1 shows the block diagram of the control system of the resonator probe. During these experiments, the phase shift between the drive and the strain signal was set near -90°. As contact (or near contact) takes place, changes in resonance frequency shift the phase angle from its preset value. Almost instantly, the PLL techniques adjusts the driving signal frequency to null the change in phase angle and producing a proportional output signal with a conversion rate of 0.73 mV Hz^{-1} . A typical probe contact characteristic against a clean aluminum surface is shown in figure 2 [4].

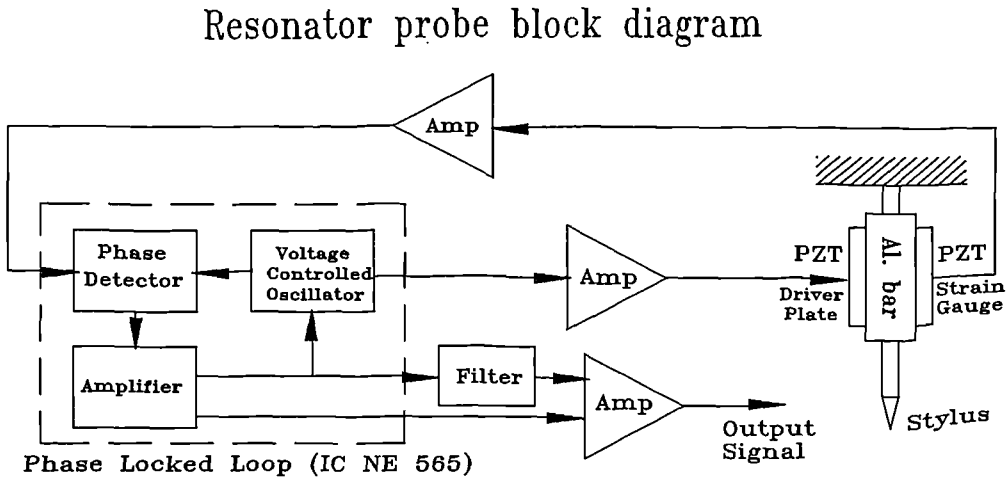

Figure 1. Schematic diagram indicating elements of the resonator probe

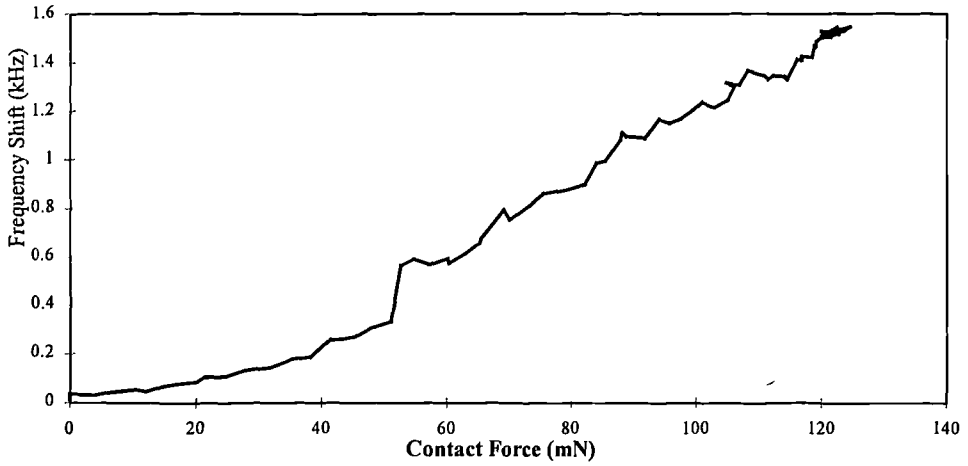

Figure 2. Frequency shift (kHz) versus interfacial force (mN) between 5 mm sapphire spherical probe and clean flat aluminum surface.[4]

For this application, the complete resonator has been mounted to the *z* translator, the underside of a vertical piezoelectric translator (QueensGate Instruments model S300 digital piezoelectric translator, DPT), the holder of which forms part of a z-axis coarse positioner. DPT consists of tubular piezoelectric actuator (PZT) with a capacitance sensor along the central axis to monitor the actual extension. The DPT translator has a linear extension range of 15 μm with noise level of 0.6 nm rms. at bandwidth of 1100 Hz. The z axis is mounted into a rigid fixed bridge above a horizontal slideway.

As shown in the schematic, figure 3, the height and mechanical properties such as elastic modulus and density variations of a surface imposes an interfacial force variations which will affect the dynamic characteristics of the probe and causing a shift in its resonance frequency. This shift is detected by the PLL which produces an output voltage ,after being filtered and amplified, proportional to surface profiles and variations in some of its physical properties. This signal is fed through a proportional -integrator - differentiator (PID) to the z-axis servo controller. The objective of the feed-back loop is to maintain the interfacial force between the stylus tip and specimen at a fairly constant level (the set static force).

Specimens were scanned beneath the probe using a high-precision glass-ceramic (Zerodur) polymer bearing slideway. The carriage is actuated by a DC motor through a transmission system consisting of micrometer and a hysteric coupling. Horizontal displacement of the carriage was monitored using a Michelson based laser interferometer system.

To obtain a trace of the surface, the specimen is first secured onto the aluminum carriage, and then aligned parallel to slideway surface using angular adjustment mechanism attached to the carriage. The probe is then brought into close contact with the surface until PLL output registers a value corresponding to the static force, half of the probe's range, at which point the control loop is closed. As the carriage traverses, at approximately 1 mm/sec, the PID error signals feeding the DPT to correct for any height/ properties variations, are recorded into an IBM-compatible PC, via an ADC data acquisition board. Simultaneously, the reading of the laser interferometer system is recorded via standard RS232 interface. Recording and analysing data were facilitated using application programmes LabView[1] and MicroSoft Excel software packages.

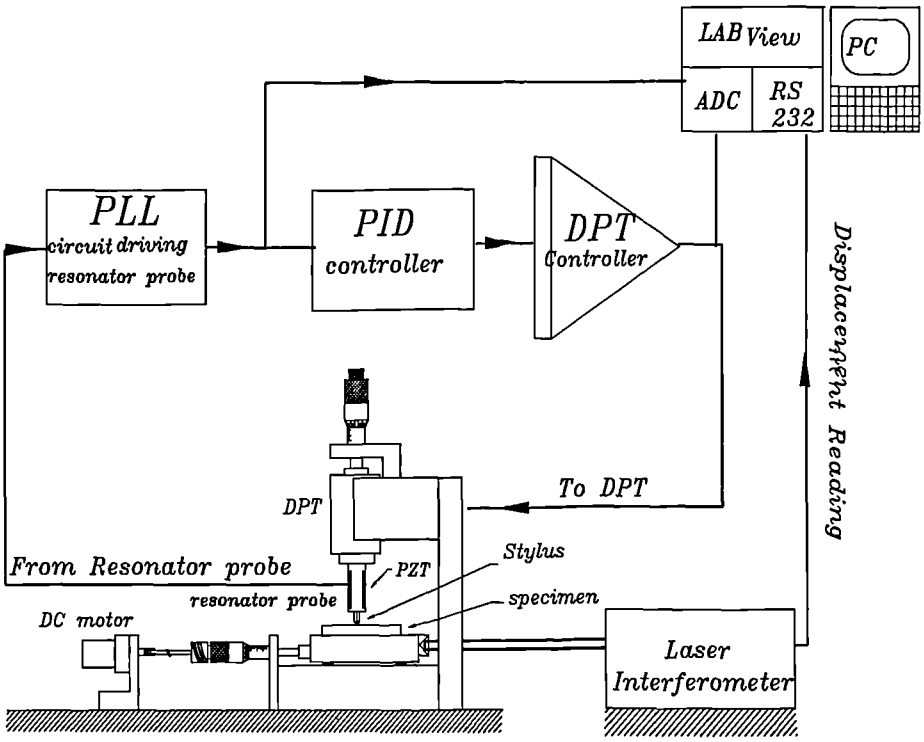

Figure 3. Schematic diagram of the resonator profilometer

4. Performance and Results

Traces over reasonably flat engineering surfaces ranging from ground and lapped steel to flat glass and silicon surfaces, some partially coated with aluminum and gold, were tested and analysed.

[1] National Instrument

Figure 4 shows a typical resonator profile over a scratched glass microscope slide surface. In this, more than 8 traces in uni-direction were recorded over the same line and the results were fairly consistent and reproducible. A similar test was conducted over a 100 nm step height etched on a silicon wafer, figure 5. Repeating the measurement shows same features and the step height measured was very close to the expected value.

Figure 6 shows typical resonator profiles over a microscopic slide partially coated with a thin film of aluminum, nominally 50 nm. In these traces, measurement starts when the probe is in contact with glass surface and traversed to cross over the aluminum film and then traversed back to the starting point. Readings over glass surface, aluminum film and at the transition region were recorded. As shown in figure 6 repeating the same traverse produced very similar profiles which indicates the consistency of the measurement. However, the interesting point that can be inferred from these traces is the behaviour of the probe when it encounters different surfaces. At the cross over region the probe exhibits rapid changes which surely do not correspond to the actual height variations but more likely it is due to sudden changes in the physical properties which forces the controller to exaggerate the probe's height displacements to about 4.5 μm, in order to compensate for these changes. After the probe crosses over completely, the controller settles down and the variations in profile can be attributed mainly to the surface topography. Comparing this with similar traces obtained using stylus type surface measuring instrument (Talystep), figure 7 shows that the transition between the surfaces is much smoother. Nonetheless, the magnitude of the film measured by the both instruments was not far out, taking into account that neither Talystep nor the resonator profilometer were reliably calibrated prior to these tests.

Similar traces were repeated over microscope slide coated with nominally 100 nm film of gold figure 8. In these similar result were observed indicating clearly the transition region between the surfaces. However, the magnitudes of jumps were less evident, about 0.5μm, compared to previous one (figure 6).

5. Conclusion

A prototype resonator profilometer has been designed and tested. Resonator traces over various reasonably flat engineering surfaces were recorded and results indicate the probe's response to the height variations (surface topography) and surface properties variations. Of particular interest are the variation in Young's modulus and density. These were evident when multi surfaces was scanned. The instrument shows high sensitivity in detecting the edge point (i.e. the transition between two surfaces).

Further work is currently underway to extend the design into 3-dimensional surface characterisation and to be able to correlate generated

profiles to some useful surface properties. This however, may require incorporating this instrument with a conventional stylus measuring device in order to differentiate topography from the interesting physical properties.

Acknowledgment

This material is based upon work supported by Coventry University Central Funding Scheme. Dr. Harb would like to thank Royal Academy for engineering and Nufflied foundation for supporting his visit to the Precision Engineering Laboratory at The University of North Carolina at Charlotte and also Mr. G. Singh and R. Edgeworth of the Precision Engineering group at UNCC Charlotte for their help and support.

Keywords: *resonator touch sensors, piezoelectric, contact force, surface characterisations, scanning force microscope (SFM), force probe, edge point detection*

References

[1] Langdon R.M. Resonator sensors-a review, *Review article, J. Phys. E: Sci. Instrum.*, **18**, 1985, 103-115.

[2] Morten, B., De Cicco, G., Prudenenziati, M. Resonant pressure sensor based on piezoelectric properties of ferroelectric thick films, *Sensors and Actuators A*, **31** (1992), 153-158.

[3] Wienmann, M. Raduis, R. and Assmus, F. Measuring profile and position by means of vibrating quartz resonators used as a tactile and nontactile sensors, *Sensors and actuators A*, **37-38** (1993) 715-722.

[4] Harb, S.M., Vidic, M. Resonator-based touch-sensitive probe, *Sensor and Actuators*, **A50** (1995), 23-29.

[5] Smith, S.T. Chetwynd D.G. *Foundations of Ultraprecision Mechanism Design,* Gordon and Breach, (1992), NY.

[6] Vidic, M., Harb, S.M., and Smith, S.T., Observation of contact measurements using a resonance based touch sensor, *Precision Engineering* submitted for publication.

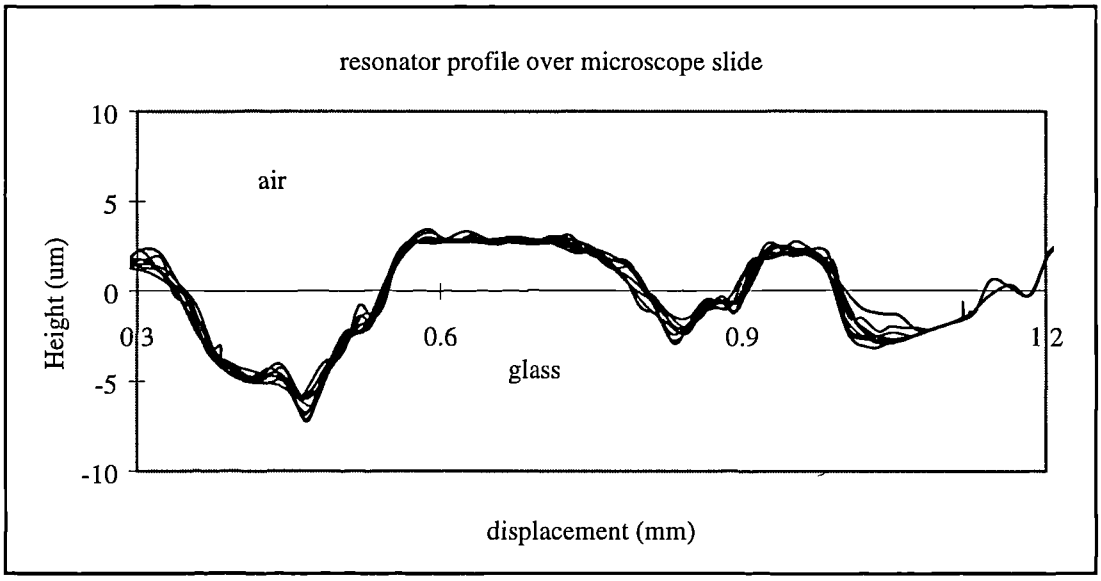

Figure 4 Typical traces over scratched microscope slide glass surface

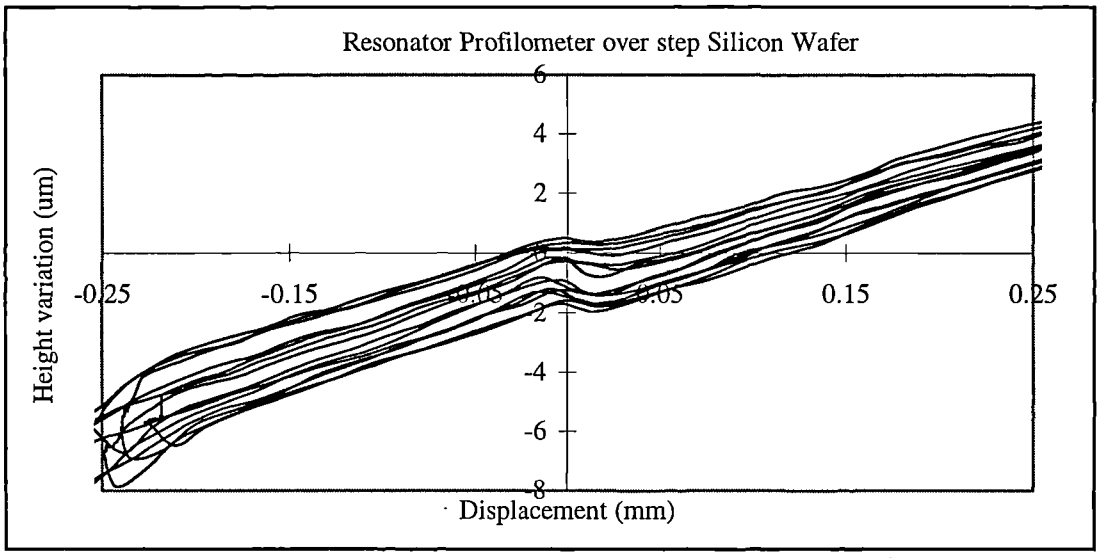

Figure 5 Typical resonator profile over a step height on a silicon wafer

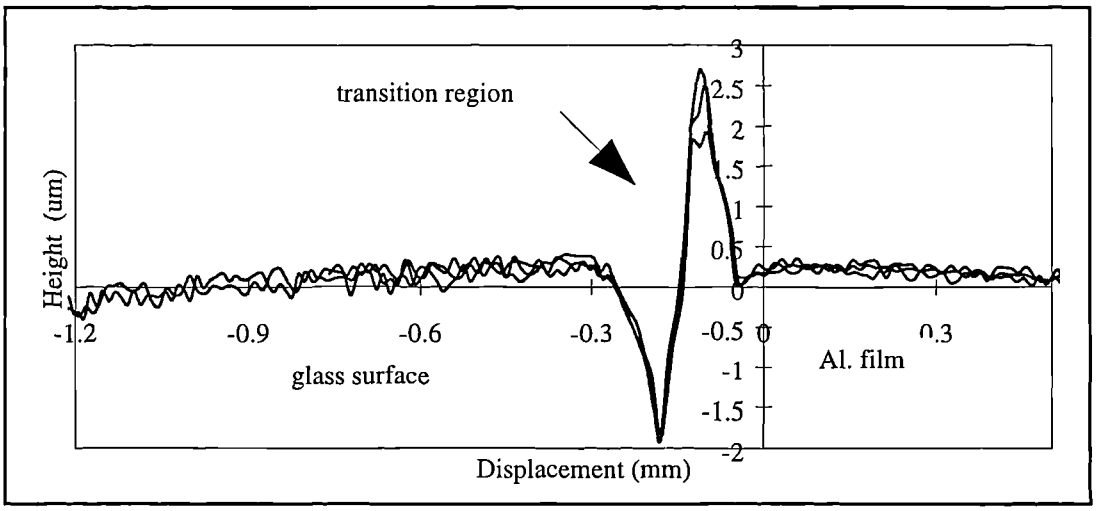

Figure 6 Profiles over a microscopic slide partially coated with 50 nm film of aluminum.

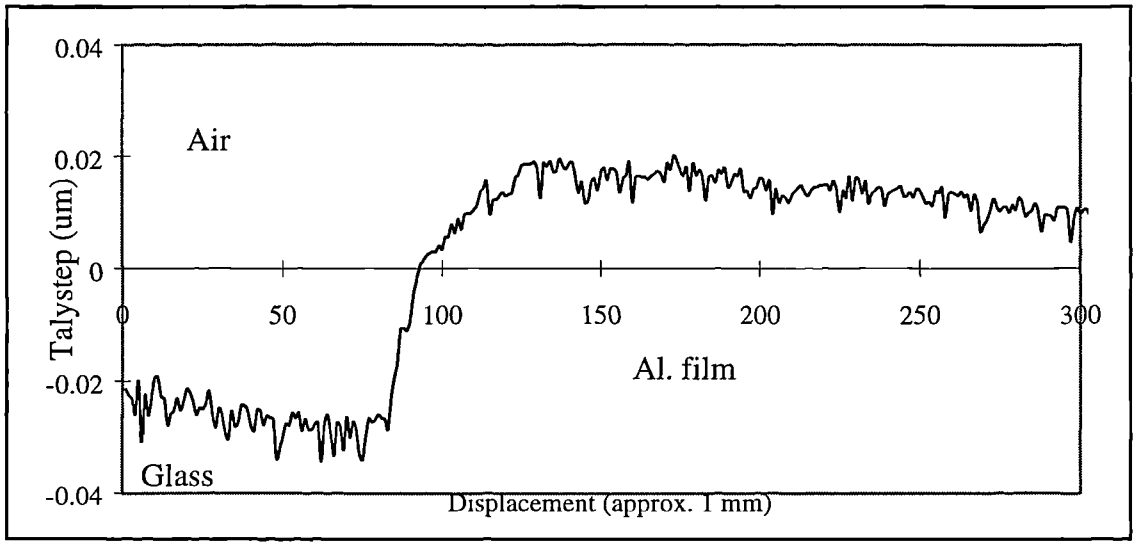

Figure 7. TalyStep trace over the same specimen in figure 5.

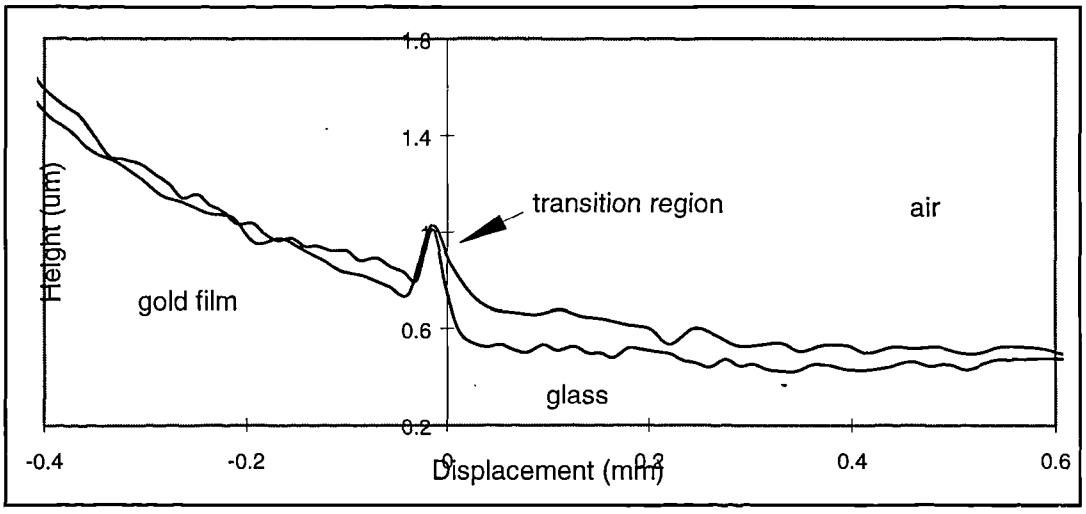

Figure 8. Resonator profile over 100 nm film of gold over glass surface